Magnetotelluric Investigation of Northern Harrat Rahat, Kingdom of Saudi Arabia

Chapter L of

Active Volcanism on the Arabian Shield—Geology, Volcanology, and Geophysics of Northern Harrat Rahat and Vicinity, Kingdom of Saudi Arabia

U.S. Geological Survey Professional Paper 1862
Saudi Geological Survey Special Report SGS–SP–2021–1

U.S. Department of the Interior
U.S. Geological Survey

Cover. Field technicians demonstrate their digging skills with an impressive installation of a vertical magnetic induction coil (1.5 meters long). The coil measures variations in natural magnetic fields and when compared with similar horizontal measurements provides information about subsurface electrical resistivity structures from depths of a few tens of meters down to tens of kilometers. This helps researchers characterize magmatic systems by imaging where magmatic fluids are in the crust. U.S. Geological Survey photograph. Background image shows northern Harrat Rahat lava flows, maars, and lava domes. U.S. Geological Survey photograph by Andrew Calvert, January 25, 2012.

Magnetotelluric Investigation of Northern Harrat Rahat, Kingdom of Saudi Arabia

By Jared R. Peacock, Paul A. Bedrosian, Maher K. Al-Dhahry, Adel Shareef, Daniel W. Feucht,
Cliff D. Taylor, Benjamin Bloss, and Hani M. Zahran

Chapter L of

**Active Volcanism on the Arabian Shield—Geology, Volcanology, and Geophysics
of Northern Harrat Rahat and Vicinity, Kingdom of Saudi Arabia**

Edited by Thomas W. Sisson, Andrew T. Calvert, and Walter D. Mooney

U.S. Geological Survey Professional Paper 1862
Saudi Geological Survey Special Report SGS–SP–2021–1

U.S. Department of the Interior
U.S. Geological Survey

U.S. Geological Survey, Reston, Virginia: 2023

Suggested citation:
Peacock, J.R., Bedrosian, P.A., Al-Dhahry, M.K., Shareef, A., Feucht, D.W., Taylor, C.D., Bloss, B., and Zahran, H.M., 2023, Magnetotelluric investigation of northern Harrat Rahat, Kingdom of Saudi Arabia, chap. L *of* Sisson, T.W., Calvert, A.T., and Mooney, W.D., eds., Active volcanism on the Arabian Shield—Geology, volcanology, and geophysics of northern Harrat Rahat and vicinity, Kingdom of Saudi Arabia: U.S. Geological Survey Professional Paper 1862 [also released as Saudi Geological Survey Special Report SGS–SP–2021–1], 111 p., https://doi.org/10.3133/pp1862L.

Associated data for this publication:
Bedrosian, P.A., Peacock, J.R., and Feucht, D.W., 2023, Magnetotelluric data from northern Harrat Rahat, Saudi Arabia, 2016: U.S. Geological Survey data release, https://doi.org/10.5066/P99H8HJ7.

ISSN 1044-9612 (print)
ISSN 2330-7102 (online)

هيئة المساحة الجيولوجية السعودية
SAUDI GEOLOGICAL SURVEY

Ministry of Industry and Mineral Resources
BANDAR BIN IBRAHIM BIN ABDULLAH AL-KHORAYEF, Minister and SGS Chairman

Saudi Geological Survey
Abdullah bin Mufter Al-Shamrani, Chief Executive Officer

Saudi Geological Survey, Jiddah, Kingdom of Saudi Arabia: 2023

Contents

Figures

Conversion Factors

International System of Units to U.S. customary units

Multiply	By	To obtain
	Length	
meter (m)	3.281	foot (ft)
kilometer (km)	0.6214	mile (mi)
kilometer (km)	0.5400	mile, nautical (nmi)
meter (m)	1.094	yard (yd)
	Flow rate	
kilometer per second (km/s)	0.6214	mile per second (mi/s)
	Density	
gram per cubic kilometer (g/cm^3)	62.4220	pound per cubic foot (lb/ft^3)

Temperature in degrees Celsius (°C) may be converted to degrees Fahrenheit (°F) as follows:

$$°F = (1.8 \times °C) + 32.$$

Datum

Vertical coordinate information is referenced to the World Geodetic System of 1984 (WGS 1984).

Abbreviations

1D	one dimensional
2D	two dimensional
3D	three dimensional
AF	anisotropy factor
AZ	anisotropy direction
C.E.	Common Era
g/L	gram per liter
Hz	hertz
LAB	lithosphere-asthenosphere boundary
Ma	mega-annum
Moho	Mohorovičić discontinuity
MT	magnetotelluric
NIMS	Narod Intelligent Magnetotelluric Systems
Ω·m	Ohm meter
rms	root mean square
s	second
S	siemen
SGS	Saudi Geological Survey
USGS	U.S. Geological Survey

Active Volcanism on the Arabian Shield
Edited by T.W. Sisson, A.T. Calvert, and W.D. Mooney
U.S. Geological Survey Professional Paper 1862
Saudi Geological Survey Special Report SGS–SP–2021–1

Chapter L

Magnetotelluric Investigation of Northern Harrat Rahat, Kingdom of Saudi Arabia

By Jared R. Peacock,[1] Paul A. Bedrosian,[1] Maher K. Al-Dhahry,[2] Adel Shareef,[2] Daniel W. Feucht,[1] Cliff D. Taylor,[1] Benjamin Bloss,[1] and Hani M. Zahran[2]

Abstract

Volcanism within the harrats (Arabic for “volcanic field”) of the Kingdom of Saudi Arabia includes at least one historical eruption occurring close to the holy city of Al Madīnah in 1256 C.E. As part of a volcanic- and seismic-hazard assessment of northern Harrat Rahat, magnetotelluric (MT) data were collected to investigate the structural setting of the area, the presence or absence of melt within the crust, and the mantle-derived magmatic source. Collected MT data were modeled in both two dimensions, where anisotropy can be estimated, and three dimensions. Interpretation of the preferred resistivity model includes a shallow sediment-filled graben beneath northern Harrat Rahat lavas, a melt-free upper crust, and a region of decompression melting in the asthenosphere below 60–70 kilometers depth. Models in two dimensions image the lower crust as anisotropic, demonstrating that a series of elongate conductivity anomalies with a strike of N. 10° E. within the lower crust of the three-dimensional model are artifacts of inverting anisotropic data with an isotropic modeling algorithm. Careful examination of the resistivity models, in combination with regional geological and geophysical data, suggests an anisotropic lower crust that is free of large zones of melt. Azimuthal anisotropy in the lower crust extends well beyond the limits of Harrat Rahat volcanic rocks, with a conductive direction oriented N. 10° E. and an anisotropy factor of 2–5 between the most and least conductive directions. Enhanced conductivity is likely caused by interconnected grain-boundary graphite, where the direction of anisotropy reflects either frozen-in fabric from the Neoproterozoic stabilization of the Arabian Shield or ductile deformation driven by channelized asthenospheric flow coupled with a thin rigid mantle lid. Asthenospheric melt is interpreted to transect the crust largely through diking, with limited melt storage and short residence times within the crustal column.

Introduction

Harrat Rahat, on the western margin of the Kingdom of Saudi Arabia, is the largest of the Arabia Plate continental, intraplate volcanic fields wholly within the Kingdom of Saudi Arabia (Coleman and others, 1983; Camp and Roobol, 1989, 1992). The Holocene eruption of 1256 C.E. (Camp and others, 1987; Downs and others, 2018) near the holy city of Al Madīnah al Munawwarah (Al Madīnah hereafter) suggests future eruptions will have societal and economic impacts. Understanding the magmatic system at depth will help in understanding impacts of future eruptions. As part of the volcanic- and seismic-hazard assessment conducted as a joint project between the Saudi Geological Survey (SGS) and the U.S. Geological Survey (USGS), a regional magnetotelluric (MT) survey was conducted. This report details how the data were collected, processed, modeled, and interpreted. See Bedrosian and others (2019) for more details on the interpretation.

Method

Magnetotellurics is a passive electromagnetic method that measures the Earth’s electrical response to natural time-varying magnetic fields (Thikonov, 1950; Cagniard, 1953; Chave and Jones, 2012). As with many geophysical methods, this process is a linear system in the frequency (ω) domain (eq. 1), where the sources are natural time-varying magnetic fields (H), the response is the Earth’s inductive electrical response (E), and the transfer function between the source and response is the impedance tensor (Z). The magnetic sources are twofold. The first operates in the frequency range of about 1 hertz (Hz) and less and is related to interaction of the Earth’s natural magnetic field with solar wind—a cloud of charged particles ejected from the sun’s constant fission and fusion. The second operates from about 1 Hz and greater and is caused by lightning strikes around the globe, where the electromagnetic impulse travels in the waveguide created by the Earth’s surface and the ionosphere.

$$E(\omega) = Z(\omega)H(\omega) \tag{1}$$

---

[1] U.S. Geological Survey.

[2] Saudi Geological Survey.

The impedance tensor *Z* is a frequency-dependent rank-2 complex matrix that contains all the information about subsurface resistivity. Multiple representations exist to visualize information in *Z*. The traditional method is to plot a scaled version of the modulus to represent the apparent resistivity ρ (eq. 2) and plot the phase angle ϕ between the real and imaginary parts of *Z* (eq. 3) versus period, the inverse of frequency ω. The indices in equations 2 and 3 represent the electric field direction, *i*, and magnetic field direction, *j*.

$$\rho(\omega) = \frac{0.2}{\omega}\left|Z_{ij}\right|^2 \tag{2}$$

$$\phi_{ij}(\omega) = \arctan\frac{\mathrm{Re}\left\{Z_{ij}\right\}}{\mathrm{Im}\left\{Z_{ij}\right\}} \tag{3}$$

Another representation of *Z* is the phase tensor developed by Caldwell and others (2004). The phase tensor is simply the ratio of the imaginary and the real part of *Z*. Graphically, this is represented as an ellipse where the long axis aligns with the preferred direction of current flow, typically geoelectric strike. The shape of the ellipse can represent dimensionality. A circle suggests electrical current flows equally in all directions (isotropic) or a more complicated anisotropic current flow (Heise and others, 2006). An elongated ellipse indicates a preferred direction of current flow in the direction of elongation. The phase-tensor ellipses are commonly colored according to variations, and a particularly useful parameter to show is the skew angle (β), which is an indication of dimensionality. Large skew angles ($|\beta| > 3°$) indicate the subsurface resistivity structure is three dimensional (3D) and (or) anisotropic (Booker, 2014). The sign of β indicates in which direction electrical currents are being skewed, where positive is clockwise.

Geomagnetic depth soundings relate natural horizontal time-varying magnetic fields (*H*) to induced vertical magnetic fields (H_z) through the linear transfer function (*W*) (eq. 4), which is a complex frequency-dependent rank-1 matrix. Structures that induce vertical magnetic fields are horizontal boundaries or structures such as faults, edges of sedimentary basins, or magmatic dikes. Graphically, *T* is represented by real and imaginary induction vectors (also known as tippers), where the real arrows point toward a conductor (in the Parkinson convention) and the imaginary arrow characterizes subsurface dimensionality.

$$H_z(\omega) = T(\omega)H(\omega) \tag{4}$$

Data

Between January and February 2016, the USGS and the SGS jointly collected 89 broadband (0.0005–1,000 Hz) and 17 long-period (1E−5 to 1 Hz) MT soundings near the city of Al Madīnah (fig. 1). In May 2016, the SGS collected another 33 broadband MT soundings in the area (fig. 1). Data were collected in a geomagnetic coordinate system with an L-configuration of 100-meter (m) dipoles, vegetation and topography permitting. Travel between stations was mostly done via an air-conditioned Bell 206 helicopter; on mandatory pilot rest days vehicles were used. At most of the long-period sounding locations a broadband measurement was collected as well. At two stations, 107 and 620 (fig. 2), the broadband measurement was collected a few kilometers away because of high-frequency noise. The two sets of transfer functions were combined at the lowest common frequency and, if needed, statically shifted to match in apparent resistivity. The magnetotelluric response functions can be found in Bedrosian and others (2023).

Broadband Measurements

Broadband soundings were collected with a Phoenix V8 multichannel receiver, Phoenix MTC-50 induction coils, and Phoenix PE5 nonpolarizing electrodes. To improve contact resistance, the electrodes were placed in a canvas bag filled with saturated bentonite clay and buried with a generous amount of water. Vertical magnetic data was collected at only a few stations because of the difficulty of fully submerging a vertical induction coil. Data were sampled at 1,024 samples per second with periodic bursts of 18,000 samples per second, for an average recording time of 20 hours. Data were processed with the Phoenix processing codes SSMT2000 and MT Editor, where synchronous stations were used as remote references. Data were reliable from 0.001 to 500 Hz and noisier stations were located near the city of Al Madīnah. Much of the tipper data was poor because of wind noise on coils that were not completely buried. Thus, many stations do not have induction vectors. Transfer functions were converted from spectral data into impedance using MTpy (Krieger and Peacock, 2014) and in-house MATLAB programs.

Long-Period Measurements

Long-period soundings were recorded with Narod Intelligent Magnetotelluric Systems (NIMS), which includes a data logger that records 8 samples per second and a triaxial ring-core magnetometer. Borin Stelth 3 Ag-AgCl electrodes placed in canvas bags containing saturated bentonite were buried with a generous amount of water. Data were recorded for 2 weeks. The health of the measurement setup was monitored using USGS health-state monitors to keep track of vital quantities like battery charge, contact resistance, and magnetic and electric field values. A message string was sent via satellite every 6 hours and, if something was amiss, the stations would be checked. Data were processed with the EMTF program developed by Egbert (1997). Remote reference pairs were compared and the one producing smaller variances was chosen for the final transfer function estimation.

Data Analysis

Different parameters describing subsurface geoelectric structure can be estimated from transfer functions to prescribe the type of modeling and inversion appropriate for the data. Geoelectric strike is an important parameter because it infers the modeling coordinate system, but more importantly

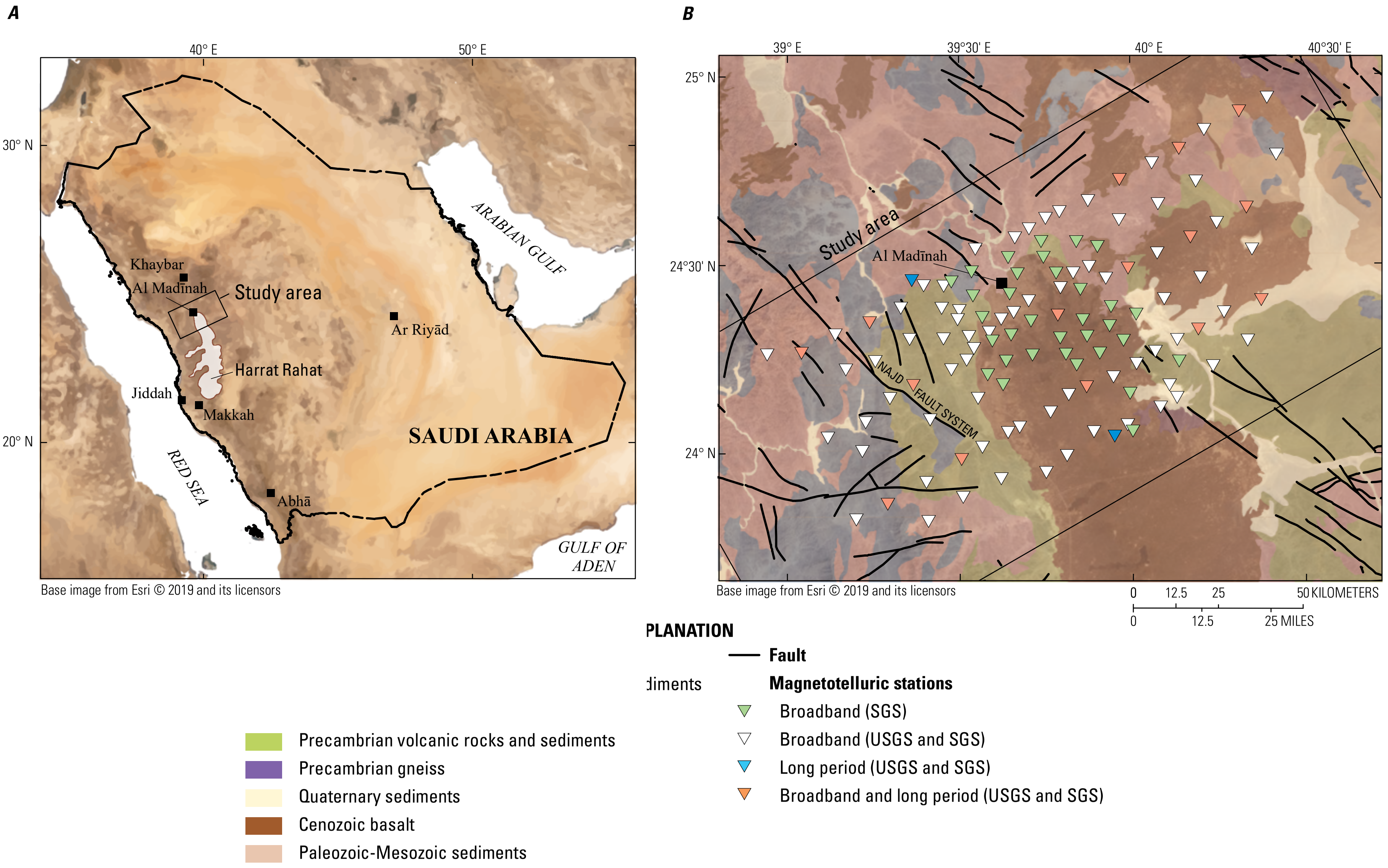

Figure 1. Map of the study area in the northern Harrat Rahat in western Saudi Arabia. *A*, Regional map showing the magnetotelluric survey area (black box) and Harrat Rahat along the western margin of the Arabian Peninsula. *B*, Basic geologic map after Pellaton (1981) showing magnetotelluric stations as triangles. The black outline represents the survey area and inversion box. SGS, Saudi Geological Survey; USGS, U.S. Geological Survey.

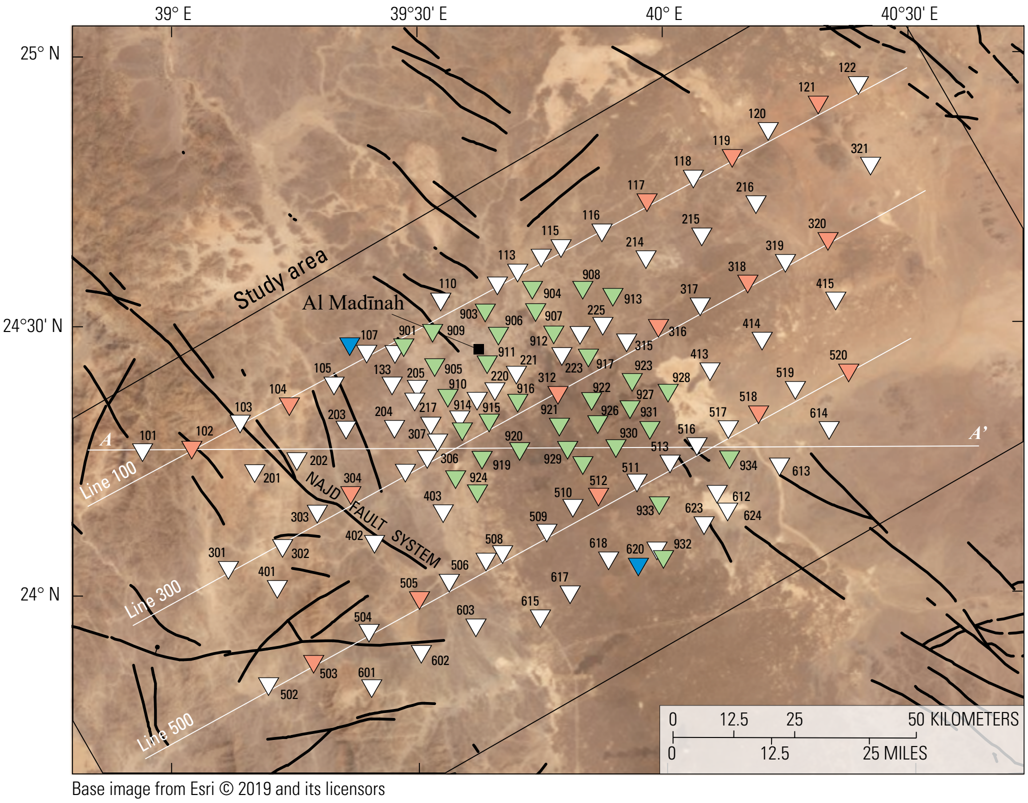

Figure 2. Map of magnetotelluric stations with station numbers and profiles shown. The black box outlines the study area. SGS, Saudi Geological Survey; USGS, U.S. Geological Survey.

characterizes changes in subsurface resistivity structure with depth and lateral direction. Here, geoelectric strike direction is estimated from the WAL invariants (Weaver and others, 2000), phase tensor azimuth (Caldwell and others, 2004), and induction vector azimuth (fig. 3).

A few key observations can be made about the geoelectric strike from the analysis. In the near surface (periods of 10^{-3}–10^{-1} seconds [s]), resistivity structure is one dimensional (1D) as described by the random strike direction, which suggests currents will flow in any direction equally well. At a period of about 0.1 s (approximately 1.5 kilometers [km] depth), the prevailing N. 30° W. strike of geologic structures is observed and persists to longer periods, and thus greater

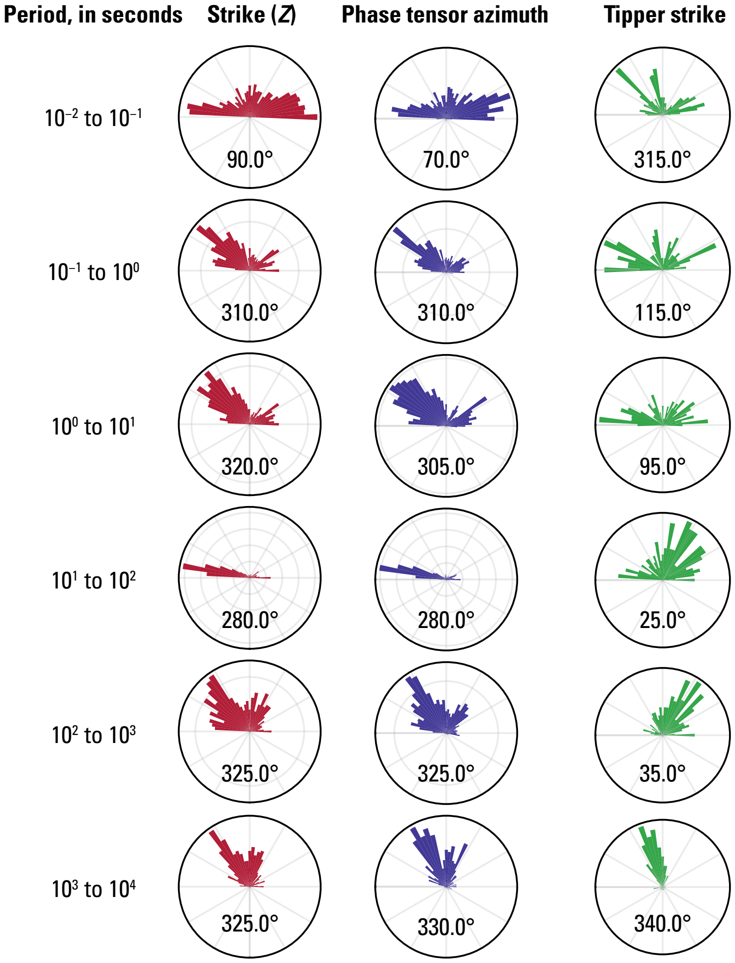

Figure 3. Plots of geoelectric strike estimations represented as polar diagrams where north (up) is 0 degrees and east (right) is 90 degrees. Each ring represents an estimated strike count of 50 and the colored number is the mode of the strike estimation. The left column shows WAL invariants (strike of the impedance tensor [*Z*] defined in eq. 1) (Weaver and others, 2000); the middle column shows the phase tensor azimuth (Caldwell and others, 2004); and the right column shows the induction vector strike (tipper strike). Each column represents a decade in period (in seconds, s), where short periods are sensitive to shallow structures and long periods are sensitive to deep structures. For periods from 10^{-2} to 10^{-1} s, the geoelectric strike represents a one-dimensional earth as no dominant strike direction appears. At 10^{-1} s, the prevailing regional strike of about N. 30° W. appears and continues deeper with a slight rotation northward. At periods between 10^{1} and 10^{2} s, however, the dominant strike direction appears to be N. 80° W. in the impedance vectors but N. 25° E. in the induction vectors, suggesting this zone in the crust is anisotropic.

depths, with a slight rotation northward at depth. There is an anomalous zone, however, between periods of 10–100 s for *Z* and 1–100 s for *W* (about 10–50 km depth) where the predominant geoelectric strike direction changes to N. 80° W. Heise and others (2006) demonstrate the major axis of the phase tensor and induction vector strike will align perpendicular to the conductive direction of anisotropy. Therefore, the anomalous strike directions are indications of anisotropy in the lower crust with a conductive orientation of N. 10° E.

Qualitative examination of the MT response reveals superposition of regional structures, one trending N. 30° W. and another unknown structure at depth trending N. 10° E. (figs. 4 and 5). Examining the data as a function of rotation, the maximal separation between principal impedances occurs when the data are rotated to N. 30° W., consistent with the rose plots in figure 3. Within this coordinate system, the entire survey can be loosely divided into two predominant sets of “type” curves (figs. 4*A, B*), based on their long-period apparent resistivity and phase characteristics (principal impedance components). These two curve types further separate geographically on either side of the Najd Fault System, suggesting it demarcates a first-order structural boundary. The region northeast of the fault includes the majority of the 119 stations, which can be further broken down into subsets based on the nature of the short-period data. Whereas most stations indicate moderate to high short-period apparent resistivity values, one subset of stations (yellow symbols in fig. 4), whose locations closely correspond to surface sediments, show much lower short-period resistivities and a steeply ascending resistivity curve. The most pronounced of these sites (fig. 5*C*) have short-period apparent resistivities at or below 1 Ohm meter (Ω·m) and are located upon sabkha (Arabic for “salt flat”) deposits, where saline brines are likely within the shallow subsurface. An additional subset of stations (fig. 5*D*), all located northeast of the Najd Fault System, have a subtle dip in apparent resistivity around 10 Hz. These sites are all located atop Harrat Rahat and are speculated to reflect the presence of conductive sediments at shallow depths (<300 m) beneath the volcanic section. A close correspondence is observed between the location of these sites and a gravity low that is attributed to a shallow structural graben beneath northern Harrat Rahat (Langenheim and others, 2019, 2023).

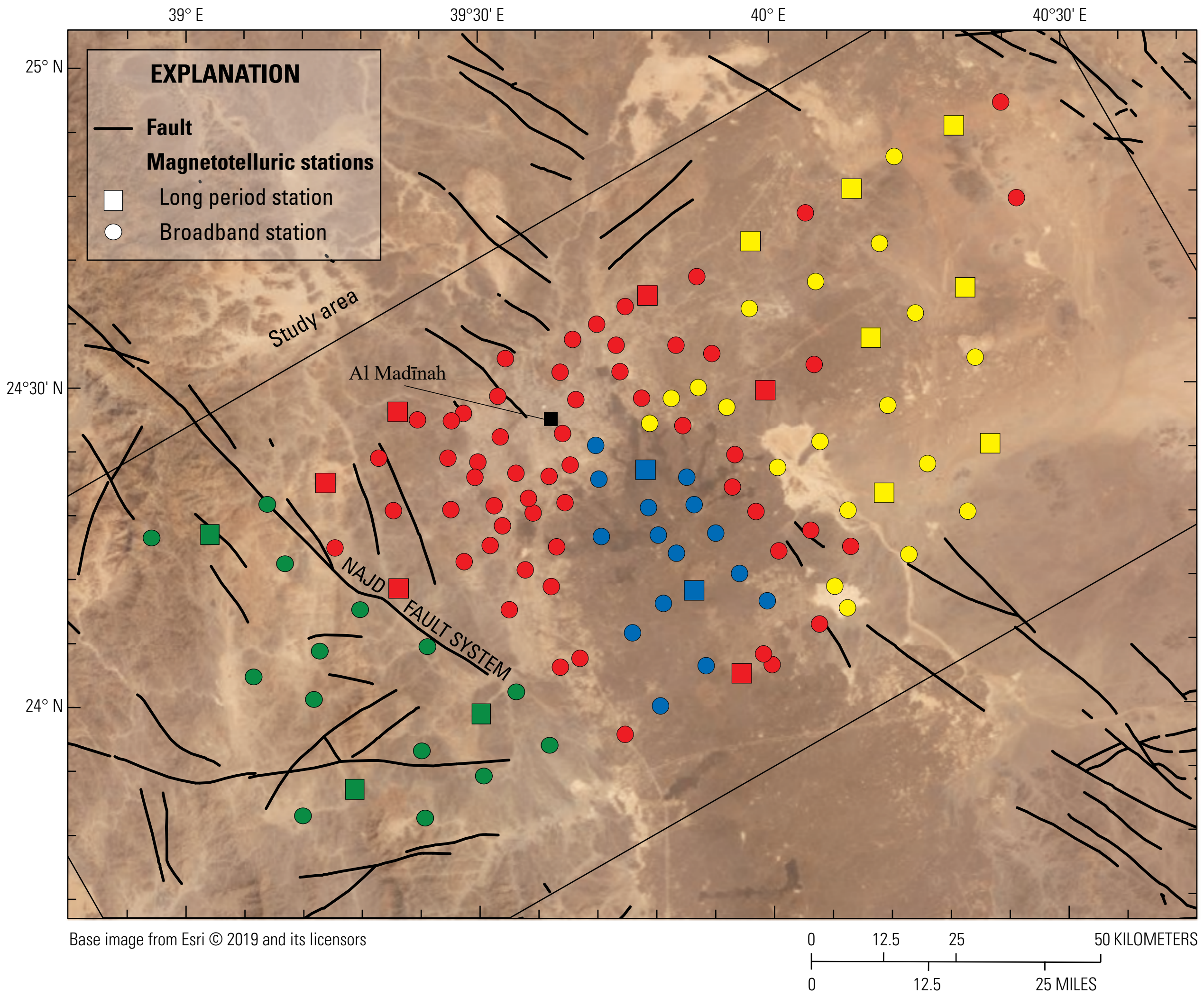

Base image from Esri © 2019 and its licensors

Figure 4. Map of magnetotelluric stations differentiated by curve type. Curves for the green stations are shown in figure 5*A*, red stations in figure 5*B*, yellow stations in figure 5*C*; and blue stations in figure 5*D*.

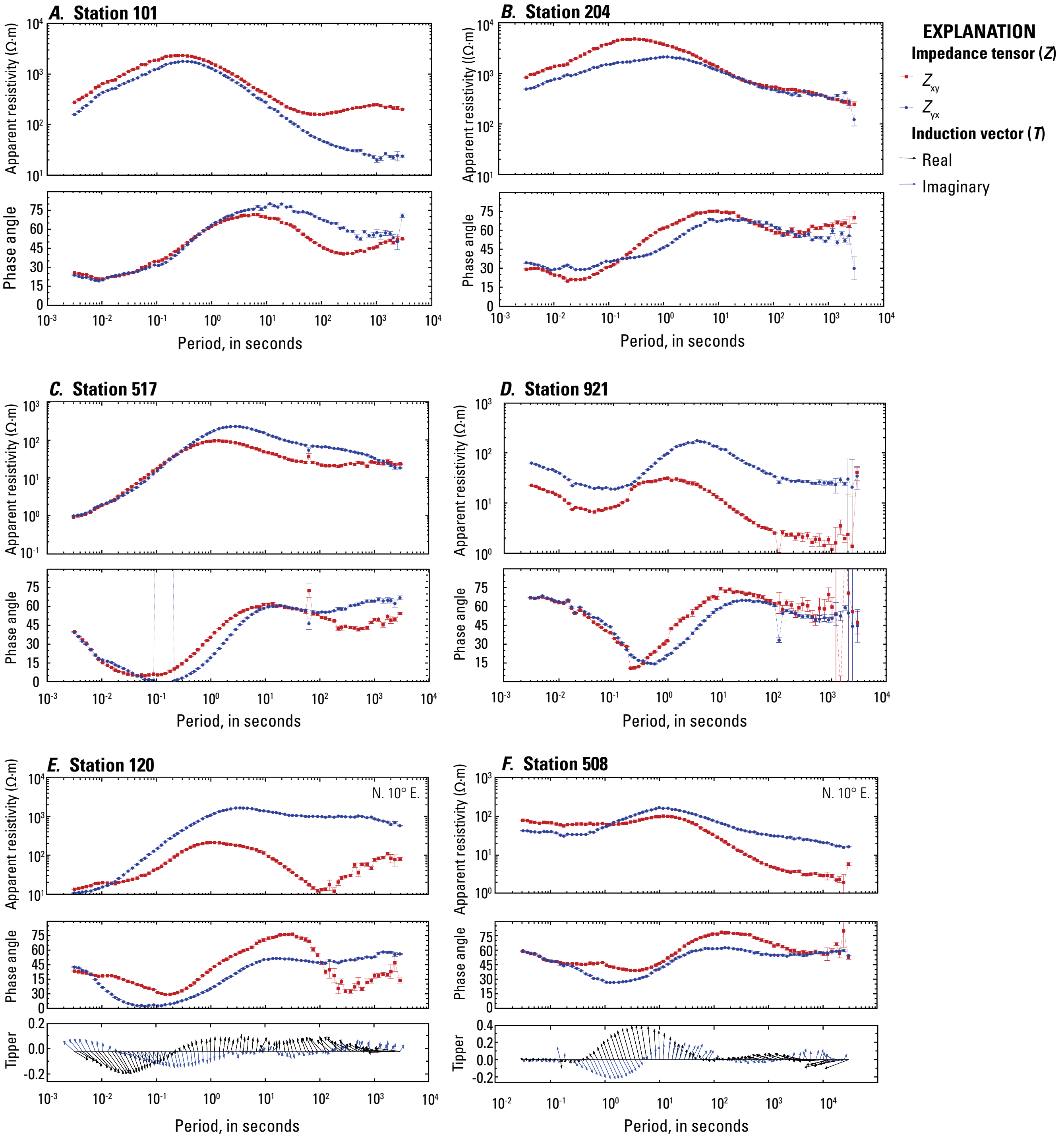

Figure 5. Plots showing characteristic magnetotelluric responses throughout the survey area. Plots show apparent resistivity (in Ohm meters, Ω·m), phase angle (in degrees), and the induction vector (both magnitude and direction of T_{zx} and T_{zy}) versus period (in seconds). Error bars show the data uncertainty. Responses are shown in the regional strike coordinate system (N. 30° W.), except where indicated. *A*, Station 101 west of the Najd Fault System (characteristic of the green stations in fig. 4). *B*, Station 204 east of the Najd Fault System (characteristic of red stations in fig. 4). *C*, Station 517 located above a conductive sedimentary basin or sabkha deposits (characteristic of yellow stations in fig. 4). *D*, Station 921 located above volcanic rocks of Harrat Rahat displays a distinct dip in apparent resistivity (and peak in phase), consistent with sediments beneath the harrat (characteristic of blue stations in fig. 4). *E*, Station 120 east of the Najd Fault System rotated into a N. 10° E. coordinate system. *F*, Station 508 east of the Najd Fault System rotated into a N. 10° E. coordinate system.

Response curves rotated to a N. 10° E. coordinate system are examined (figs. 5*E, F*). Given the obliquity (40–45°) of this coordinate system to regional strike, apparent resistivity of the two principle components should be similar at periods shorter than 10–100 s. This is true at short periods, however, at longer periods a split in the apparent resistivity curves and a characteristic "over-under" split in the impedance phase is observed (figs. 5*E, F*). Tipper data, where acquired, are commonly small at periods greater than 10 s. This behavior is only clearly discernible at stations northeast of the Najd Fault System.

Properties of the phase tensor provide insight into the dimensionality of the MT response functions. An invariant parameter of the phase tensor is the skew angle (β), which describes how electrical current paths are skewed by 3D structures. Skew angles where $|\beta| > 3°$ infer subsurface resistivity structure is anisotropic in three dimensions (Caldwell and others, 2004; Bibby and others, 2005). A two-dimensional (2D) anisotropic resistivity structure will have a skew angle near zero, a circular phase tensor, and small induction vectors (Heise and others, 2006; Booker, 2014). Moreover, Heise and others (2006) demonstrate that phase tensor ellipses change shape and have larger skew angles at the boundaries of isotropic and anisotropic structures.

A phase tensor pseudosection of line 500 shows that for periods less than about 1 s, skew angles are typically above 3° or below −3°, suggesting that the upper crust has 3D resistivity structures, likely fault dominated as indicated by the alternating skew angles (fig. 6). Between 1 and 100 s, the skew angle is nearly zero, the ellipses are circular, and the induction vectors are small, suggesting that the middle to lower crust is anisotropic. At periods larger than 100 s, the skew angle is nearly uniform, and the induction vectors align in the same direction (N. 90° W. to N. 110° W.), suggesting resistivity structure is 3D with a strong conductor to the west. Finally, an apparent boundary between stations 504 and 505 is imaged, which is coincident with the Najd Fault System, and roughly corresponds to the change between green and red symbols in figure 4.

Diagnostic parameters of subsurface resistivity dimensionality and complexity, namely geoelectric strike angle and the skew angle, indicate subsurface resistivity structure is complicated. Between periods of 0.002 and 1 s (approximately 0–5 km depth), the resistivity structure is 2D with some 3D features. Between 1 and 100 s (approximately 5–50 km depth), resistivity structure is likely anisotropic as evidenced from low skew angles, small induction vectors, and a strong rotation in the strike angle. At periods larger than 100 s, resistivity

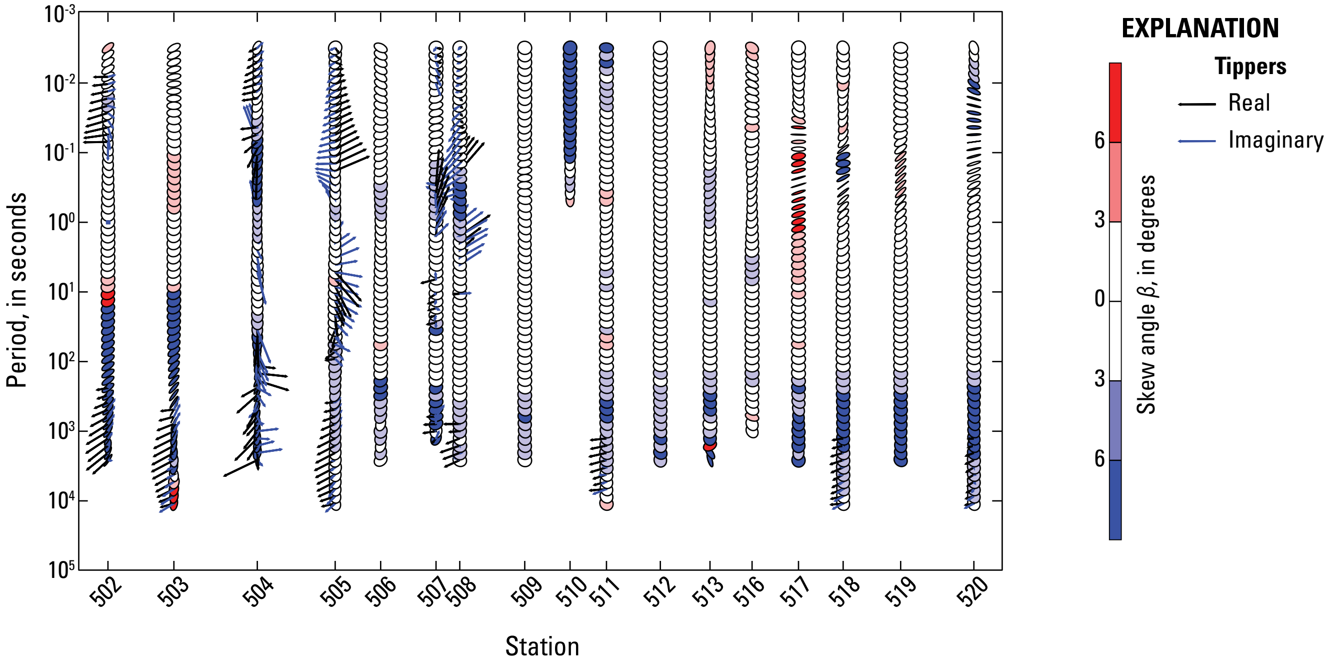

Figure 6. Phase tensor pseudosection of line 500 (see fig. 2 for location) showing induction vectors (tippers). Note that depth sensitivity depends on apparent resistivity and period and, thus, not all stations sample the same depth at each period. Skew angles where $|\beta| > 3°$ represent three-dimensional (3D) subsurface resistivity structure, smaller skew angles represent 2D or 1D anisotropy, and skew angles of zero represent 1D resistivity structure. Induction vectors point toward good conductors (Parkinson convention) and small values represent 1D structure or 1D anisotropy. From periods of 10^{-2} to 10^{0} seconds, the skew angle alternates and induction vectors are large in the west, suggesting upper crustal structure is fault dominated, with larger faults to the west. Between 10^{0} and 10^{2} seconds, the skew angle is near zero, the ellipses are circular, and the tippers are near zero, suggesting anisotropy. Periods longer than 10^{2} seconds have nearly uniform skew angles below −3°, suggesting counter-clockwise (westward) rotation of electrical currents towards a large conductor to the west, as suggested by the tippers.

structure is 3D. These observations suggest that different modeling techniques are needed to characterize resistivity structure as a function of depth and lateral distance.

Modeling

To convert the MT responses from frequency to depth and lateral distance, an inversion program is needed. The type of program is prescribed by the estimated dimensionality diagnostic parameters. The data are at least 2D and likely 3D, therefore the 3D isotropic inversion code ModEM (Egbert and Kelbert, 2012; Kelbert and others, 2014) is used to infer the overall resistivity structure of the study area. Because the data exhibit anisotropy, the 3D isotropic inversion code does not correctly characterize anisotropic zones, therefore MARE2DEM (Key, 2016), a 2D inversion code that can account for anisotropy, and Pek1D (Pek and Verner, 1997), a 1D anisotropic forward-modeling code, are used to complement the 3D model. Note that no 3D anisotropic inversion code is currently available. The final model will be a combination of models from these different modeling programs.

Three-Dimensional Isotropic Modeling

To image the subsurface of the study area in 3D, the inversion code ModEM is used. Note that ModEM is an isotropic inversion code and therefore will not characterize anisotropic data properly. Nevertheless, it provides a starting point for basic interpretations. Prior to setting up the inversion, the data are edited to remove obvious outliers. The data and the model are rotated to a N. 30° W. coordinate system to align the main modes of Z with the inversion grid. The model grid has 2×2 km cells within the station area and cells increasing by a factor of 1.2 outside the station area to reduce edge effects. The cell size varies exponentially with depth. The grid dimensions are $60 \times 110 \times 60$ cells and $760 \times 860 \times 730$ km. Inversions are run on the USGS's supercomputer Yeti, where average iteration times are 30–40 minutes.

To reach a final model, a three-step inversion approach is used (Bedrosian and others, 2018). In the first step, the inversion is run with an error floor on Z of $0.07\sqrt{(Z_{xy} \times Z_{yx})}$, a covariance of 0.3 applied twice, a starting lambda of 10,000, and a starting model of a 100-Ω·m half-space that includes the Red Sea. After 144 iterations, the model converged to a normalized root-mean-square error (rms) of 2.02. In the next step, the converged model from step 1 is used as a prior model and only the induction vectors (T) are inverted with an absolute error floor of 0.06, the same covariance and starting model, and the lambda value set to 100. After 52 iterations, the inversion converged with a normalized rms of 1.05. In the third step, the converged model from step 2 is used as a prior model and both Z and W are inverted with error floors of $0.07\sqrt{(Z_{xy} \times Z_{yx})}$ and 0.06, respectively, the covariance and starting model are the same, and the lambda value is set to 100. After 168 iterations, the final normalized rms is 1.56.

Between steps, the converged model and data fits are assessed to make sure the inversion is running properly. After step 1, the top 1.5 km of the crust is modeled as having a conductive anomaly (<30 Ω·m) that persists near Cenozoic basalt flows. Down to 10 km depth, the crust is modeled as nearly uniformly resistive (>3,000 Ω·m). At 10 km depth, the western side of the study area is predicted to be more conductive. The region between 10 and 50 km depth is modeled as having parallel conductive and resistive features that trend N. 10° E. At 60–100 km depth, the middle of the survey area is inferred as more conductive than the background at around 50 Ω·m. In step 2, the region between 10 and 50 km depth is replaced with a nearly homogenous value of about 30 Ω·m, and is predicted to be slightly more conductive on the western side of the survey area. Conversely, the apparent striping of step 1, lost in step 2, returns in step 3. This behavior is indicative of anisotropy.

Two-Dimensional Anisotropic Inversion

To estimate lateral anisotropy, the 2D inversion code MARE2DEM is used, which can account for anisotropy parallel and perpendicular to the profile. The goals of inverting in two dimensions are to test if the data are indeed influenced by crustal anisotropy, and to get a lower bound on the anisotropic ratio. Data are masked prior to inversion where obvious outlier data points are removed. A profile perpendicular to N. 10° E. is taken across the survey starting at station 101 (fig. 1), where the data are rotated to the coordinate system. An error floor of 10 percent for Z and an absolute error floor of 0.03 for the inline components of W are set. Different rotation angles were tested to estimate the influence of angle on anisotropy, which demonstrated that data in a coordinate system oriented 45° relative to the anisotropic direction is insensitive to anisotropy (see appendix 1 for more details).

The model mesh is made up of finite elements, where the shape and size changes with depth and areas of interest. Here, the area of interest is the width of the profile and to a depth of 60 km. The model is divided into four layers: 0–2 km, 2–6 km, 6–30 km, and 30–60 km depth, each with increasingly large triangular mesh elements. Away from the area of interest are triangles of increasing size extending to at least 1,000 km away to remove edge effects. The starting model is a 100-Ω·m half-space with no topography. Anisotropy is incorporated into the inversion through the model roughness term of the objective function, which contains a measure of the difference between the profile-perpendicular (ρ_{xx}) and profile-parallel (ρ_{yy}) resistivity models, regularized by an anisotropy penalty factor, α. The value of α can vary from 0 (allowing maximum anisotropy) to 1 (exclusively isotropic) and is defined by the user prior to inversion. For the anisotropic inverse models in this study, $\alpha = 0.1$. Multiple models were run to optimize rms and structure.

The results of the 2D models show an isotropic upper crust, an anisotropic lower crust, and an isotropic upper mantle (fig. 7). The Najd Fault System separates lithology with a possible vertical offset of a few kilometers. The recovered ρ_{xx} (50 Ω·m) and ρ_{yy} (25 Ω·m) resistivities 20–40 km beneath Harrat Rahat are considered lower bounds on the anisotropy

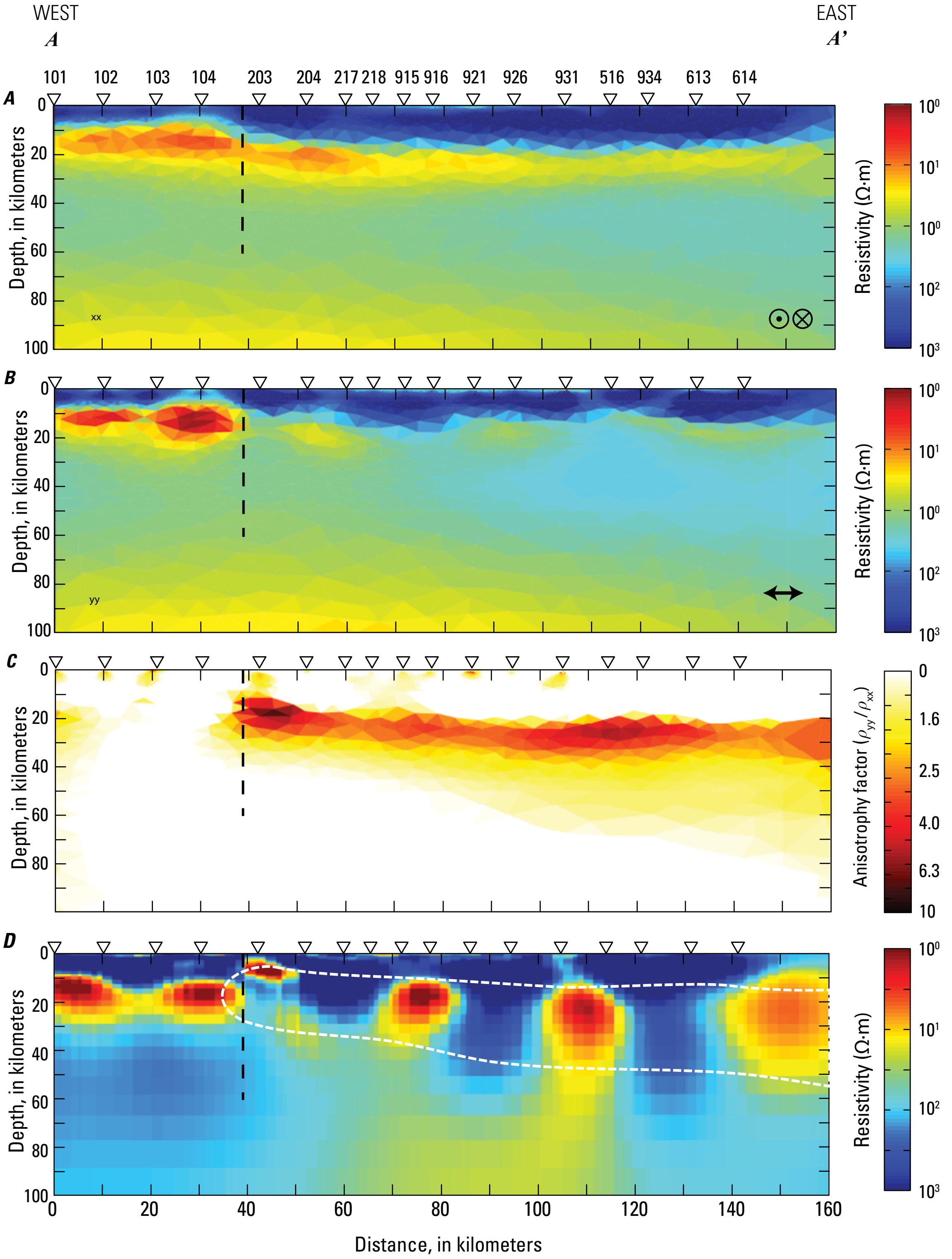

Figure 7. Cross sections of profile *A*–*A'*; location shown in figure 2. Two-dimensional resistivity (in Ohm meters, Ω·m) models from MARE2DEM allow for anisotropy perpendicular (*A*) and parallel (*B*) to the profile. The ratio of *B* and *A* is represented in *C*, where a positive anisotropic factor represents out-of-the-plane anisotropy. Notice the distinct anisotropic layer between 15 and 40 kilometers (km) depth that has a ratio greater than 2. This layer, outlined in the white, is represented in the three-dimensional model (*D*) as a series of evenly spaced apparent conductors and resistors. The dashed black line in each cross section represents the Najd Fault System.

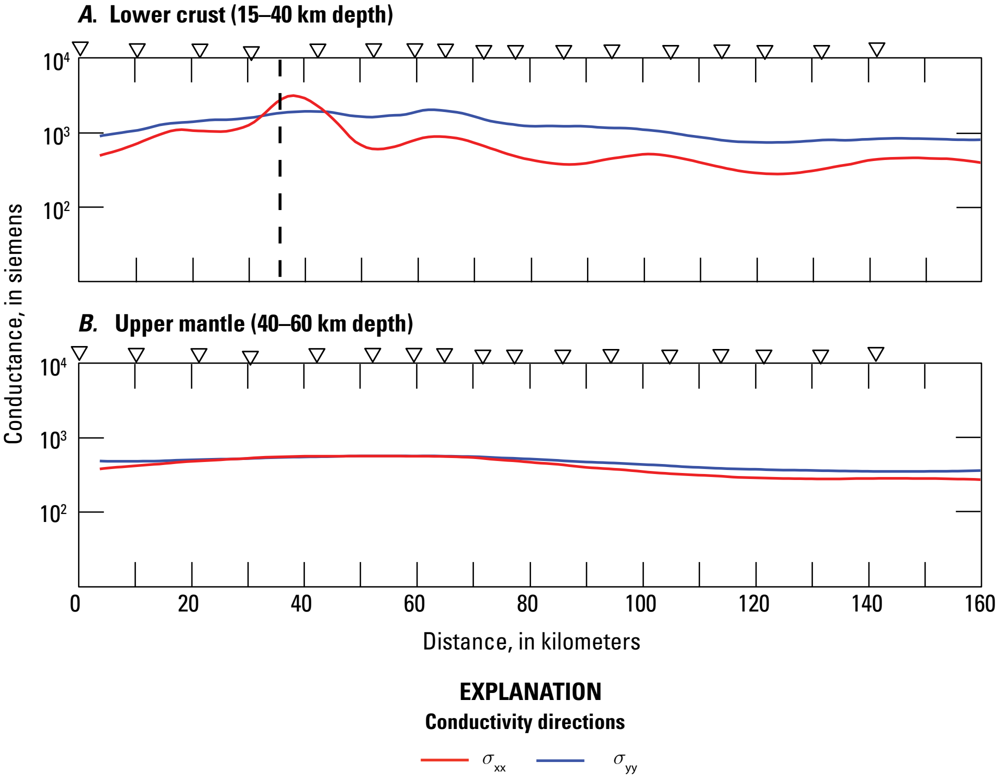

Figure 8. Plot of electrical conductance of the (*A*) lower crust (15–40 kilometers [km] depth) and (*B*) upper mantle lithosphere (40–60 km depth) computed from the two-dimensional anisotropic models shown in figures 7*A* and 7*B*. Note the difference in conductance values for the different conductivity directions in the lower crust, where σ_{xx} (conductance perpendicular to the profile, N. 10° E.) is more conductive than the σ_{yy} direction (conductance parallel to the profile, N. 80° W.). Black dashed line in *A* represents the Najd Fault System.

factor ($\rho_{yy}/\rho_{xx} = 2$). The true anisotropy factor is expected to be somewhat larger given the results of synthetic inversions (appendix 1). The lower crustal conductance, the total electrical conductance over a specified volume measured in siemens (S), as a function of profile distance for both the lower crust (15–40 km) and uppermost mantle (40–60 km) can be estimated (fig. 8). Lower crustal conductance is estimated at 1,000 S in the direction parallel to anisotropy (N. 10° E.) and 500 S perpendicular to the direction of anisotropy. For comparison, upper mantle conductance is largely uniform across the profile and isotropic.

One-Dimensional Anisotropic Modeling

Because MARE2DEM only allows anisotropy to vary perpendicular to the profile and commonly underestimates the anisotropic ratio, a different modeling approach is used to investigate the anisotropic layer. The forward modeling code Pek1D (Pek and Verner, 1997) is used to model the MT response for a simplistic model simulating the general resistivity structure of the study area including an anisotropic layer. The resistivity model includes five layers, from top to bottom: 0–1 km is 10 Ω·m, 1–10 km is 1,000 Ω·m, 10–40 km is anisotropic, 40–70 km is 100 Ω·m, and 70 km and deeper is 30 Ω·m (fig. 9). The angle of anisotropy relative to the profile direction and the ratio of high to low resistivity were varied. The angles tested were 0, 30, and 45 degrees and the ratios of resistivities tested were 50/25, 50/10, and 100/10 Ω·m (for an anisotropy factor of 2, 5, and 10) (fig. 9).

The anisotropic model with an angle of 45° and a ratio of 50/25 best represented measured MT data and was used as input values for a 3D inversion using ModEM to demonstrate the striped model is a result of anisotropy. The 1D anisotropic MT response was used to make a grid of stations like that in the MT survey. The model grid was similar to the one used for inverted measured MT data with 2 × 2 km cell sizes within the survey area with the same vertical extent. All components of *Z* were inverted with an error floor of 5 percent in a similar period range as collected data. The same covariance factor of 0.3 and starting lambda of 10,000 were used to run the

Figure 9 (page 11). Plots demonstrating the reasoning behind the interpretation of an isotropic lower crust beneath Harrat Rahat. *A*, Schematic Earth model based upon the three-dimensional isotropic inverse model and the two-dimensional anisotropic inverse model (see fig. 7). The lower crustal anisotropic layer at 15–40 kilometers (km) depth is modeled in *B* with variable directions and factors of anisotropy. *B*, Plots of principle impedance response at a site located over the center of the model as a function of anisotropy direction (either 0°, 30°, or 45° relative to strike) and factor (either 2, 5, or 10). Plots show apparent resistivity (in Ohm meters, Ω·m) and phase angle (in degrees) versus period (in seconds). Induction vectors are very small, and thus not plotted. The three-dimensional inverse model at 8 km (*C*) and 25 km depth (*D*) are derived from inversion of the synthetic responses of the schematic model. Note the similarity in structure (striping, direction of striping, and maximum and minimum resistivity) to that observed through inversion of the measured data (fig. 10).

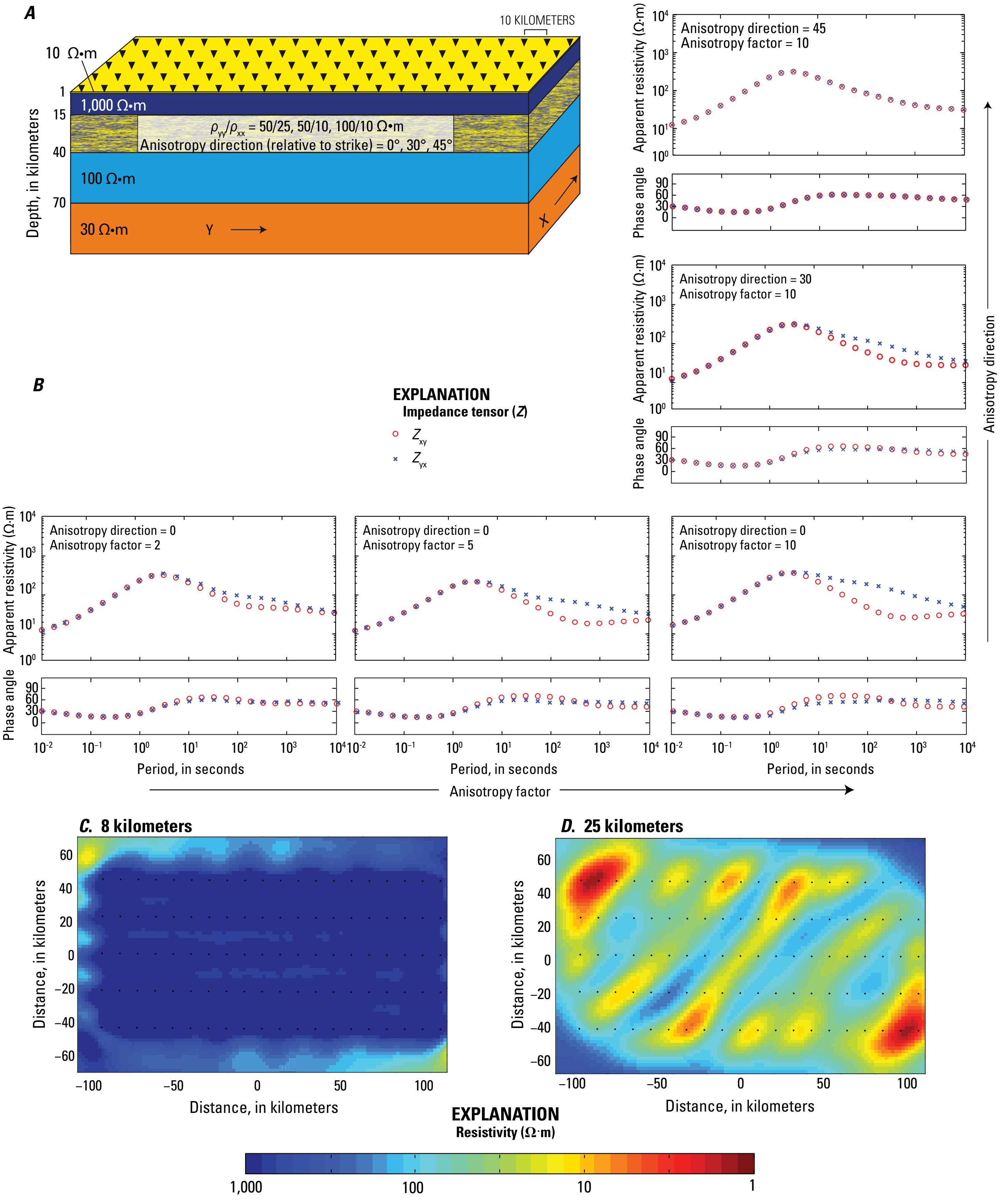
A
10 KILOMETERS
10 Ω•m
1,000 Ω•m
ρyy/ρxx = 50/25, 50/10, 100/10 Ω•m
Anisotropy direction (relative to strike) = 0°, 30°, 45°
100 Ω•m
30 Ω•m
Y
X
Depth, in kilometers
1
15
40
70
B
EXPLANATION
Impedance tensor (Z)
Zxy
Zyx
Anisotropy direction = 45
Anisotropy factor = 10
Anisotropy direction = 30
Anisotropy factor = 10
Anisotropy direction = 0
Anisotropy factor = 2
Anisotropy direction = 0
Anisotropy factor = 5
Anisotropy direction = 0
Anisotropy factor = 10
Apparent resistivity (Ω·m)
Phase angle
10⁰
10¹
10²
10³
10⁴
0
30
60
90
10⁻²
10⁻¹
Period, in seconds
Anisotropy factor
Anisotropy direction
C. 8 kilometers
D. 25 kilometers
Distance, in kilometers
60
40
20
0
−20
−40
−60
−100
−50
50
100
EXPLANATION
Resistivity (Ω·m)
1,000
100
10
1

inversion. After 95 iterations, the inversion converged with an rms of 1.03. Between a depth of 10 and 40 km, a pattern of parallel resistive and conductive stripes oriented 45° are observed, whereas the rest of the model is akin to the 1D model (fig. 9*C*).

The modeling demonstrates that survey design is important when dealing with anisotropy (figs. 10*D*–*F*). The survey aperture must be at least 4 times the depth to the anisotropic layer or else a resistive-conductive-resistive pattern will result. This pattern can be misinterpreted as a real subsurface feature. An example of this type of myopic study is from Aboud and others (2018), in which their survey was about 50 km wide across Harrat Rahat. Their subsequent 3D isotropic inversion imaged a resistive-conductive-resistive pattern directly under the Harrat Rahat at 20 km depth, where they interpreted the conductive stripe as a zone of partial melt. Though there might be small isolated zones of partial melt within the lower crust, a voluminous zone as large as one of the conductive stripes is highly unlikely (see geologic reasoning in Stelten and others, 2018, 2023).

Results and Discussion

The electrical resistivity model can be broken down into 5 layers: a thin (<500 m) veneer of Quaternary sediments and lava flows, a 10–15 km thick resistive upper crust, a 20-km thick anisotropic lower crust, a moderately resistive lithosphere, and a conductive upper asthenosphere (fig. 11). The main structures and interpretation of each layer are described below.

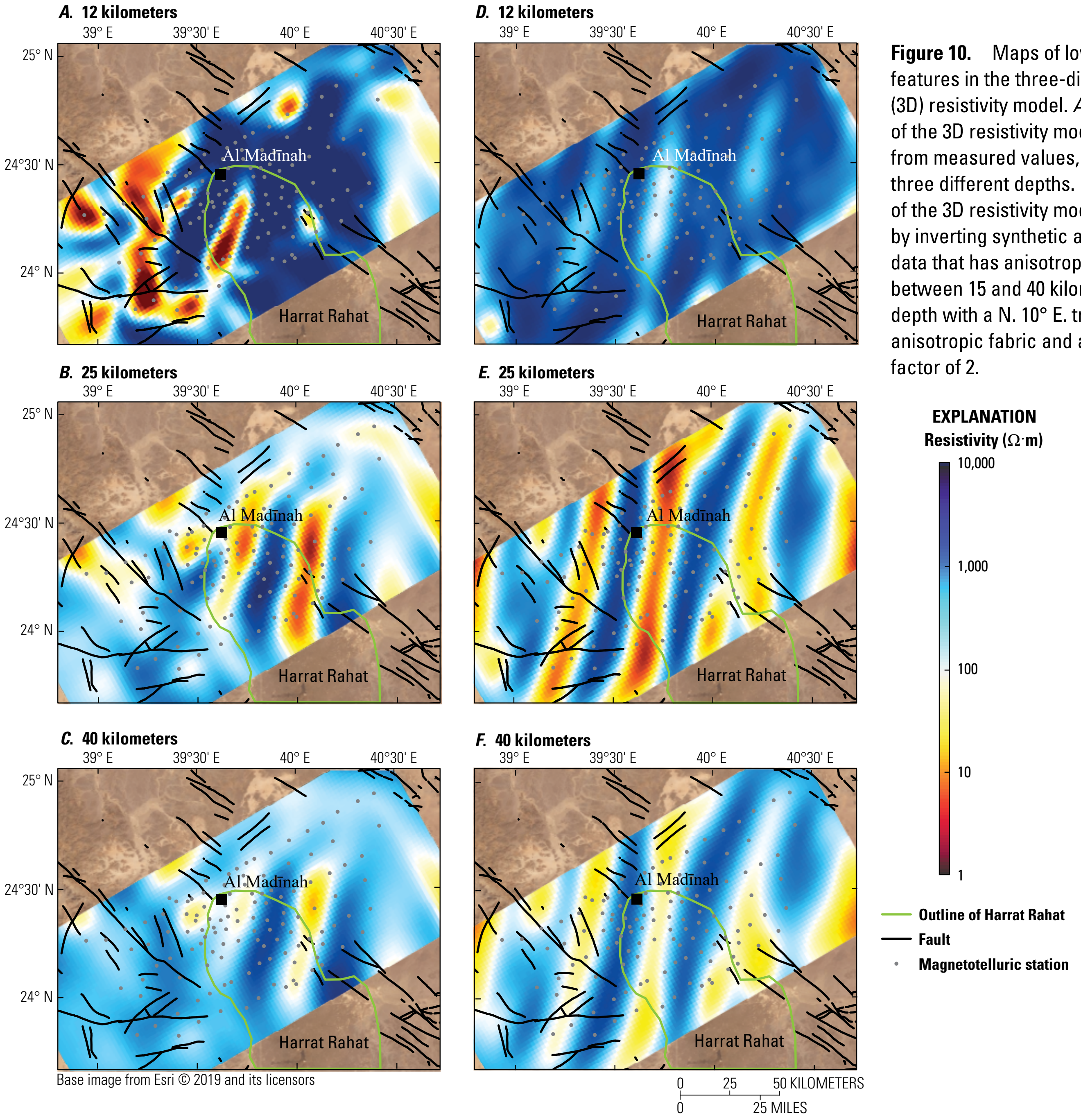

Figure 10. Maps of lower crustal features in the three-dimensional (3D) resistivity model. *A*–*C*, Images of the 3D resistivity model inverted from measured values, shown at three different depths. *D*–*F*, Images of the 3D resistivity model predicted by inverting synthetic anisotropic data that has anisotropic layer between 15 and 40 kilometers (km) depth with a N. 10° E. trending anisotropic fabric and an anisotropy factor of 2.

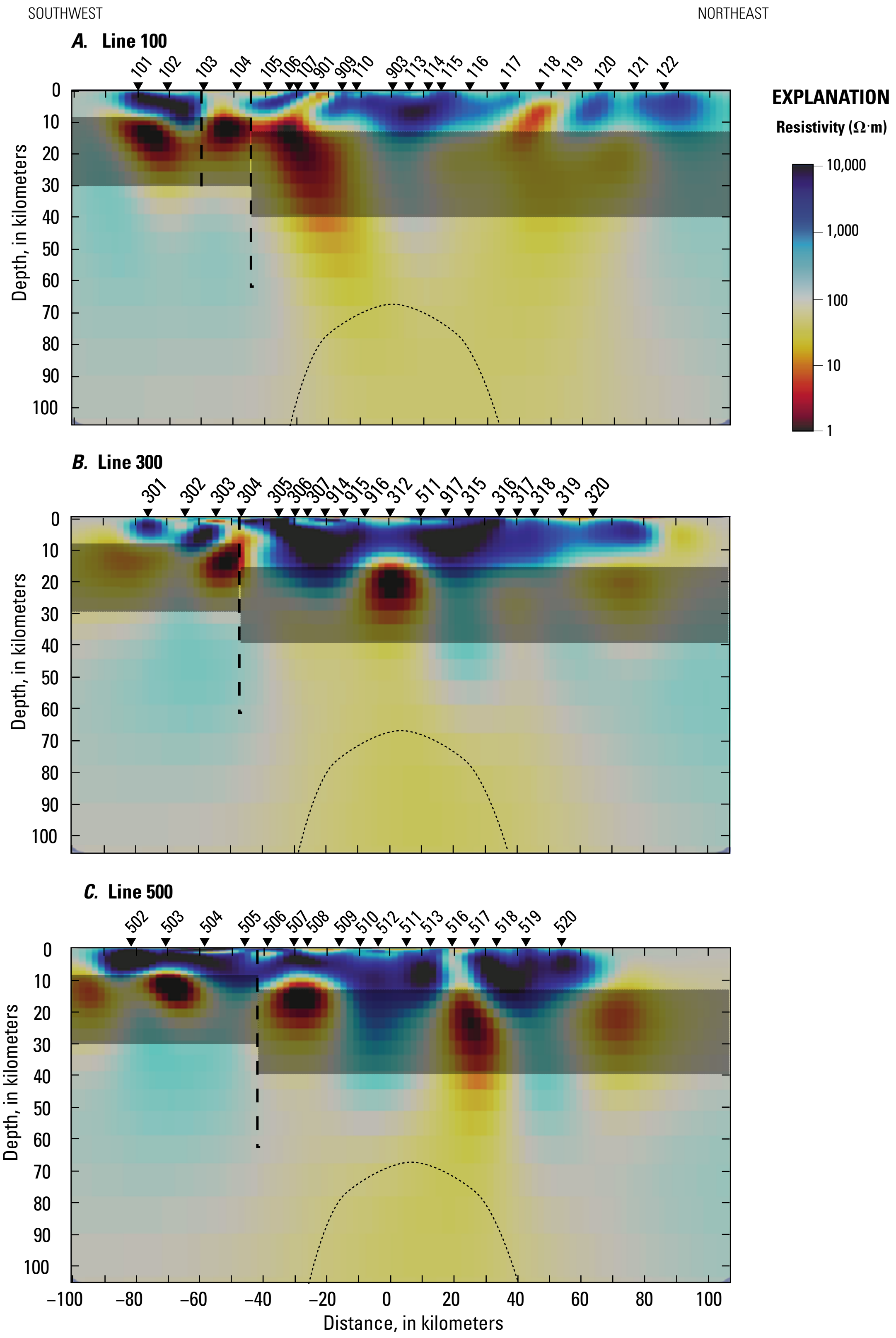

Figure 11. Profiles along (*A*) line 100, (*B*) line 300, and (*C*) line 500; locations in figure 2. The shaded region between 10 and 40 kilometers (km) depth is the electrically anisotropic layer. The dashed vertical line represents the general location of the Najd Fault System. The dotted line below 60 km depth represents the magmatic source zone for Harrat Rahat.

Top 1 Kilometer

The top 1 km of the electrical resistivity model is mostly resistive (>1,000 Ω·m) except for the area below recent lava flows, where a depression in the basement occurs (Langenheim and others, 2018). Within the depression, the resistivity varies between 1 and 100 Ω·m and the less resistive zones are near the deepest parts of the basin (fig. 12). The higher conductivity (1–30 Ω·m) under recent lava flows is likely related to weathering of the flows and fluids collecting in the pore space as there are multiple water wells in the area (Loni, 2005) and Al Madīnah was established because of abundant springs and near-surface groundwater emanating from the base of the volcanic section. The higher conductivity suggests brackish water with a salinity of between 1 and 10 grams per liter (g/L) (sea water is 35 g/L) and (or) indicates higher temperatures (<50 degrees Celsius [°C]) closer to the volcanic axis, consistent with measured water-well temperatures (Roobol and others, 2007).

Two near-surface resistive anomalies exist (>1,000 Ω·m) within Harrat Rahat, namely below the Matan trachyte dome along the main vent axis, which extends ~10 km southwest. The other is similarly oriented, connecting the Um Rgaibah trachyte dome and the Al Wabarah crater. These resistive features suggest the eruptive pathway toward the surface of the trachyte eruptions is more extensive than neighboring basaltic vents. Moreover, the trachyte eruptive centers are preserved in the subsurface as cold dense material defined by elevated resistivities.

Major mapped faults of the Najd Fault System are imaged to be more conductive than surrounding rocks in the upper 1 km. This could be caused by meteoric fluids penetrating the fault or related to fault gouge of these sinistral faults. If the elevated conductivity was related to fault gouge, then the fault should be imaged with higher conductivity with depth. This is not observed in the resistivity model, suggesting a near-surface process like infiltration of meteoric water.

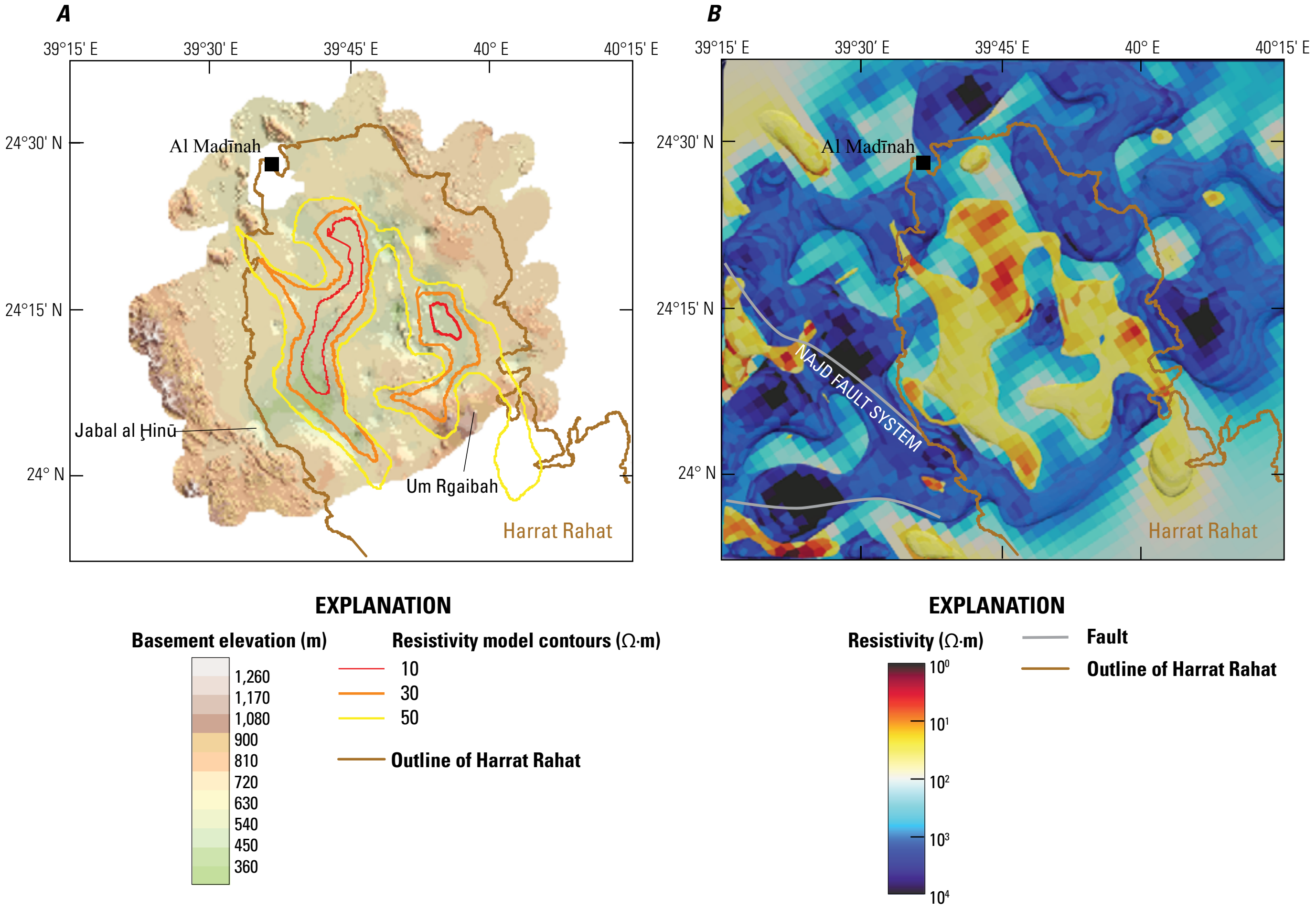

Figure 12. Maps comparing the near-surface structure beneath Harrat Rahat. *A*, Basement elevation, in meters (m), estimated from potential-field data (adopted from Langenheim and others, 2018). The colored contour lines show the electrically conductive parts of the three-dimensional resistivity model (from *B*) at 50, 30, and 10 Ohm meters (Ω·m). *B*, Electrical conductivity model of the top 1 kilometer of the study area. The conductive threshold is 50 Ω·m and the resistive threshold is 1,000 Ω·m. Note that the conductive outlines in *A* correlate with the deepest parts of the basin.

Upper Crust

The upper crust (top 10 km) is imaged as almost uniformly resistive (>1,000 Ω·m) except for a north-northeast elongated conductive anomaly just west of Al Madīnah between 4 and 10 km depth (C1) and a conductive anomaly in the southwest corner of the survey area (C2) (fig. 13). Conductive anomaly C1 correlates with Precambrian sedimentary and volcanic rocks exposed at the surface (Pellaton, 1981), which are adjacent to Precambrian plutons and arc-related volcanic rocks. Similarly, conductive anomaly C2 lies in a similar geologic setting as C1. Anomalies C1 and C2 lie on opposite sides of the Najd Fault System, separated by about 40 km of left-lateral offset, suggesting that the enhanced conductivity of C1 and C2 are related. The anomalous conductivity could have been produced by contact metamorphism upon pluton emplacement, which is commonly observed in arc systems (for example, Bedrosian and others, 2018).

Uniform resistivity of the upper crust precludes zones of partial melt, specifically below Quaternary vents, at the resolution of the survey. If a zone of partial melt were present, even on the order of 1 percent, resistivity would be on the order of 50 Ω·m and less. The lowest resistivity observed below Harrat Rahat at upper crustal depths is 100 Ω·m (fig. 13), which is much too great to encompass partial melt. The two isolated zones of reduced resistivity (<200 Ω·m) could be related to past eruption paths toward the surface, but currently contain zero melt.

Lower Crust

The middle and lower crust (here collectively referred to as lower crust), with a depth range from 12 km to the Mohorovičić discontinuity (Moho) (~40 km), is electrically distinct from the upper crust. One important feature of the lower crust is a change across the Najd Fault System at depths below 12 km. On the west side of the fault, the

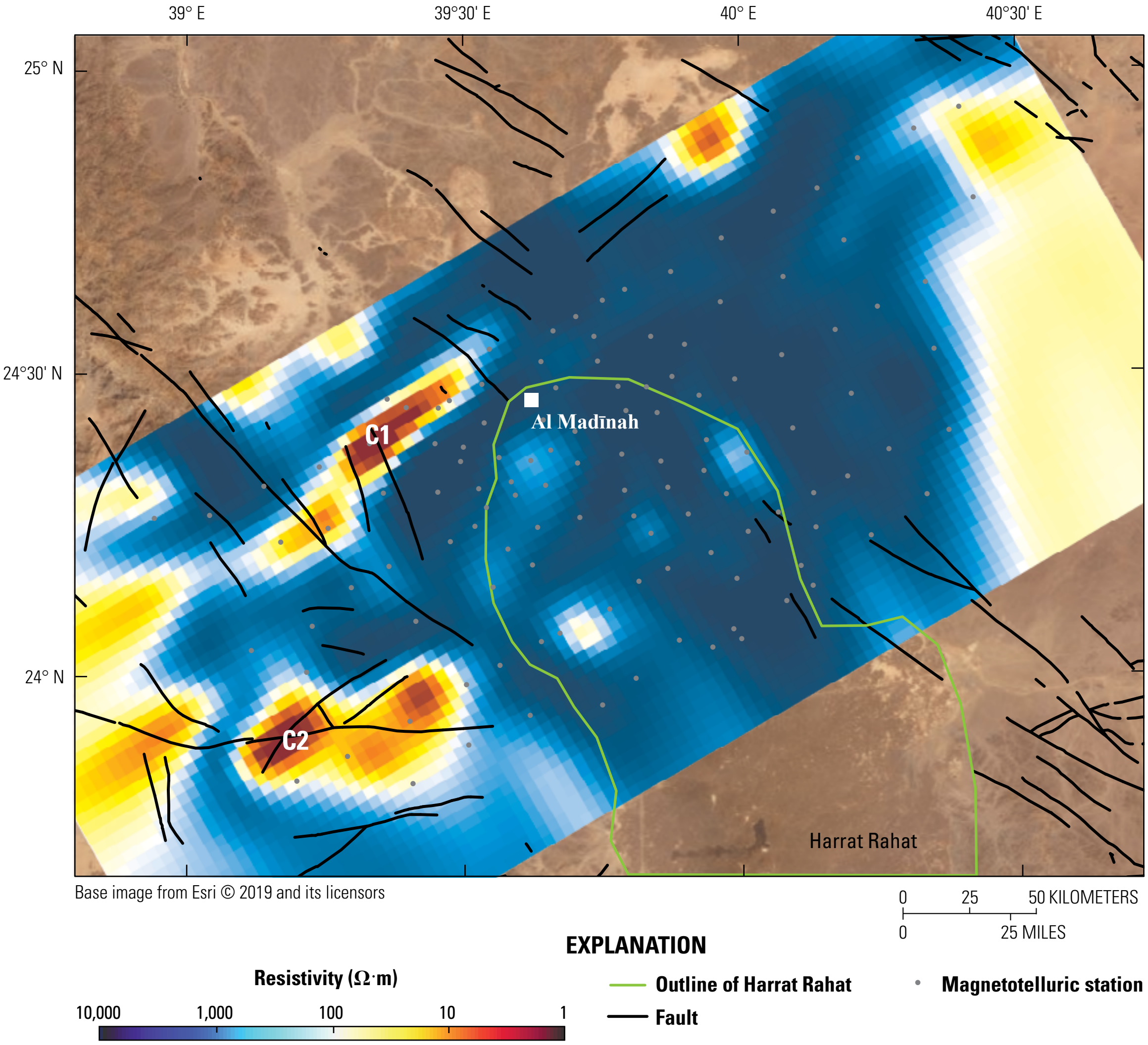

Base image from Esri © 2019 and its licensors

Figure 13. Map showing a 7-kilometer-depth slice of the three-dimensional resistivity model. Conductive anomalies C1 and C2 are labeled.

subsurface appears to be more isotropic and relatively resistive (200 Ω·m). Whereas on the east side, a series of alternating apparent resistive and conductive stripes trending N. 10° E. are imaged (figs. 10*A–C*) and extend spatially beyond the Harrat Rahat. Individual conductive (1–10 Ω·m) and resistive (100–1,000 Ω·m) features are modeled as about 20 km wide, comparable to their vertical depth. The tops of the apparent conductive features occur at about 12 km depth in the west and slightly deeper in the east and the resistive lower crustal stripes are indistinct from the overlying resistive upper crust, suggesting the eastern side of the Najd Fault System is down-dropped relative to the western side. The modeled regularly spaced alternating conductive and resistive features are artifacts indicative of electrical anisotropy and can be accounted for as such, as previously discussed (fig. 10).

The source of electrical anisotropy within the lower crust is enigmatic. The minimum extent of the anisotropic layer includes northern Harrat Rahat, much of Harrat Khaybar to the northeast (data modeled but not shown), and the region in between that connects them and has not been a source of Quaternary volcanism.

Seismic studies (for example, Mooney and others, 1985; DESERT group, 2004) image a 35–40 km thick crust beneath the Arabian Shield, including a layered crustal section with a prominent Conrad discontinuity at ~20 km and lower crustal velocities (P-wave velocities of 6.7–7.2 kilometers per second [km/s]), consistent with a mafic lower crust. An additional boundary at ~30 km within the lower crust is also imaged, characterized by velocities of 7.2–7.8 km/s. A mafic lower crust is further suggested by gravity modeling (Brew and others, 2001), which suggests a dense lower crust (2.87–2.92 grams per cubic centimeter [g/cm^3]) below about 20 km depth. Importantly, lower crustal xenoliths entrained in mafic lavas from harrats surrounding, but not from, Harrat Rahat reveal magmatic textures and mafic mineralogy that suggest basaltic cumulates crystallized within a hot (700–900 °C) lower crust at 20–30 km depth (Al-Mishwat and Nasir, 2004). Finally, isotopic constraints from lower crustal xenoliths suggest the lower crust formed in the Neoproterozoic as a juvenile addition sourced from the mantle, possibly via ponding and fractionation of arc-related magmas (Stern and Johnson, 2010, and references therein).

Seismic anisotropy is relatively uniform throughout the Arabian Shield and has a dominant splitting direction subparallel to that of lower crustal electrical anisotropy. Though it is correlative, the magnitude of seismic SKS splitting is large enough to originate predominantly in the mantle (Wolfe, 1999; Hansen and others, 2006). Some authors argue that the orientation of SKS splitting is a superposition of the regional northeast-directed absolute plate motion and the northwest-directed Red Sea rifting (Hansen and others, 2006). Regardless, seismic anisotropy is unable to discriminate between a Cenozoic origin caused by northward plate motion or fossil anisotropy within the lithosphere formed during east-west compression in the late Neoproterozoic.

Partial Melt

Similar patterns of lower crustal electrical anisotropy are observed in active rifting zones like the Rio Grande Rift (Feucht and others, 2017), where the anisotropic layer was interpreted to include aligned zones of partial melt related to extension. Given ongoing extension and volcanism, the lower crust beneath the western Arabian Shield may be thermally primed and maintain a degree of long-lived partial melt. Erupted lavas record repeated differentiation sequences from alkali basalt to trachyte that lasted as long as 10,000 to 25,000 years (Stelten and others, 2018), suggesting magma storage at mid-crustal levels may occur for similar durations.

To investigate melt as a potential source, the minimum melt fraction required to produce the minimum lower crustal conductance is calculated (fig. 8) and then compared to independent seismic constraints. The minimum conductance (500 S) is derived from the ρ_{yy} 2D anisotropic model (fig. 7). However, because ρ_{xx} is at least twice as conductive, 500 S is considered a minimum lower crustal conductance for subsequent calculations. Two end-member melt scenarios are computed: a uniformly distributed melt throughout the lower crust and a sill composed of pure melt. Although not explicitly detailed below, a similar analysis can be carried out to estimate the minimum amounts of saline fluids required to produce the minimum conductance.

The conductivity of silicate melts is dependent upon several factors, including temperature, pressure, and SiO_2, H_2O, and Na_2O content of the melt. Parameters used for estimated melt resistivity are 45.7 weight percent SiO_2 (Moufti and others, 2012), 3.4 weight percent Na_2O (Moufti and others, 2012), 0–1 weight percent H_2O (Kereszturi and others, 2016), and 900 °C (McGuire and Bohannon, 1989; Stern and Johnson, 2010). Pure melt conductivities are calculated using these compositional and thermal constraints using the SIGMELTS program (Pommier and Le-Trong, 2011). For the evenly distributed end-member scenario, melt fraction is estimated using a mixing law that assumes melt is distributed along interconnected grain boundaries (Waff, 1974). This estimates a minimum melt fraction of 15 percent wet or 29 percent dry basaltic melt is required to explain the lower crustal conductance. The sill of pure melt at the mid-crustal levels end-member scenario would require a sill at least 1.3 km thick in the case of wet basalt or 2.6 km thick in the dry basalt case. It is important to note that a more evolved melt composition (for example, trachyte) would require even greater melt fractions or sill thicknesses because of the higher SiO_2 content.

The minimum estimates of partial melt that would be needed to explain the modeled bulk resistivity would also cause detectable reductions in seismic velocity. Active margins and rift settings with conductive lower crust (such as Tibet, Altiplano-Puna, Rio Grande Rift, and Basin and Range) are accompanied by reduced lower crustal seismic velocities. In contrast, the Arabian Shield is characterized by a pronounced Conrad discontinuity, with elevated body- and shear-wave velocities in the lower crust. P-wave velocities are estimated to be between 6.7 and 7.4 km/s (Mooney and others, 1985; DESERT Group, 2004), suggestive of a mafic lower crust devoid of melt or aqueous fluids. Similarly, shear-wave velocities in the lower crust are generally greater than 4 km/s (Civilini, 2018; Mokhtar and others, 2001), again inconsistent with our minimum estimated melt fractions. As a point of comparison, P- and S-wave velocities of 2.3 and 1.1 km/s, respectively, are attributed to 30 percent rhyolitic melt at 800 °C and 5 km depth beneath Yellowstone Caldera (Chu and others, 2010). The elevated seismic velocities beneath the Arabian Shield are inconsistent with even a small percentage of lower crustal melt.

At a local scale, Abdelwahed and others (2016) and Civilini (2018) both image reduced seismic velocity within a small patch of lower crust beneath the fissure vent source of the 1256 C.E. eruption. Unlike the broad zone of electrical anisotropy that extends hundreds of kilometers, the low velocity zone is a mere 10–20 km wide, and Civilini (2018) argue that elevated temperature alone are sufficient to explain the modest reduction in shear-wave velocity. Such a localized potentially melt-bearing zone may be superimposed upon the broad anisotropic signature but is indistinguishable. Based on seismic constraints, this localized zone is absent outside of the local area of the 1256 C.E. eruptive vent. Thus, reduced seismic velocity is likely caused by elevated but subsolidus temperatures and that partial melt, if present in the lower crust, is highly localized and at low melt fractions. Finally, the presence of thin melt lenses near the top of the electrically anisotropic zone (10–15 km depth) cannot be ruled out. This depth in the model is marked as a complicated transition between the resistive upper crust and the anisotropic lower crust. Modeling anisotropic structure within the context of an isotropic inversion, even in three dimensions, limits the ability to interpret this transition zone. In summary, the inconsistency of partial melt with elevated seismic velocities rules out any large, well-connected, melt-based explanation for the broad zone of lower crustal anisotropy. Nevertheless, resolution of both MT and seismic tomography cannot rule out small (meter scale) pockets of partial melt.

Graphite

Lower crustal electrical anisotropy aligned with regional tectonic structure is identified beneath several shield terranes. Unlike in the current investigation, these studies are in regions devoid of recent tectonism. Many researchers speculate the anisotropy arises from either hot, saline fluids or an interconnected network of graphite localized along structurally controlled microfractures (Rasmussen, 1988; Kellett and others, 1992; Leibecker and others, 2002; Unsworth and others, 2005; Wannamaker and others, 2008; Brasse and others, 2009; Feucht and others, 2017). As opposed to melt or saline fluids, interconnected graphite is considered the most likely explanation for the lower crustal conductivity and anisotropy beneath the western Arabian Shield. Two possible explanations are examined for the graphitic source and microfracture direction: ductile deformation related to Cenozoic tectonics and Neoproterozoic fabric developed during the amalgamation and stabilization of the Arabian Shield.

Several lines of evidence (seismic, petrologic, and geochemical) support the hypothesis of a localized channel of north-directed asthenospheric flow beneath the Makkah-Madīnah-Nafud volcanic line within a corrugation in the overriding lithosphere (Camp and Roobol, 1992; Hansen and others, 2006; Yao and others, 2017). Such flow may reasonably couple into the ductile lower crust through traction along the base of the thin rigid lithosphere. Thus, the observed conductivity and anisotropy may reflect grain-boundary graphite interconnected via deformation fabric in the lower crust. However, the apparent termination of the anisotropic zone across a Neoproterozoic fault suggests deformation alone is an inadequate explanation. Ductile flow in the lower crust would be expected to mirror flow in the asthenosphere and be modulated by lower crustal rheology, a function of temperature and composition. The channel of north-directed mantle flow is broad (300 km; Yao and others, 2017), so lower crustal flow is thus expected to diminish smoothly away from the Makkah-Madīnah-Nafud volcanic line rather than sharply transition from an (anisotropic) flow to (isotropic) no-flow regime. Whereas modeling suggests the crust is not in thermal equilibrium following lithospheric thinning around 12 million years ago (Ma) (Blanchette and others, 2018), there is little reason to suspect sharp thermal or compositional heterogeneity across a Neoproterozoic fault.

Anisotropy in other shields appears to reflect ancient fabric frozen into the lower crust. The upper crust of the Arabian Shield exhibits variable fabric, both geological and geophysical, reflecting Neoproterozoic amalgamation of various magmatic arcs, their stabilization into continental crust, and the subsequent dissection by the Najd Fault System. The Arabian Shield formed via a protracted process of convergent margin terrane accretion, and isotopic evidence suggests a juvenile mafic lower crust formed near the end of convergence (Stern and Johnson, 2010). Lithospheric delamination has been proposed to explain widespread, rapid exhumation, late orogenic calc-alkaline and alkaline igneous activity, and the formation of extensional grabens around 630–590 Ma (Avigad and Gvirtzman, 2009). Delamination, in which lithospheric mantle and possibly lower crust was replaced by asthenospheric mantle, would explain variability in lithospheric thickness, layering, and composition between the Arabian Shield and Arabian Platform (Stern and Johnson, 2010). Both the prominent Conrad discontinuity at 20 km depth and elevated lower crustal velocities are consistent with delamination and regrowth of a mafic lower crust. A mafic lower crust is further suggested by gravity modeling (Brew and others, 2001), which suggests a dense lower crust (2.87–2.92 g/cm^3) below about 20 km depth. Importantly, lower crustal xenoliths entrained in non-Harrat-Rahat mafic lavas reveal magmatic textures and mafic mineralogies that suggest basaltic cumulates crystallized within a hot (700–1,000 °C) lower crust at 20–30 km depth (Al-Mishwat and Nasir, 2004). A continuum from more fractionated plagioclase-rich to more primitive pyroxene-rich xenoliths are found, suggestive of a stratified lower crust. Finally, isotopic constraints from lower crustal xenoliths suggest the lower crust formed in the Neoproterozoic as a juvenile addition sourced from the mantle, possibly via ponding and fractionation of arc-related magmas (Stern and Johnson, 2010, and references therein).

Late stages of amalgamation were also marked by motion along the Najd Fault System. It is plausible that magnetic lineaments and surface faulting reflect only the latest dissection by the Najd Fault System and that the lower crust preserves a different record of the Neoproterozoic crustal amalgamation and stabilization. Given a presumably hot lithosphere (from delamination or arc magmatism), crustal deformation may have been vertically decoupled, with east-west compression (Moore, 1979) facilitated by N. 30° W. faulting in the brittle upper crust and north-directed ductile flow in the lower crust. Electrical anisotropy may thus reflect fabric frozen into the lower crust as it cooled and stabilized.

Upper Mantle

The inversion model constrains upper mantle resistivity structure to a depth of at most 150 km. A moderate conductor (15–30 Ω·m) is imaged in the upper mantle within an otherwise resistive (100–500 Ω·m) lithospheric mantle (fig. 11). The center of this conductor is located slightly northeast of Harrat Rahat, where northward extension remains unconstrained. The top of the conductor is around 60–70 km depth, similar to the depth of the lithosphere-asthenosphere boundary (LAB) estimated from seismic receiver functions (Hansen and others, 2007), and dips to more than 100 km depth at the edges of the site array.

The mantle conductor is interpreted to be shallow asthenosphere beneath a thinned mantle lithosphere. This interpretation is consistent with surface-wave tomography, which finds a north-south trending low-velocity zone beneath the western Arabian Shield, interpreted to reflect northward flow of hot asthenosphere from the Afar Hot Spot (Yao and others, 2017). The top of the low-velocity zone occurs at a depth of 60 km, consistent with the top of our imaged mantle conductor. The geometry and conductivity of this zone are further consistent with petrologic and isotopic constraints, which suggest that Harrat Rahat basalts are generated as peridotite melts (with melt fractions less than 10 percent) within the garnet stability field (>75 km depth) at temperatures of 1,420–1,450 °C (Salters and others, 2023; Sisson and others, 2023).

Summary

To better understand the magmatic system feeding Harrat Rahat near the city of Al Madīnah, magnetotelluric (MT) data were jointly collected by the U.S. Geological Survey and Saudi Geological Survey at 122 broadband stations and 17 long-period stations in a grid spanning about 150 × 50 km oriented perpendicular to Harrat Rahat. The MT response from these data characterize the middle and lower crust (12–40 km depth) as anisotropic, prescribing the need for different modeling techniques. The survey results were subsequently modeled using ModEM, a 3D isotropic inversion program; MARE2DEM, a 2D anisotropic inversion program; and Pek1D, a 1D anisotropic modeling program. A schematic geologic interpretation of the resistivity models is summarized in fig. 14.

The preferred 3D resistivity model images the near surface (down to 1 km depth) as having a conductive (<50 Ω·m) basin filled with brackish fluids about 500 meters deep, below Quaternary lava flows of the Harrat Rahat. Down to about 12 km depth, the upper crust is resistive (>1,000 Ω·m),

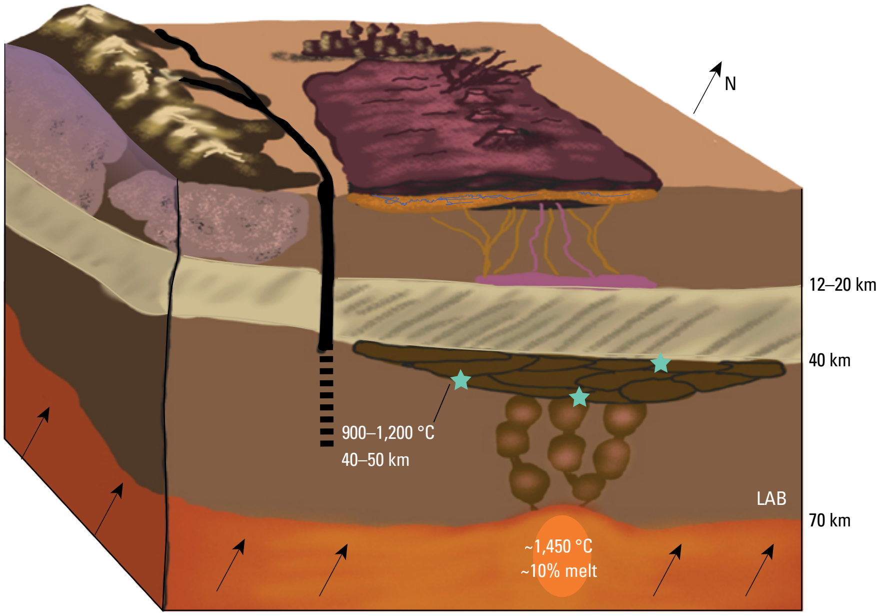

Figure 14. Cartoon summarizing the interpretation of the electrical resistivity model. In the near surface, below Quaternary lava flows, is a basin (<50 Ohm meters [Ω·m]) with a maximum depth of 500 meters (m) that is filled with brackish fluids. The upper crust (down to 12 kilometers [km]) is an amalgamation of Precambrian rocks (>1,000 Ω·m). The lower crust (12–40 km) is electrically anisotropic with an orientation of N. 10° E. and a ratio of resistivities of 50/25 Ω·m for the resistive and conductive directions. This layer slightly dips toward the east and may be offset by the Najd Fault System by 40 km of left-lateral offset and possibly 1 km of vertical offset. The stars show estimated depths of where xenoliths collected at the surface are interpreted to have formed. The lithosphere-asthenosphere boundary (LAB) is at around 70 km depth, below which the Harrat Rahat magmatic source is estimated to contain 10 percent (%) melt. Asthenospheric flow is indicated by the arrows in a dominantly northward direction.

indicative of amalgamated Precambrian terranes. Two conductivity anomalies are present west of Harrat Rahat between 4 and 8 km depth and are possibly related to contact metamorphism upon pluton emplacement in the Precambrian. These two anomalies are on opposite sides of the Najd Fault System sinisterly offset by 40 km. Between 12 and 40 km depth is an electrically anisotropic region with a N. 10° E. orientation and modeled with a lower bound ratio of 50/25 resistive to conductive directions. This layer is interpreted to reflect interconnected graphitic fractures within the fabric of a deforming lower crust that formed in response to channeled asthenospheric flow coupled through a thin, rigid mantle lid. The resistivity results suggest a crust that is largely barren of melt. Within this region, melt transects the crust primarily through diking and remains suprasolidus for geologically short time intervals (~10,000 years). Melt storage is likewise limited to short-lived episodes of enhanced magma flux from the asthenosphere. A conductive anomaly (<30 Ω·m) at 60 km depth represents the magmatic source near the LAB with a partial melt content of 10 percent. This is consistent with seismic estimates of the base of a thinned lithosphere, and with petrologic and isotopic studies suggesting the mafic lavas of Harrat Rahat are sourced within the asthenosphere at depths greater than 75 km and with mantle potential temperatures greater than 1,400 °C.

This study demonstrates the need to take expected subsurface resistivity structures into consideration when designing a survey. Specifically, if an anisotropic layer is expected, the survey aperture should be at least four times the depth to the layer to ensure full coverage and that artifacts of modeling are not incorrectly interpreted. Moreover, choosing the correct modeling method based on the dimensionality and distortion of the data is imperative for accurate interpretation of resulting resistivity models.

Acknowledgments

The authors would like to thank the Saudi Geological Survey for supplying all field support, reviewers Darcy McPhee and Drew Downs, editor Monica Erdman, and layout designer Kimber Petersen.

References Cited

Abdelwahed, M.F., El-Masry, N., Moufti, M.R., Kenedi, C.L., Zhao, D., Zahran, H., and Shawali, J., 2016, Imaging of magma intrusions beneath Harrat Al Madīnah in Saudi Arabia: Journal of Asian Earth Sciences, v. 120, p. 17–28, https://doi.org/10.1016/j.jseaes.2016.01.023.

Aboud, E., Wameyo, P., Alqahtani, F., and Moufti, M.R., 2018, Imaging subsurface northern Rahat Volcanic Field, Madinah City, Saudi Arabia, using magnetotelluric study: Journal of Applied Geophysics, v. 159, p. 564–572, https://doi.org/10.1016/j.jappgeo.2018.10.005.

Al-Mishwat, A.T., and Nasir, S.J., 2004, Composition of the lower crust of the Arabian Plate—A xenolith perspective: Lithos, v. 72, p. 45–72, https://doi.org/10.1016/j.lithos.2003.08.003.

Avigad, D., and Gvirtzman, Z., 2009, Late Neoproterozoic rise and fall of the northern Arabian–Nubian Shield—The role of lithospheric mantle delamination and subsequent thermal subsidence: Tectonophysics, v. 477, p. 217–228, https://doi.org/10.1016/j.tecto.2009.04.018.

Bedrosian P.A., Peacock J.R., Bowles-Martinez, E., Schultz, A., and Hill, G.J., 2018, Crustal inheritance and a top-down control on arc magmatism at Mount St Helens: Nature Geoscience, v. 11, p. 865–870, https://doi.org/10.1038/s41561-018-0217-2.

Bedrosian, P.A., Peacock, J.R., Dhary, M., Sharif, A., Feucht, D.W., and Zahran, H., 2019, Crustal magmatism and anisotropy beneath the Arabian Shield—A cautionary tale: Journal of Geophysical Research, Solid Earth, v. 124, https://doi.org/10.1029/2019JB017903.

Bedrosian, P.A., Peacock, J.R., and Feucht, D.W., 2023, Magnetotelluric data from northern Harrat Rahat, Saudi Arabia, 2016: U.S. Geological Survey data release, https://doi.org/10.5066/P99H8HJ7.

Bibby, H.M., Caldwell, T.G., and Brown, C., 2005, Determinable and non-determinable parameters of galvanic distortion in magnetotellurics: Geophysical Journal International, v. 163, p. 915–930, https://doi.org/10.1111/j.1365-246X.2005.02779.x.

Blanchette, A.R., Klemperer, S.L., Mooney, W.D., and Zahran, H.M., 2018, Two-stage Red Sea rifting inferred from mantle earthquakes in Neoproterozoic lithosphere: Earth and Planetary Science Letters, v. 497, p. 92–101, https://doi.org/10.1016/j.epsl.2018.05.048.

Booker, J.R., 2014, The magnetotelluric phase tensor—A critical review: Surveys in Geophysics, v. 35, no. 7, p. 7–40, https://doi.org/10.1007/s10712-013-9234-2.

Brasse, H., Kapinos, G., Li, Y., Mütschard, L., Soyer, W. and Eydam, D., 2009, Structural electrical anisotropy in the crust at the South-Central Chilean continental margin as inferred from geomagnetic transfer functions: Physics of the Earth and Planetary Interiors, v. 173, p. 7–16, https://doi.org10.1016/j.pepi.2008.10.017.

Brew, G., Barazangi, M., Al-Maleh, A.K., Sawaf, T., 2001, Tectonic and geologic evolution of Syria: GeoArabia, v. 6, p. 573–616.

Cagniard, L., 1953, Basic theory of the magneto-telluric method of geophysical prospecting: Geophysics, v. 18, no. 3, p. 605–635, https://doi.org/10.1190/1.1437915.

Caldwell, T.G., Bibby, H.M., and Brown, C., 2004, The magnetotelluric phase tensor: Geophysical Journal International, v. 158, p. 457–469, https://doi.org/10.1111/j.1365-246X.2004.02281.x.

Camp, V.E., Hooper, P.R., Roobol, J.M., and White, D.L., 1987, The Madinah eruption, Saudi Arabia—Magma mixing and simultaneous extrusion of three basaltic chemical types: Bulletin of Volcanology, v. 49, p. 489–508.

Camp, V.E., and Roobol, J.M., 1989, The Arabian continental alkali basalt province; Part I—Evolution of Harrat Rahat, Kingdom of Saudi Arabia: Geological Society of America Bulletin, v. 101, p. 71–95, https://doi.org/10.1130/0016-7606(1989)101<0071:tacabp>2.3.co;2.

Camp, V.E., and Roobol, J.M., 1992, Upwelling asthenosphere beneath western Arabia and its regional implications: Journal of Geophysical Research, v. 97, p. 15255–15271, https://doi.org/10.1029/92JB00943.

Chave, A.D., and Jones, A.G., eds., 2012, The Magnetotelluric Method—Theory and Practice: Cambridge University Press, 552 p., https://doi.org/10.1017/CBO9781139020138.

Chu, R., Helmberger, D.V., Sun, D., Jackson, J.M., and Zhu, L., 2010, Mushy magma beneath Yellowstone: Geophysical Research Letters, v. 37, https://doi.org/10.1029/2009GL041656.

Civilini, F., 2018, Determining seismic shear velocity from ambient noise sources at regional and local scales: Wellington, New Zealand, Victoria University of Wellington, Ph.D. thesis, 313 p.

Coleman, R.G., Gregory, R.T., and Brown, G.F., 1983, Cenozoic volcanic rocks of Saudi Arabia: U.S. Geological Survey Open-File Report 83–788, 82 p., 1 plate, https://doi.org/10.3133/ofr83788.

DESERT Group, Weber, M., Abu-Ayyash, K., Abueladas, A., Agnon, A., Al-Amoush, H., Babeyko, A., Bartov, Y., Baumann, M., Ben-Avraham, Z., Bock, G., Bribach, J., El-Kelani, R., Förster, A., Förster, H.-J., Frieslander, U., Garfunkel, Z., Grunewald, G., Götze, H.J., Haak, V., Haberland, Ch., Hassouneh, M., Helwig, S., Hofstetter, A., Jäckel, K.-H., Kesten, D., Kind, R., Maercklin, N., Mechie, J., Mohsen, A., Neubauer, F.M., Oberhänsli, R., Qabbani, I., Ritter, O., Rümpker, G., Rybakov, M., Ryberg, T., Scherbaum, F., Schmidt, J., Schulze, A., Sobolev, S., Stiller, M., Thoss, H., Weckmann, U., Wylegalla K., 2004, The crustal structure of the Dead Sea Transform: Geophysical Journal International, v. 156, p. 655–681, https://doi.org/10.1111/j.1365-246X.2004.02143.x.

Downs, D.T., Stelten, M.E., Champion, D.E., Dietterich, H.R., Nawab, Z., Zahran, H., Hassan, K., and Shawali, J., 2018, Volcanic history of the northernmost part of the Harrat Rahat volcanic field, Saudi Arabia: Geosphere, v. 14, no. 3, p. 1253–1282, https://doi.org/10.1130/GES01625.1.

Egbert, G.D., 1997, Robust multiple-station magnetotelluric data processing: Geophysical Journal International, v. 130, p. 475–496, https://doi.org/10.1111/j.1365-246X.1997.tb05663.x.

Egbert, G.D., and Kelbert, A., 2012, Computational recipes for electromagnetic inverse problems: Geophysical Journal International, v. 189, p. 251–267, https://doi.org/10.1111/j.1365-246x.2011.05347.x.

Feucht, D.W., Sheehan, A.F., and Bedrosian, P.A., 2017, Magnetotelluric imaging of lower crustal melt and lithospheric hydration in the Rocky Mountain Front Transition Zone, Colorado, USA: Journal of Geophysical Research, v. 122, no. 12, p. 9489–9510, https://doi.org/10.1002/2017JB014474.

Hansen, S., Rodgers, A.J., Schwartz, S.Y., and Al-Amni, A., 2007, Imaging ruptured lithosphere beneath the Red Sea and Arabian Peninsula: Earth and Planetary Science Letters, v. 259, no. 3-4, p. 256–265, https://doi.org/10.1016/j.epsl.2007.04.035.

Hansen, S., Schwartz, S., Al-Amni, A., and Rodgers, A., 2006, Combined plate motion and density-driven flow in the asthenosphere beneath Saudi Arabia—Evidence from shear-wave splitting and seismic anisotropy: Geology, v. 34, p. 869–872, https://doi.org/10.1130/g22713.1.

Heise, W., Caldwell, T.G., Bibby, H.M., and Brown, C., 2006, Anisotropy and phase splits in magnetotellurics: Physics of the Earth and Planetary Interiors, v. 158, p. 107–121, https://doi.org/10.1016/j.pepi.2006.03.021.

Kelbert, A., Meqbel, N., Egbert, G.D., and Tandon, K., 2014, ModEM—A modular system for inversion of electromagnetic geophysical data: Computers & Geosciences, v. 66, p. 40–53, https://doi.org/10.1016/j.cageo.2014.01.010.

Kellett, R.L., Mareschal, M., and Kurtz, R.D., 1992, A model of lower crustal electrical anisotropy for the Pontiac Subprovince of the Canadian Shield: Geophysics Journal International, v. 111, p. 141–150, https://doi.org/10.1111/j.1365-246X.1992.tb00560.x.

Kereszturi, G., Németh, K., Moufti, M.R., Cappello, A., Murcia, H., Ganci, G., Del Negro, C., Procter, J. and Zahran, H.M., 2016, Emplacement conditions of the 1256 AD Al Madīnah lava flow field in Harrat Rahat, Kingdom of Saudi Arabia—Insights from surface morphology and lava flow simulations: Journal of Volcanology and Geothermal Research, v. 309, p. 14–30, https://doi.org/10.1016/j.jvolgeores.2015.11.002.

Key, K., 2016, MARE2DEM—A 2D inversion code for controlled-source electromagnetic and magnetotelluric data: Geophysical Journal International, v. 207, no. 1, p. 571–588, https://doi.org/10.1093/gji/ggw290.

Kreiger, L., and Peacock, J.R., 2014, MTpy—A Python toolbox for magnetotellurics: Computers & Geoscience, v. 72, p. 167–175, https://doi.org/10.1016/j.cageo.2014.07.013.

Langenheim, V.E., Ritsinger, B.T., Zahran, H., Shareef, A., and Al-dahri, M., 2019, Crustal structure of the northern Harrat Rahat volcanic field (Saudi Arabia) from gravity and aeromagnetic data: Tectonophysics, v. 750, p. 9–21, https://doi.org/10.1016/j.tecto.2018.11.005.

Langenheim, V.E., Ritzinger, B.T., Zahran, H.M., Shareef, A., and Al-Dhahry, M.K., 2023, Depth to basement and crustal structure of the northern Harrat Rahat volcanic field, Kingdom of Saudi Arabia, from gravity and aeromagnetic data, chap. K *of* Sisson, T.W., Calvert, A.T., and Mooney, W.D., eds., Active volcanism on the Arabian Shield—Geology, volcanology, and geophysics of northern Harrat Rahat and vicinity, Kingdom of Saudi Arabia: U.S. Geological Survey Professional Paper 1862 [also released as Saudi Geological Survey Special Report SGS–SP–2021–1], 18 p., https://doi.org/10.3133/pp1862K.

Leibecker, J., Gatzemeier, A., Hönig, M., Kuras, O., and Soyer, W., 2002, Evidence of electrical anisotropic structures in the lower crust and the upper mantle beneath the Rhenish Shield: Earth and Planetary Science Letters, v. 202, p. 289–302, https://doi.org/10.1016/s0012-821x(02)00783-5.

Loni, O.A., 2005, Geophysical characteristics of the subsurface structures in northeastern Al Madīnah Al-Munawarah (Harrat Al-Aqul), Central Arabian Shield: Riyadh, Saudi Arabia, King Saud University, M.S. thesis, 257 p.

McGuire, A.V., and Bohannon, R.G., 1989, Timing of mantle upwelling—Evidence for a passive origin for the Red Sea rift: Journal of Geophysical Research, v. 94, no. B2, p. 1677–1682, https://doi.org/10.1029/JB094iB02p01677.

Mokhtar, T.A., Ammon, C.J., Herrmann, R.B., and Ghalib, H.A.A., 2001, Surface wave velocities across Arabia: Pure and Applied Geophysics, v. 158, p. 1425–1444, https://doi.org/10.1007/pl00001228.

Mooney, W.D., Gettings, M.E., Blank, H.R., and Healy, J.H., 1985, Saudi Arabian seismic-refraction profile—A traveltime interpretation of crustal and upper mantle structure: Tectonophysics, v. 111, p. 173–246, https://doi.org/10.1016/0040-1951(85)90287-2.

Moore, J.M., 1979, Tectonics of the Najd transcurrent fault system, Saudi Arabia: Journal of the Geological Society of London, v. 136, p. 441–454, https://doi.org/10.1144/gsjgs.136.4.0441.

Moufti, M.R., Moghazi, A.M., and Ali, K.A., 2012, Geochemistry and Sr-Nd-Pb isotopic composition of the Harrat Al Madīnah Volcanic Field, Saudi Arabia: Gondwana Research, v. 21, p. 670–689, https://doi.org/10.1016/j.gr.2011.06.003.

Pek, J., and Verner, T., 1997, Finite-difference modelling of magnetotelluric fields in two-dimensional anisotropic media: Geophysical Journal International, v. 128, p. 505–521, https://doi.org/10.1111/j.1365-246X.1997.tb05314.x.

Pellaton, C., 1981, Geologic map of the Al Madinah quadrangle, sheet 24D, Kingdom of Saudi Arabia: Saudi Arabian Deputy Ministry for Mineral Resources Geoscience Map GM–52, scale 1:250,000, 19 p.

Pommier, A., and Le-Trong, E., 2011, “SIGMELTS”—A web portal for electrical conductivity calculations in geosciences: Computers & Geosciences, v. 37, p. 1450–1459, https://doi.org/10.1016/j.cageo.2011.01.002.

Rasmussen, T.M., 1988, Magnetotellurics in southwestern Sweden—Evidence for electrical anisotropy in the lower crust?: Journal of Geophysical Research, v. 93, p. 7897–7907, https://doi.org/10.1029/jb093ib07p07897.

Roobol, J.M., Bankher, K., and Bamufleh, S., 2007, Geothermal anomalies along the MMN volcanic line including the cities of Al Madinah al Munawwarah and Makkah al Mukarramah: Saudi Geological Survey Technical Report SGS–TR–2007–6, 95 p.

Salters, V.J.M., Sachi-Kocher, A., Downs, D.T., Stelten, M.E., and Sisson, T.W., 2023, Isotopic and geochemical evidence for the source of volcanism at Harrat Rahat, Kingdom of Saudi Arabia, chap. J *of* Sisson, T.W., Calvert, A.T., and Mooney, W.D., eds., Active volcanism on the Arabian Shield—Geology, volcanology, and geophysics of northern Harrat Rahat and vicinity, Kingdom of Saudi Arabia: U.S. Geological Survey Professional Paper 1862 [also released as Saudi Geological Survey Special Report SGS–SP–2021–1], 30 p., https://doi.org/10.3133/pp1862J.

Sisson, T.W., Downs, D.T., Calvert, A.T., Dietterich, H.R., Mahood, G.A., Salters, V.J.M., Stelten, M.E., and Shawali, J., 2023, Mantle origin and crustal differentiation of basalts and hawaiites of northern Harrat Rahat, Kingdom of Saudi Arabia, chap. I *of* Sisson, T.W., Calvert, A.T., and Mooney, W.D., eds., Active volcanism on the Arabian Shield—Geology, volcanology, and geophysics of northern Harrat Rahat and vicinity, Kingdom of Saudi Arabia: U.S. Geological Survey Professional Paper 1862 [also released as Saudi Geological Survey Special Report SGS–SP–2021–1], 42 p., https://doi.org/10.3133/pp1862I.

Stelten, M.E., Downs, D.T., Dietterich, H.R., Mahood, G.A., Calvert, A.T., Sisson, T.W., Zahran, H., and Shawali, J., 2018, Timescales of magmatic differentiation from alkali basalt to trachyte within the Harrat Rahat volcanic field, Kingdom of Saudi Arabia: Contributions to Mineralogy and Petrology, v. 173, no. 68, https://doi.org/10.1007/s00410-018-1495-9.

Stelten, M.E., Downs, D.T., Champion, D.E., Dietterich, H.R., Calvert, A.T., Sisson, T.W., Mahood, G.A., and Zahran, H.M., 2023, Eruptive history of northern Harrat Rahat—Volume, timing, and composition of volcanism over the past 1.2 million years, chap. D *of* Sisson, T.W., Calvert, A.T., and Mooney, W.D., eds., Active volcanism on the Arabian Shield—Geology, volcanology, and geophysics of northern Harrat Rahat and vicinity, Kingdom of Saudi Arabia: U.S. Geological Survey Professional Paper 1862 [also released as Saudi Geological Survey Special Report SGS–SP–2021–1], 46 p., https://doi.org/10.3133/pp1862D.

Stern, R.J., and Johnson, P., 2010, Continental lithosphere of the Arabian Plate—A geologic, petrologic, and geophysical synthesis: Earth Science Reviews, v. 101, p. 29–67, https://doi.org/10.1016/j.earscirev.2010.01.002.

Tikhonov, A.N., 1950, Determination of the electrical characteristics of the deep state of the earth's crust: Proceedings of the USSR Academy of Sciences, v. 73, no. 2, p. 295–297.

Unsworth, M.J., Jones, A.G., Wei, W., Marquis, G., Gokarn, S.G., Spratt, J.E., and the INDEPTH-MT team, 2005, Crustal rheology of the Himalaya and Southern Tibet inferred from magnetotelluric data: Nature, v. 438, p. 78–81, https://doi.org/10.1038/nature04154.

Waff, H.S., 1974, Theoretical considerations of electrical conductivity in a partially molten mantle with implications for geothermometry: Journal of Geophysical Research, v. 79, p. 4003–4010, https://doi.org/10.1029/jb079i026p04003.

Wannamaker, P.E., Hasterok, D.P., Johnston, J.M., Stodt, J.A., Hall, D.B., Sodergren, T.L., Pellerin, L., Maris, V., Doerner, W.M., Groenewold, K.A., and Unsworth, M.J., 2008, Lithospheric dismemberment and magmatic processes of the Great Basin-Colorado Plateau transition, Utah, implied from magnetotellurics: Geochemistry, Geophysics, Geosystems, v. 9, no. 5, https://doi.org/10.1029/2007GC001886.

Weaver, J.T., Agarwal, A.K., Lilley, F.E.M., 2000, Characterization of the magnetotelluric tensor in terms of its invariants: Geophysical Journal International, v. 141, no. 2, p. 321–336, https://doi.org/10.1046/j.1365-246X.2000.00089.x.

Wolfe, C.J., 1999, Shear-wave splitting across western Saudi Arabia—The pattern of upper mantle anisotropy at a Proterozoic Shield: Geophysical Research Letters, v. 26, no. 6, p. 779–782, https://doi.org/10.1029/1999gl900056.

Yao, Z., Mooney, W.D., Zahran, H.M., and Youssef, S.E-H., 2017, Upper mantle velocity structure beneath the Arabian shield from Rayleigh surface wave tomography and its implications: Journal of Geophysical Research Solid Earth, v. 122, p. 6552–6568, https://doi.org/10.1002/2016JB013805.

Appendix 1. Anisotropic Modeling

MARE2DEM Sensitivity to Anisotropy Factor

Because anisotropic modeling codes are only available in two dimensions (Key, 2016), testing sensitivity of the anisotropy factor is important. The test model is similar to figure 9 of the main text, with an isotropic upper crust (0–15 kilometers [km]; 1,000 Ohm meters [Ω·m]), an anisotropic lower crust (15–40 km; varied), and an isotropic upper mantle (40–100 km; 30 Ω·m). The anisotropy factor of the lower crust was tested for three ratios: 2 (50/25 Ω·m), 5 (50/10 Ω·m), and 10 (100/10 Ω·m). The magnetotelluric response for these three models was modeled using the one-dimensional (1D) anisotropic code Pek1D (Pek and Verner, 1997). The 1D response for each model was copied along a two-dimensional (2D) profile line, which was used as input data to the 2D anisotropic inversion program MARE2DEM (fig. 1.1).

The results (fig. 1.1) demonstrate that the inversion underestimates the anisotropic factor. For an anisotropic factor of 2, the inversion estimates 1.8; for a factor of 5, the inversion estimates 2.8, and for a factor of 10, the inversion estimates 3. The xx direction (perpendicular to the profile) is more accurate than the yy direction (parallel to the profile). As compensation for underestimation, the inversion puts more anisotropy into isotropic layers because that is an easy way of fitting the data. Moreover, the thickness of the anisotropic layer changes depending on the anisotropic factor as the inversion program is sensitive to conductance. Depths to the top of layers is well resolved, but the overall thickness is not, a common shortcoming of magnetotellurics. With increasing anisotropy factors, the thickness of the anisotropic layer is closer to the real model, however the layer below is compensated by having more yy conductivity. To get an accurate estimate of anisotropy, the depth and layer thickness need to be known ahead of time or tested. The model at the appropriate depths can then be set to be anisotropic.

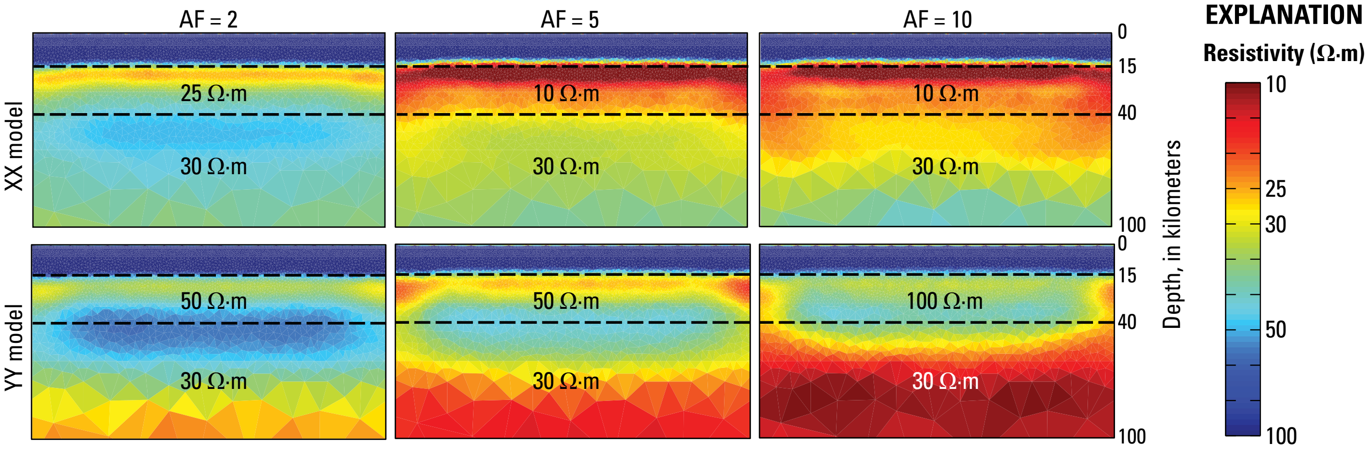

Figure 1.1 Cross sections showing the results of inverting anisotropic magnetotelluric data for different anisotropy factors (AF) using the MARE2DEM program. The anisotropic layer is between 15 and 40 kilometers depth. Note the inversion underestimates the anisotropy factor in all cases and has trouble estimating the thickness of the anisotropy layer. Resistivities are given in Ohm meters (Ω·m). The azimuth is 0 degrees.

MARE2DEM Sensitivity to Anisotropy Direction

The MARE2DEM inversion program can only model lateral anisotropy parallel and perpendicular to the modeling domain; therefore, knowing the direction of anisotropy is important to setting up the model domain. The data were prepared in the same way as described in the previous section. Here, the data were rotated into three different coordinate systems to test the sensitivity of MARE2DEM to the anisotropic direction (fig. 1.2). The three rotation angles of the coordinate systems were 0°, 30°, and 45° relative to the anisotropy direction. This gives a profile that is parallel and perpendicular to the anisotropy direction, a profile that is oblique to the anisotropy direction, and a profile that is nearly 45° to the anisotropy direction. Each dataset was then inverted using MARE2DEM (fig. 1.1).

The results demonstrate the need to know the anisotropy angle ahead of time. When the model coordinate system is in the “true” coordinate system of anisotropy, the inversion closely models the true model (see previous section on anisotropy factor). When the model coordinate system is oblique to the direction of anisotropy, the anisotropy factor is underestimated, and the maximum underestimation is for a model coordinate system oriented 45° relative to the anisotropy direction. In fact, at 45°, the inversion does not need anisotropy to fit the data because the anisotropy is sufficiently mixed such that the xx and yy directions are equivalent. This is true for any anisotropy factor.

References Cited

Key, K., 2016, MARE2DEM—A 2-D inversion code for controlled-source electromagnetic and magnetotelluric data: Geophysical Journal International, v. 207, no. 1, p. 571–588, https://doi.org/10.1093/gji/ggw290.

Pek, J., and Verner, T., 1997, Finite-difference modelling of magnetotelluric fields in two-dimensional anisotropic media: Geophysical Journal International, v. 128, p. 505–521, https://doi.org/10.1111/j.1365-246X.1997.tb05314.x.

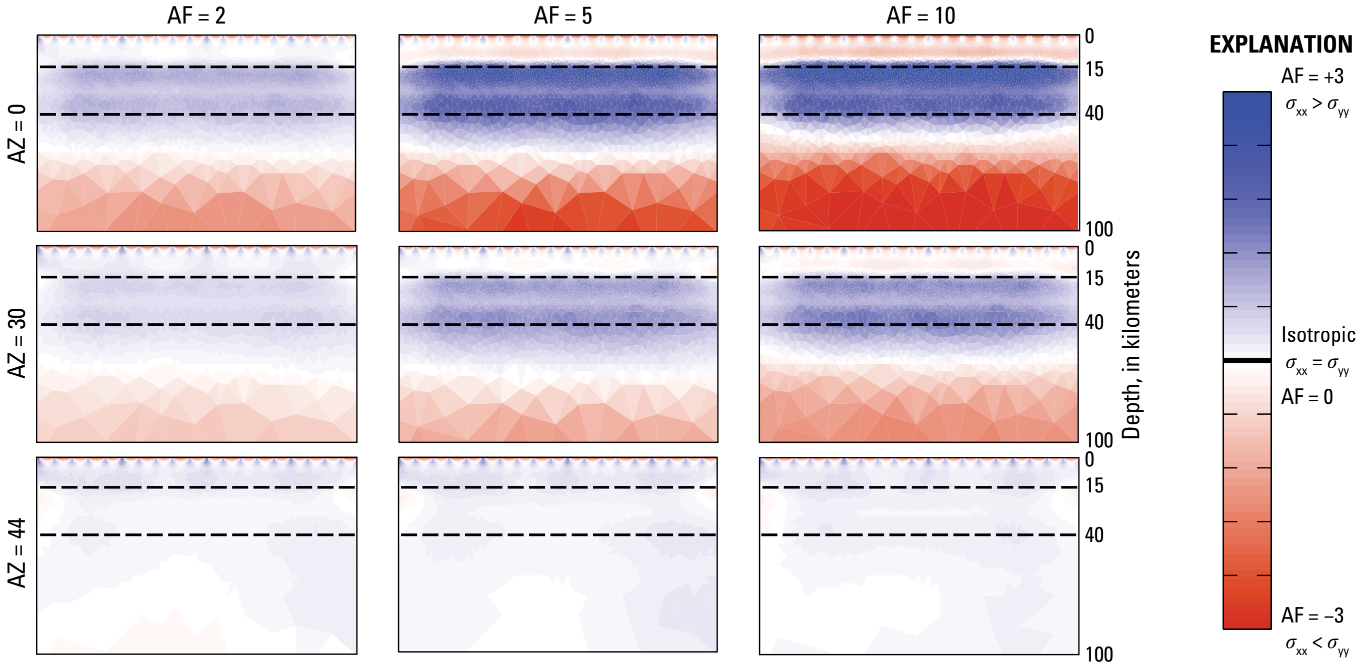

Figure 1.2. Cross sections showing the results of inverting anisotropic magnetotelluric data using the MARE2DEM program for different rotation angles relative to the anisotropy direction (AZ) and different anisotropy factors (AF). Note that when the modeling coordinate system is 45° from the anisotropy direction, the resulting model does not need anisotropy. σ_{xx}, conductance perpendicular to the profile (N. 10° E.); σ_{yy}, conductance parallel to the profile (N. 80° W.).

Appendix 2. Map View of Data Fits

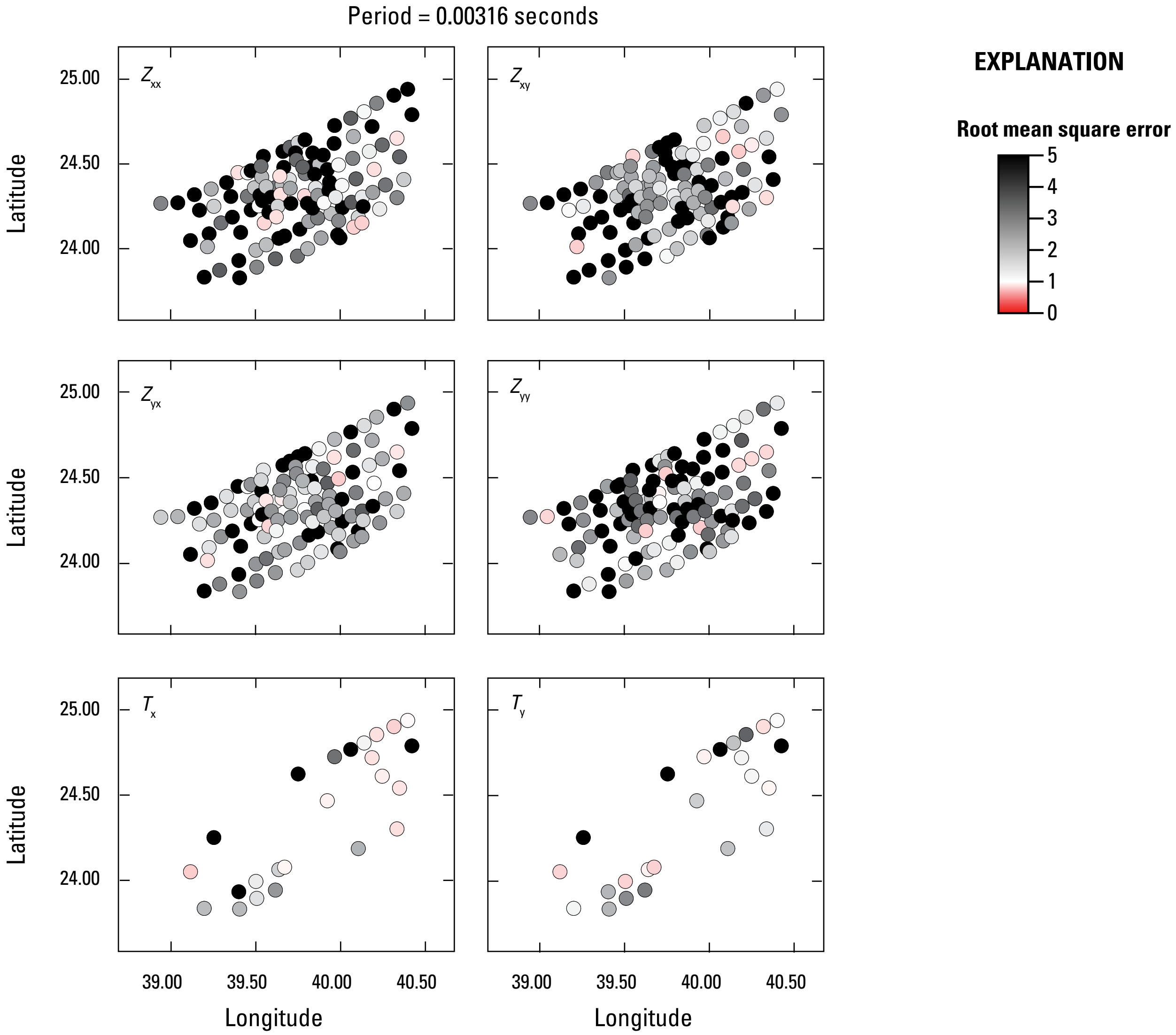

Figure 2.1. Map views of the normalized root mean square at a period of 0.00316 seconds showing each component of the impedance tensor (*Z*) and the induction vector (*T*) inverted for at each station.

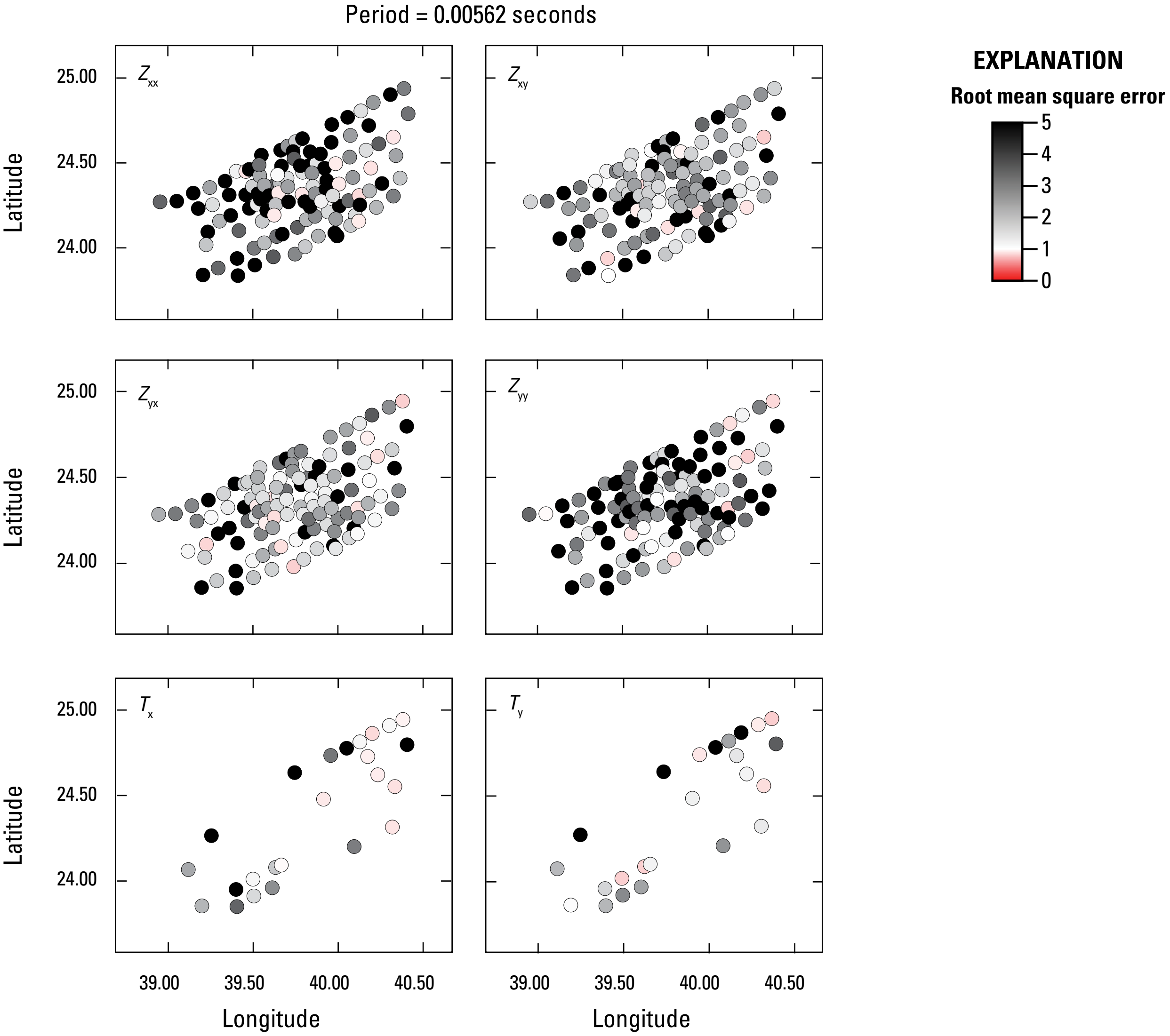

Figure 2.2. Map views of the normalized root mean square at a period of 0.00562 seconds showing each component of the impedance tensor (*Z*) and the induction vector (*T*) inverted for at each station.

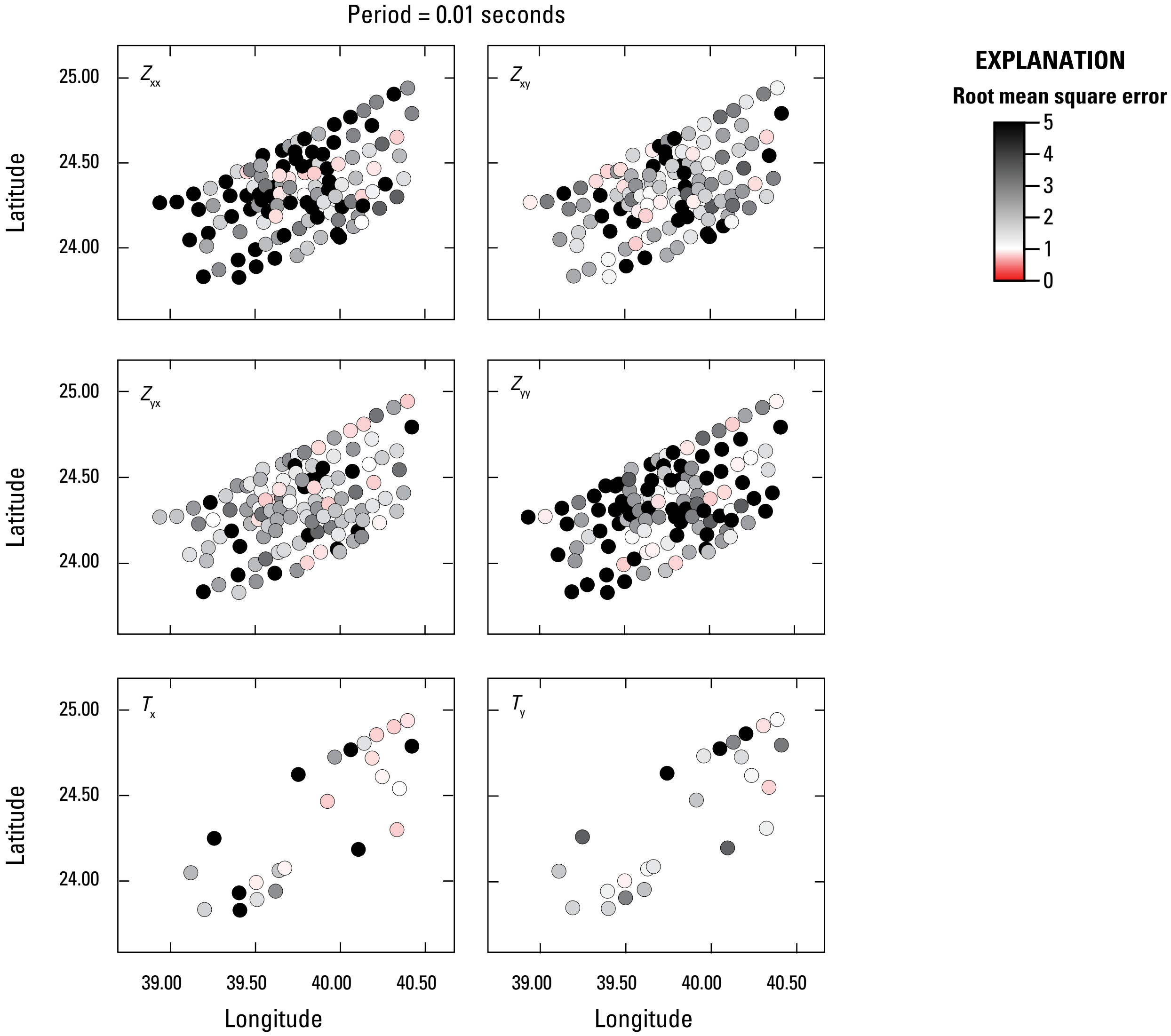

Figure 2.3. Map views of the normalized root mean square at a period of 0.01 seconds showing each component of the impedance tensor (*Z*) and the induction vector (*T*) inverted for at each station.

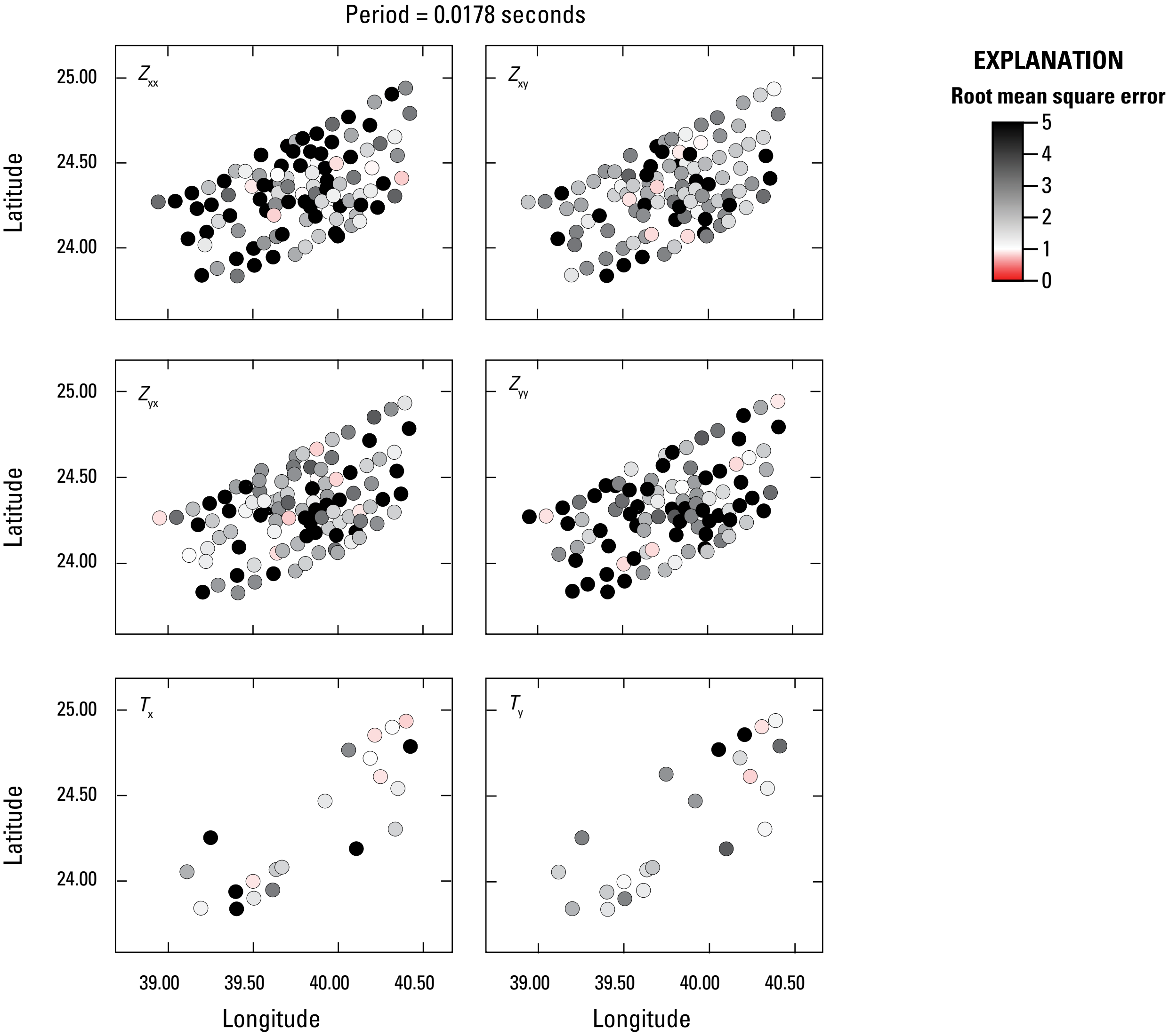

Figure 2.4. Map views of the normalized root mean square at a period of 0.0178 seconds showing each component of the impedance tensor (*Z*) and the induction vector (*T*) inverted for at each station.

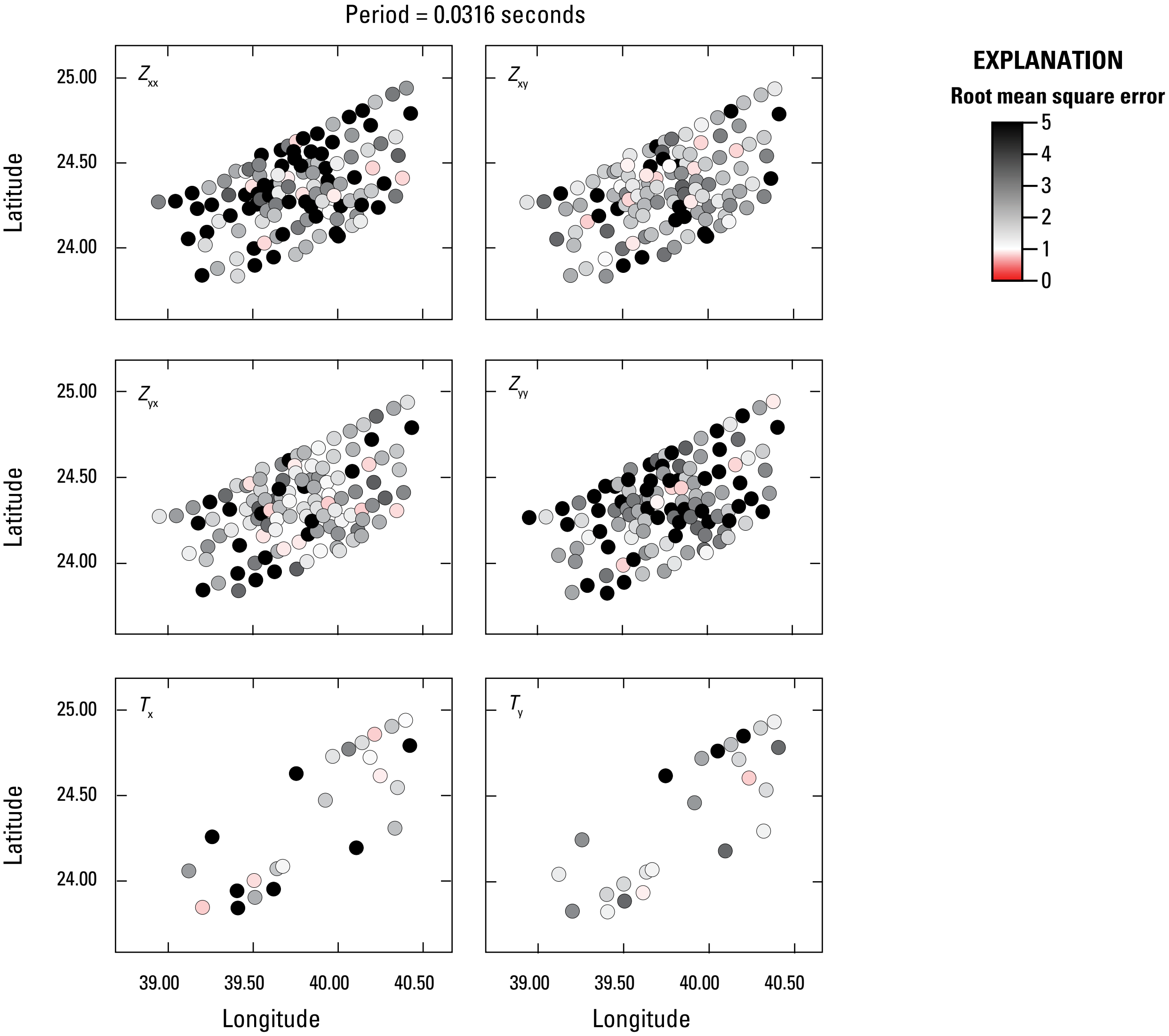

Figure 2.5. Map views of the normalized root mean square at a period of 0.0316 seconds showing each component of the impedance tensor (*Z*) and the induction vector (*T*) inverted for at each station.

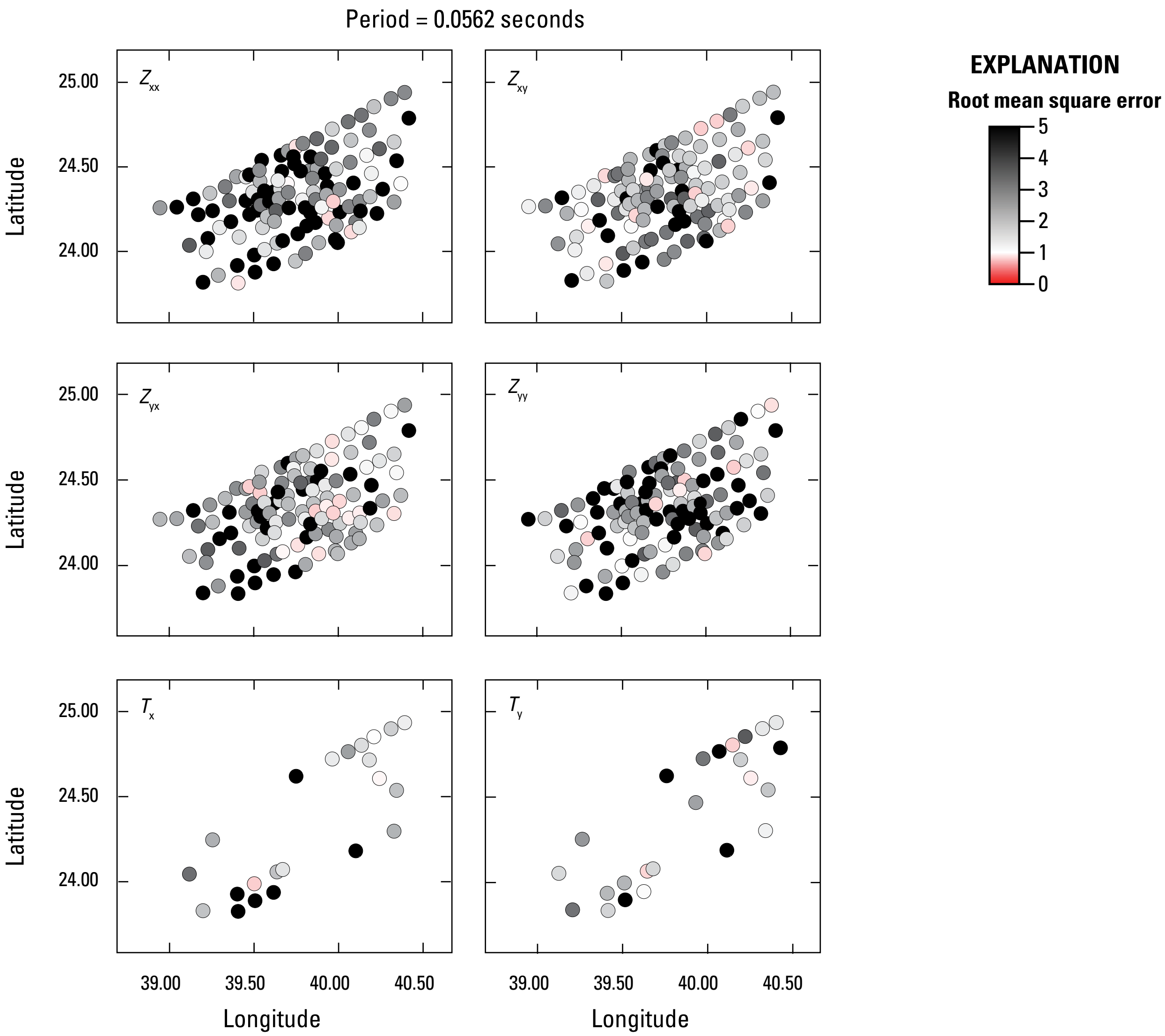

Figure 2.6. Map views of the normalized root mean square at a period of 0.0562 seconds showing each component of the impedance tensor (*Z*) and the induction vector (*T*) inverted for at each station.

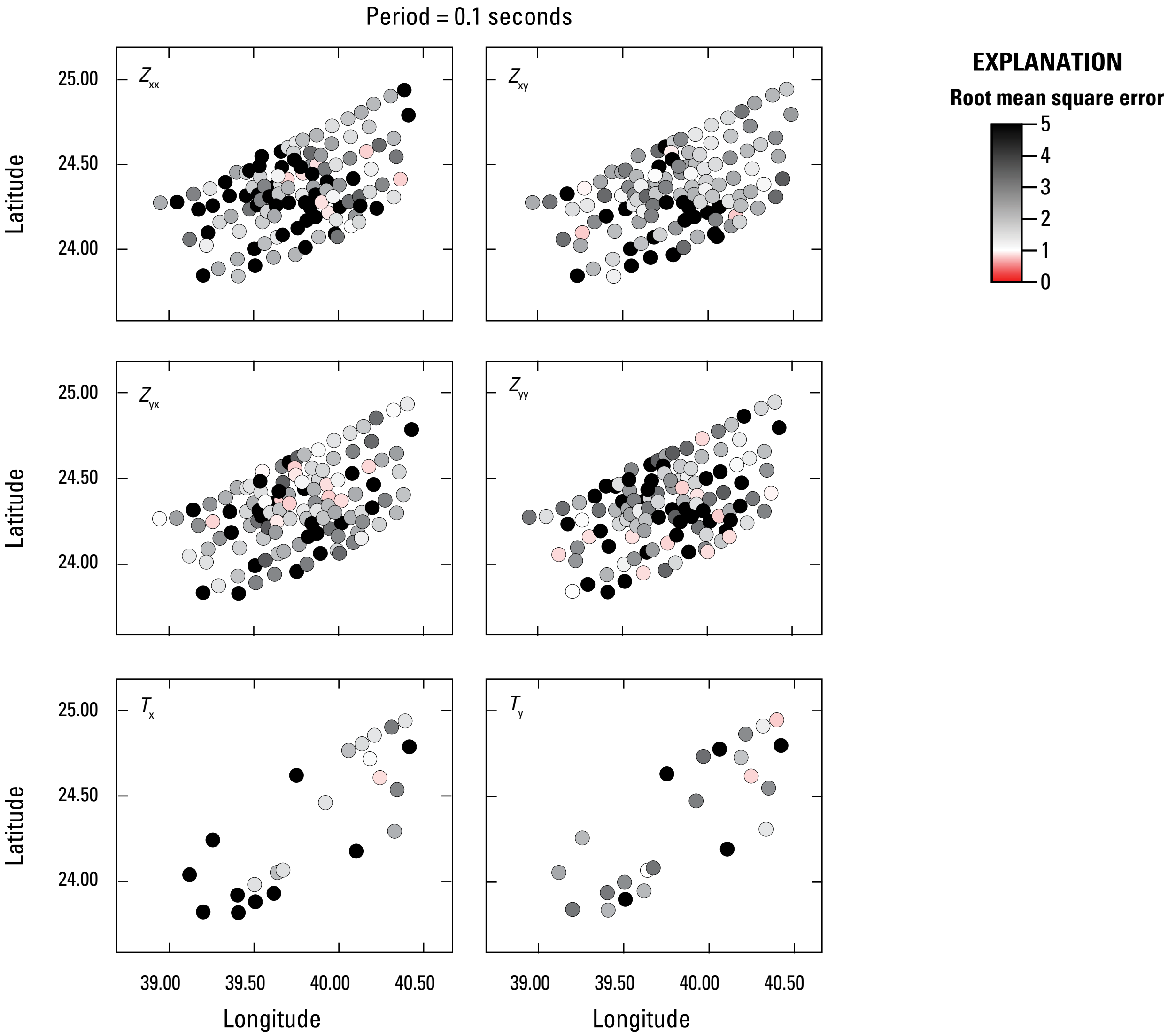

Figure 2.7. Map views of the normalized root mean square at a period of 0.1 seconds showing each component of the impedance tensor (*Z*) and the induction vector (*T*) inverted for at each station.

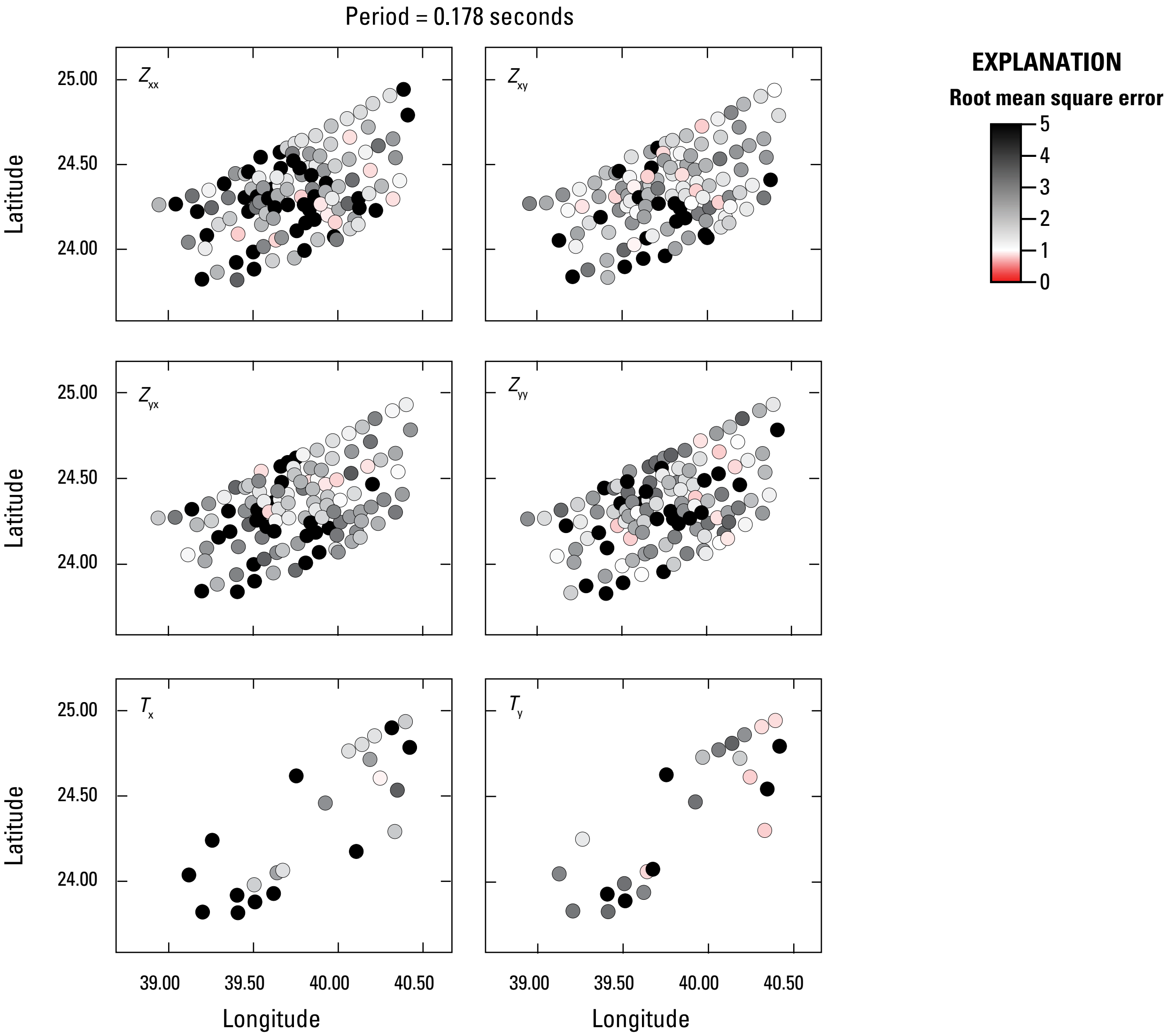

Figure 2.8. Map views of the normalized root mean square at a period of 0.178 seconds showing each component of the impedance tensor (*Z*) and the induction vector (*T*) inverted for at each station.

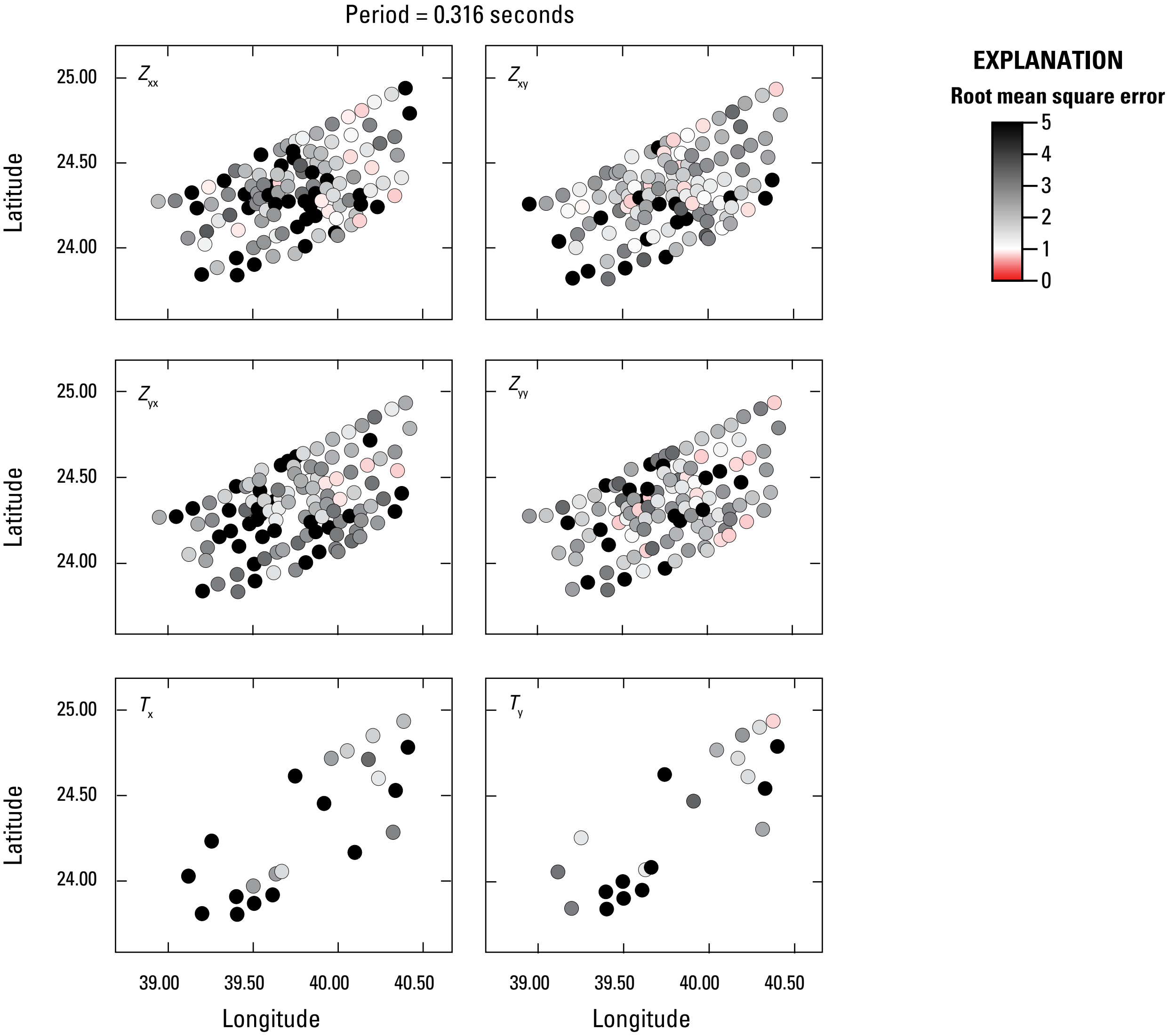

Figure 2.9. Map views of the normalized root mean square at a period of 0.316 seconds showing each component of the impedance tensor (*Z*) and the induction vector (*T*) inverted for at each station.

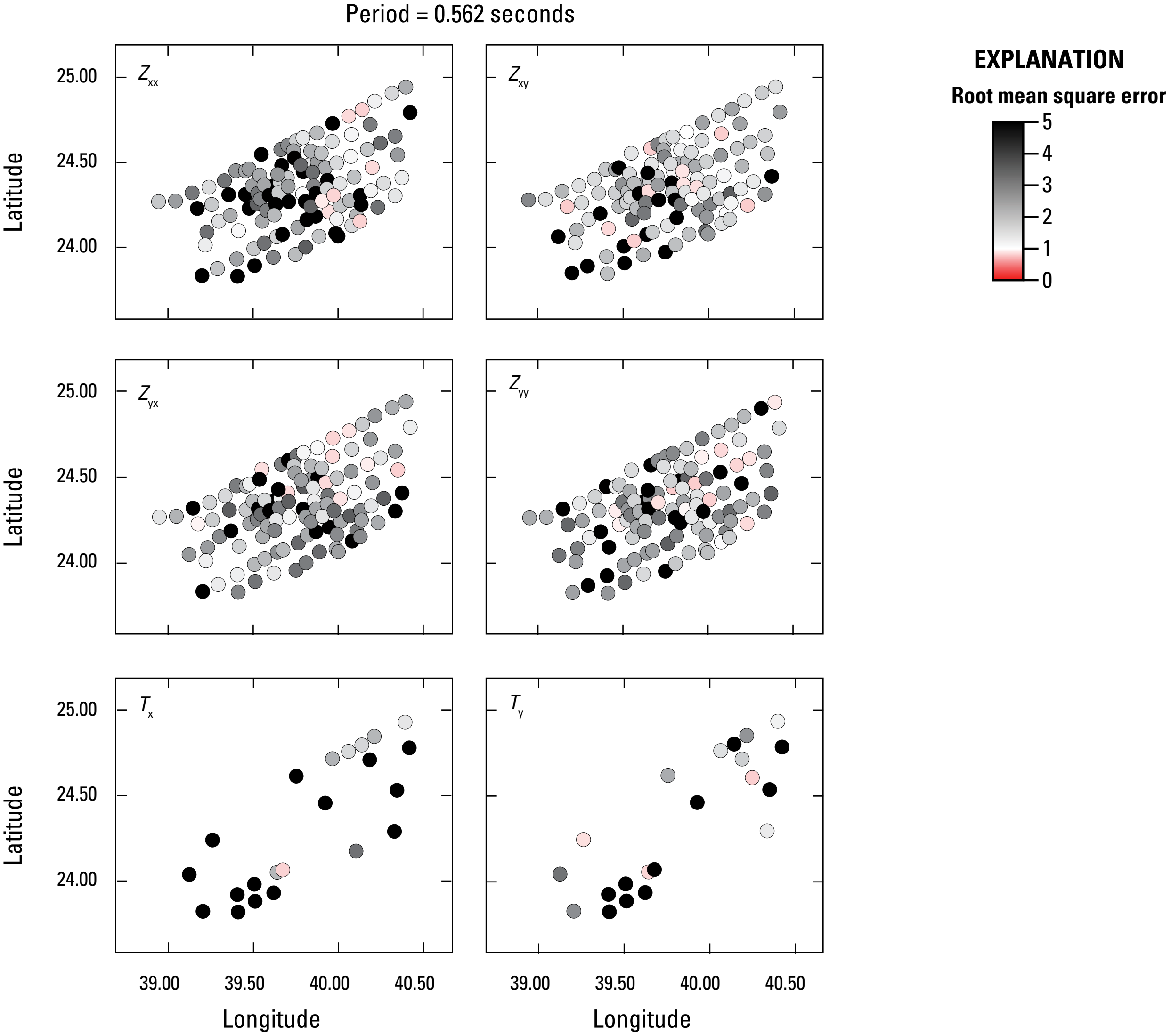

Figure 2.10. Map views of the normalized root mean square at a period of 0.562 seconds showing each component of the impedance tensor (*Z*) and the induction vector (*T*) inverted for at each station.

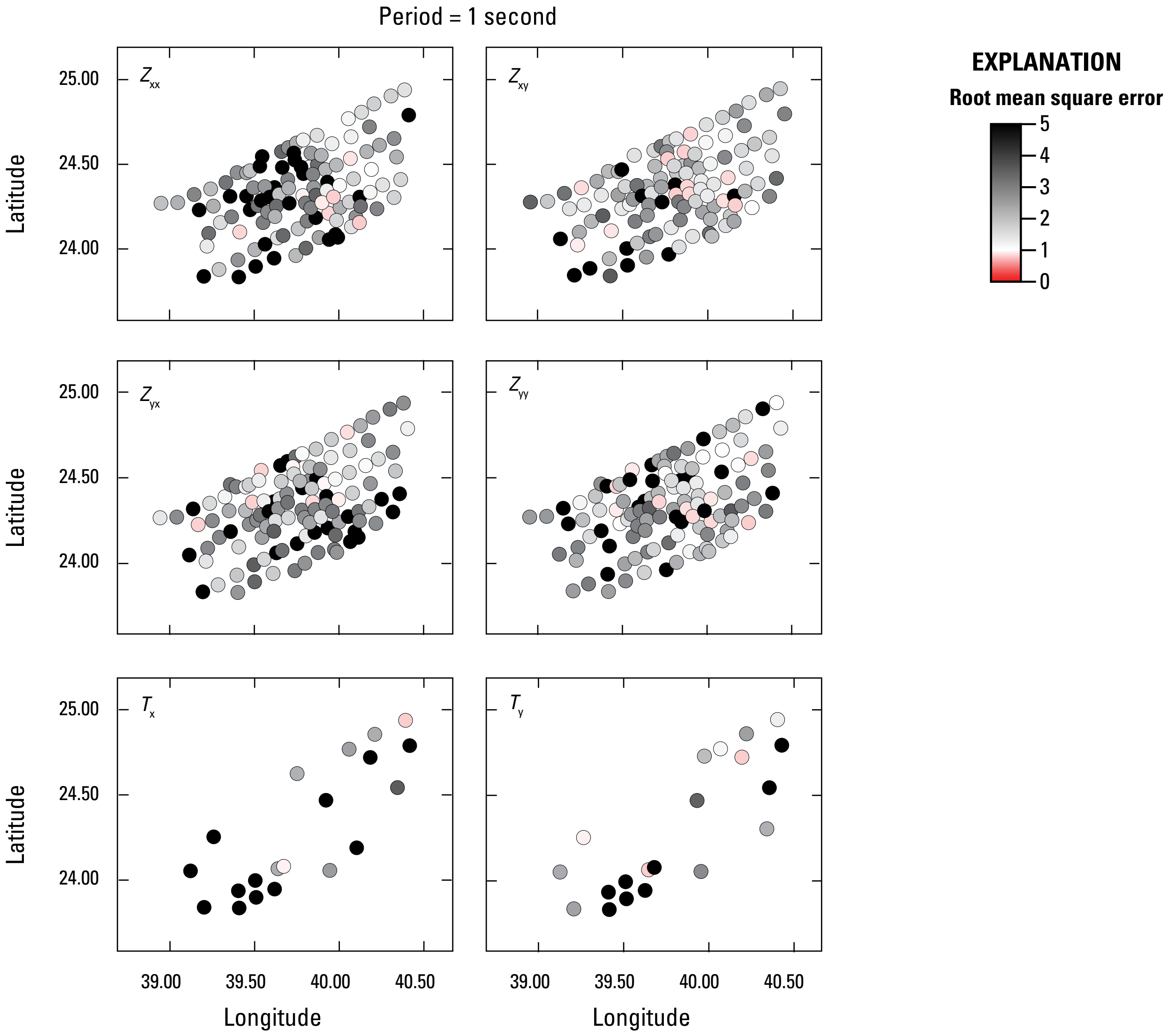

Figure 2.11. Map views of the normalized root mean square at a period of 1 second showing each component of the impedance tensor (*Z*) and the induction vector (*T*) inverted for at each station.

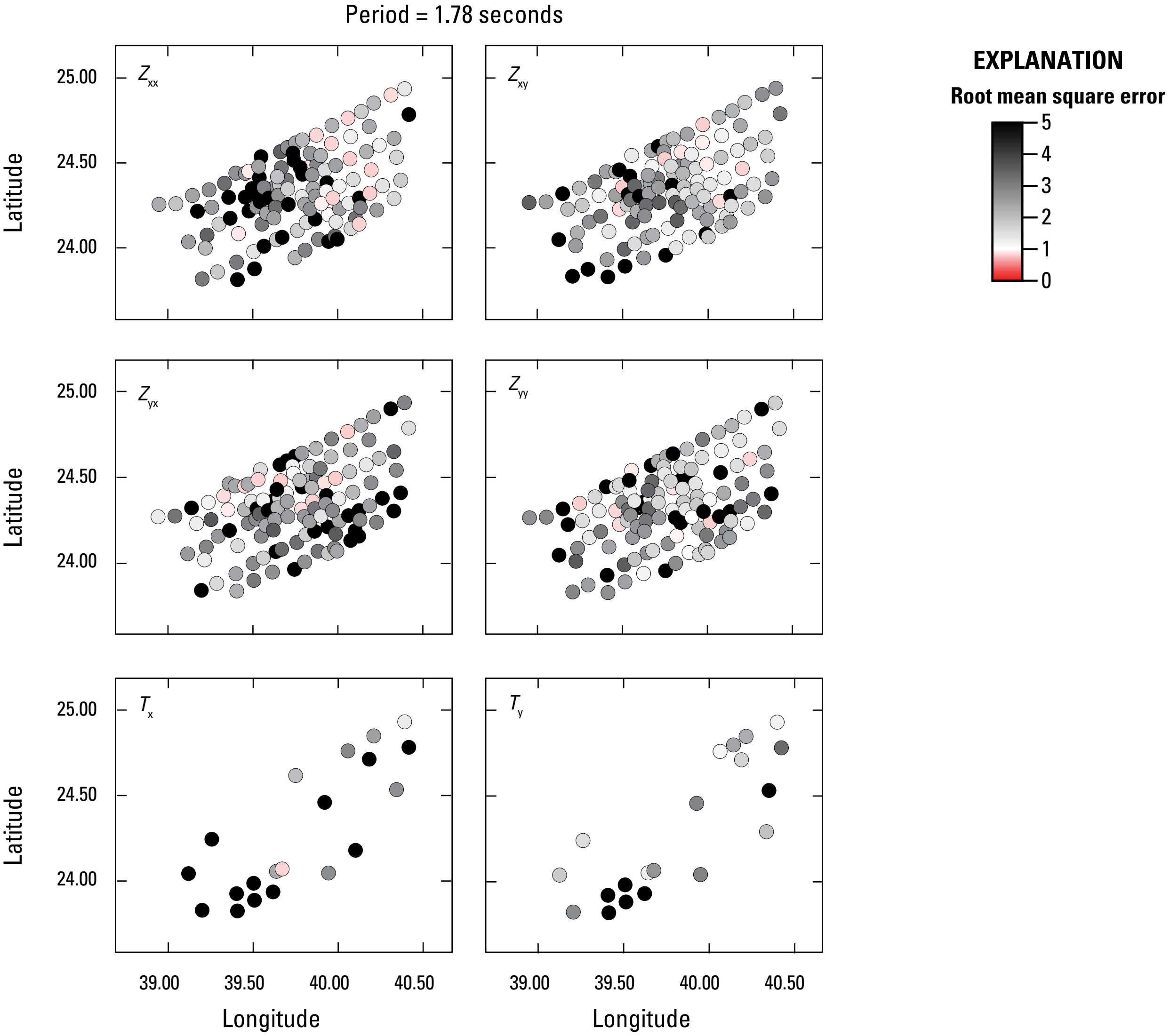

Figure 2.12. Map views of the normalized root mean square at a period of 1.78 seconds showing each component of the impedance tensor (*Z*) and the induction vector (*T*) inverted for at each station.

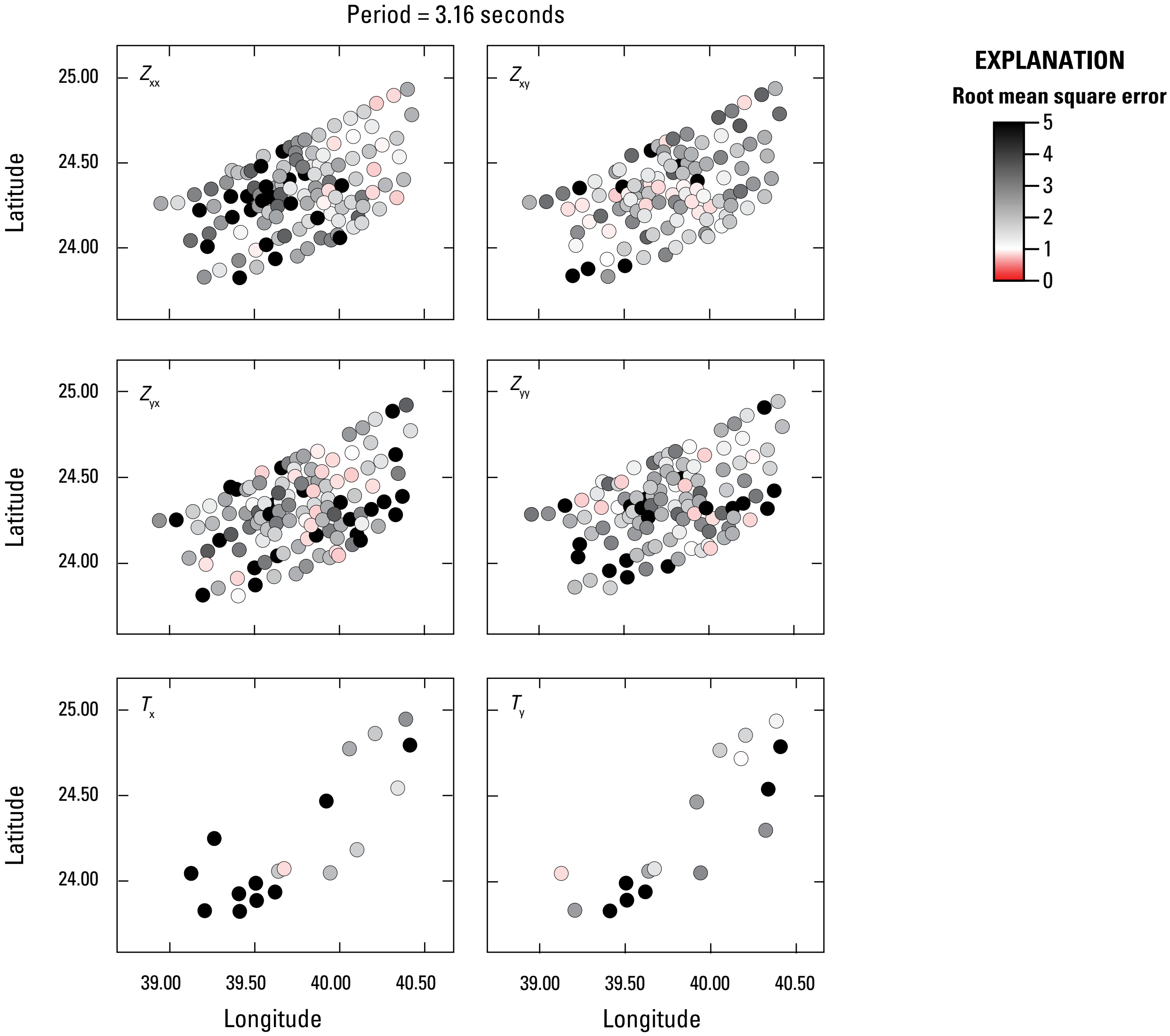

Figure 2.13. Map views of the normalized root mean square at a period of 3.16 seconds showing each component of the impedance tensor (*Z*) and the induction vector (*T*) inverted for at each station.

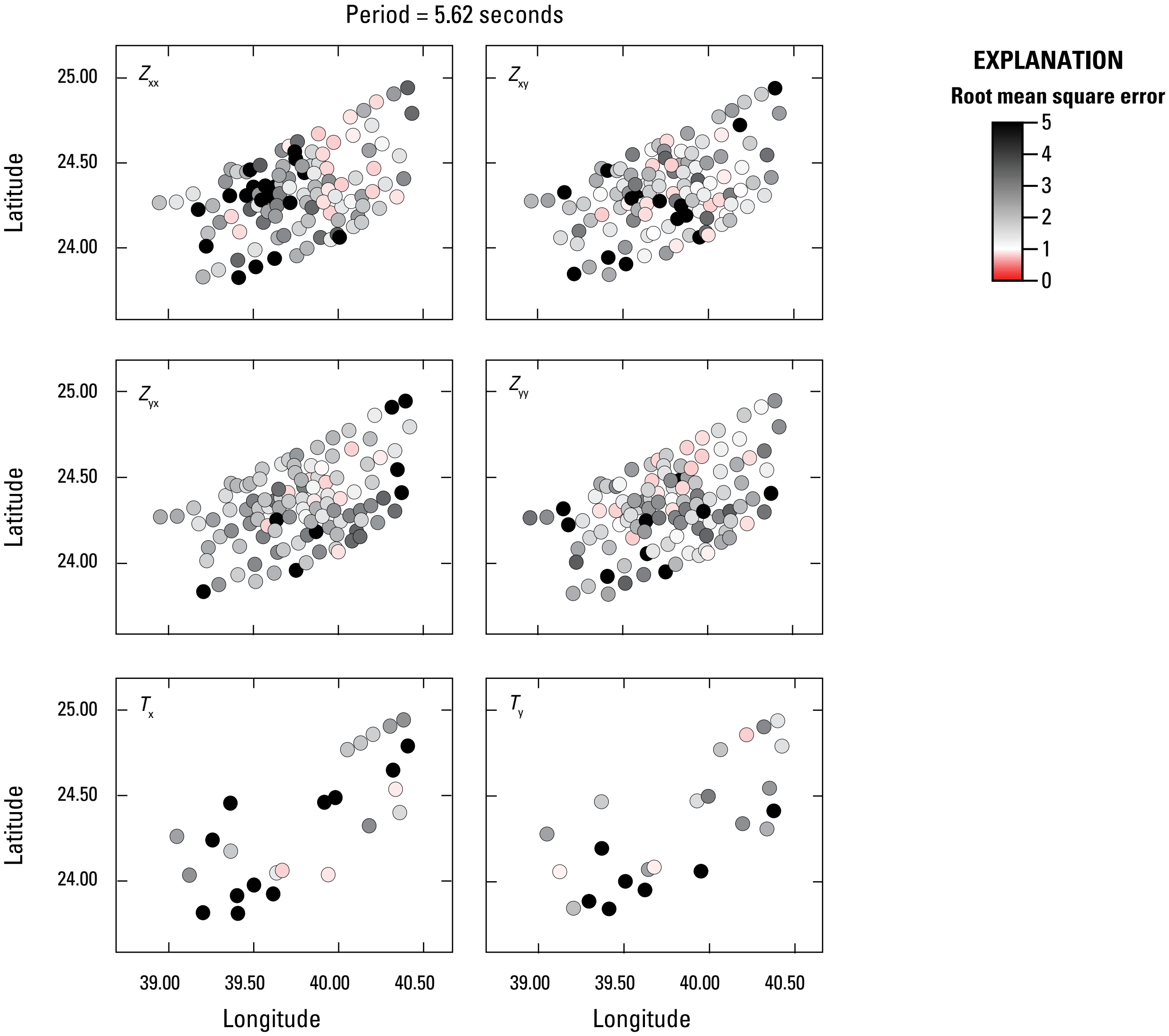

Figure 2.14. Map views of the normalized root mean square at a period of 5.62 seconds showing each component of the impedance tensor (*Z*) and the induction vector (*T*) inverted for at each station.

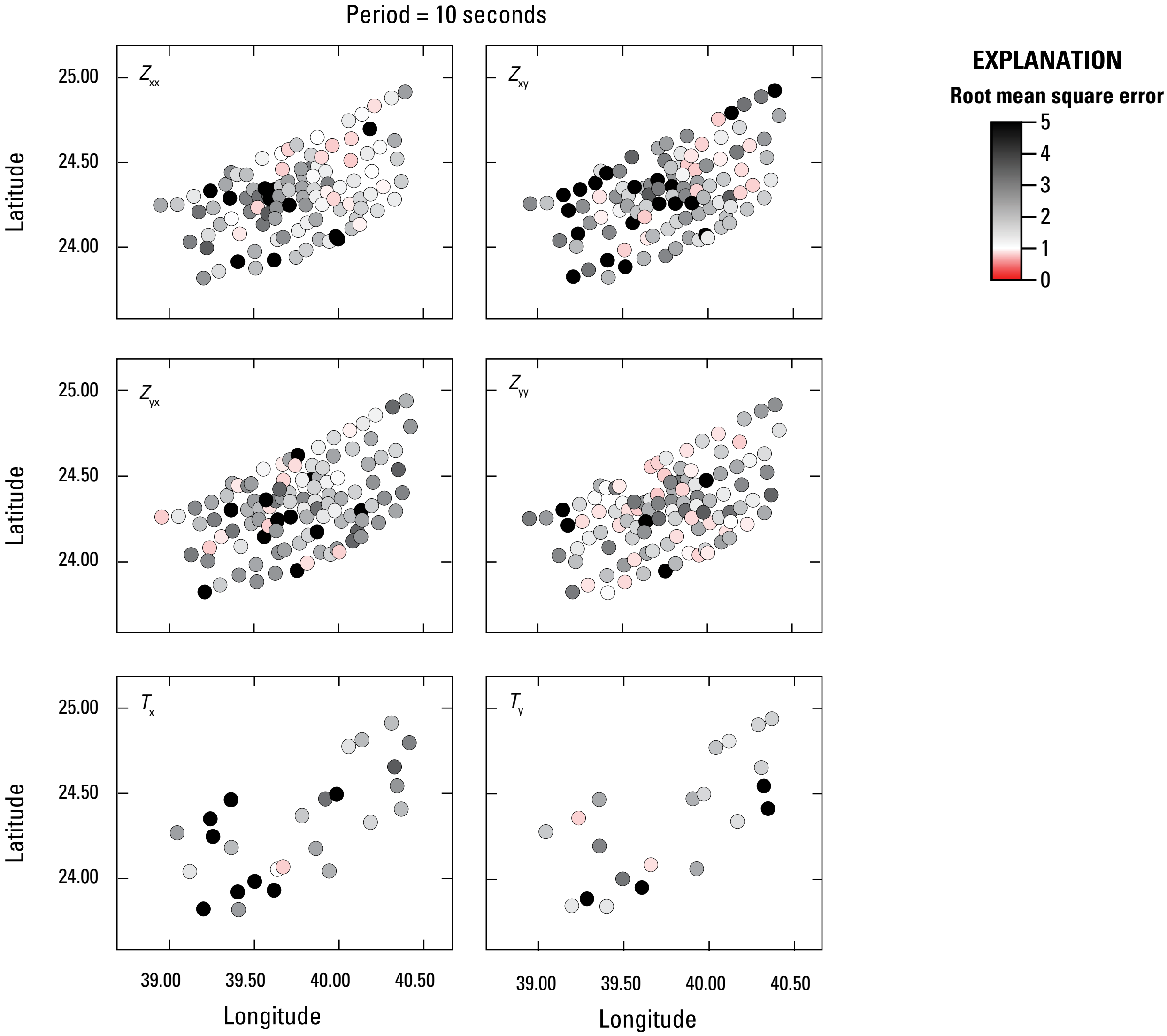

Figure 2.15. Map views of the normalized root mean square at a period of 10 seconds showing each component of the impedance tensor (*Z*) and the induction vector (*T*) inverted for at each station.

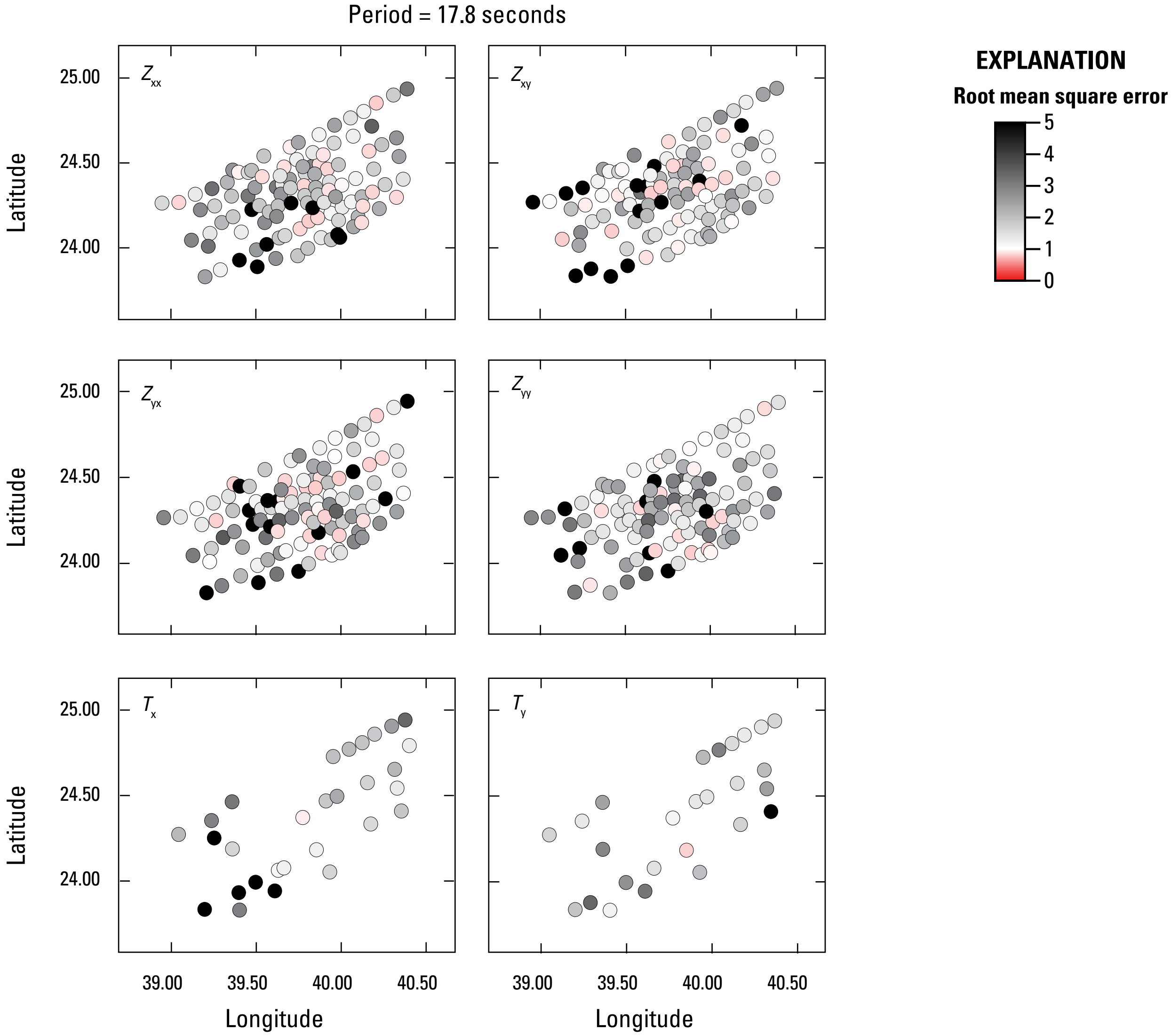

Figure 2.16. Map views of the normalized root mean square at a period of 17.8 seconds showing each component of the impedance tensor (*Z*) and the induction vector (*T*) inverted for at each station.

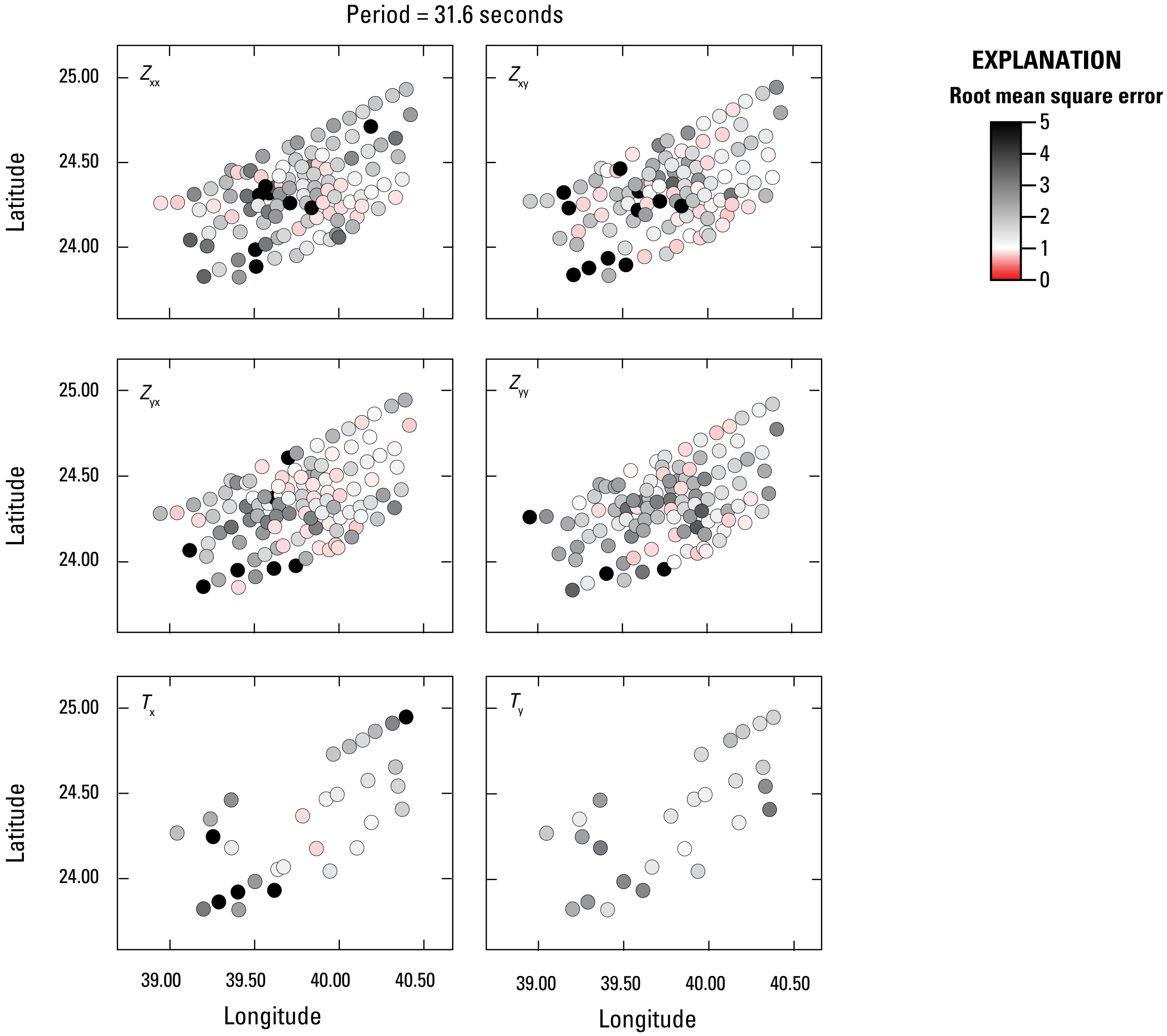

Figure 2.17. Map views of the normalized root mean square at a period of 31.6 seconds showing each component of the impedance tensor (*Z*) and the induction vector (*T*) inverted for at each station.

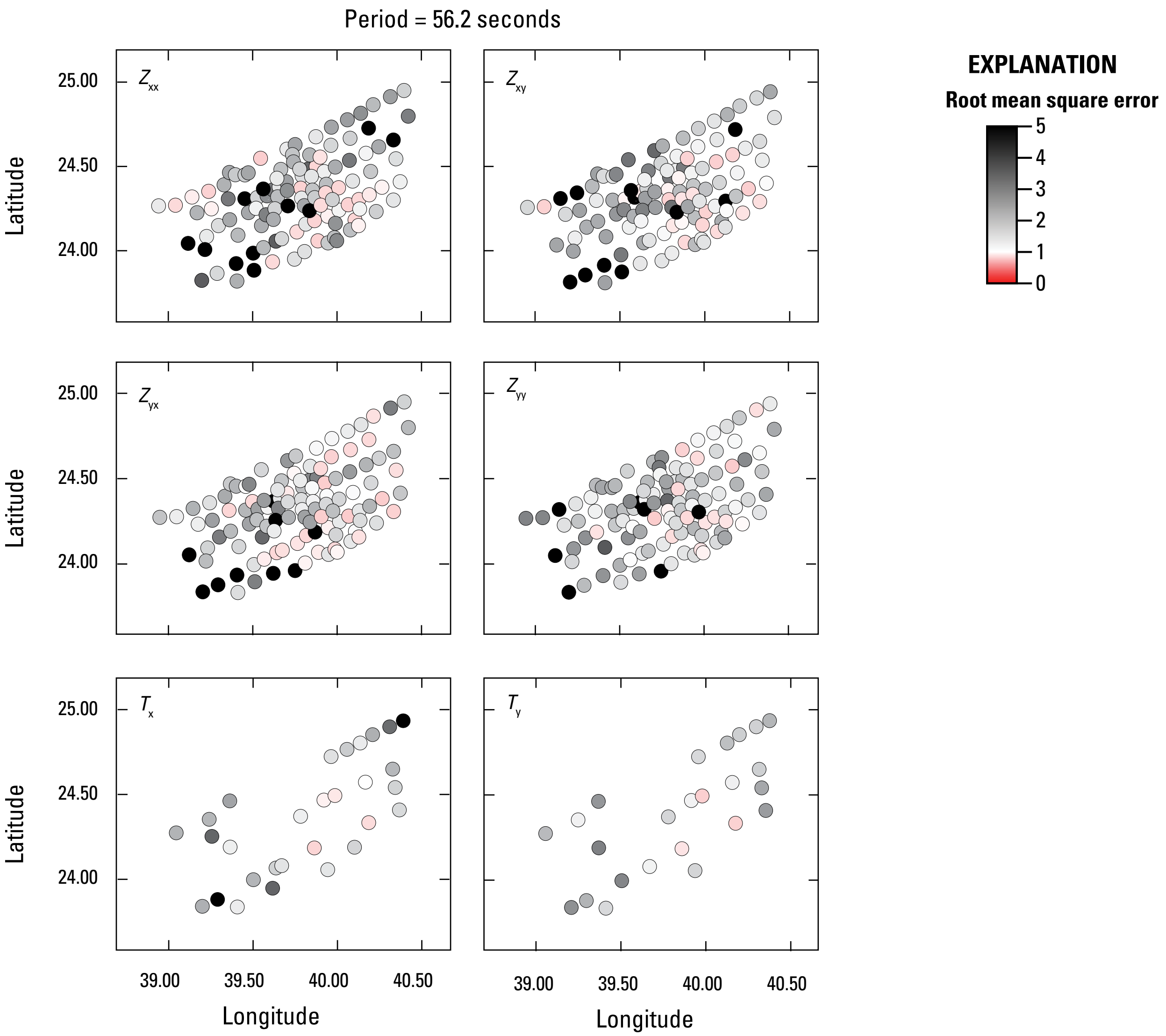

Figure 2.18. Map views of the normalized root mean square at a period of 56.2 seconds showing each component of the impedance tensor (*Z*) and the induction vector (*T*) inverted for at each station.

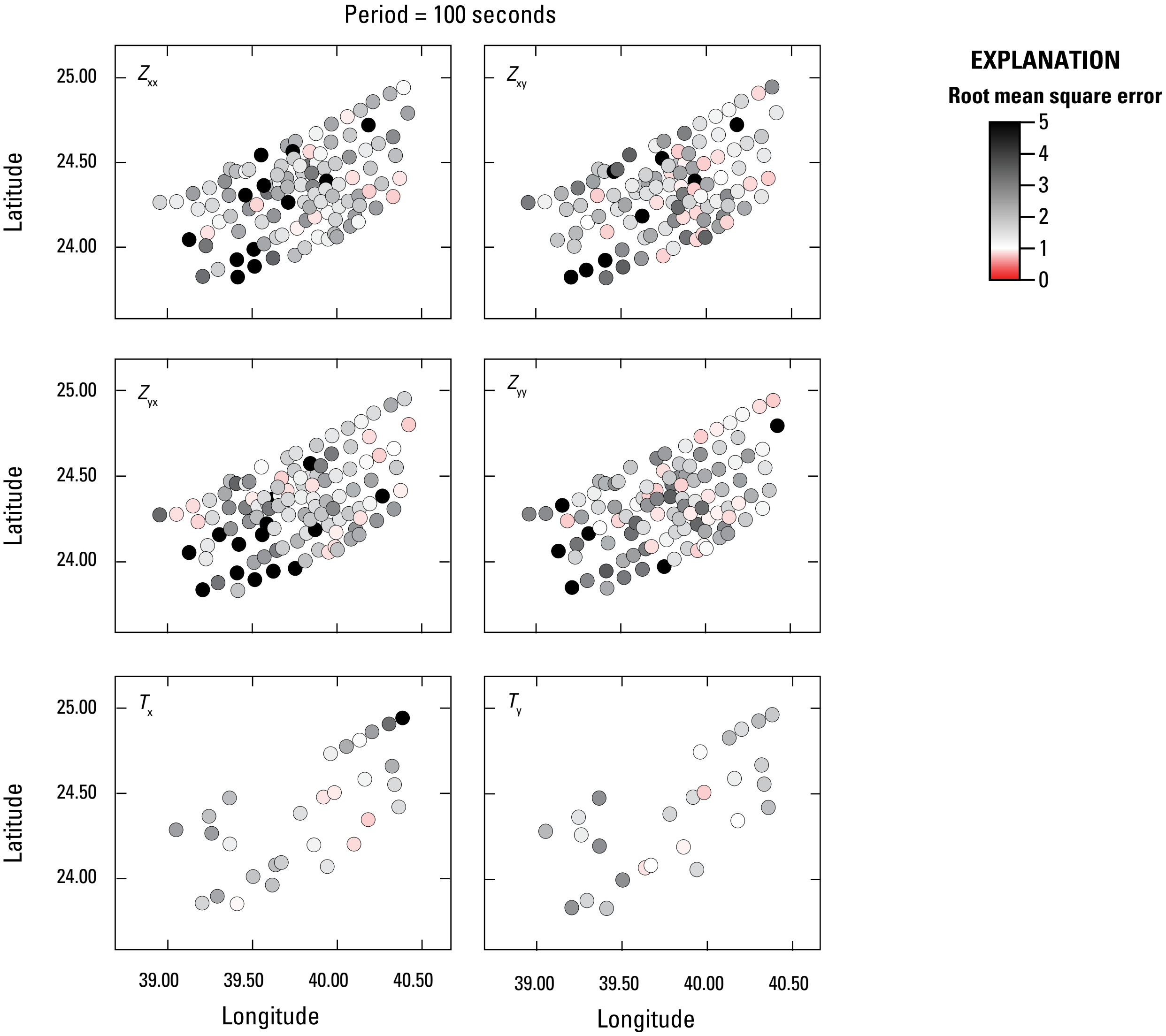

Figure 2.19. Map views of the normalized root mean square at a period of 100 seconds showing each component of the impedance tensor (*Z*) and the induction vector (*T*) inverted for at each station.

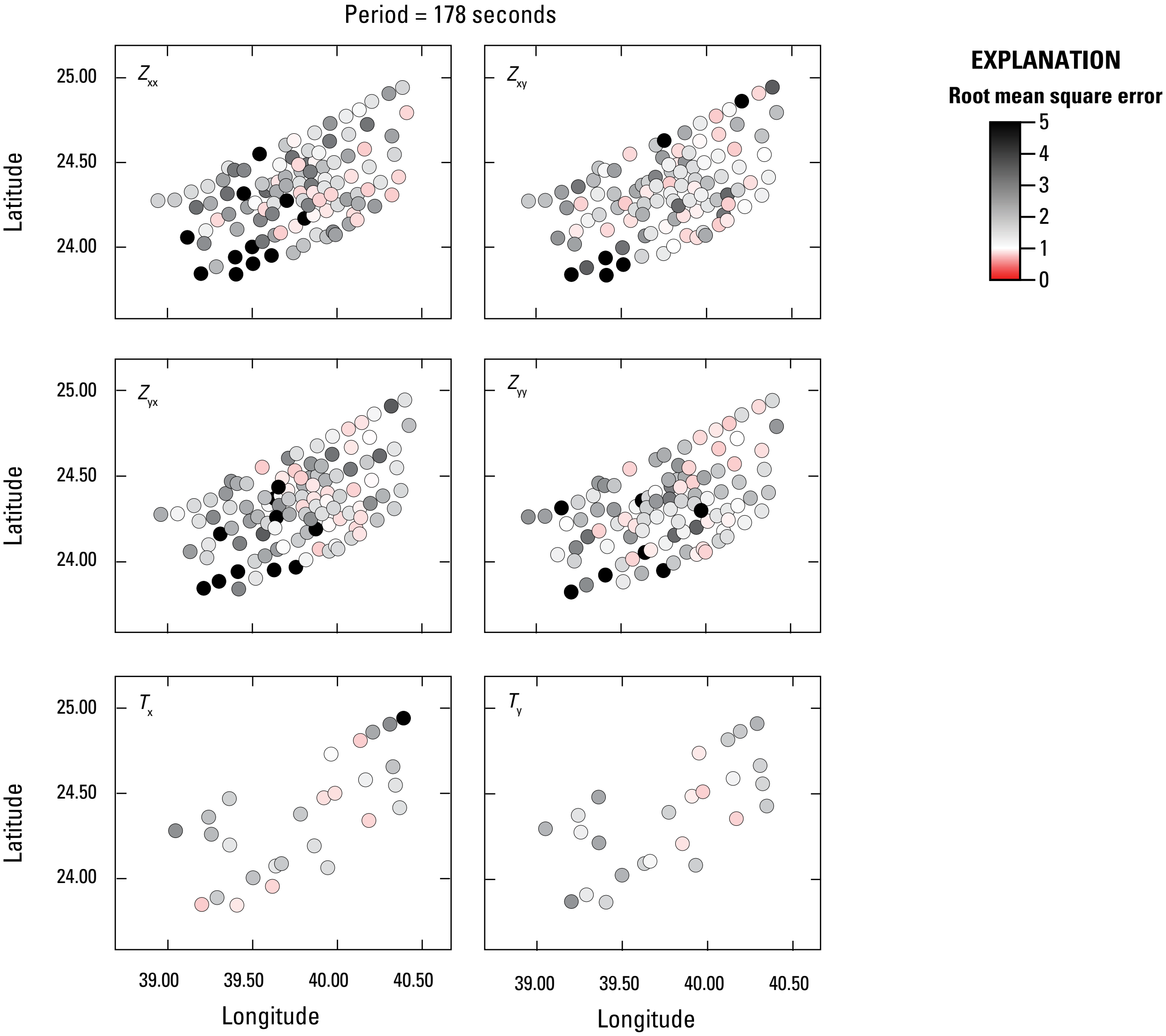

Figure 2.20. Map views of the normalized root mean square at a period of 178 seconds showing each component of the impedance tensor (*Z*) and the induction vector (*T*) inverted for at each station.

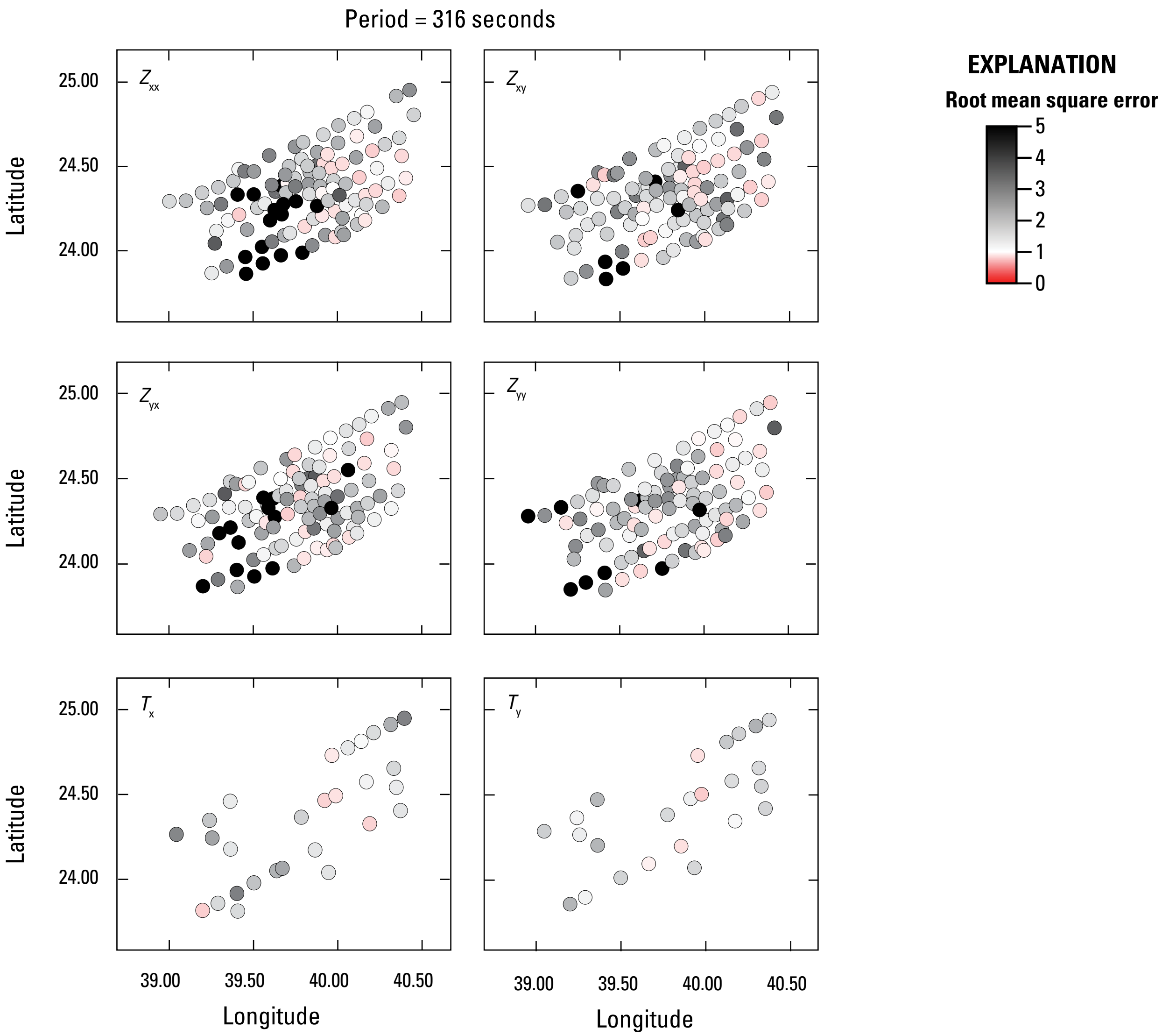

Figure 2.21. Map views of the normalized root mean square at a period of 316 seconds showing each component of the impedance tensor (*Z*) and the induction vector (*T*) inverted for at each station.

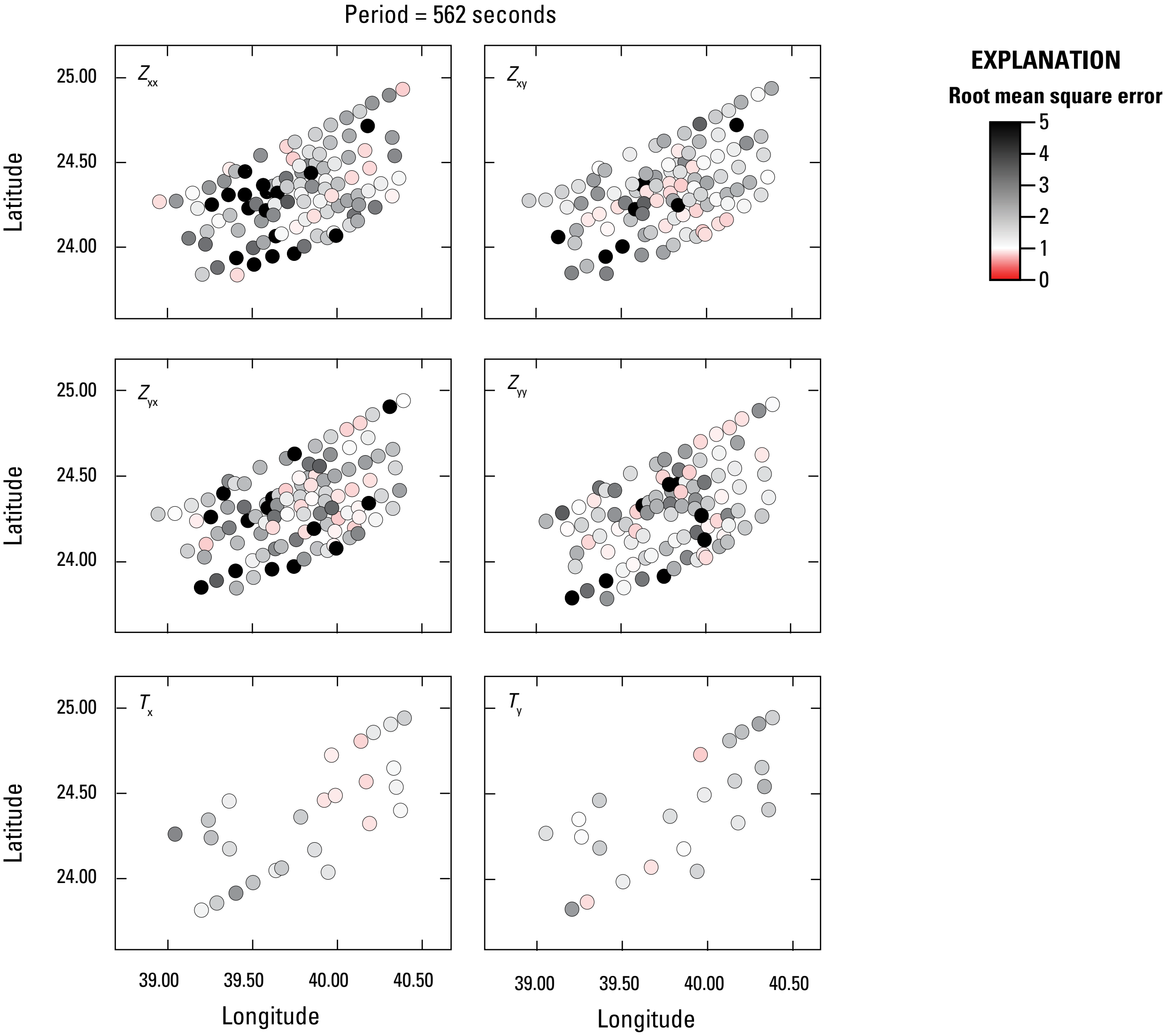

Figure 2.22. Map views of the normalized root mean square at a period of 562 seconds showing each component of the impedance tensor (*Z*) and the induction vector (*T*) inverted for at each station.

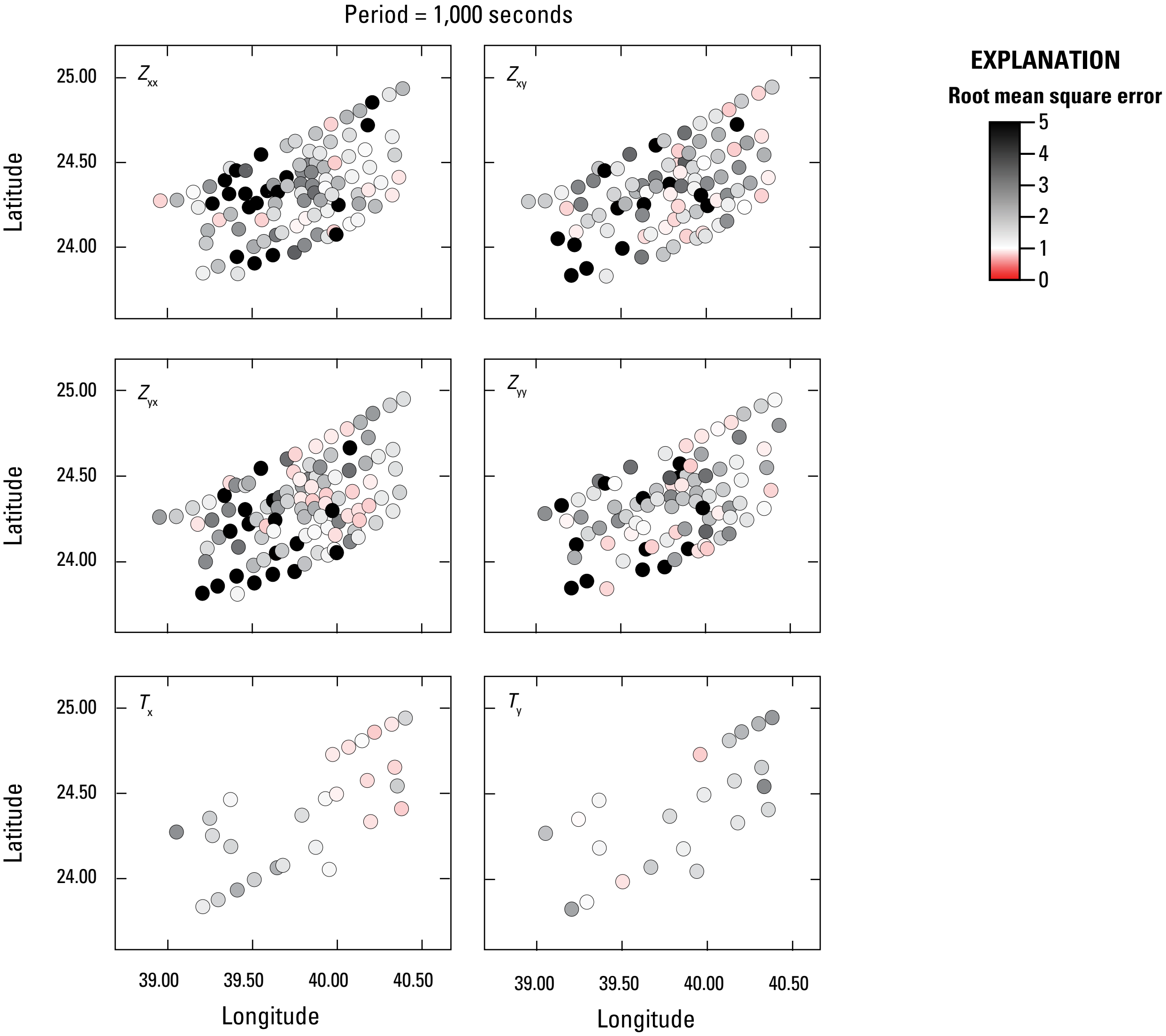

Figure 2.23. Map views of the normalized root mean square at a period of 1,000 seconds showing each component of the impedance tensor (*Z*) and the induction vector (*T*) inverted for at each station.

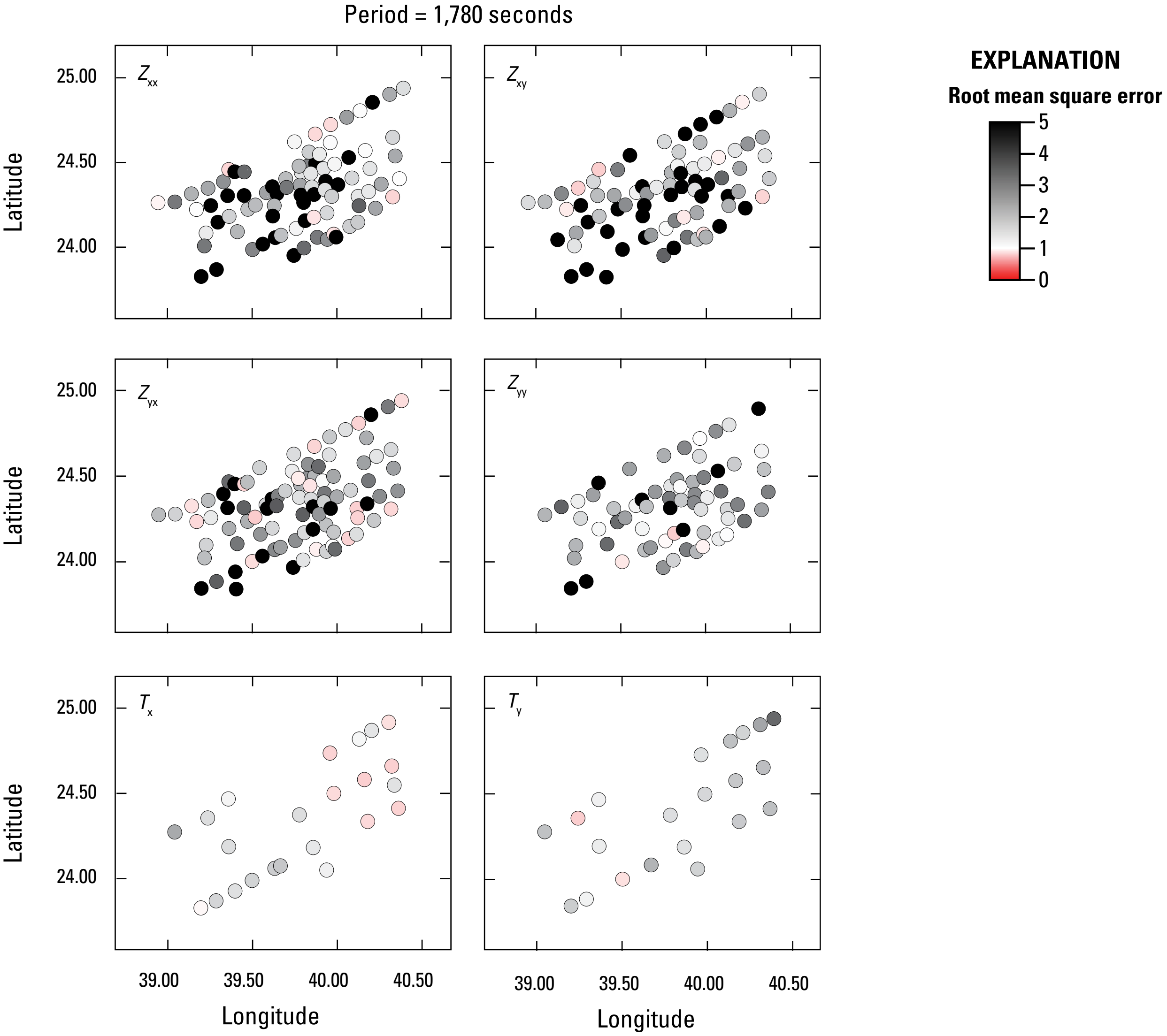

Figure 2.24. Map views of the normalized root mean square at a period of 1,780 seconds showing each component of the impedance tensor (*Z*) and the induction vector (*T*) inverted for at each station.

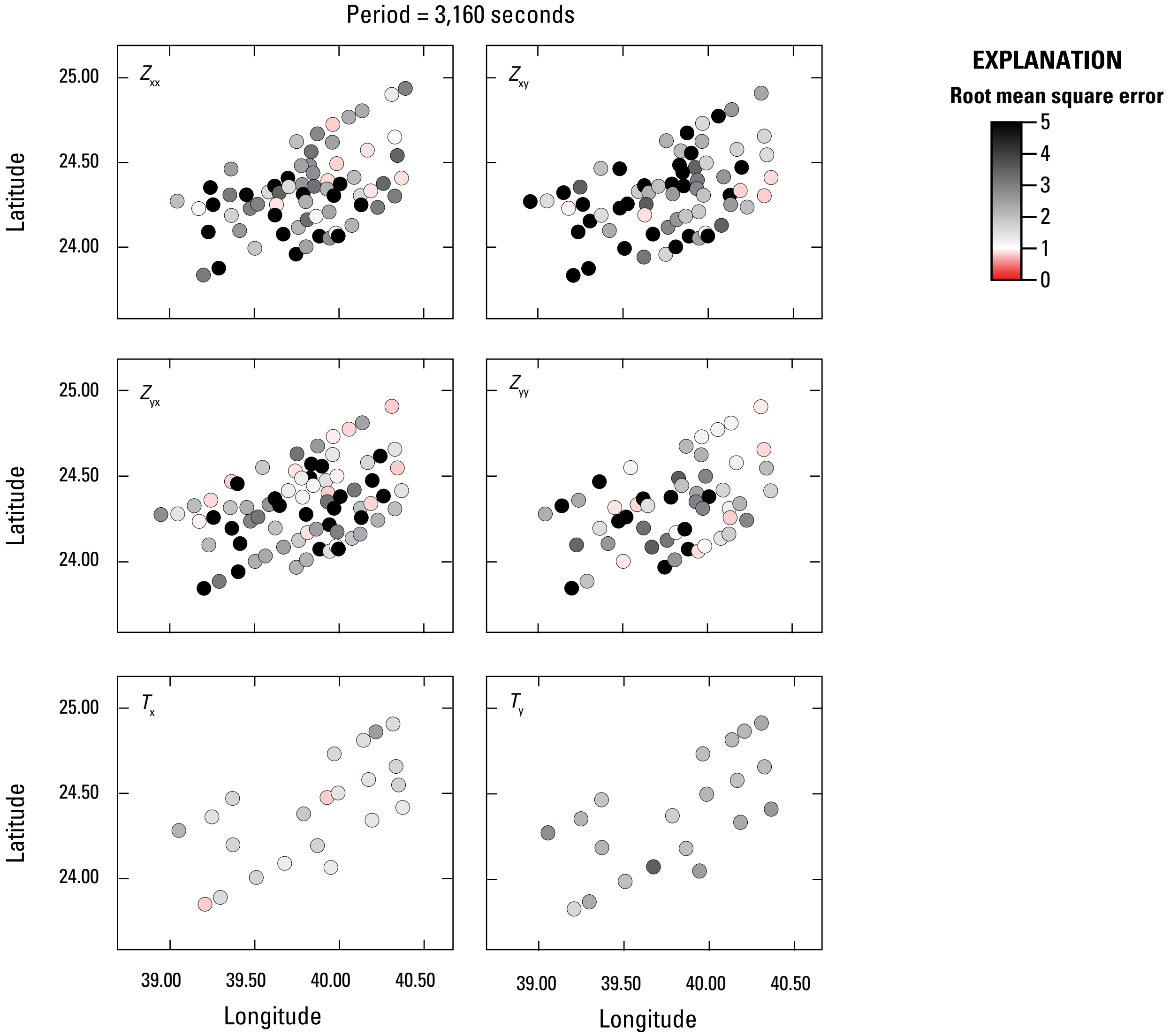

Figure 2.25. Map views of the normalized root mean square at a period of 3,160 seconds showing each component of the impedance tensor (*Z*) and the induction vector (*T*) inverted for at each station.

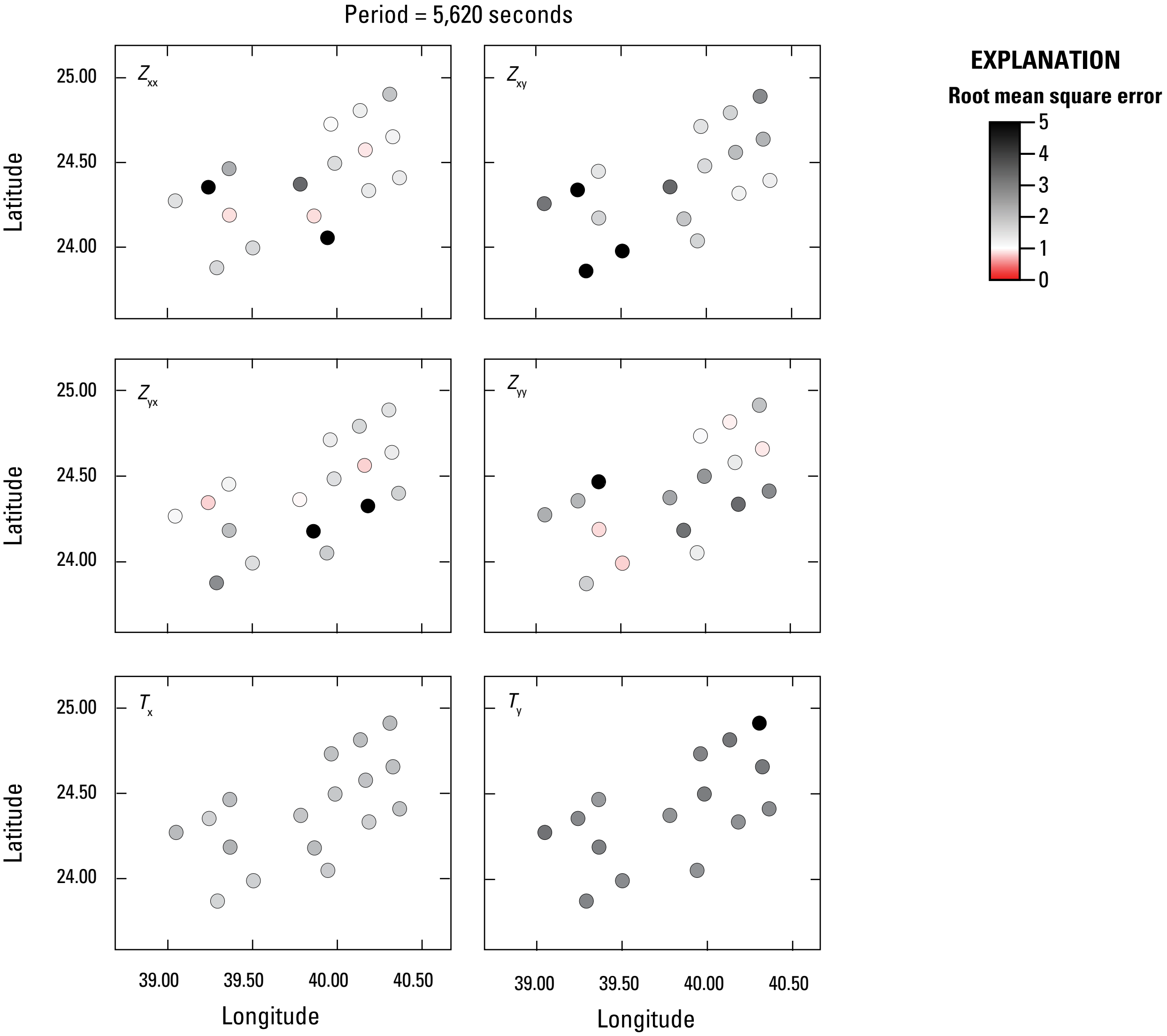

Figure 2.26. Map views of the normalized root mean square at a period of 5,620 seconds showing each component of the impedance tensor (*Z*) and the induction vector (*T*) inverted for at each station.

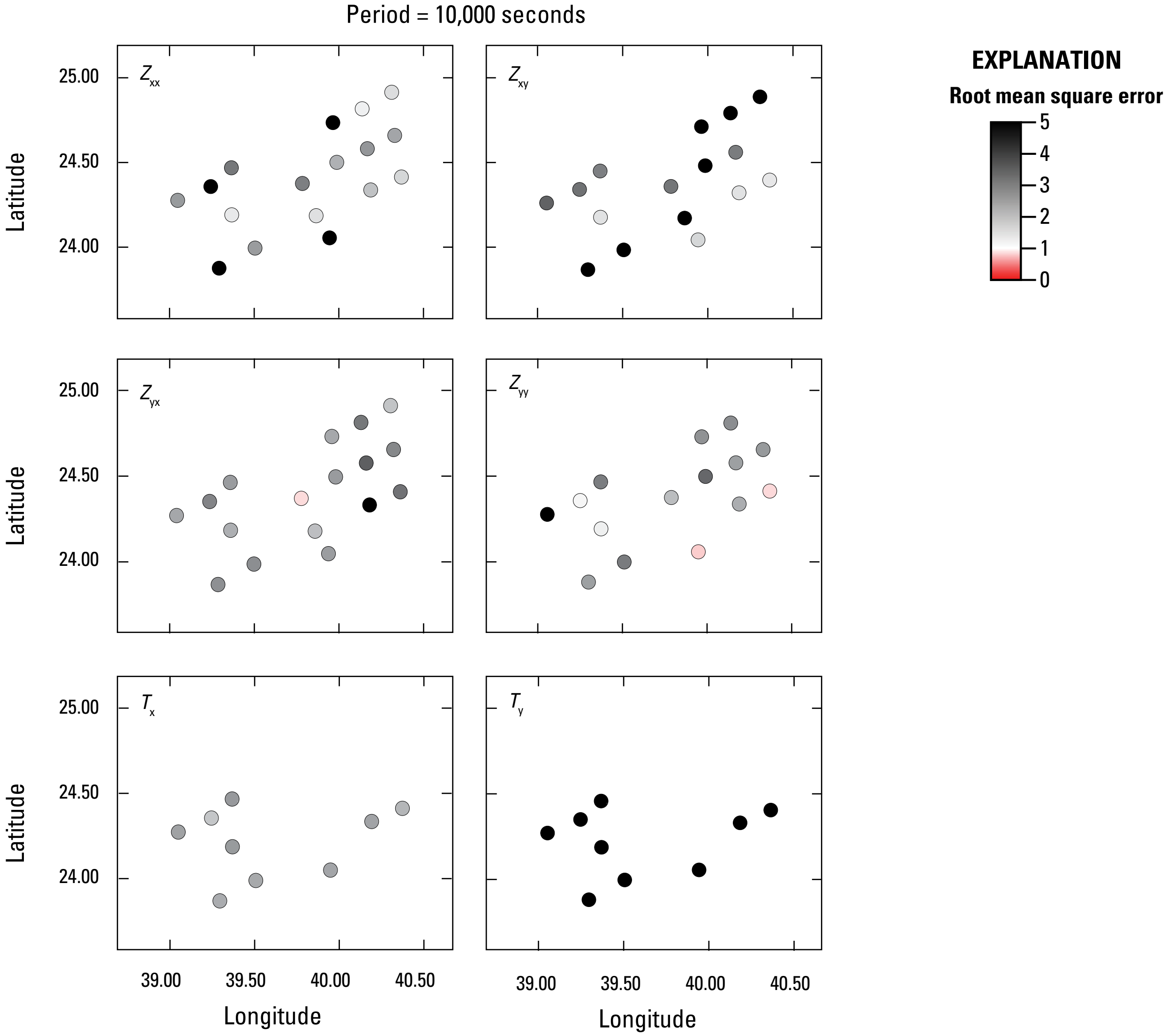

Figure 2.27. Map views of the normalized root mean square at a period of 10,000 seconds showing each component of the impedance tensor (*Z*) and the induction vector (*T*) inverted for at each station.

Appendix 3. Data and Model Responses

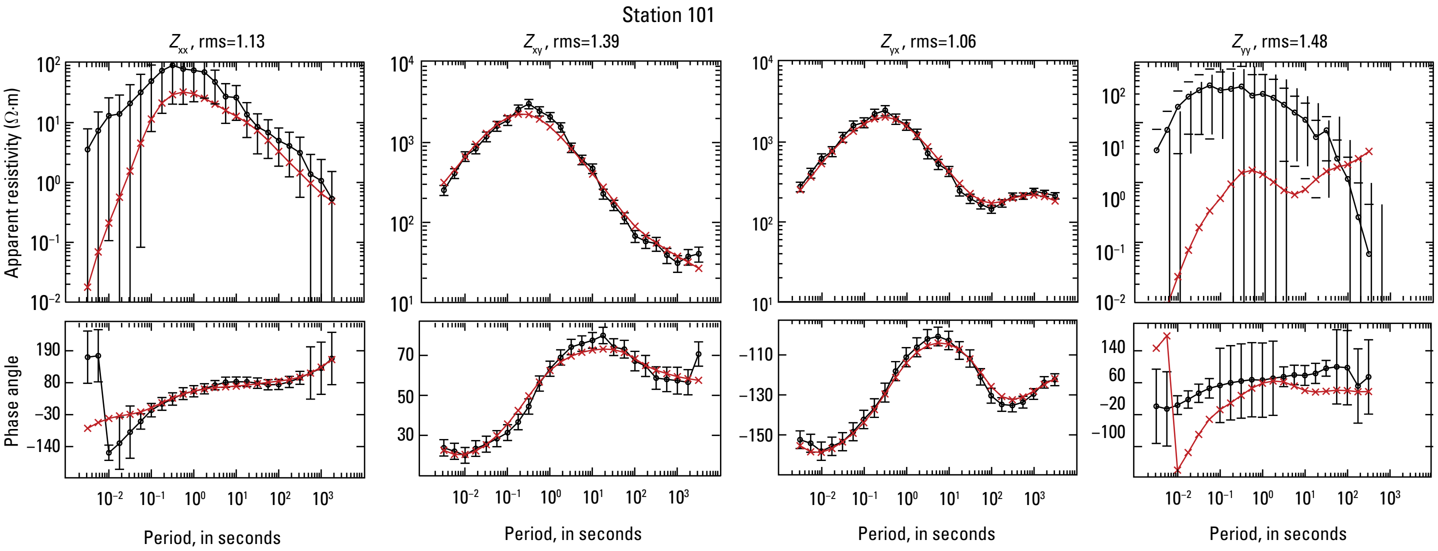

Figure 3.1. Station 101. Plots showing the data inverted (black) and the resistivity model response (red). Shown are all components of the impedance tensor (*Z*) as apparent resistivity (in Ohm meters, Ω·m) and phase angle (in degrees). Data error bars are shown for the inverted data.

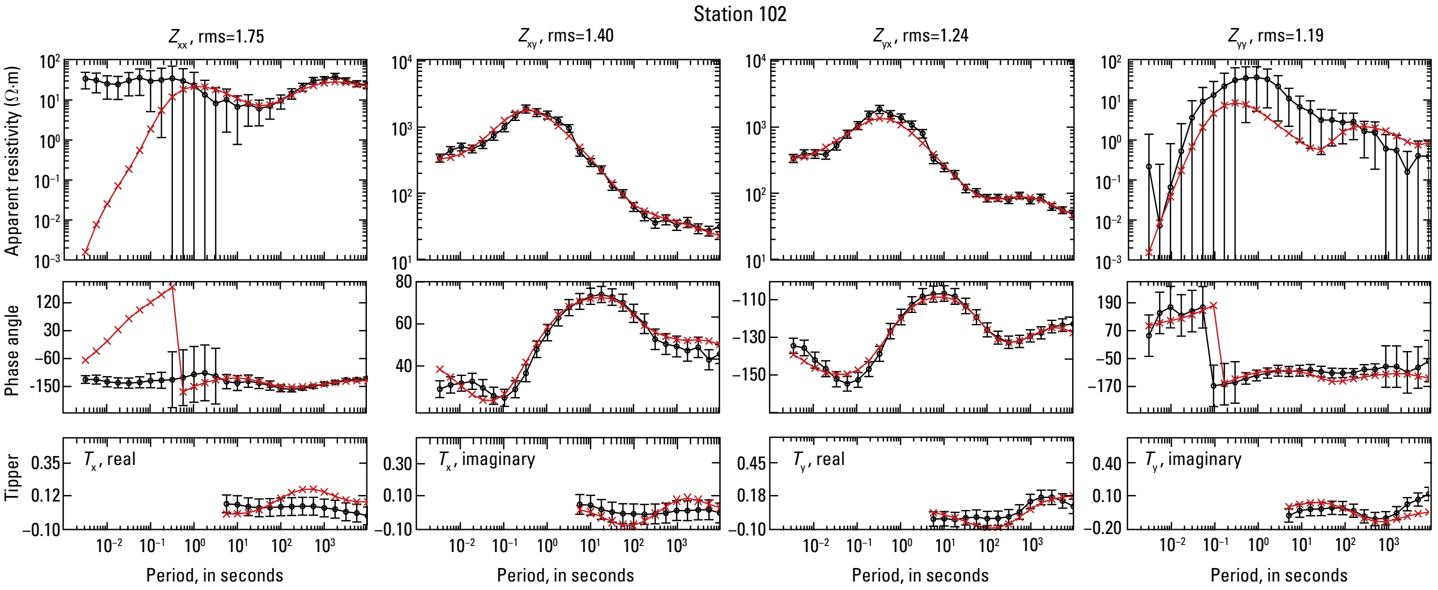

Figure 3.2. Station 102. Plots showing the data inverted (black) and the resistivity model response (red). Shown are all components of the impedance tensor (*Z*) as apparent resistivity (in Ohm meters, Ω·m) and phase angle (in degrees) and the induction vector (*T*), or tipper, as both real and imaginary parts of *T*. Data error bars are shown for the inverted data.

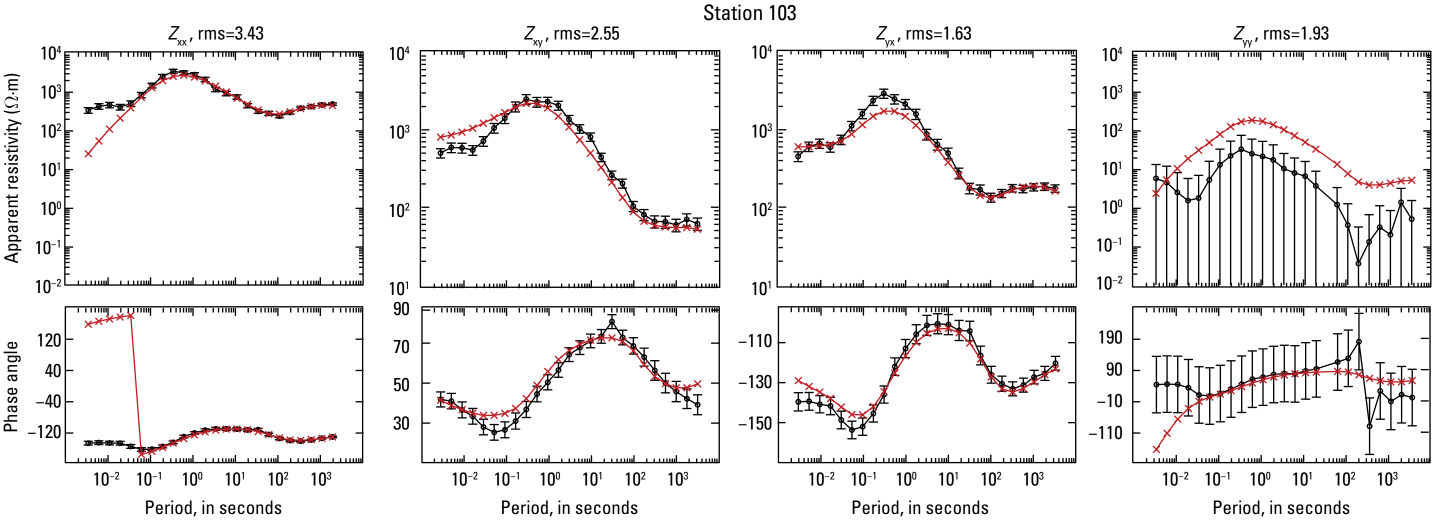

Figure 3.3. Station 103. Plots showing the data inverted (black) and the resistivity model response (red). Shown are all components of the impedance tensor (*Z*) as apparent resistivity (in Ohm meters, Ω·m) and phase angle (in degrees). Data error bars are shown for the inverted data.

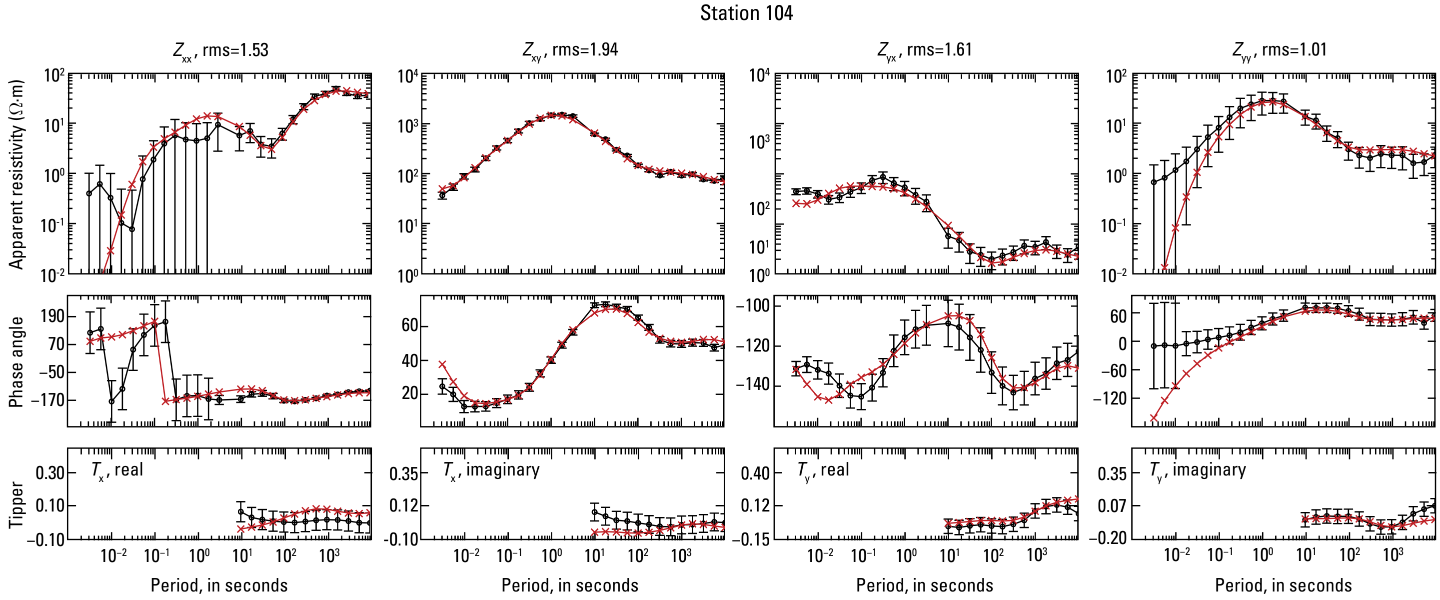

Figure 3.4. Station 104. Plots showing the data inverted (black) and the resistivity model response (red). Shown are all components of the impedance tensor (*Z*) as apparent resistivity (in Ohm meters, Ω·m) and phase angle (in degrees) and the induction vector (*T*), or tipper, as both real and imaginary parts of *T*. Data error bars are shown for the inverted data.

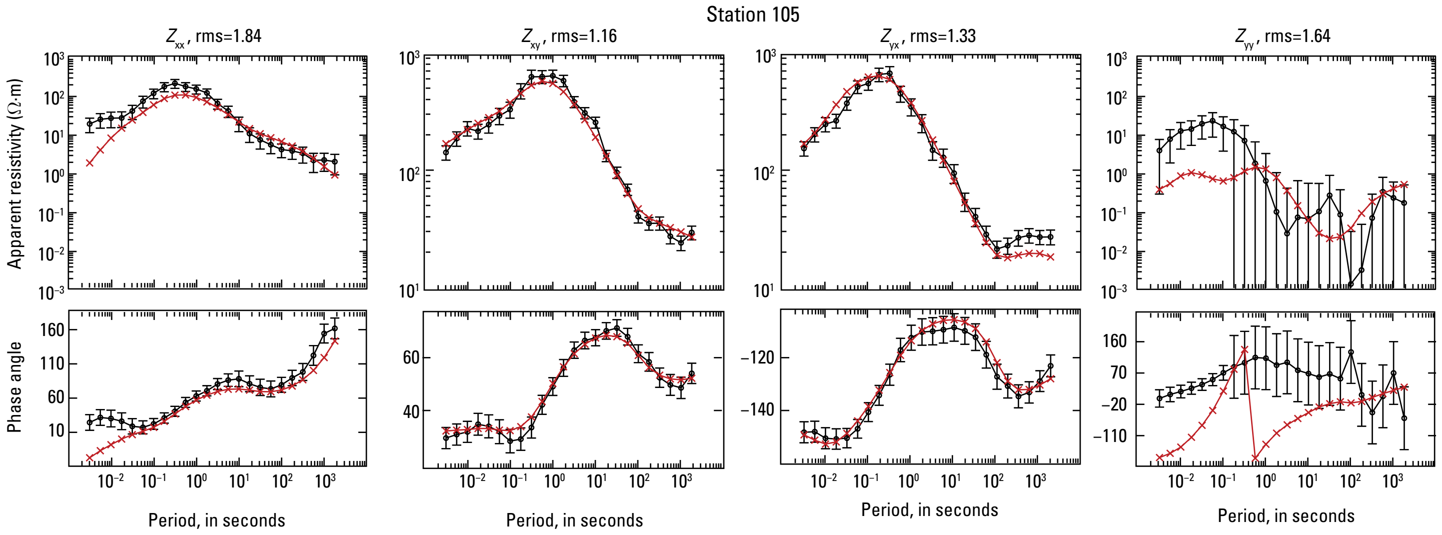

Figure 3.5. Station 105. Plots showing the data inverted (black) and the resistivity model response (red). Shown are all components of the impedance tensor (*Z*) as apparent resistivity (in Ohm meters, Ω·m) and phase angle (in degrees). Data error bars are shown for the inverted data.

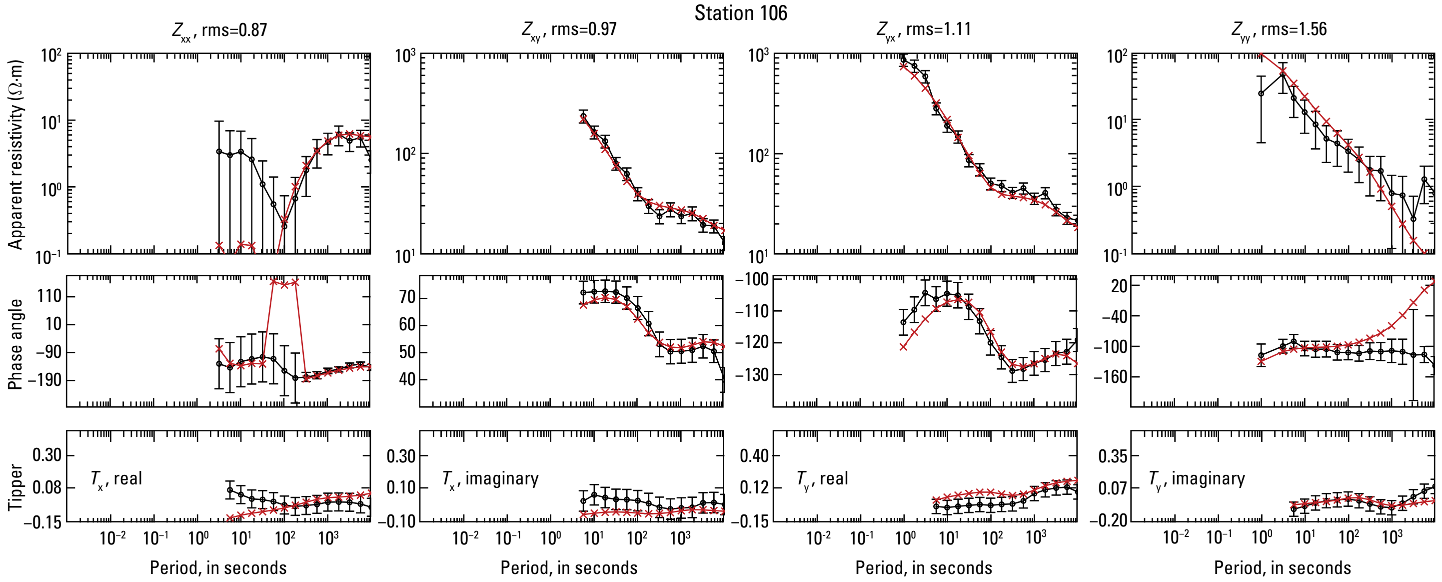

Figure 3.6. Station 106. Plots showing the data inverted (black) and the resistivity model response (red). Shown are all components of the impedance tensor (*Z*) as apparent resistivity (in Ohm meters, Ω·m) and phase angle (in degrees) and the induction vector (*T*), or tipper, as both real and imaginary parts of *T*. Data error bars are shown for the inverted data.

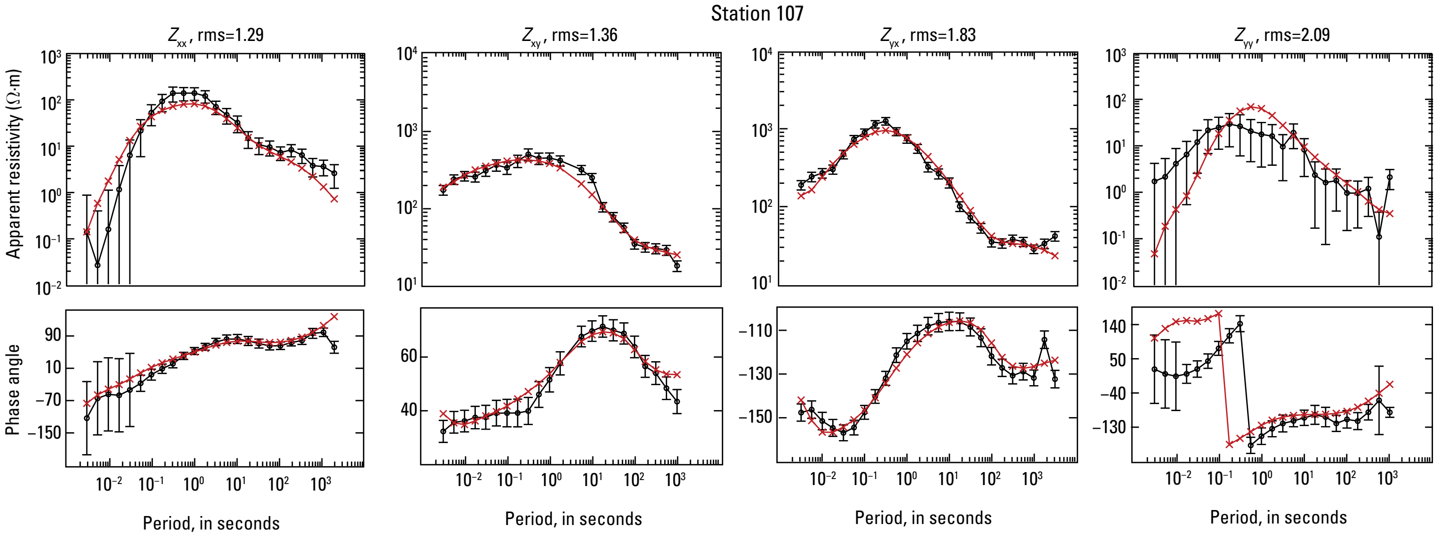

Figure 3.7. Station 107. Plots showing the data inverted (black) and the resistivity model response (red). Shown are all components of the impedance tensor (*Z*) as apparent resistivity (in Ohm meters, Ω·m) and phase angle (in degrees). Data error bars are shown for the inverted data.

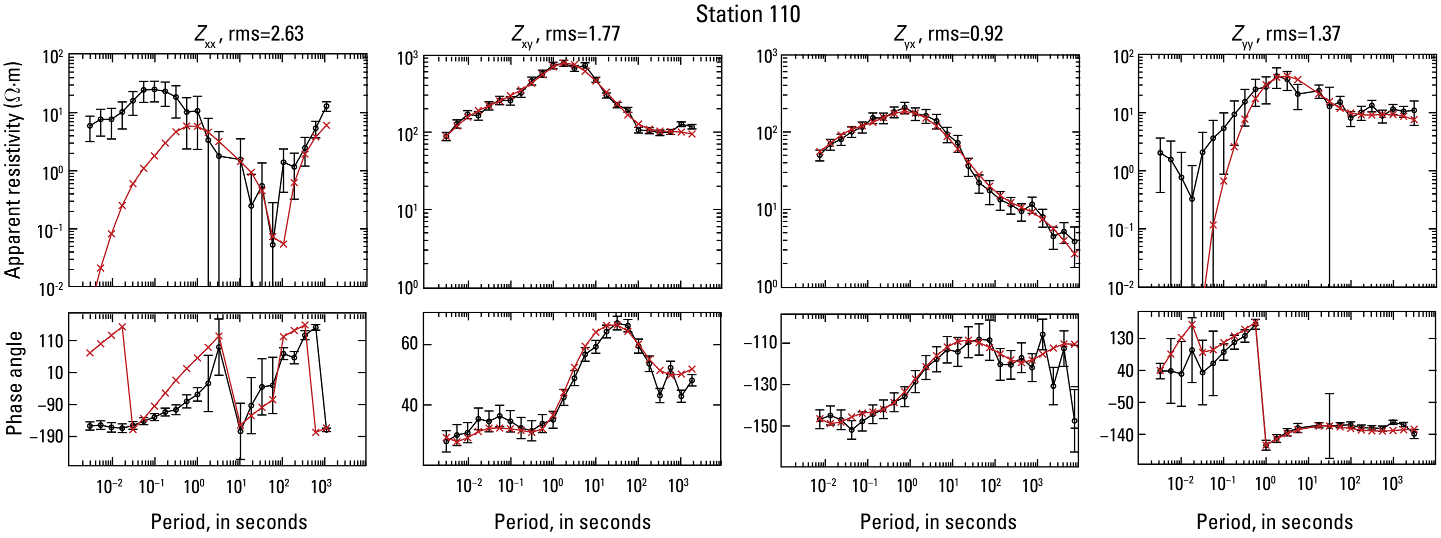

Figure 3.8. Station 110. Plots showing the data inverted (black) and the resistivity model response (red). Shown are all components of the impedance tensor (*Z*) as apparent resistivity (in Ohm meters, Ω·m) and phase angle (in degrees). Data error bars are shown for the inverted data.

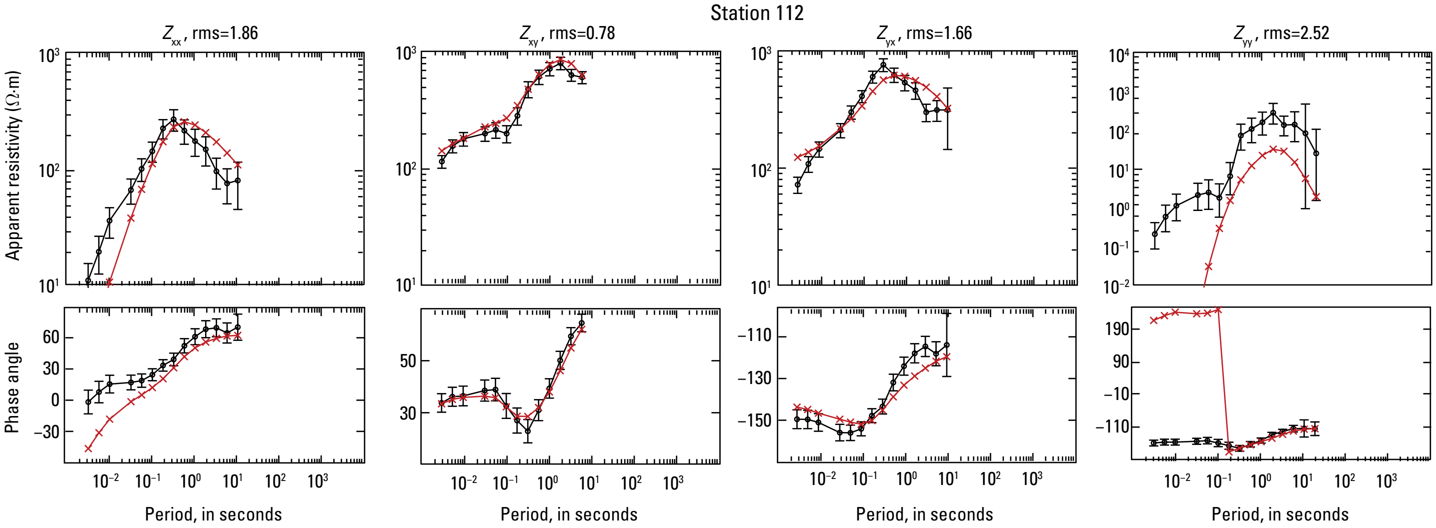

Figure 3.9. Station 112. Plots showing the data inverted (black) and the resistivity model response (red). Shown are all components of the impedance tensor (*Z*) as apparent resistivity (in Ohm meters, Ω·m) and phase angle (in degrees). Data error bars are shown for the inverted data.

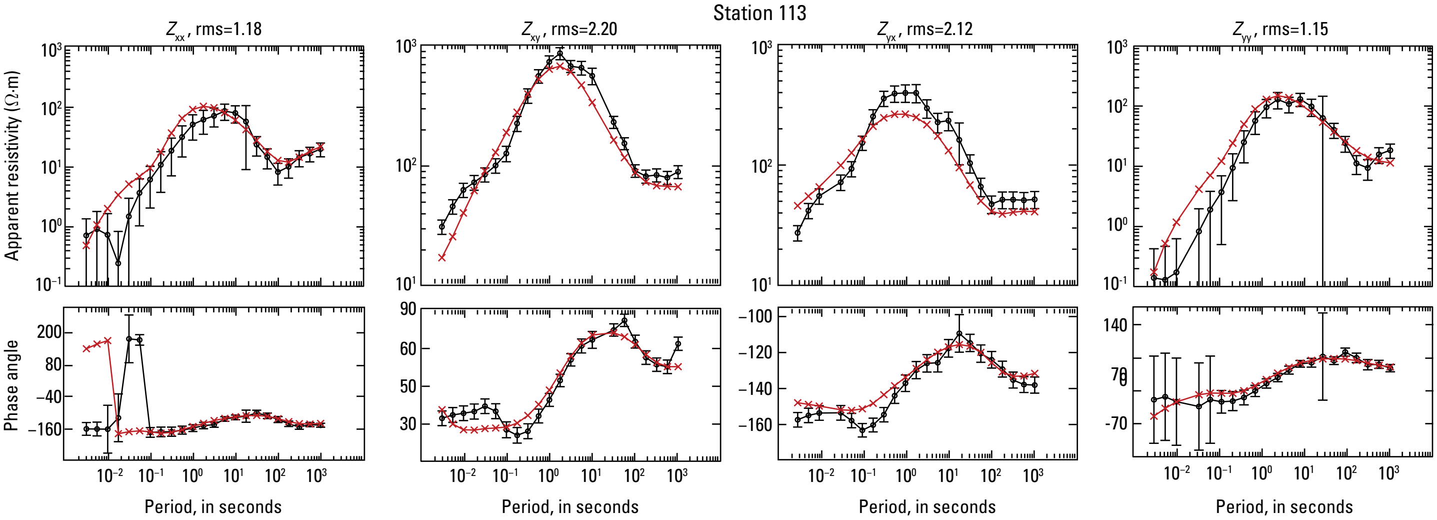

Figure 3.10. Station 113. Plots showing the data inverted (black) and the resistivity model response (red). Shown are all components of the impedance tensor (*Z*) as apparent resistivity (in Ohm meters, Ω·m) and phase angle (in degrees). Data error bars are shown for the inverted data.

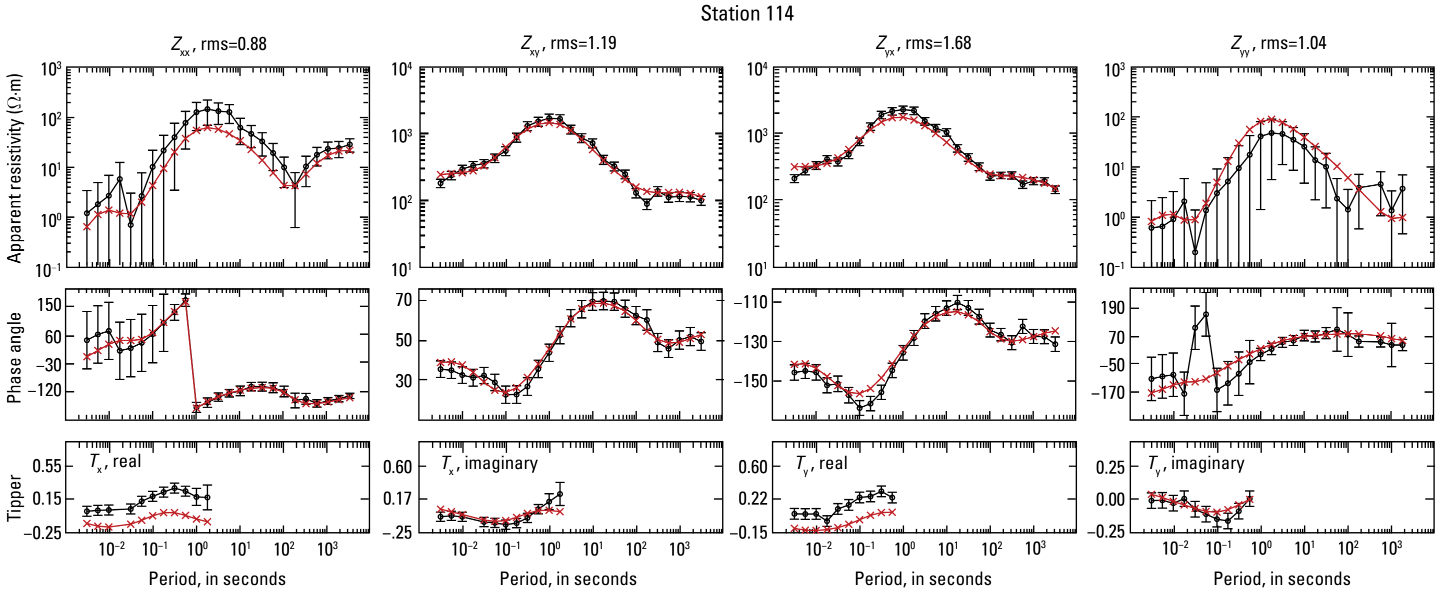

Figure 3.11. Station 114. Plots showing the data inverted (black) and the resistivity model response (red). Shown are all components of the impedance tensor (*Z*) as apparent resistivity (in Ohm meters, Ω·m) and phase angle (in degrees) and the induction vector (*T*), or tipper, as both real and imaginary parts of *T*. Data error bars are shown for the inverted data.

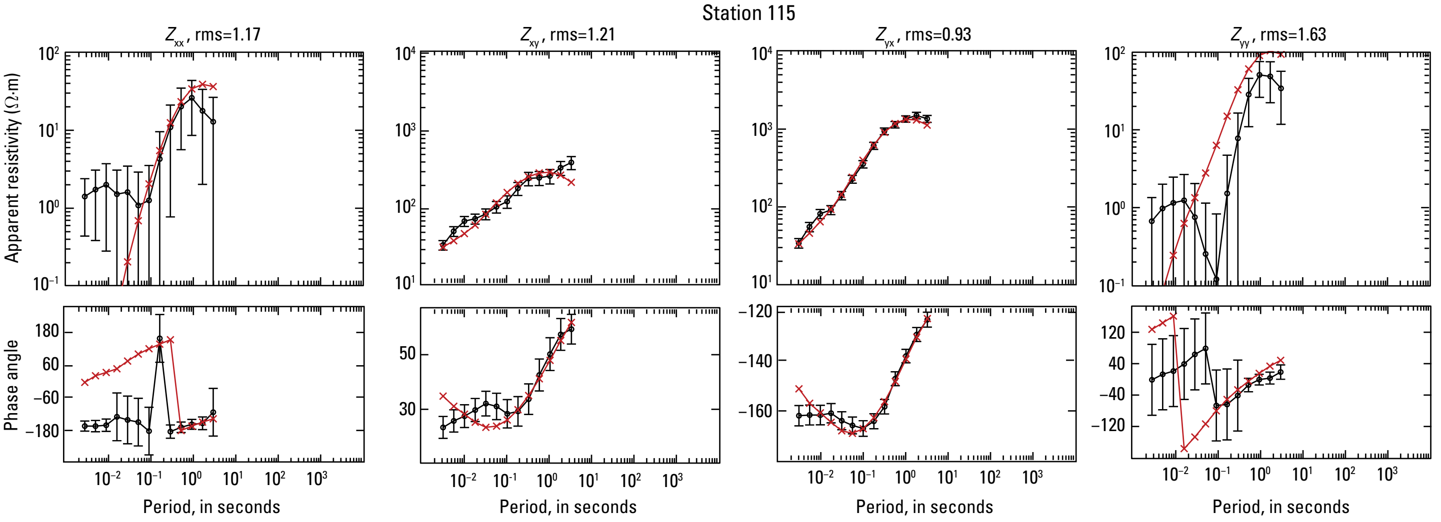

Figure 3.12. Station 115. Plots showing the data inverted (black) and the resistivity model response (red). Shown are all components of the impedance tensor (*Z*) as apparent resistivity (in Ohm meters, Ω·m) and phase angle (in degrees). Data error bars are shown for the inverted data.

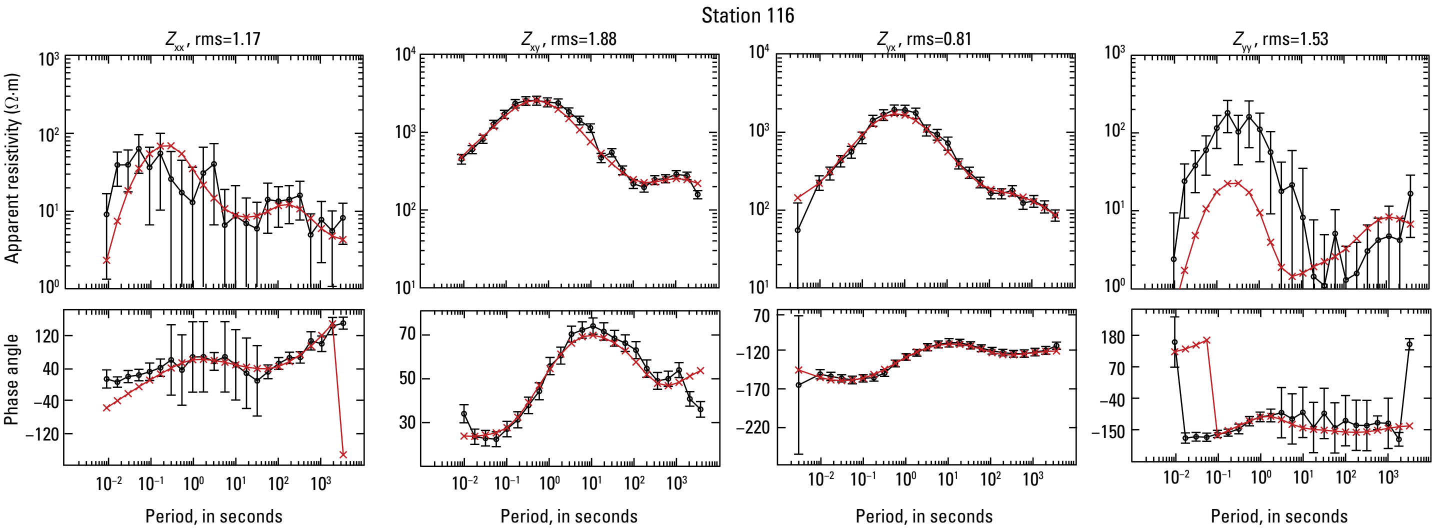

Figure 3.13. Station 116. Plots showing the data inverted (black) and the resistivity model response (red). Shown are all components of the impedance tensor (*Z*) as apparent resistivity (in Ohm meters, Ω·m) and phase angle (in degrees). Data error bars are shown for the inverted data.

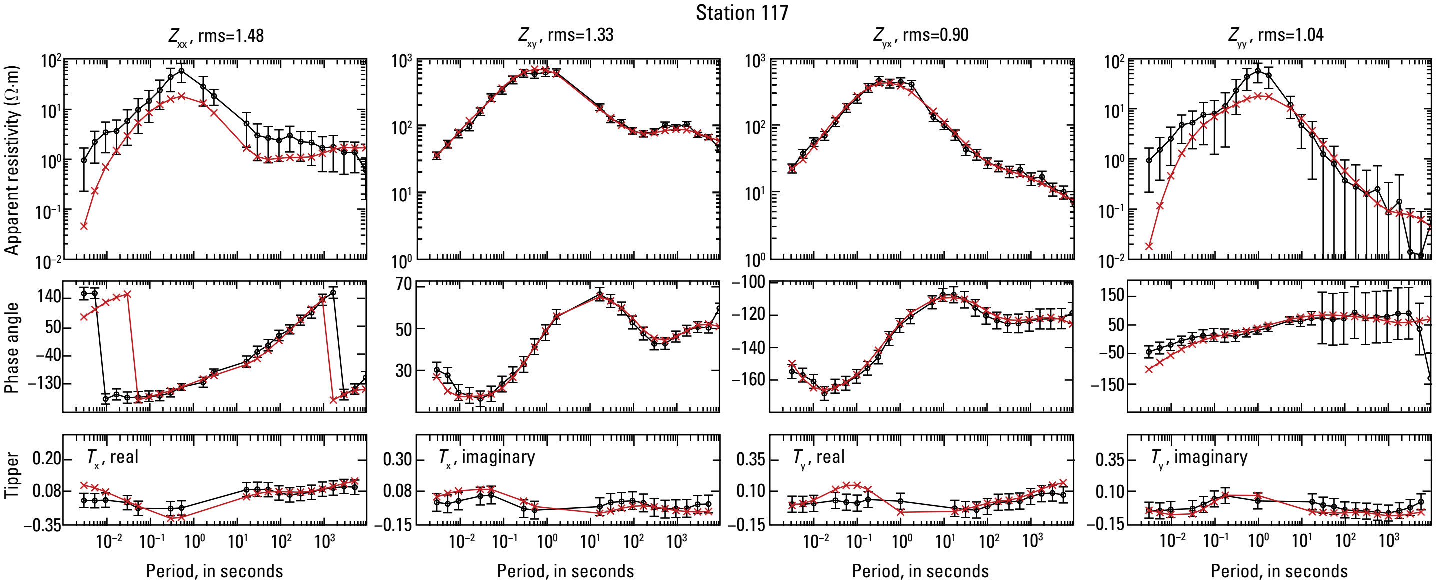

Figure 3.14. Station 117. Plots showing the data inverted (black) and the resistivity model response (red). Shown are all components of the impedance tensor (*Z*) as apparent resistivity (in Ohm meters, Ω·m) and phase angle (in degrees) and the induction vector (*T*), or tipper, as both real and imaginary parts of *T*. Data error bars are shown for the inverted data.

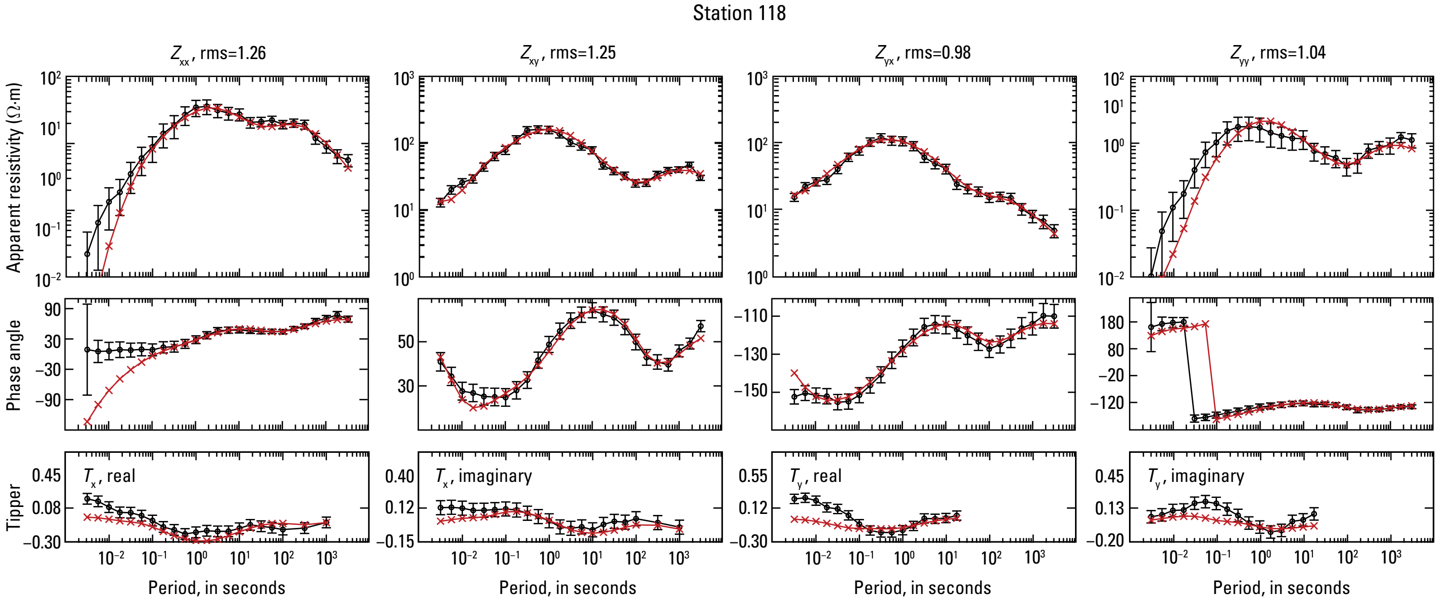

Figure 3.15. Station 118. Plots showing the data inverted (black) and the resistivity model response (red). Shown are all components of the impedance tensor (*Z*) as apparent resistivity (in Ohm meters, Ω·m) and phase angle (in degrees) and the induction vector (*T*), or tipper, as both real and imaginary parts of *T*. Data error bars are shown for the inverted data.

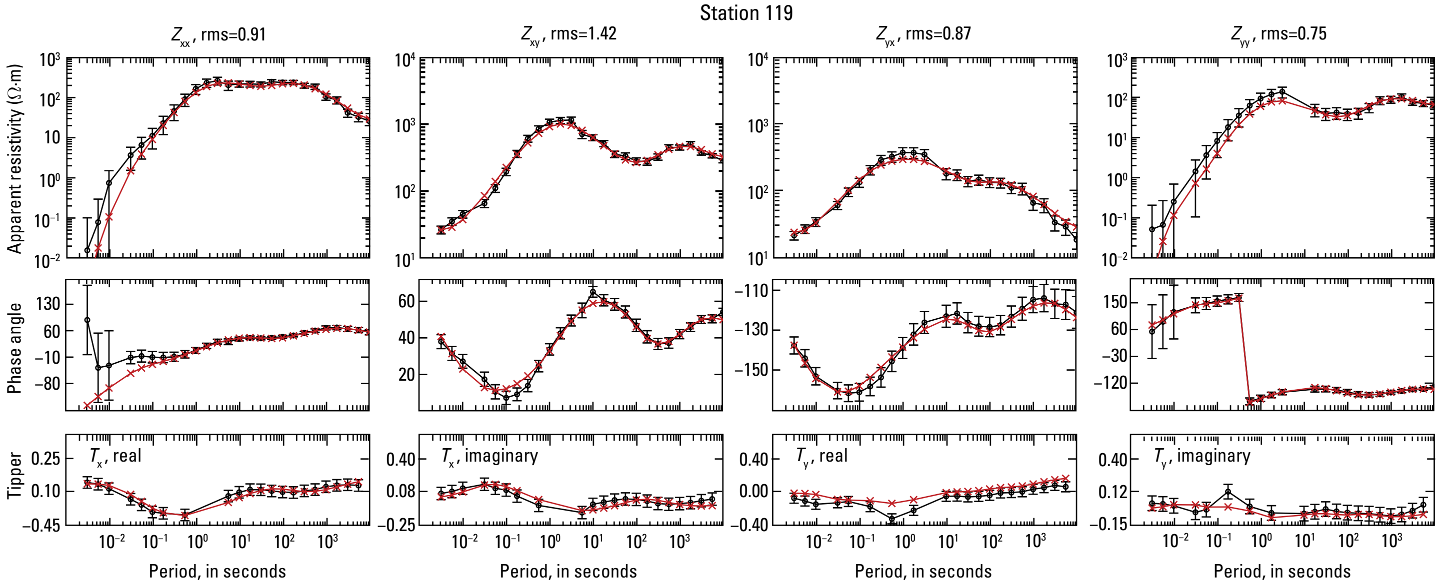

Figure 3.16. Station 119. Plots showing the data inverted (black) and the resistivity model response (red). Shown are all components of the impedance tensor (*Z*) as apparent resistivity (in Ohm meters, Ω·m) and phase angle (in degrees) and the induction vector (*T*), or tipper, as both real and imaginary parts of *T*. Data error bars are shown for the inverted data.

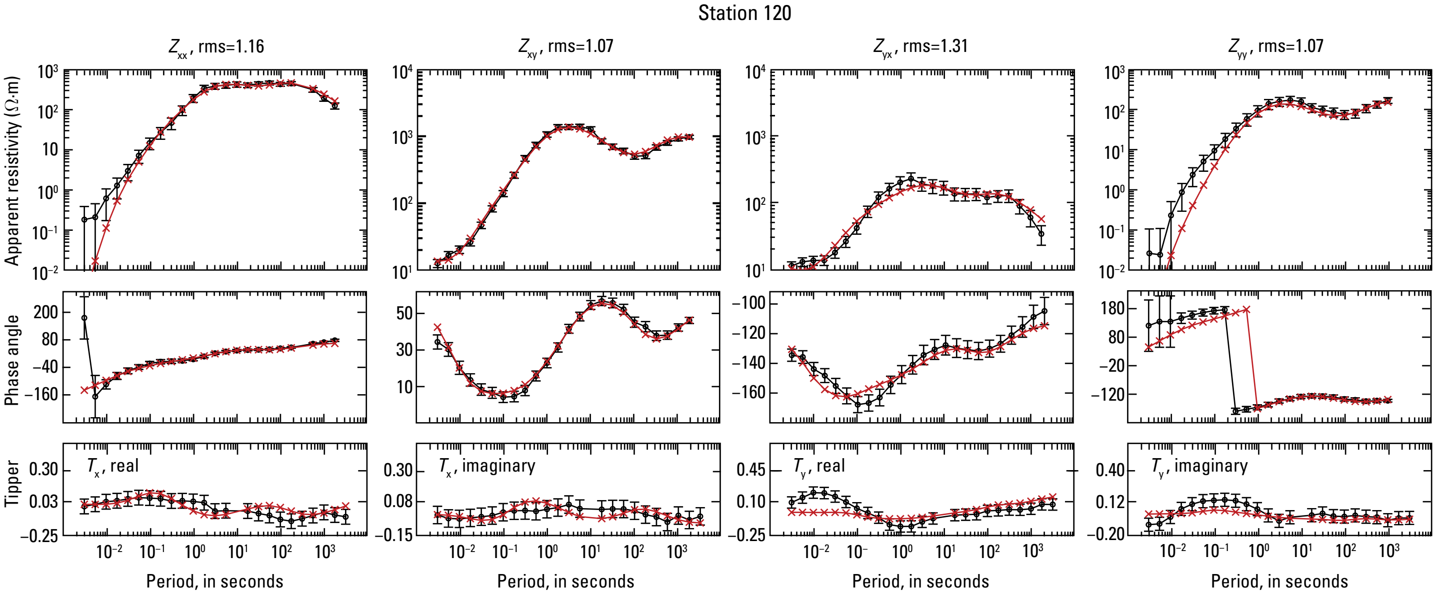

Figure 3.17. Station 120. Plots showing the data inverted (black) and the resistivity model response (red). Shown are all components of the impedance tensor (*Z*) as apparent resistivity (in Ohm meters, Ω·m) and phase angle (in degrees) and the induction vector (*T*), or tipper, as both real and imaginary parts of *T*. Data error bars are shown for the inverted data.

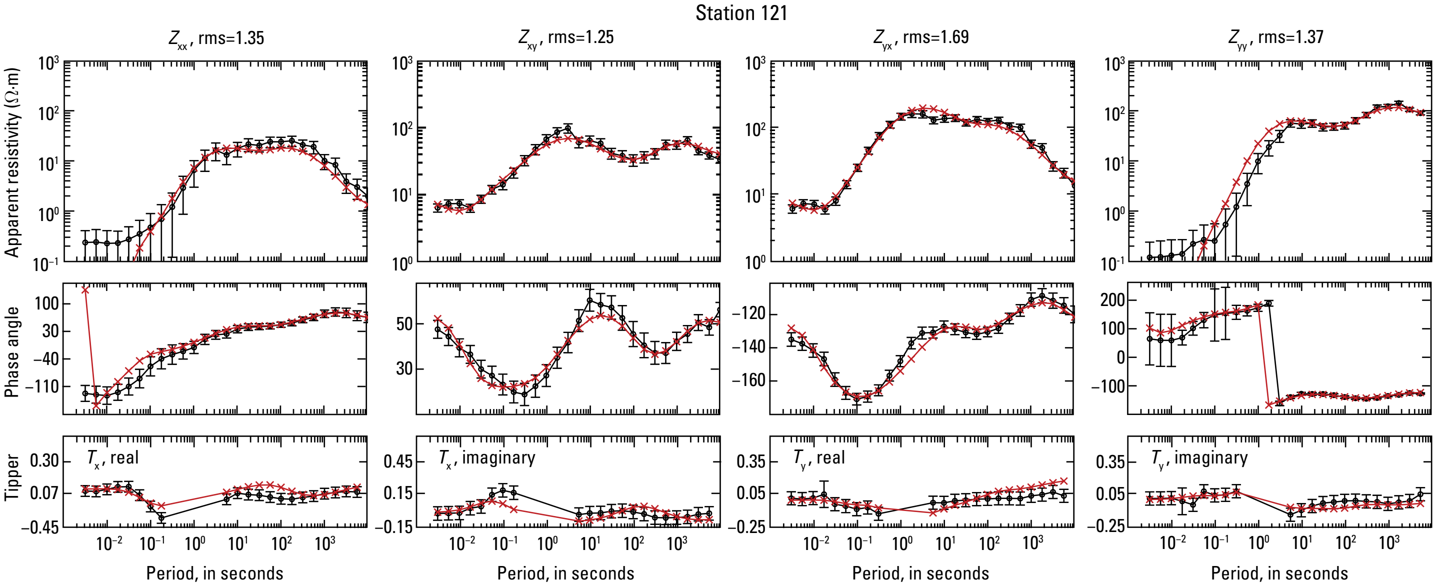

Figure 3.18. Station 121. Plots showing the data inverted (black) and the resistivity model response (red). Shown are all components of the impedance tensor (*Z*) as apparent resistivity (in Ohm meters, Ω·m) and phase angle (in degrees) and the induction vector (*T*), or tipper, as both real and imaginary parts of *T*. Data error bars are shown for the inverted data.

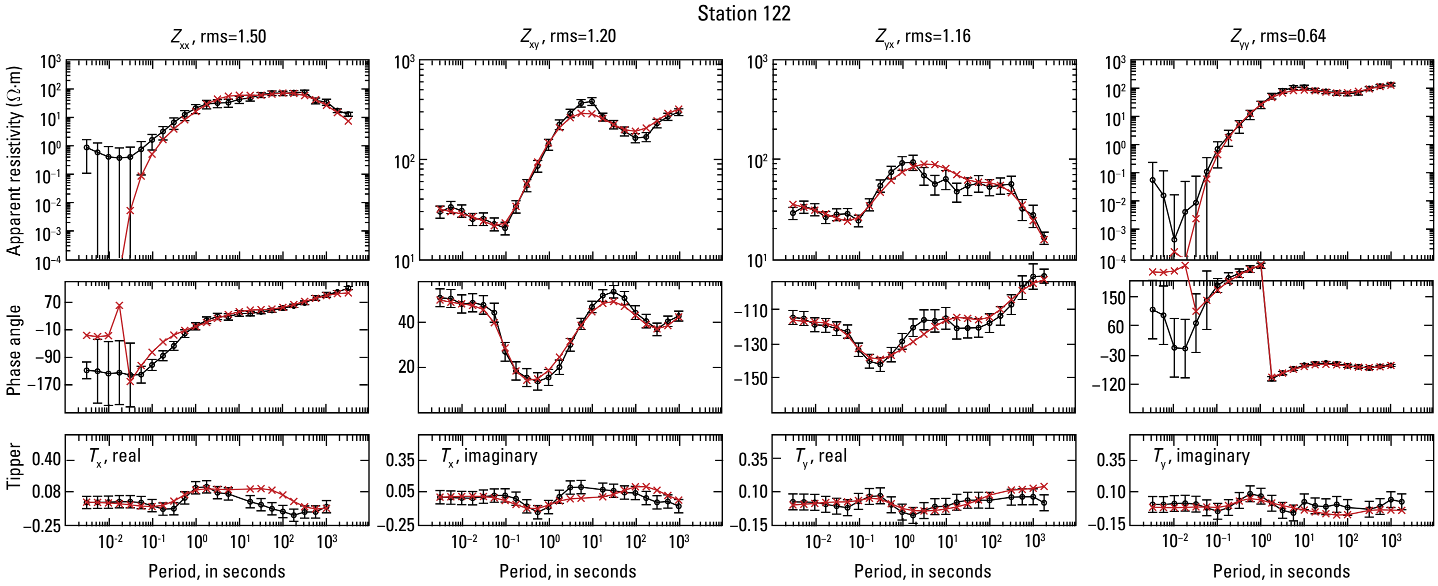

Figure 3.19. Station 122. Plots showing the data inverted (black) and the resistivity model response (red). Shown are all components of the impedance tensor (*Z*) as apparent resistivity (in Ohm meters, Ω·m) and phase angle (in degrees) and the induction vector (*T*), or tipper, as both real and imaginary parts of *T*. Data error bars are shown for the inverted data.

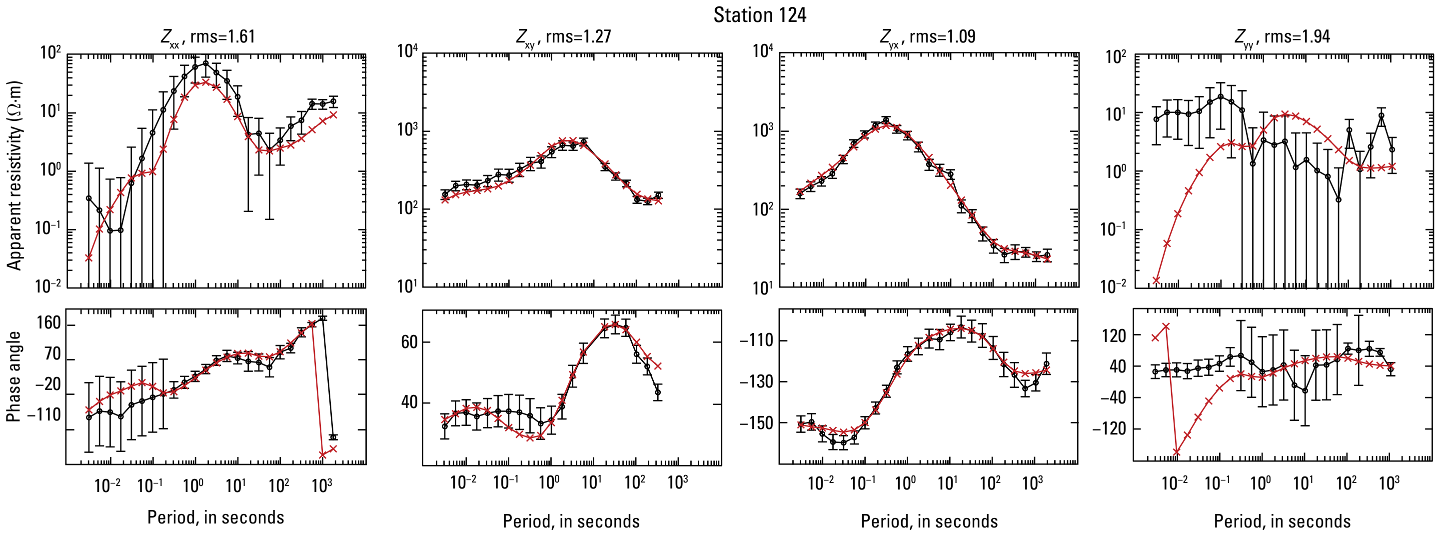

Figure 3.20. Station 124. Plots showing the data inverted (black) and the resistivity model response (red). Shown are all components of the impedance tensor (*Z*) as apparent resistivity (in Ohm meters, Ω·m) and phase angle (in degrees). Data error bars are shown for the inverted data.

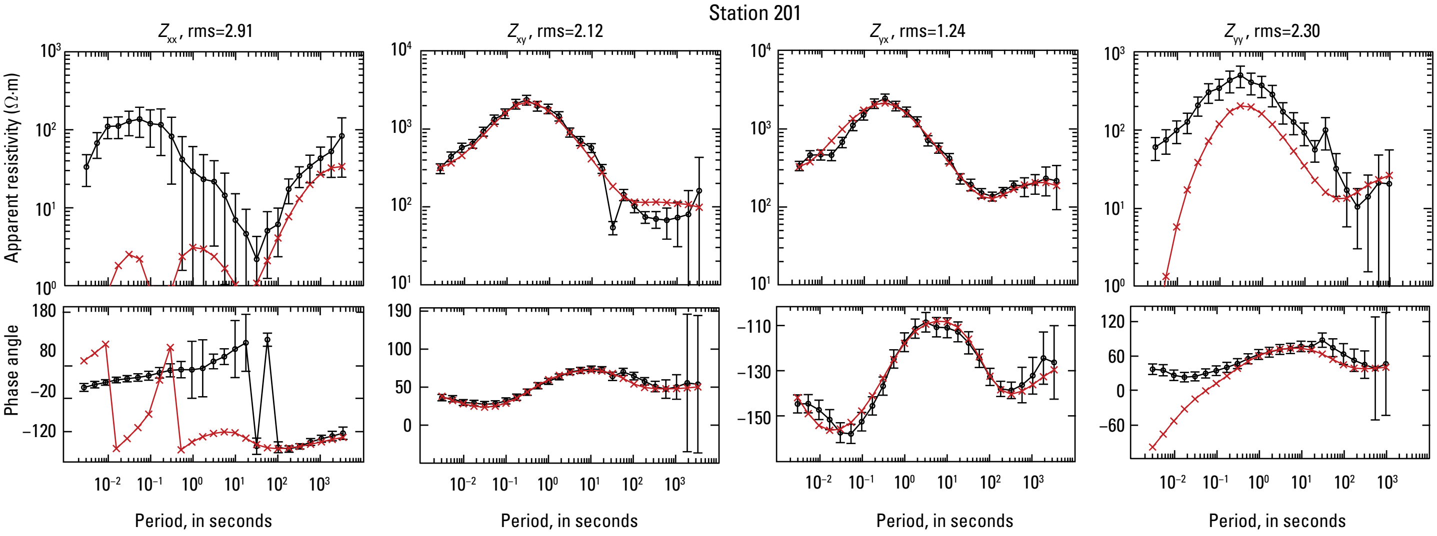

Figure 3.21. Station 201. Plots showing the data inverted (black) and the resistivity model response (red). Shown are all components of the impedance tensor (*Z*) as apparent resistivity (in Ohm meters, Ω·m) and phase angle (in degrees). Data error bars are shown for the inverted data.

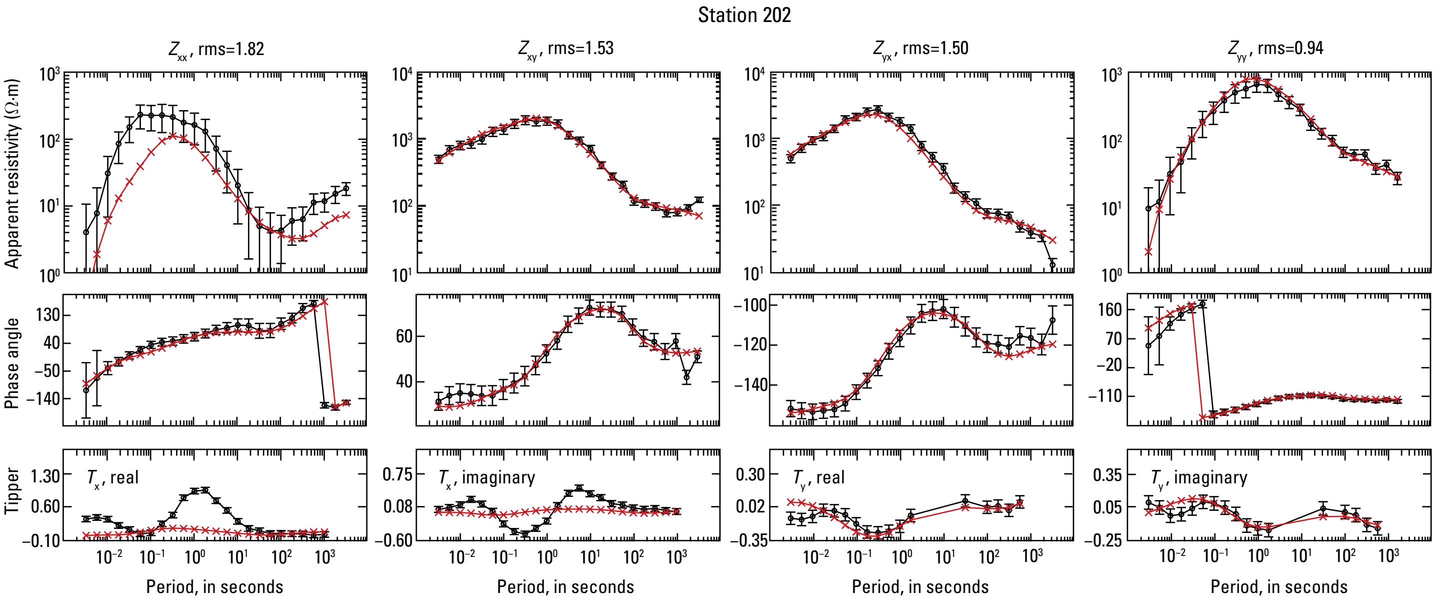

Figure 3.22. Station 202. Plots showing the data inverted (black) and the resistivity model response (red). Shown are all components of the impedance tensor (*Z*) as apparent resistivity (in Ohm meters, Ω·m) and phase angle (in degrees) and the induction vector (*T*), or tipper, as both real and imaginary parts of *T*. Data error bars are shown for the inverted data.

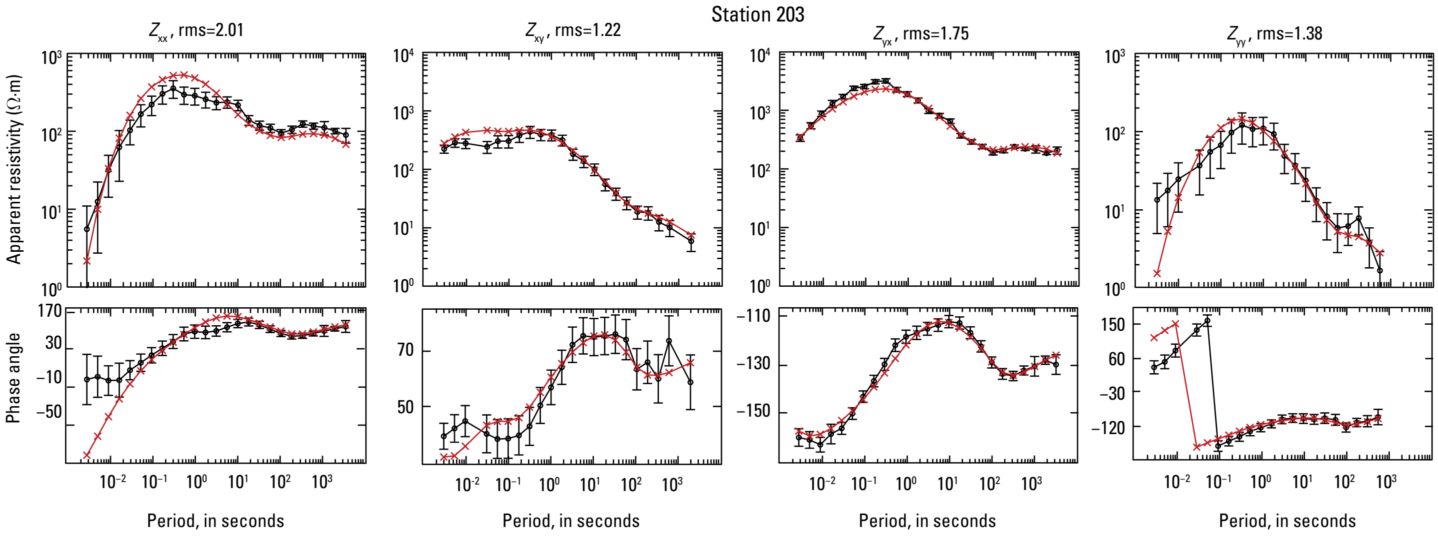

Figure 3.23. Station 203. Plots showing the data inverted (black) and the resistivity model response (red). Shown are all components of the impedance tensor (*Z*) as apparent resistivity (in Ohm meters, Ω·m) and phase angle (in degrees). Data error bars are shown for the inverted data.

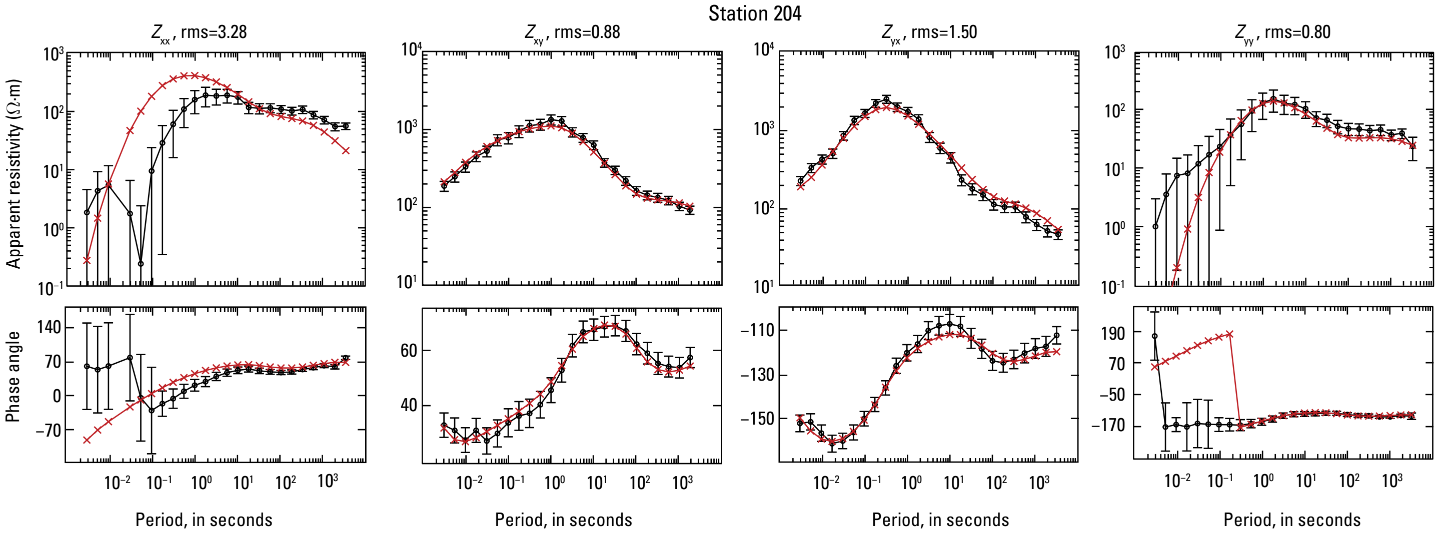

Figure 3.24. Station 204. Plots showing the data inverted (black) and the resistivity model response (red). Shown are all components of the impedance tensor (*Z*) as apparent resistivity (in Ohm meters, Ω·m) and phase angle (in degrees). Data error bars are shown for the inverted data.

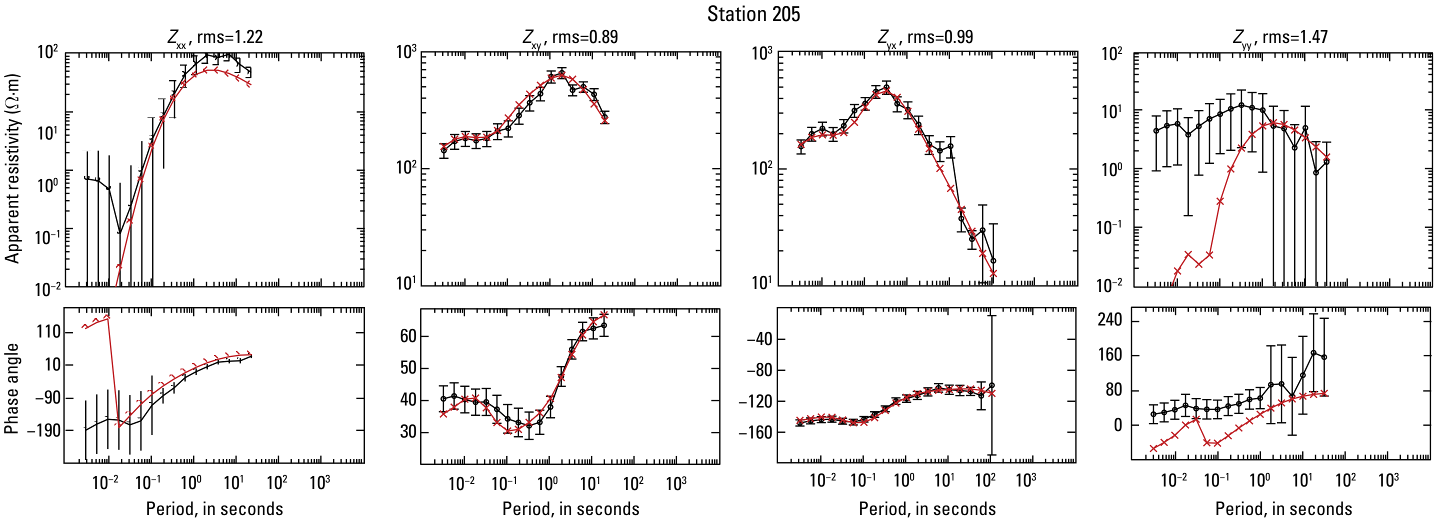

Figure 3.25. Station 205. Plots showing the data inverted (black) and the resistivity model response (red). Shown are all components of the impedance tensor (*Z*) as apparent resistivity (in Ohm meters, Ω·m) and phase angle (in degrees). Data error bars are shown for the inverted data.

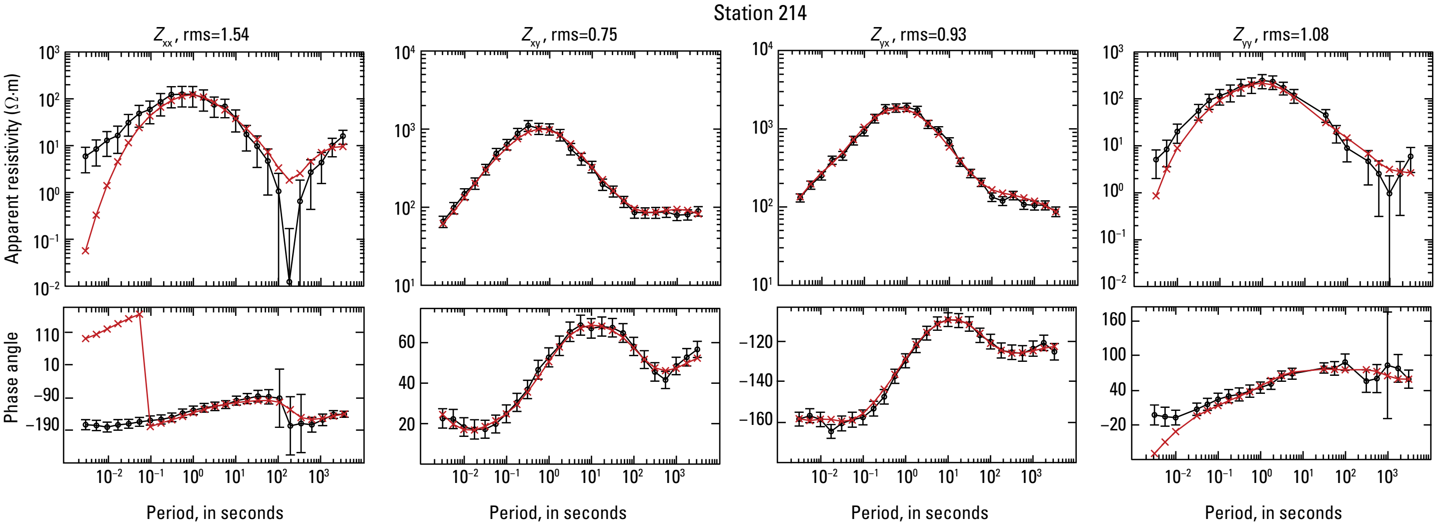

Figure 3.26. Station 214. Plots showing the data inverted (black) and the resistivity model response (red). Shown are all components of the impedance tensor (*Z*) as apparent resistivity (in Ohm meters, Ω·m) and phase angle (in degrees). Data error bars are shown for the inverted data.

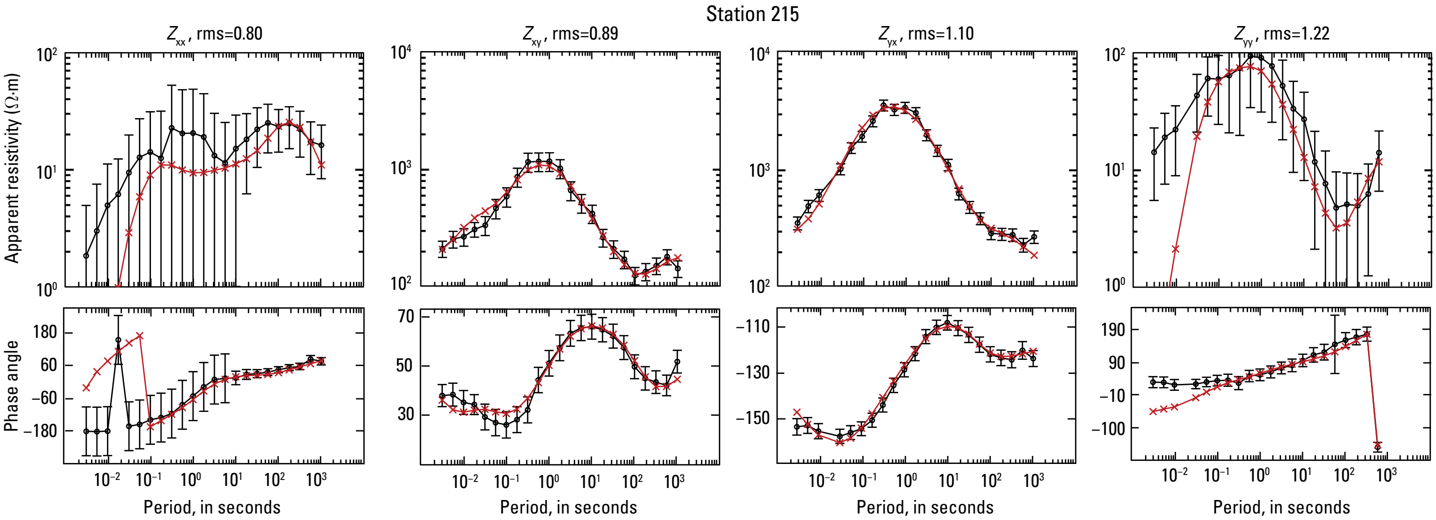

Figure 3.27. Station 215. Plots showing the data inverted (black) and the resistivity model response (red). Shown are all components of the impedance tensor (*Z*) as apparent resistivity (in Ohm meters, Ω·m) and phase angle (in degrees). Data error bars are shown for the inverted data.

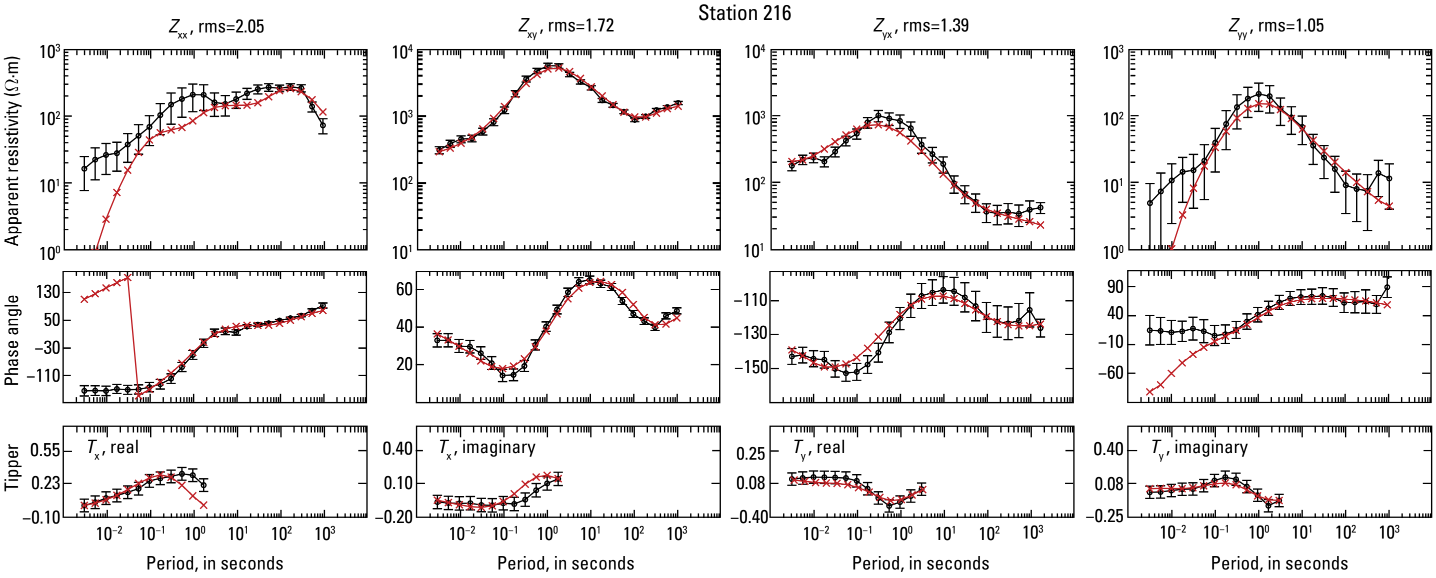

Figure 3.28. Station 216. Plots showing the data inverted (black) and the resistivity model response (red). Shown are all components of the impedance tensor (*Z*) as apparent resistivity (in Ohm meters, Ω·m) and phase angle (in degrees) and the induction vector (*T*), or tipper, as both real and imaginary parts of *T*. Data error bars are shown for the inverted data.

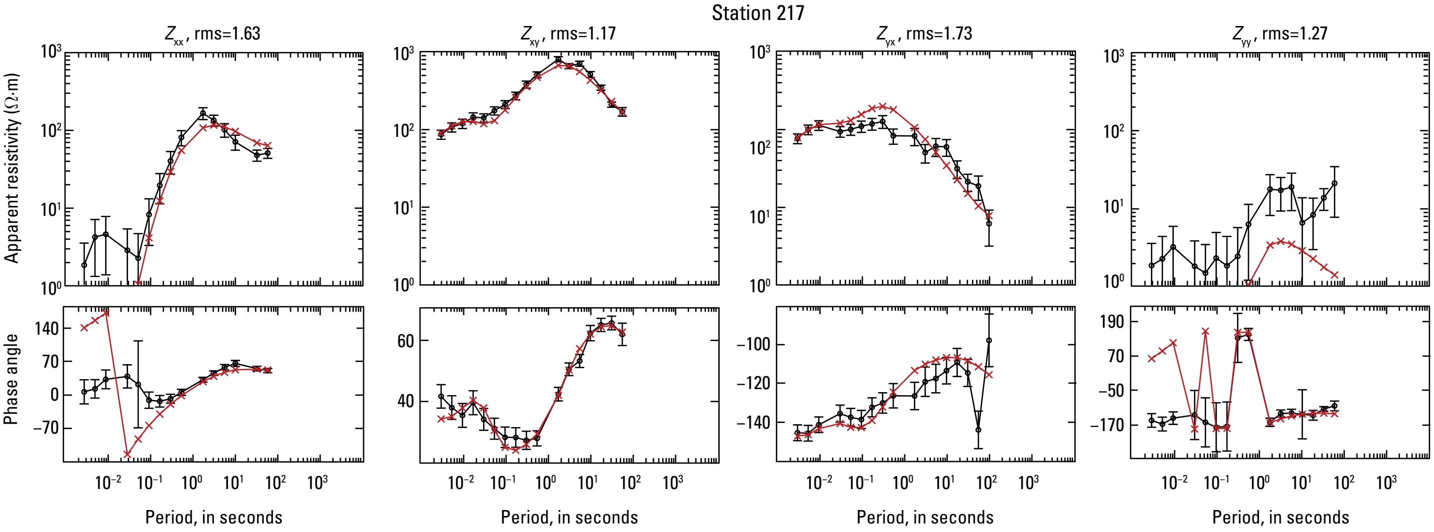

Figure 3.29. Station 217. Plots showing the data inverted (black) and the resistivity model response (red). Shown are all components of the impedance tensor (*Z*) as apparent resistivity (in Ohm meters, Ω·m) and phase angle (in degrees). Data error bars are shown for the inverted data.

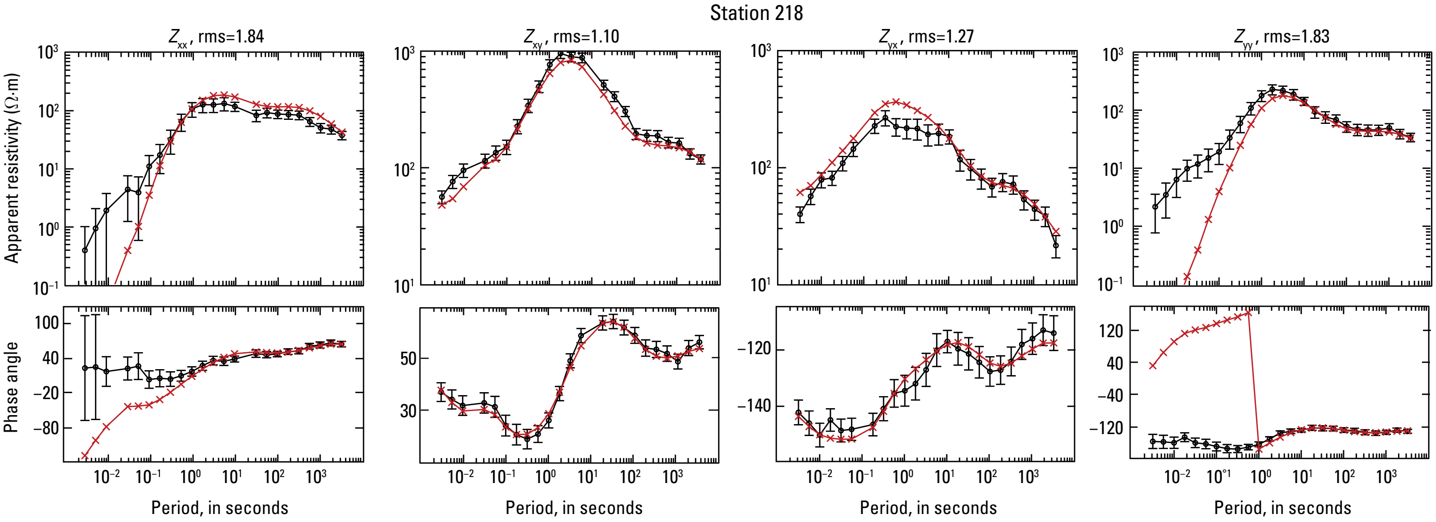

Figure 3.30. Station 218. Plots showing the data inverted (black) and the resistivity model response (red). Shown are all components of the impedance tensor (*Z*) as apparent resistivity (in Ohm meters, Ω·m) and phase angle (in degrees). Data error bars are shown for the inverted data.

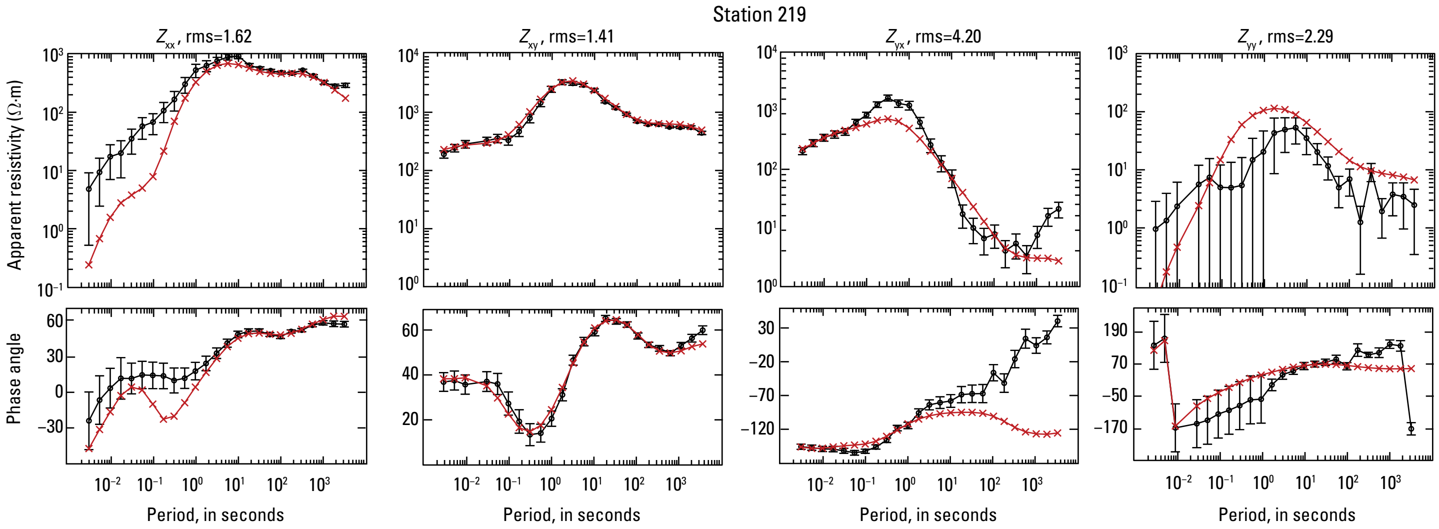

Figure 3.31. Station 219. Plots showing the data inverted (black) and the resistivity model response (red). Shown are all components of the impedance tensor (*Z*) as apparent resistivity (in Ohm meters, Ω·m) and phase angle (in degrees). Data error bars are shown for the inverted data.

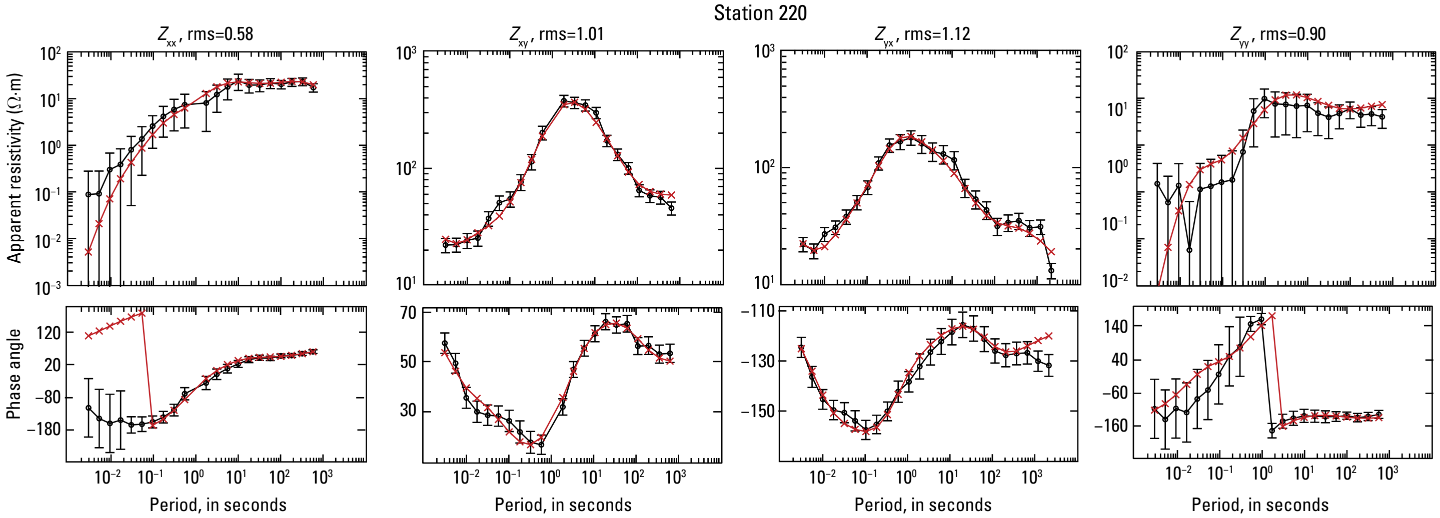

Figure 3.32. Station 220. Plots showing the data inverted (black) and the resistivity model response (red). Shown are all components of the impedance tensor (*Z*) as apparent resistivity (in Ohm meters, Ω·m) and phase angle (in degrees). Data error bars are shown for the inverted data.

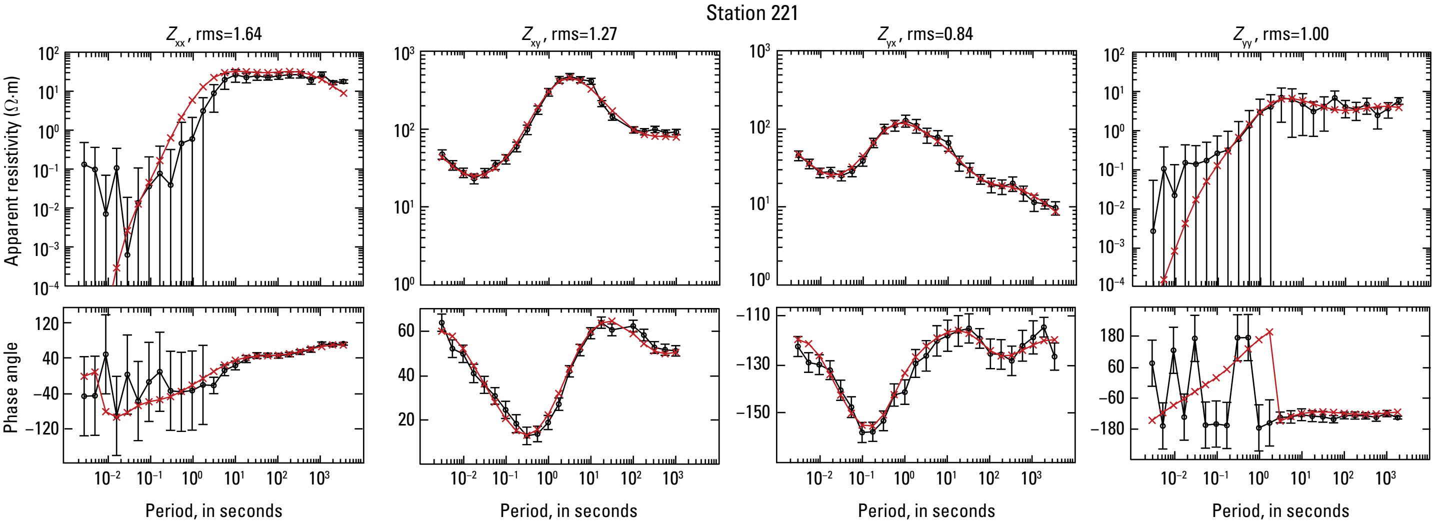

Figure 3.33. Station 221. Plots showing the data inverted (black) and the resistivity model response (red). Shown are all components of the impedance tensor (*Z*) as apparent resistivity (in Ohm meters, Ω·m) and phase angle (in degrees). Data error bars are shown for the inverted data.

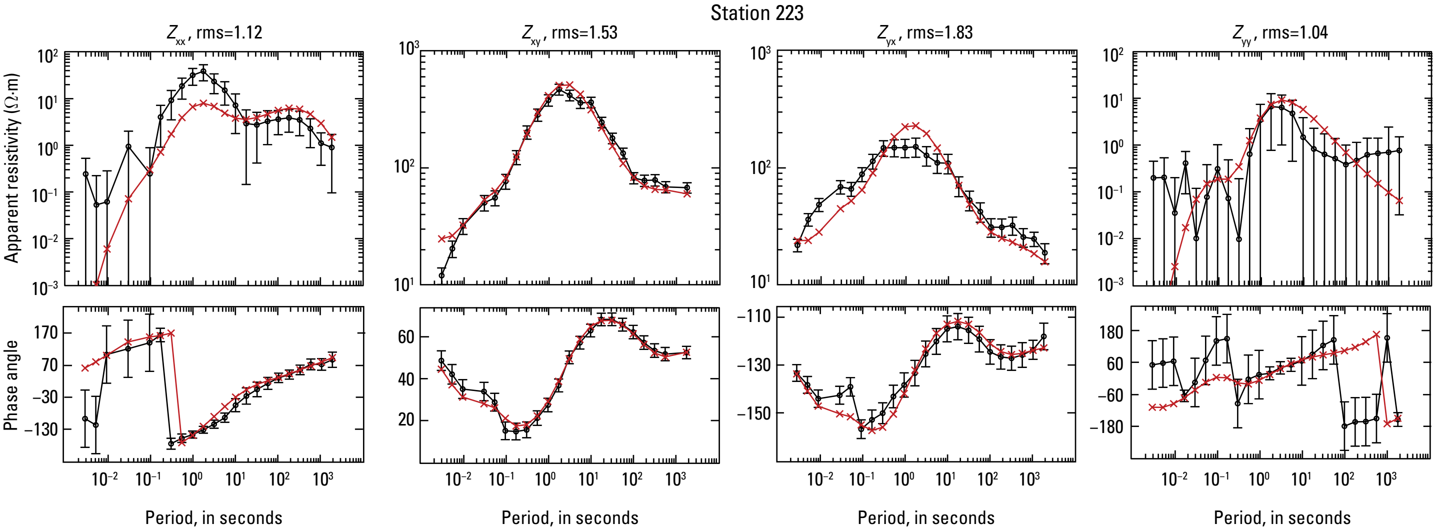

Figure 3.34. Station 223. Plots showing the data inverted (black) and the resistivity model response (red). Shown are all components of the impedance tensor (*Z*) as apparent resistivity (in Ohm meters, Ω·m) and phase angle (in degrees). Data error bars are shown for the inverted data.

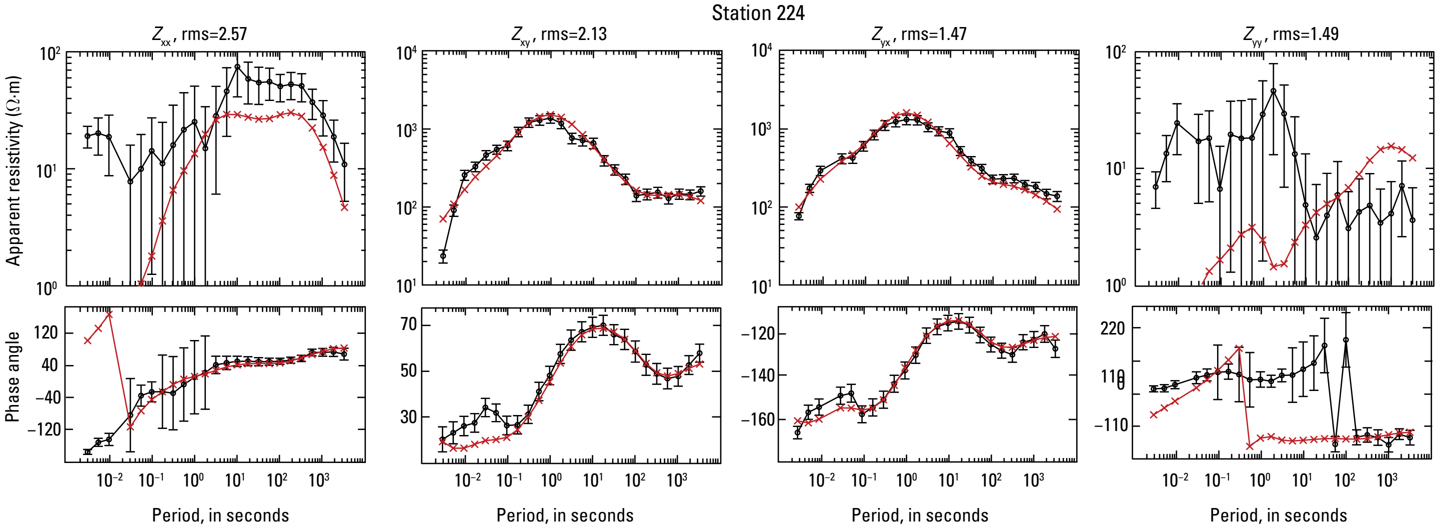

Figure 3.35. Station 224. Plots showing the data inverted (black) and the resistivity model response (red). Shown are all components of the impedance tensor (*Z*) as apparent resistivity (in Ohm meters, Ω·m) and phase angle (in degrees). Data error bars are shown for the inverted data.

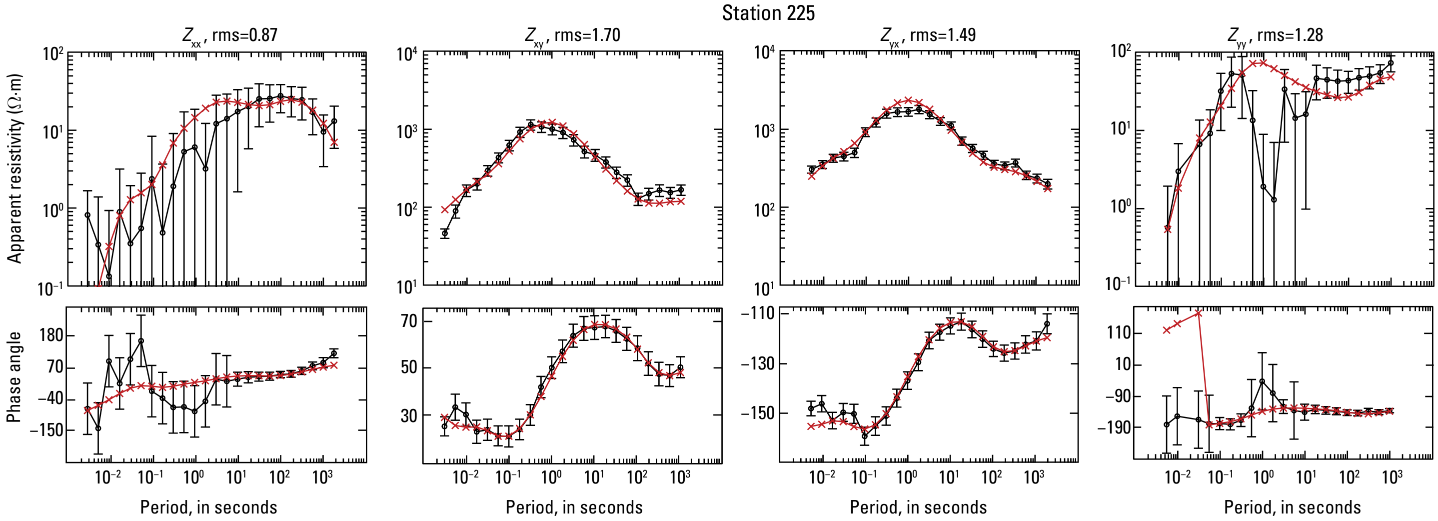

Figure 3.36. Station 225. Plots showing the data inverted (black) and the resistivity model response (red). Shown are all components of the impedance tensor (*Z*) as apparent resistivity (in Ohm meters, Ω·m) and phase angle (in degrees). Data error bars are shown for the inverted data.

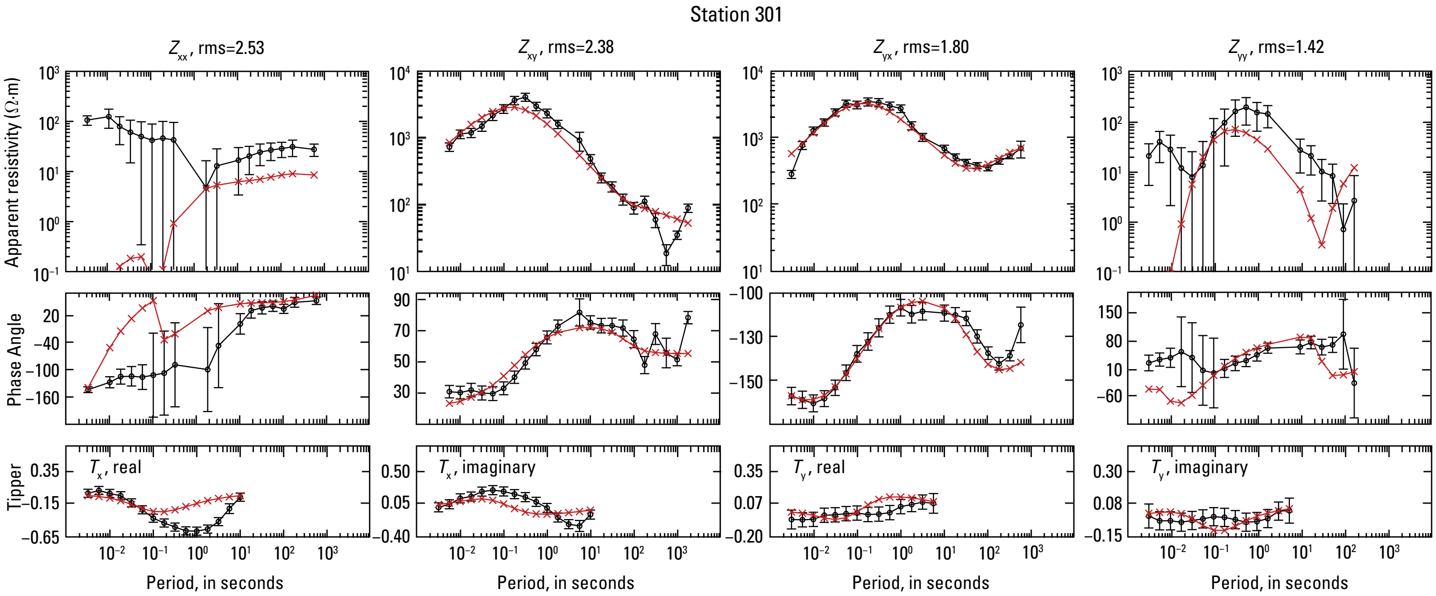

Figure 3.37. Station 301. Plots showing the data inverted (black) and the resistivity model response (red). Shown are all components of the impedance tensor (*Z*) as apparent resistivity (in Ohm meters, Ω·m) and phase angle (in degrees) and the induction vector (*T*), or tipper, as both real and imaginary parts of *T*. Data error bars are shown for the inverted data.

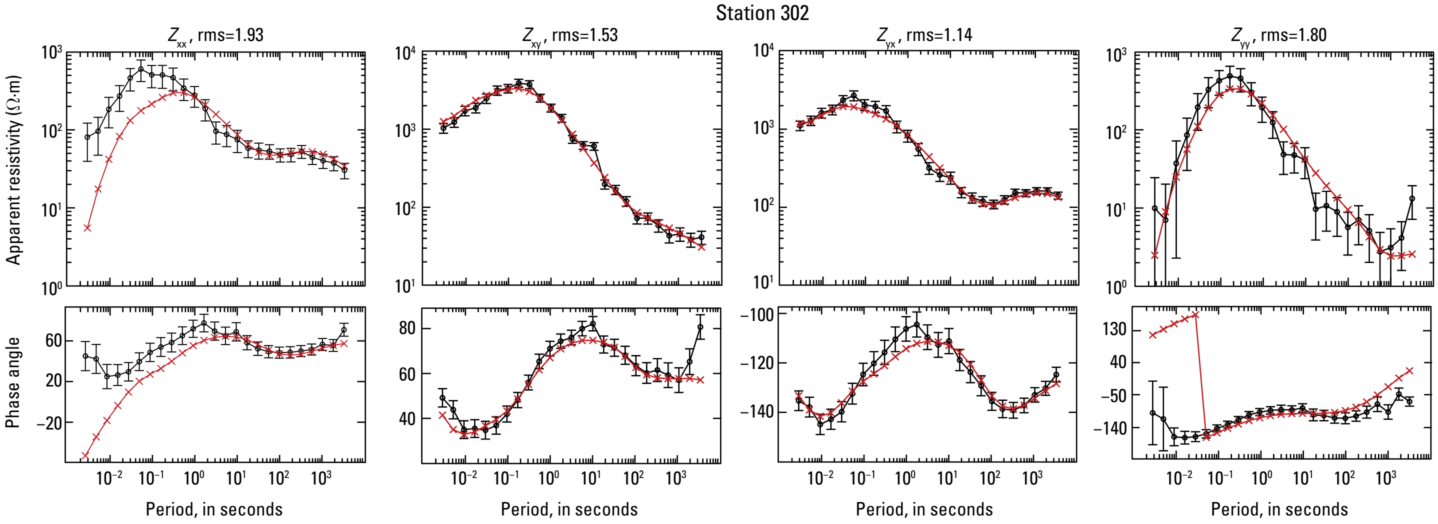

Figure 3.38. Station 302. Plots showing the data inverted (black) and the resistivity model response (red). Shown are all components of the impedance tensor (*Z*) as apparent resistivity (in Ohm meters, Ω·m) and phase angle (in degrees). Data error bars are shown for the inverted data.

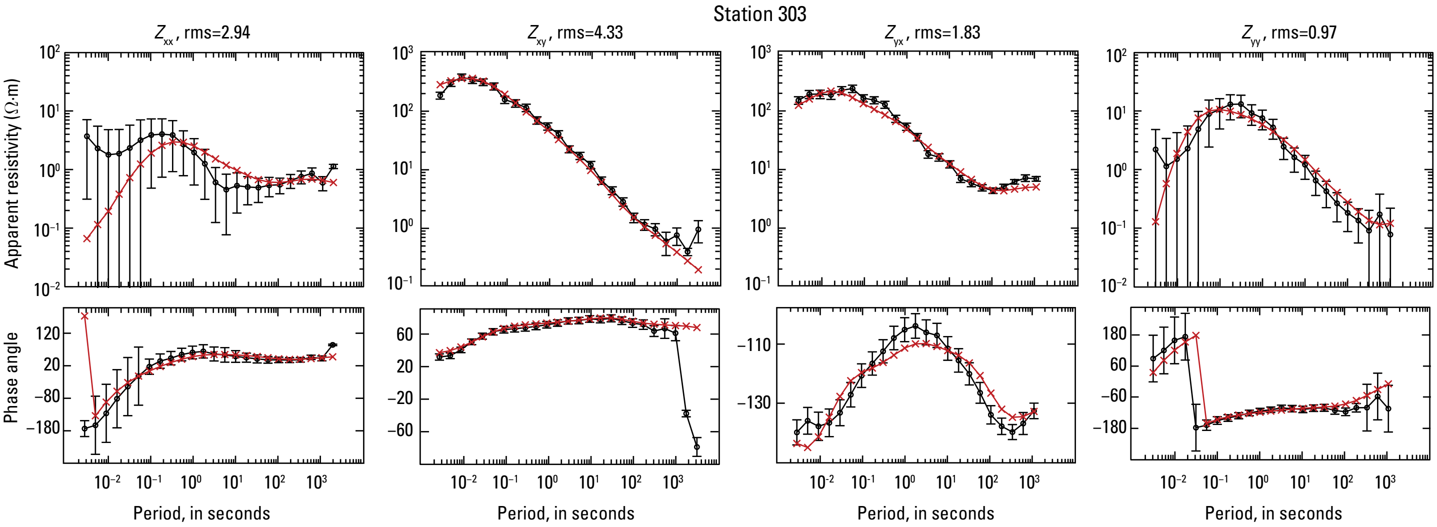

Figure 3.39. Station 303. Plots showing the data inverted (black) and the resistivity model response (red). Shown are all components of the impedance tensor (*Z*) as apparent resistivity (in Ohm meters, Ω·m) and phase angle (in degrees). Data error bars are shown for the inverted data.

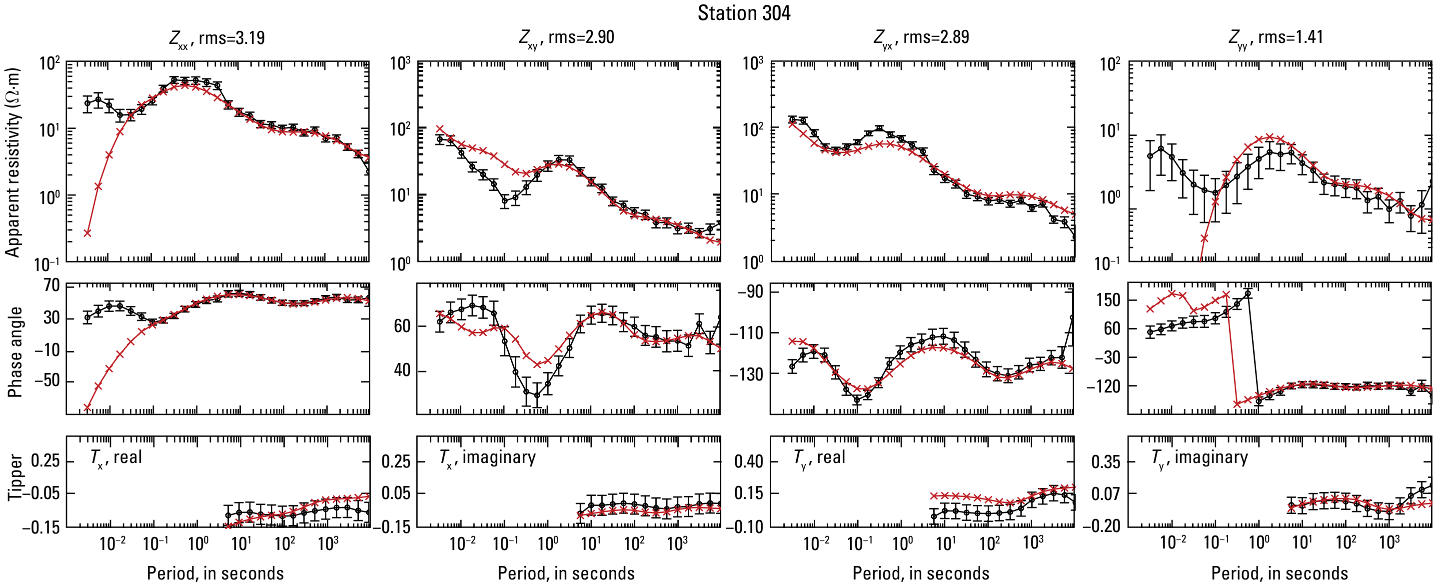

Figure 3.40. Station 304. Plots showing the data inverted (black) and the resistivity model response (red). Shown are all components of the impedance tensor (*Z*) as apparent resistivity (in Ohm meters, Ω·m) and phase angle (in degrees) and the induction vector (*T*), or tipper, as both real and imaginary parts of *T*. Data error bars are shown for the inverted data.

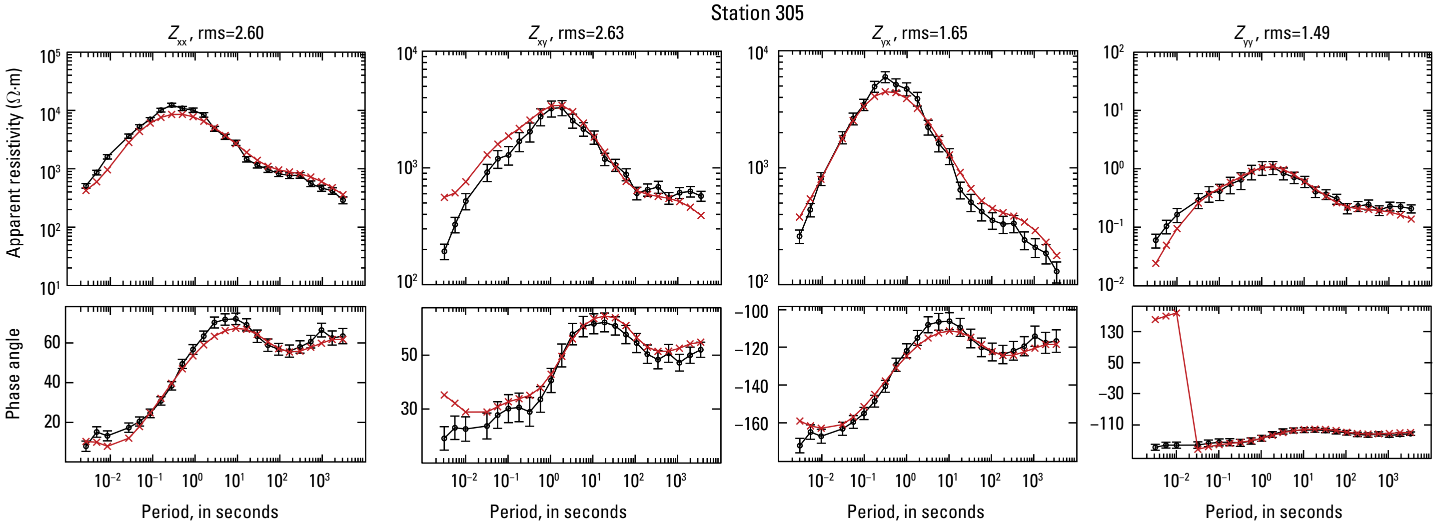

Figure 3.41. Station 305. Plots showing the data inverted (black) and the resistivity model response (red). Shown are all components of the impedance tensor (*Z*) as apparent resistivity (in Ohm meters, Ω·m) and phase angle (in degrees). Data error bars are shown for the inverted data.

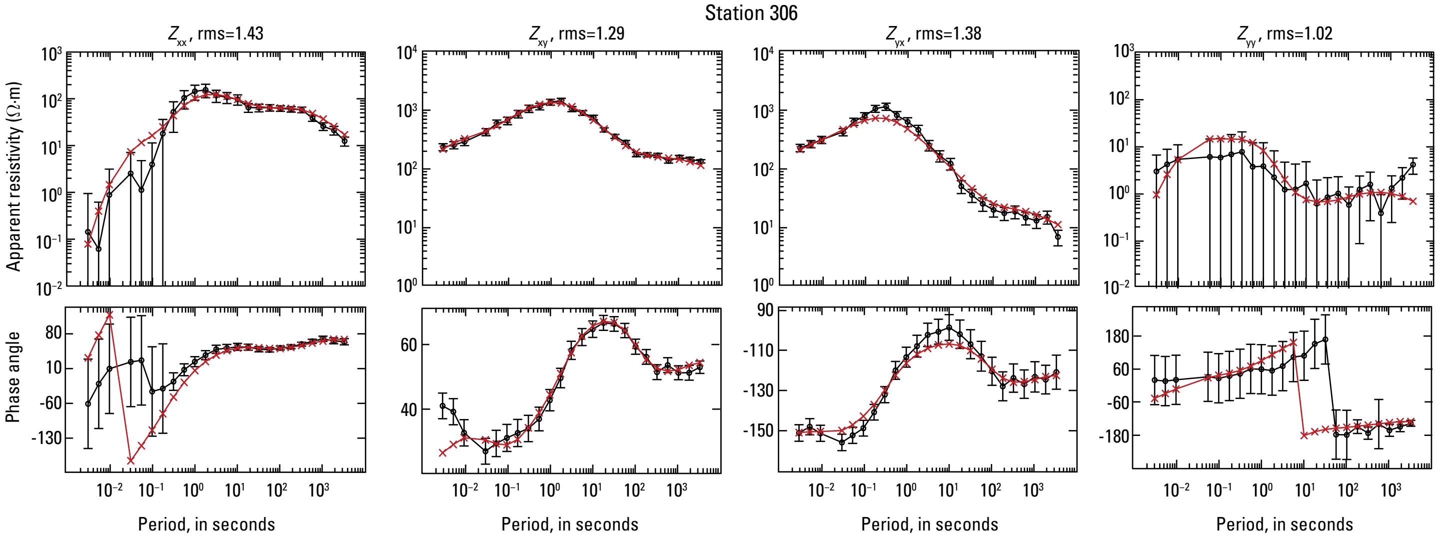

Figure 3.42. Station 306. Plots showing the data inverted (black) and the resistivity model response (red). Shown are all components of the impedance tensor (*Z*) as apparent resistivity (in Ohm meters, Ω·m) and phase angle (in degrees). Data error bars are shown for the inverted data.

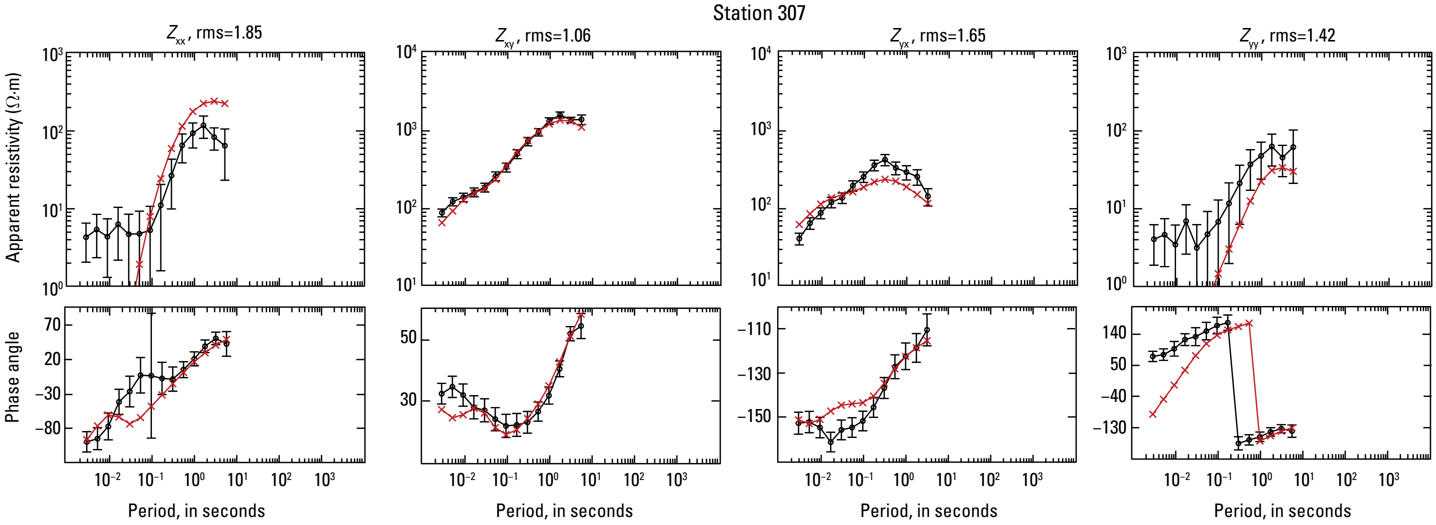

Figure 3.43. Station 307. Plots showing the data inverted (black) and the resistivity model response (red). Shown are all components of the impedance tensor (*Z*) as apparent resistivity (in Ohm meters, Ω·m) and phase angle (in degrees). Data error bars are shown for the inverted data.

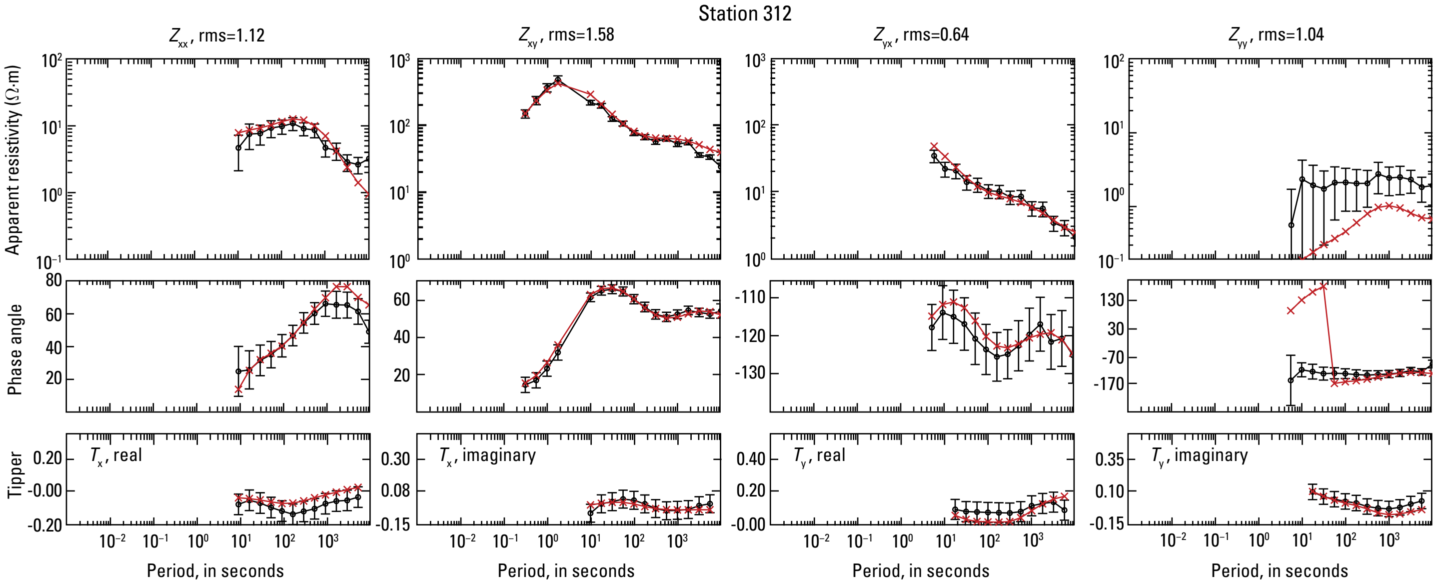

Figure 3.44. Station 312. Plots showing the data inverted (black) and the resistivity model response (red). Shown are all components of the impedance tensor (*Z*) as apparent resistivity (in Ohm meters, Ω·m) and phase angle (in degrees) and the induction vector (*T*), or tipper, as both real and imaginary parts of *T*. Data error bars are shown for the inverted data.

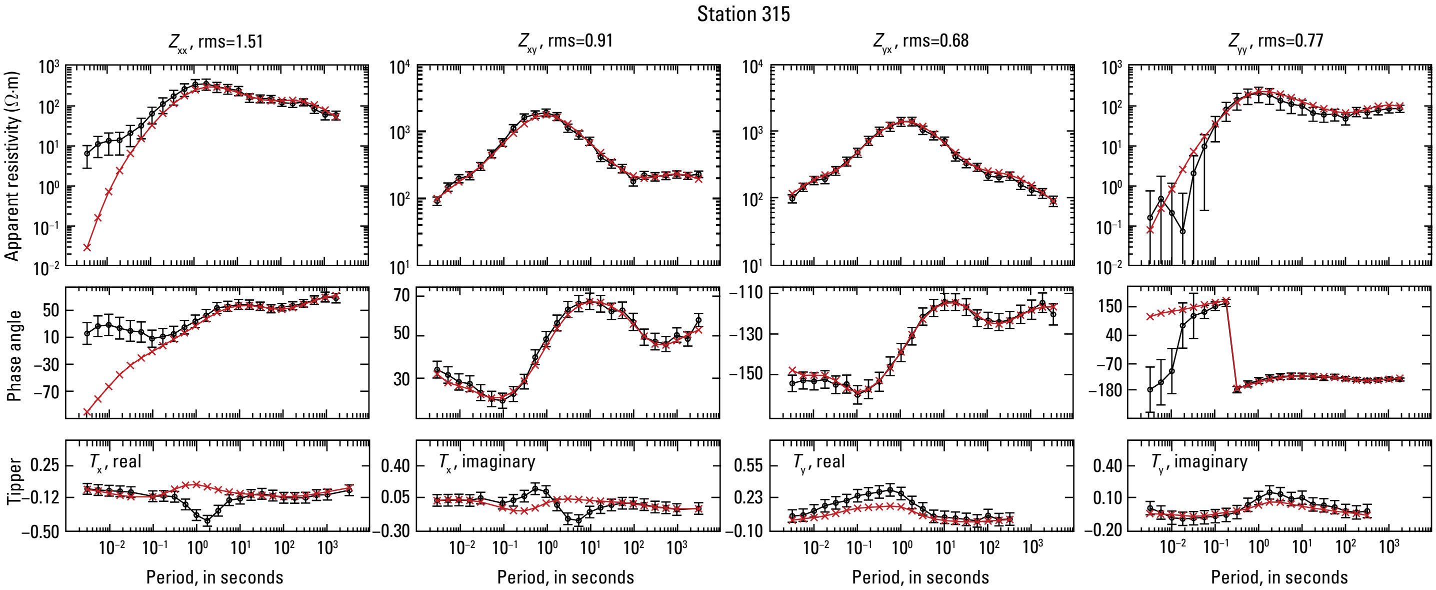

Figure 3.45. Station 315. Plots showing the data inverted (black) and the resistivity model response (red). Shown are all components of the impedance tensor (*Z*) as apparent resistivity (in Ohm meters, Ω·m) and phase angle (in degrees) and the induction vector (*T*), or tipper, as both real and imaginary parts of *T*. Data error bars are shown for the inverted data.

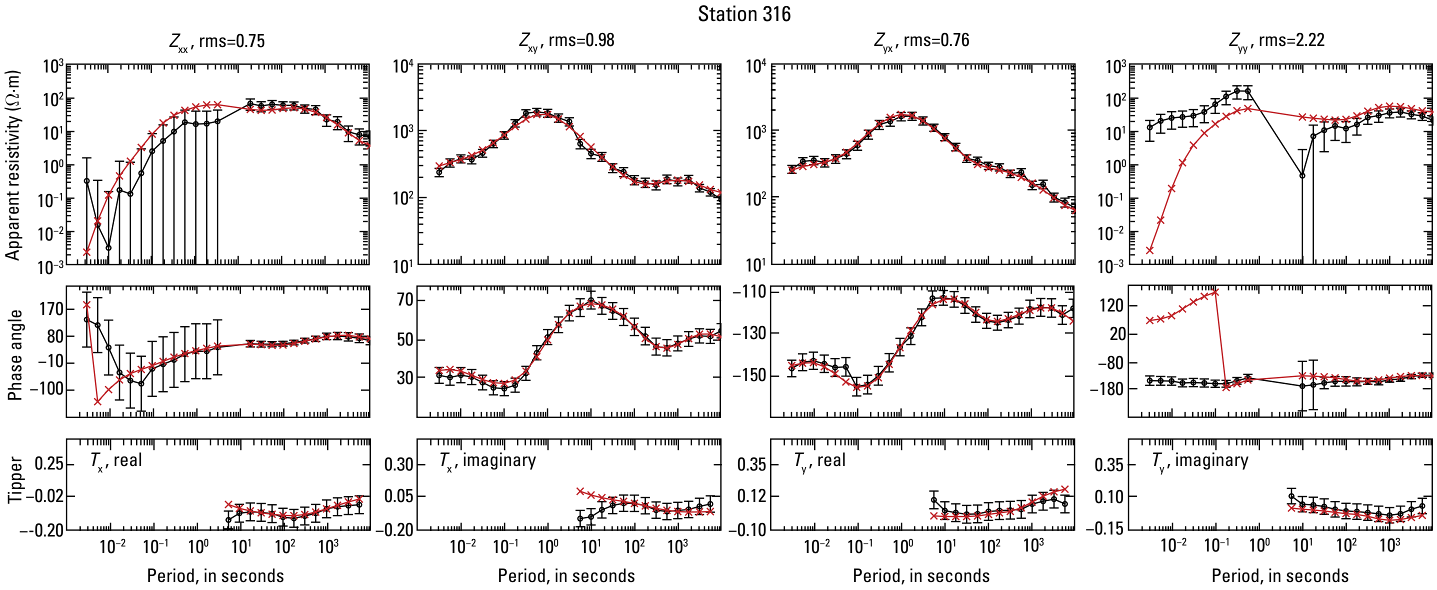

Figure 3.46. Station 316. Plots showing the data inverted (black) and the resistivity model response (red). Shown are all components of the impedance tensor (*Z*) as apparent resistivity (in Ohm meters, Ω·m) and phase angle (in degrees) and the induction vector (*T*), or tipper, as both real and imaginary parts of *T*. Data error bars are shown for the inverted data.

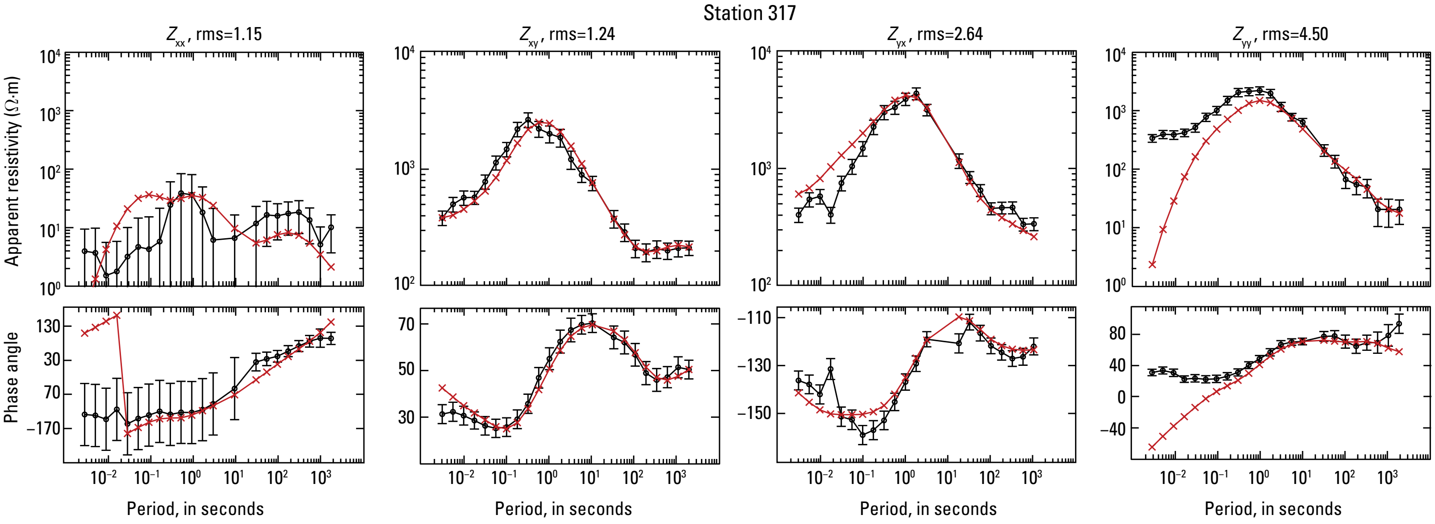

Figure 3.47. Station 317. Plots showing the data inverted (black) and the resistivity model response (red). Shown are all components of the impedance tensor (*Z*) as apparent resistivity (in Ohm meters, Ω·m) and phase angle (in degrees). Data error bars are shown for the inverted data.

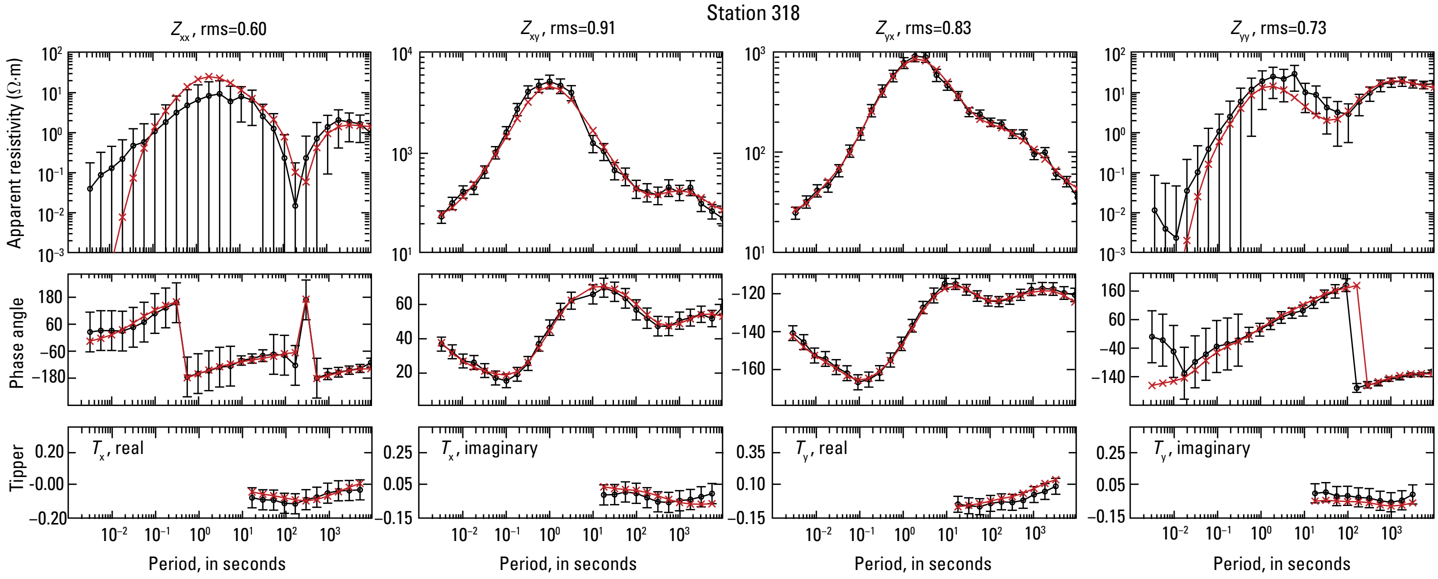

Figure 3.48. Station 318. Plots showing the data inverted (black) and the resistivity model response (red). Shown are all components of the impedance tensor (*Z*) as apparent resistivity (in Ohm meters, Ω·m) and phase angle (in degrees) and the induction vector (*T*), or tipper, as both real and imaginary parts of *T*. Data error bars are shown for the inverted data.

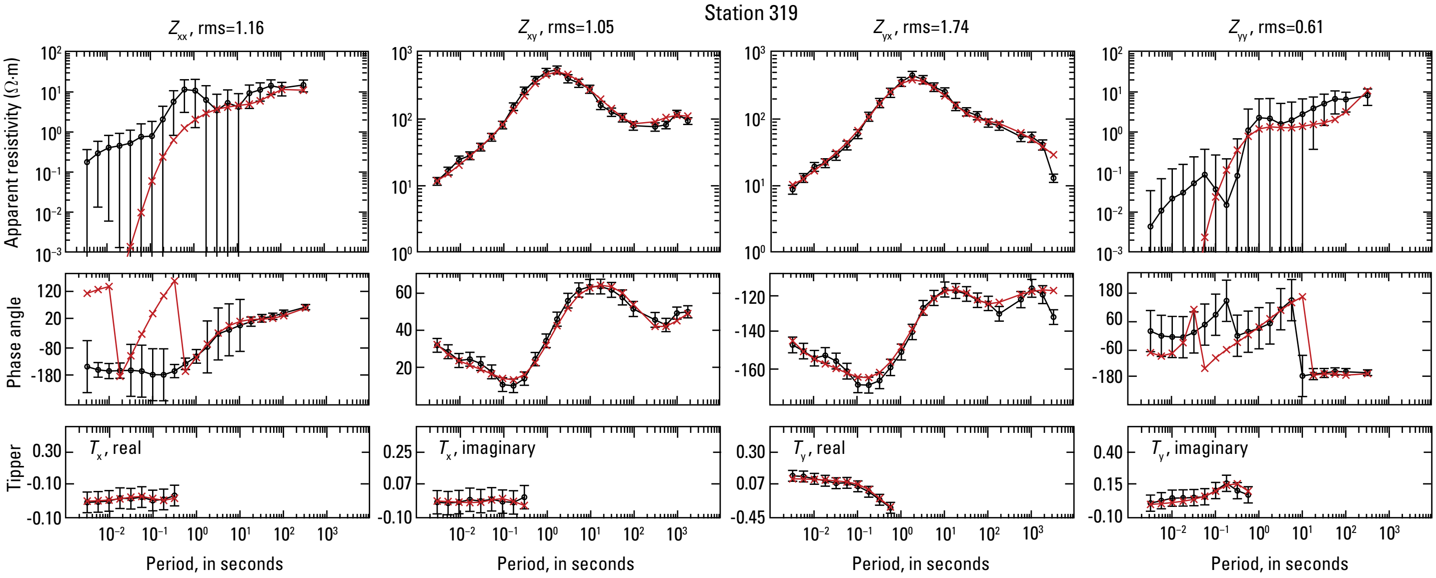

Figure 3.49. Station 319. Plots showing the data inverted (black) and the resistivity model response (red). Shown are all components of the impedance tensor (*Z*) as apparent resistivity (in Ohm meters, Ω·m) and phase angle (in degrees) and the induction vector (*T*), or tipper, as both real and imaginary parts of *T*. Data error bars are shown for the inverted data.

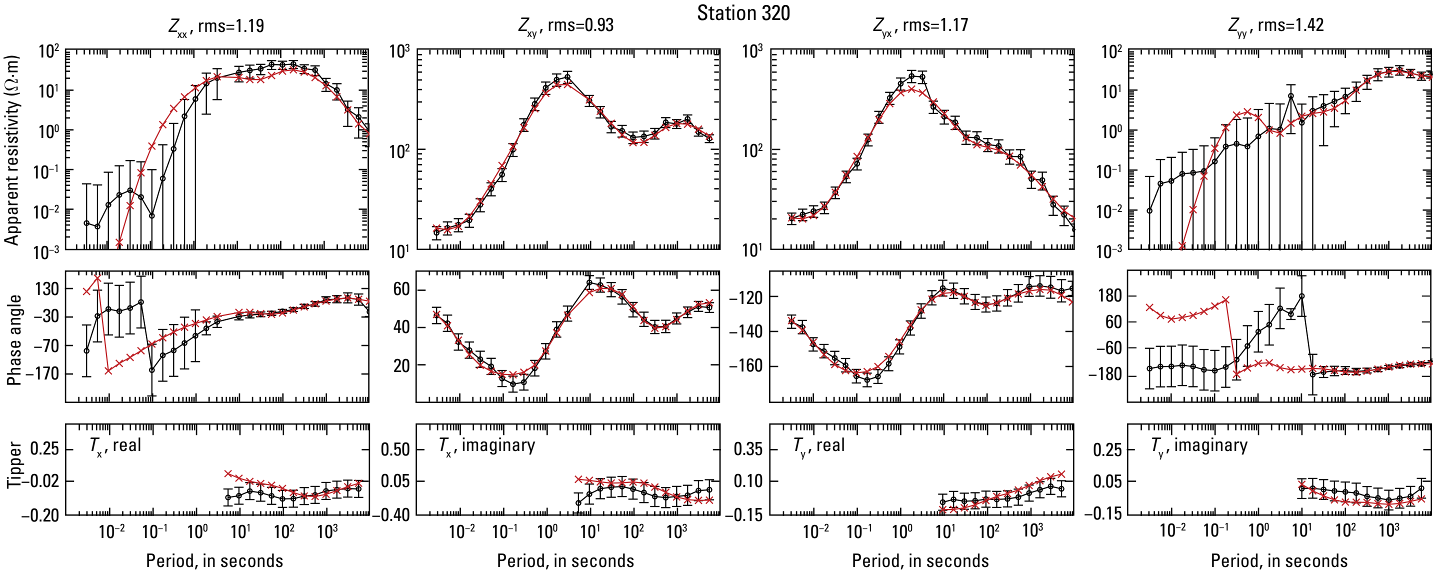

Figure 3.50. Station 320. Plots showing the data inverted (black) and the resistivity model response (red). Shown are all components of the impedance tensor (*Z*) as apparent resistivity (in Ohm meters, Ω·m) and phase angle (in degrees) and the induction vector (*T*), or tipper, as both real and imaginary parts of *T*. Data error bars are shown for the inverted data.

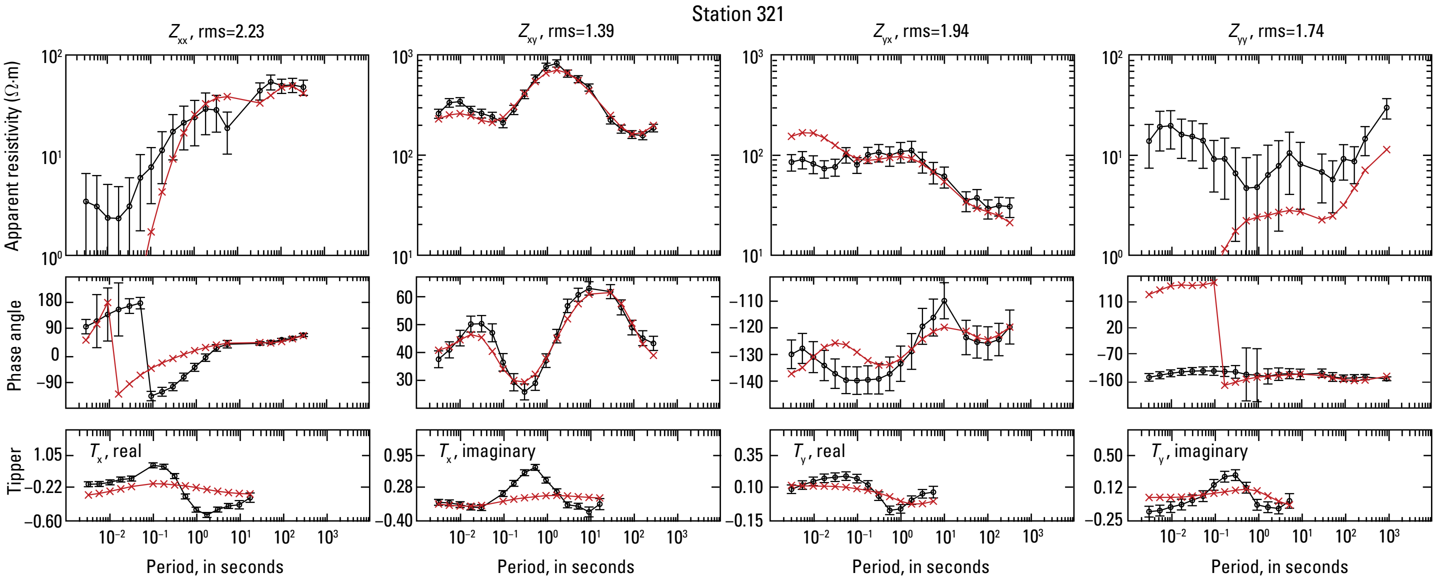

Figure 3.51. Station 321. Plots showing the data inverted (black) and the resistivity model response (red). Shown are all components of the impedance tensor (*Z*) as apparent resistivity (in Ohm meters, Ω·m) and phase angle (in degrees) and the induction vector (*T*), or tipper, as both real and imaginary parts of *T*. Data error bars are shown for the inverted data.

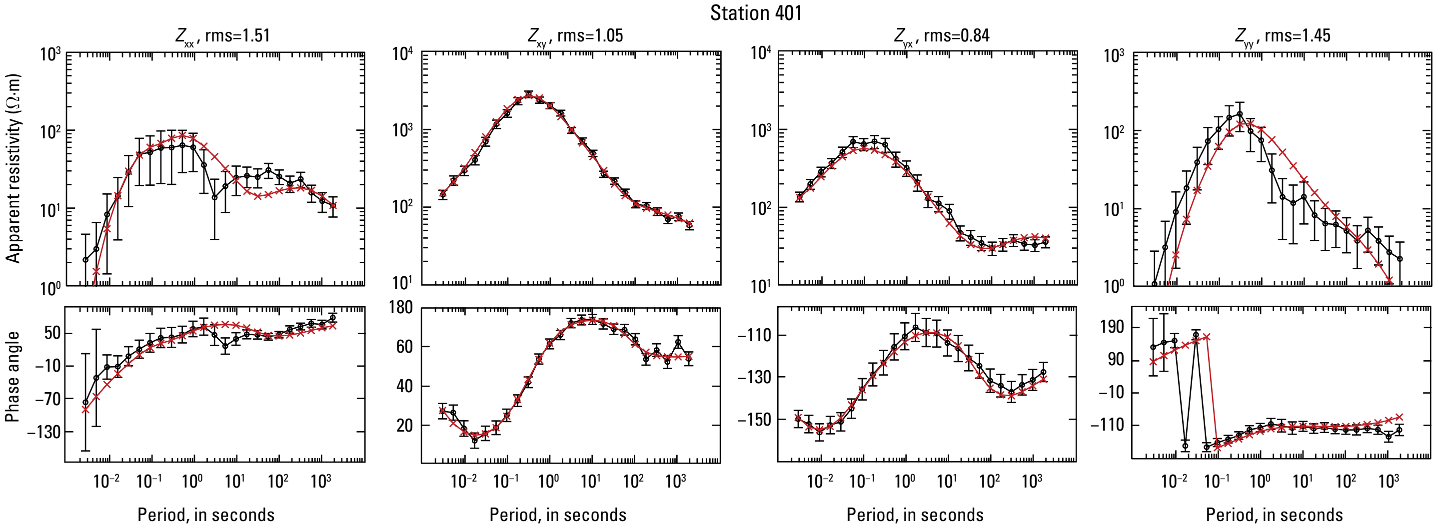

Figure 3.52. Station 401. Plots showing the data inverted (black) and the resistivity model response (red). Shown are all components of the impedance tensor (*Z*) as apparent resistivity (in Ohm meters, Ω·m) and phase angle (in degrees). Data error bars are shown for the inverted data.

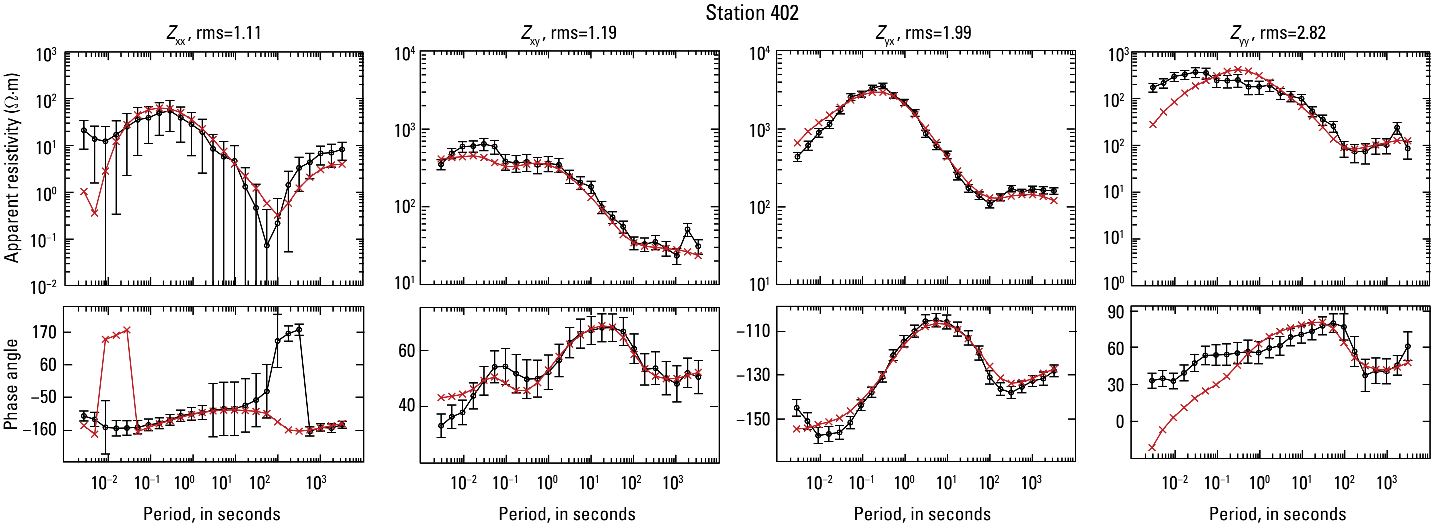

Figure 3.53. Station 402. Plots showing the data inverted (black) and the resistivity model response (red). Shown are all components of the impedance tensor (*Z*) as apparent resistivity (in Ohm meters, Ω·m) and phase angle (in degrees). Data error bars are shown for the inverted data.

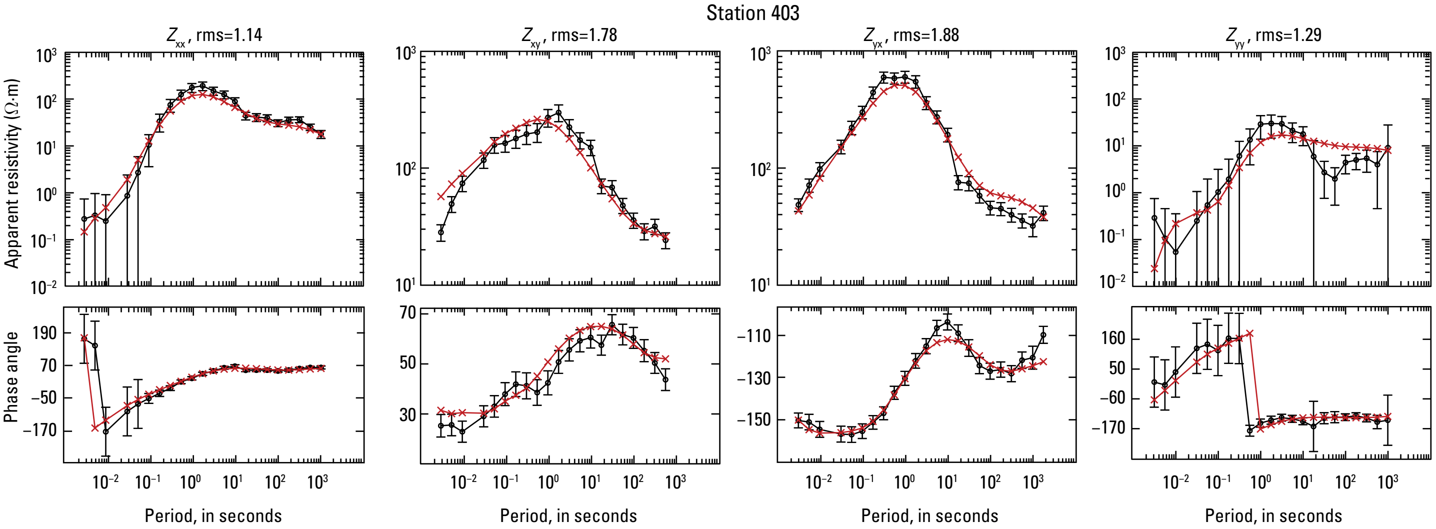

Figure 3.54. Station 403. Plots showing the data inverted (black) and the resistivity model response (red). Shown are all components of the impedance tensor (*Z*) as apparent resistivity (in Ohm meters, Ω·m) and phase angle (in degrees). Data error bars are shown for the inverted data.

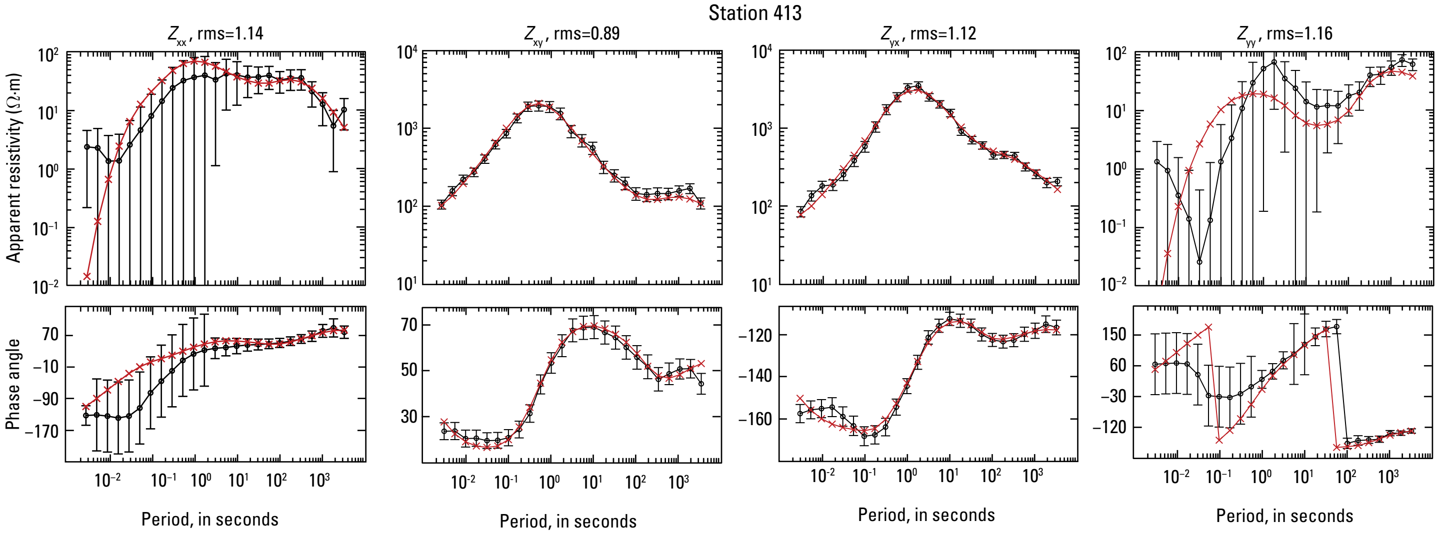

Figure 3.55. Station 413. Plots showing the data inverted (black) and the resistivity model response (red). Shown are all components of the impedance tensor (*Z*) as apparent resistivity (in Ohm meters, Ω·m) and phase angle (in degrees). Data error bars are shown for the inverted data.

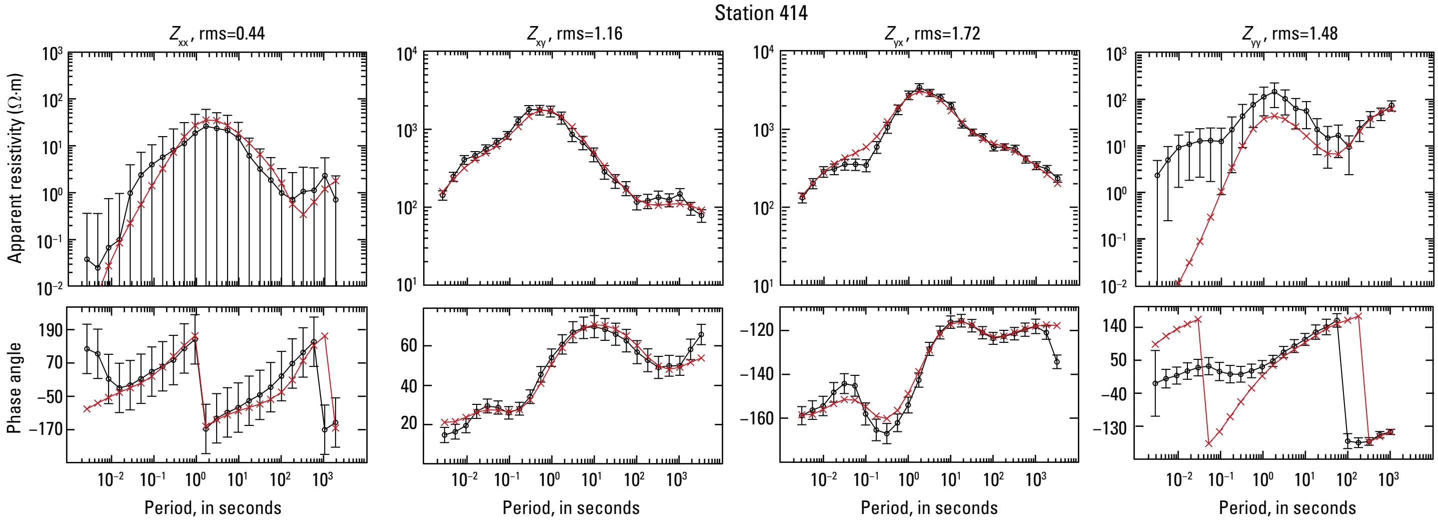

Figure 3.56. Station 414. Plots showing the data inverted (black) and the resistivity model response (red). Shown are all components of the impedance tensor (*Z*) as apparent resistivity (in Ohm meters, Ω·m) and phase angle (in degrees). Data error bars are shown for the inverted data.

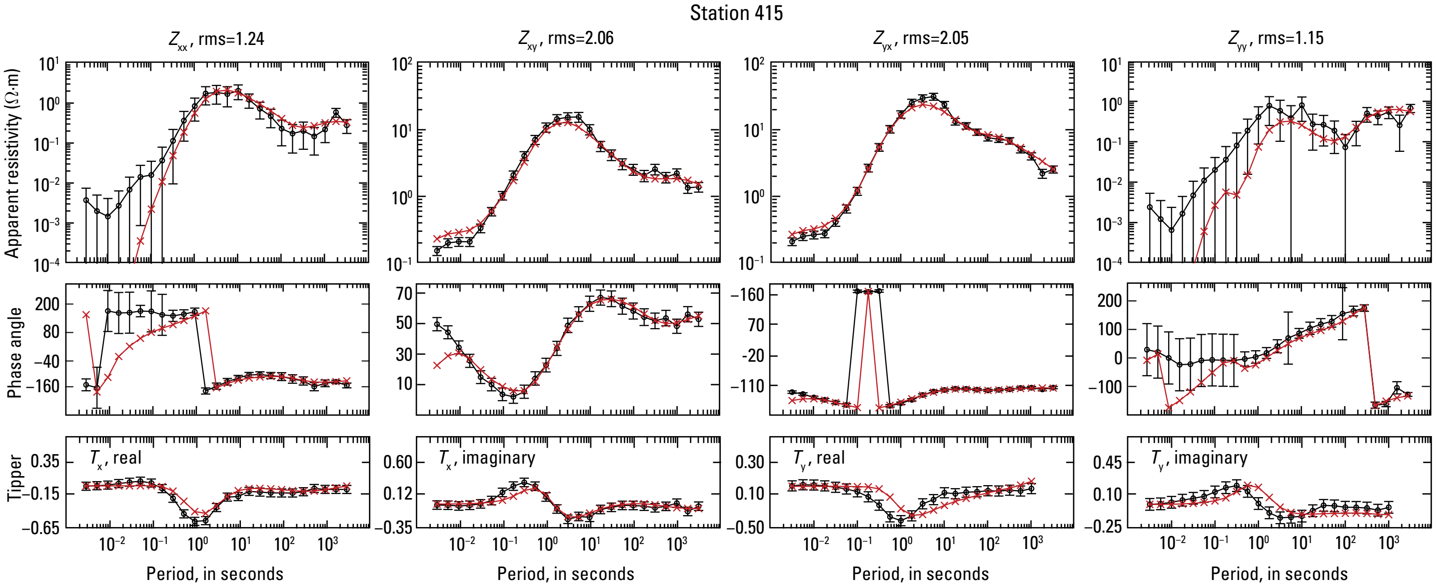

Figure 3.57. Station 415. Plots showing the data inverted (black) and the resistivity model response (red). Shown are all components of the impedance tensor (*Z*) as apparent resistivity (in Ohm meters, Ω·m) and phase angle (in degrees) and the induction vector (*T*), or tipper, as both real and imaginary parts of *T*. Data error bars are shown for the inverted data.

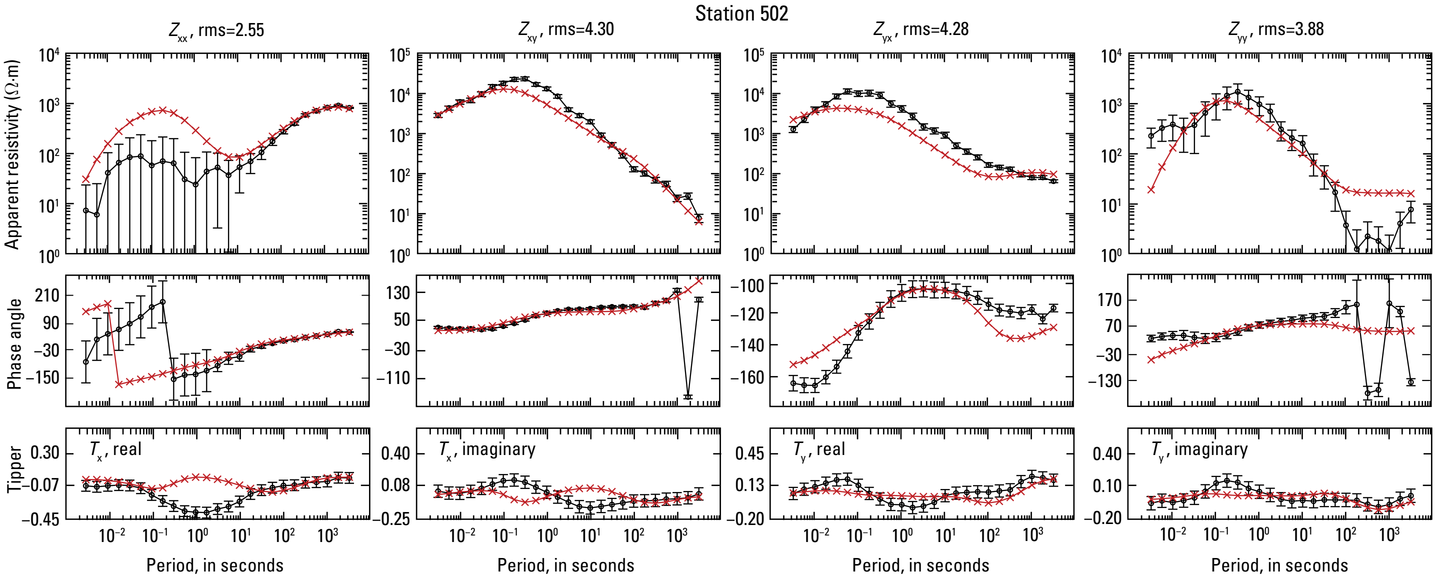

Figure 3.58. Station 502. Plots showing the data inverted (black) and the resistivity model response (red). Shown are all components of the impedance tensor (*Z*) as apparent resistivity (in Ohm meters, Ω·m) and phase angle (in degrees) and the induction vector (*T*), or tipper, as both real and imaginary parts of *T*. Data error bars are shown for the inverted data.

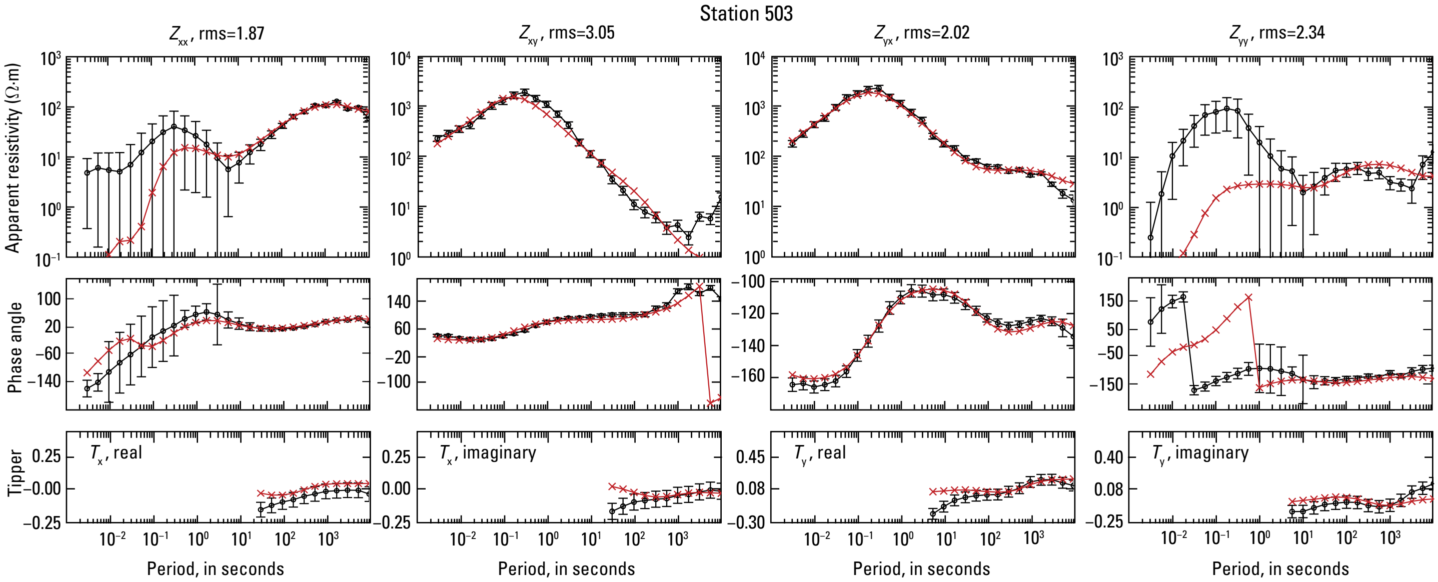

Figure 3.59. Station 503. Plots showing the data inverted (black) and the resistivity model response (red). Shown are all components of the impedance tensor (*Z*) as apparent resistivity (in Ohm meters, Ω·m) and phase angle (in degrees) and the induction vector (*T*), or tipper, as both real and imaginary parts of *T*. Data error bars are shown for the inverted data.

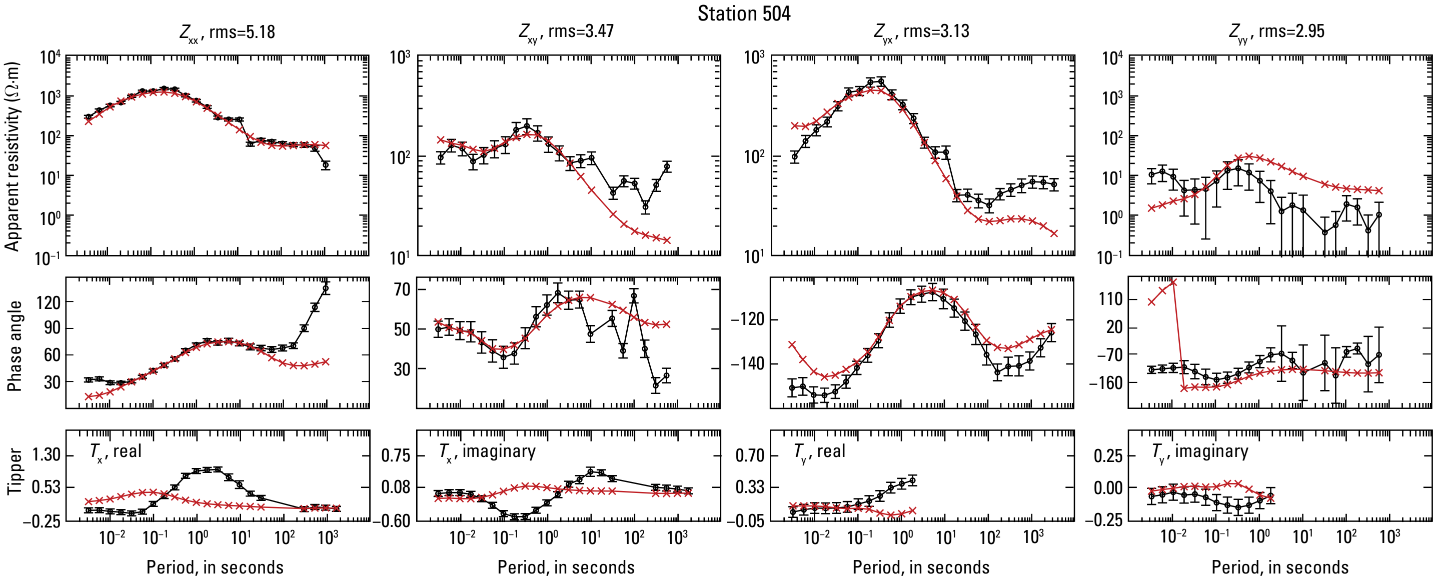

Figure 3.60. Station 504. Plots showing the data inverted (black) and the resistivity model response (red). Shown are all components of the impedance tensor (*Z*) as apparent resistivity (in Ohm meters, Ω·m) and phase angle (in degrees) and the induction vector (*T*), or tipper, as both real and imaginary parts of *T*. Data error bars are shown for the inverted data.

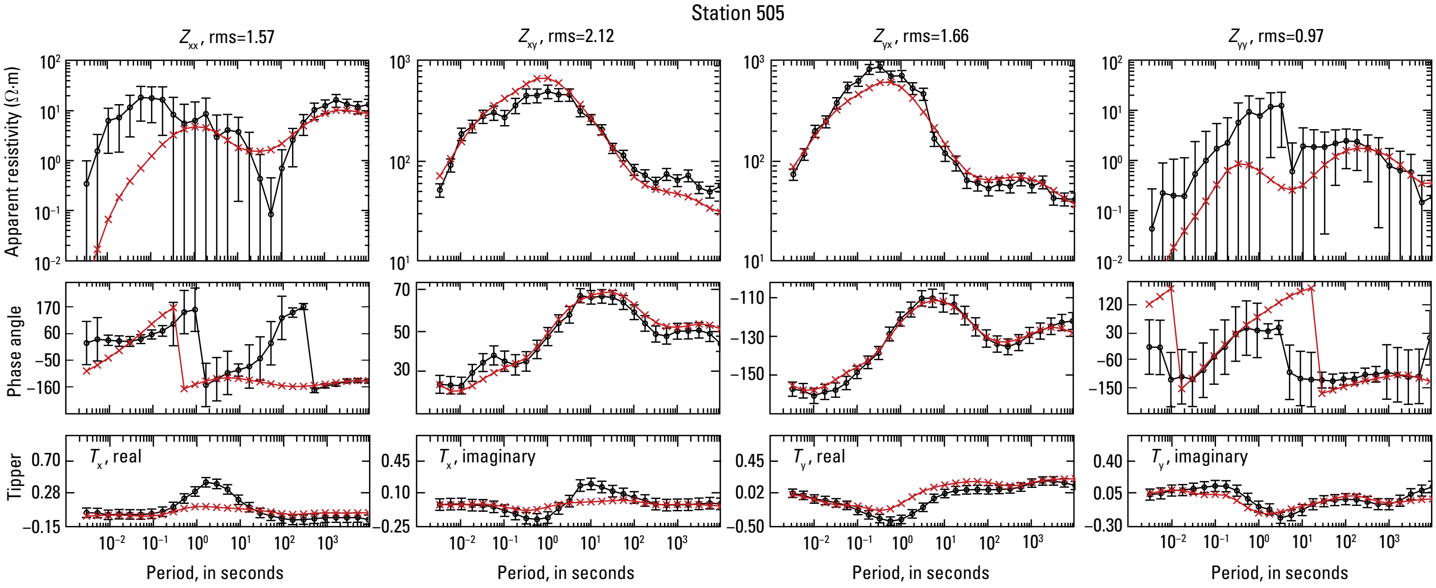

Figure 3.61. Station 505. Plots showing the data inverted (black) and the resistivity model response (red). Shown are all components of the impedance tensor (*Z*) as apparent resistivity (in Ohm meters, Ω·m) and phase angle (in degrees) and the induction vector (*T*), or tipper, as both real and imaginary parts of *T*. Data error bars are shown for the inverted data.

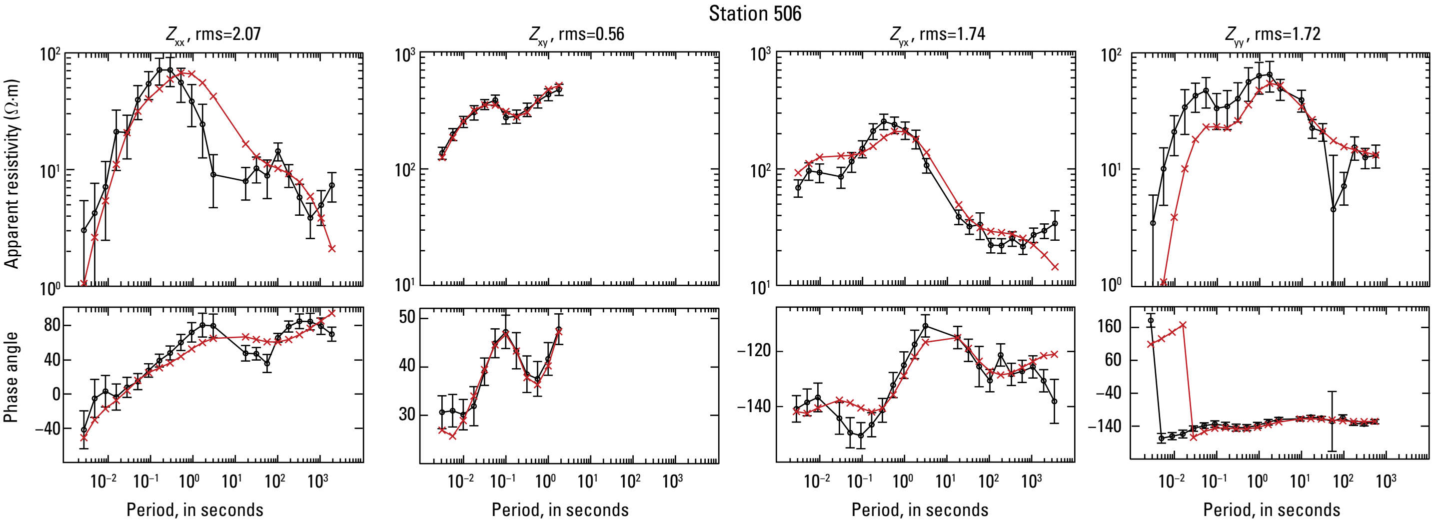

Figure 3.62. Station 506. Plots showing the data inverted (black) and the resistivity model response (red). Shown are all components of the impedance tensor (*Z*) as apparent resistivity (in Ohm meters, Ω·m) and phase angle (in degrees). Data error bars are shown for the inverted data.

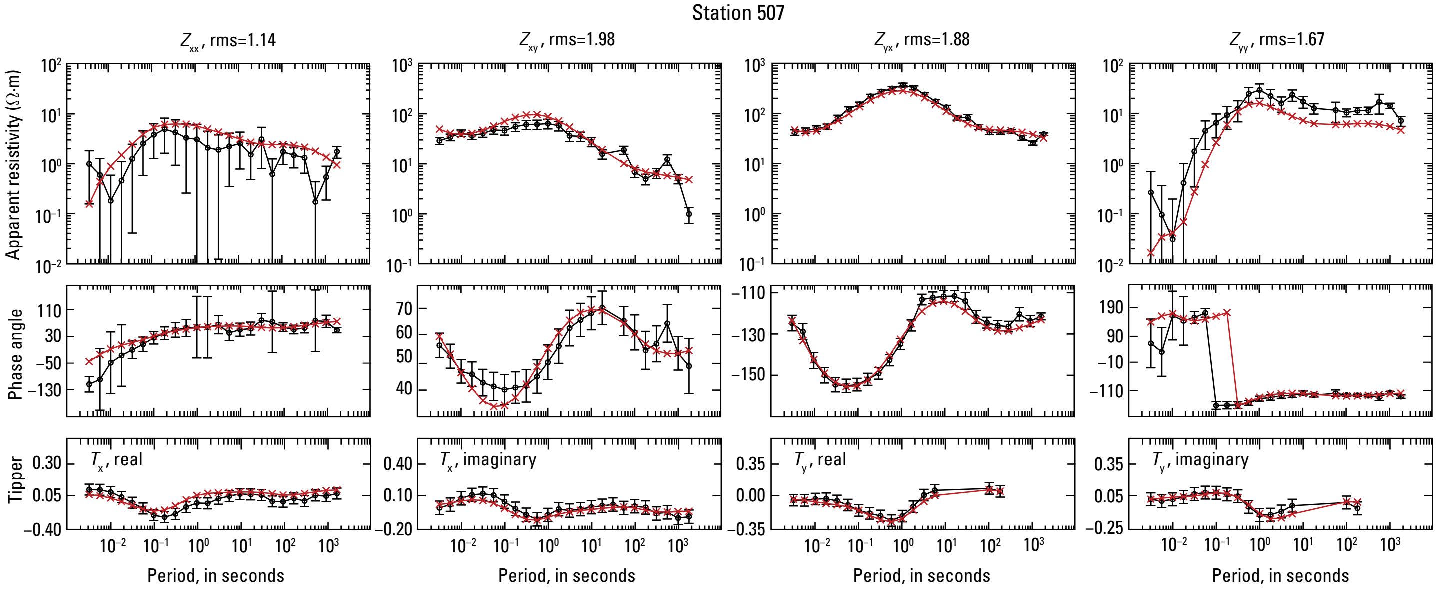

Figure 3.63. Station 507. Plots showing the data inverted (black) and the resistivity model response (red). Shown are all components of the impedance tensor (*Z*) as apparent resistivity (in Ohm meters, Ω·m) and phase angle (in degrees) and the induction vector (*T*), or tipper, as both real and imaginary parts of *T*. Data error bars are shown for the inverted data.

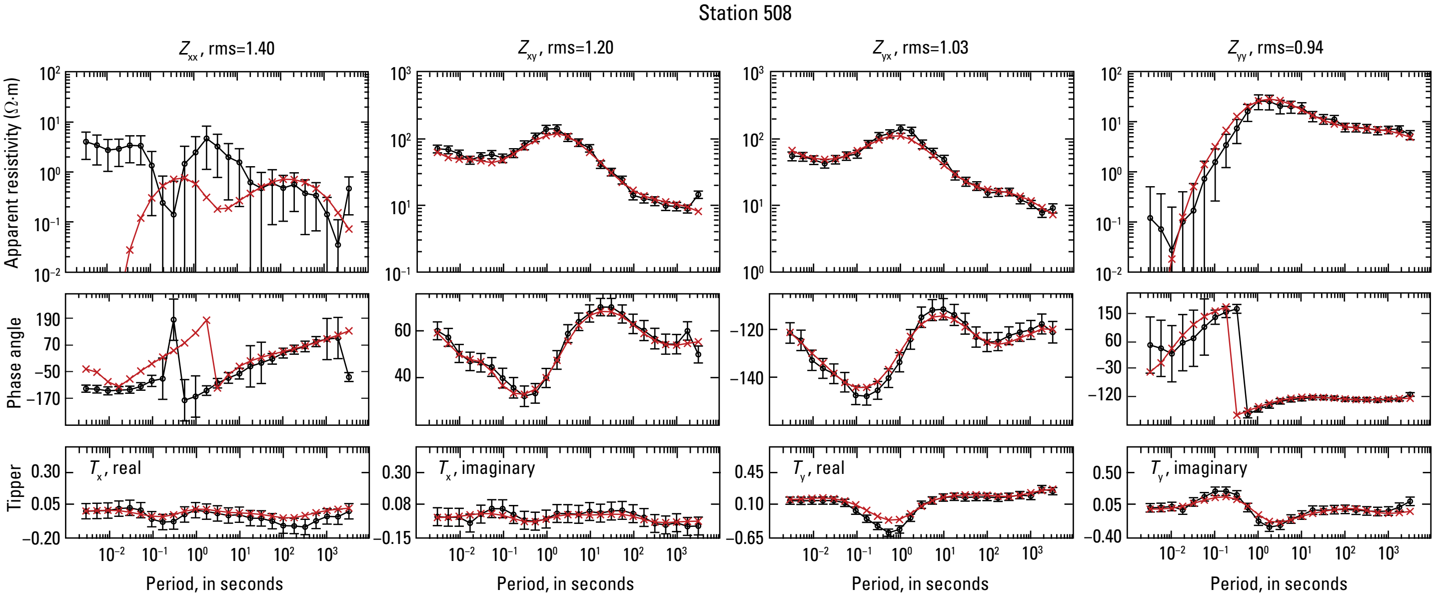

Figure 3.64. Station 508. Plots showing the data inverted (black) and the resistivity model response (red). Shown are all components of the impedance tensor (*Z*) as apparent resistivity (in Ohm meters, Ω·m) and phase angle (in degrees) and the induction vector (*T*), or tipper, as both real and imaginary parts of *T*. Data error bars are shown for the inverted data.

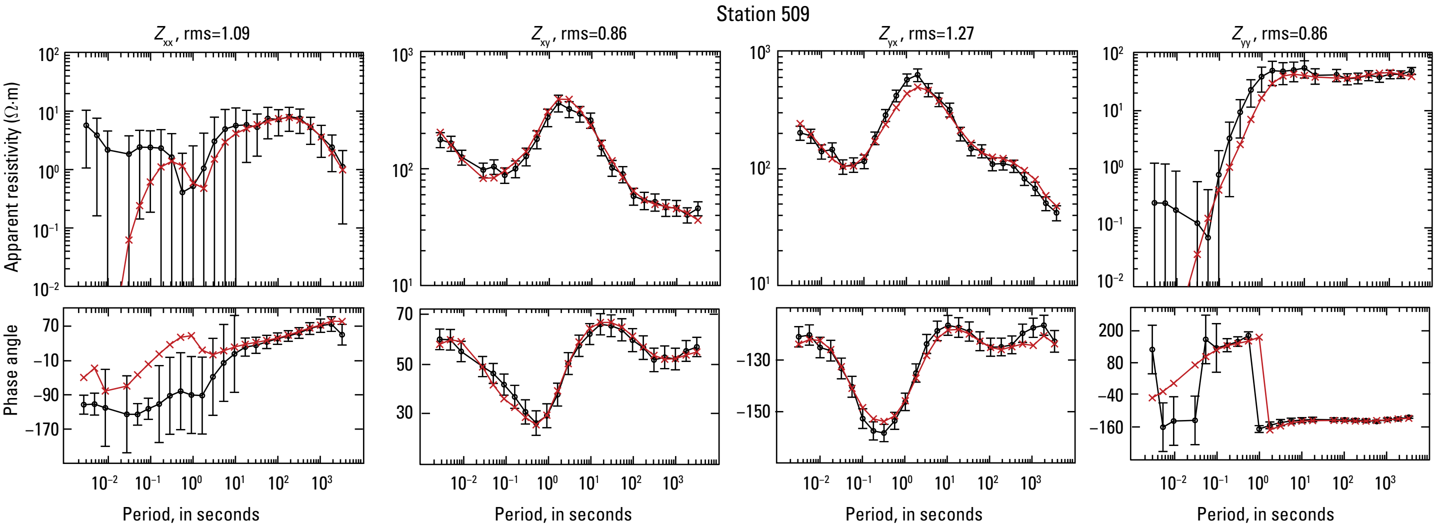

Figure 3.65. Station 509. Plots showing the data inverted (black) and the resistivity model response (red). Shown are all components of the impedance tensor (*Z*) as apparent resistivity (in Ohm meters, Ω·m) and phase angle (in degrees). Data error bars are shown for the inverted data.

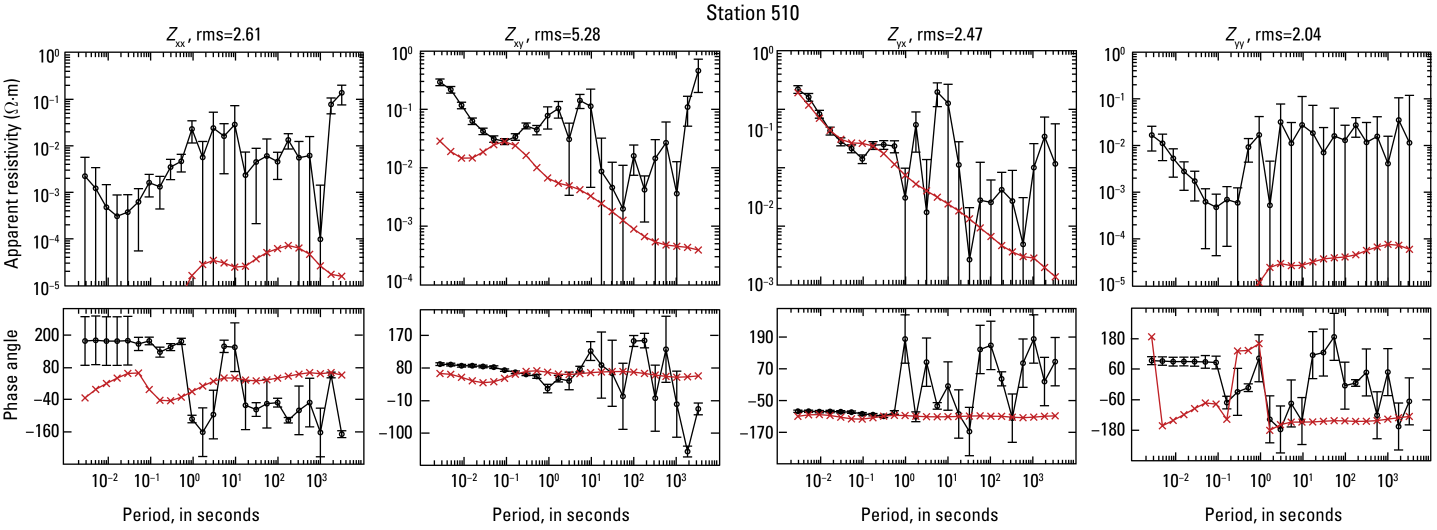

Figure 3.66. Station 510. Plots showing the data inverted (black) and the resistivity model response (red). Shown are all components of the impedance tensor (*Z*) as apparent resistivity (in Ohm meters, Ω·m) and phase angle (in degrees). Data error bars are shown for the inverted data.

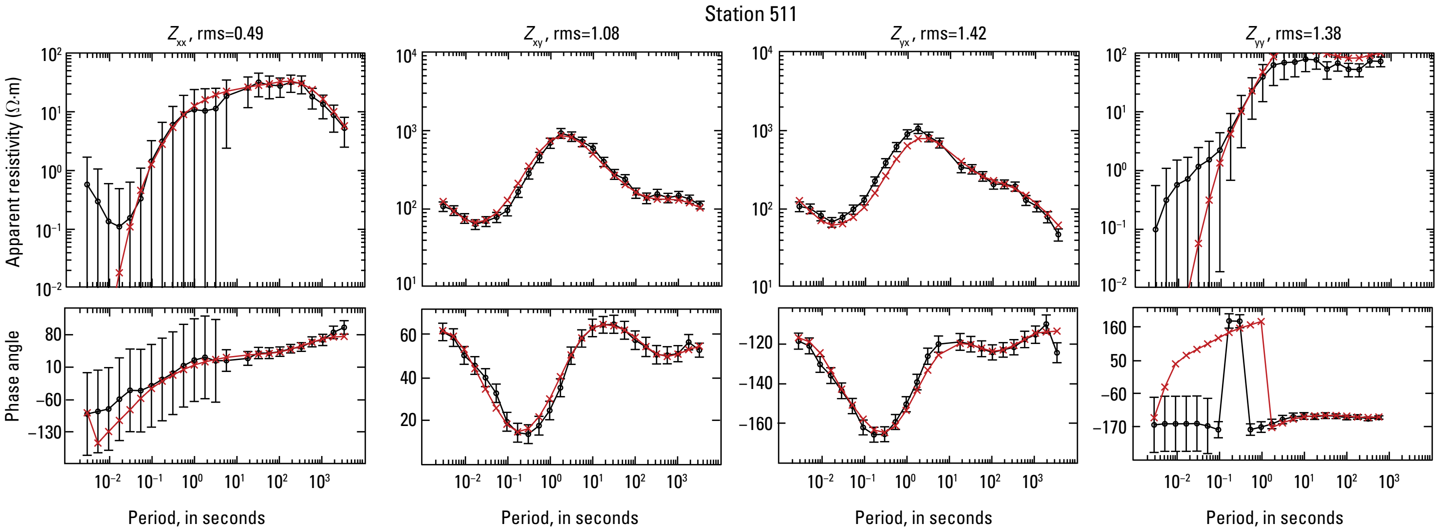

Figure 3.67. Station 511. Plots showing the data inverted (black) and the resistivity model response (red). Shown are all components of the impedance tensor (*Z*) as apparent resistivity (in Ohm meters, Ω·m) and phase angle (in degrees). Data error bars are shown for the inverted data.

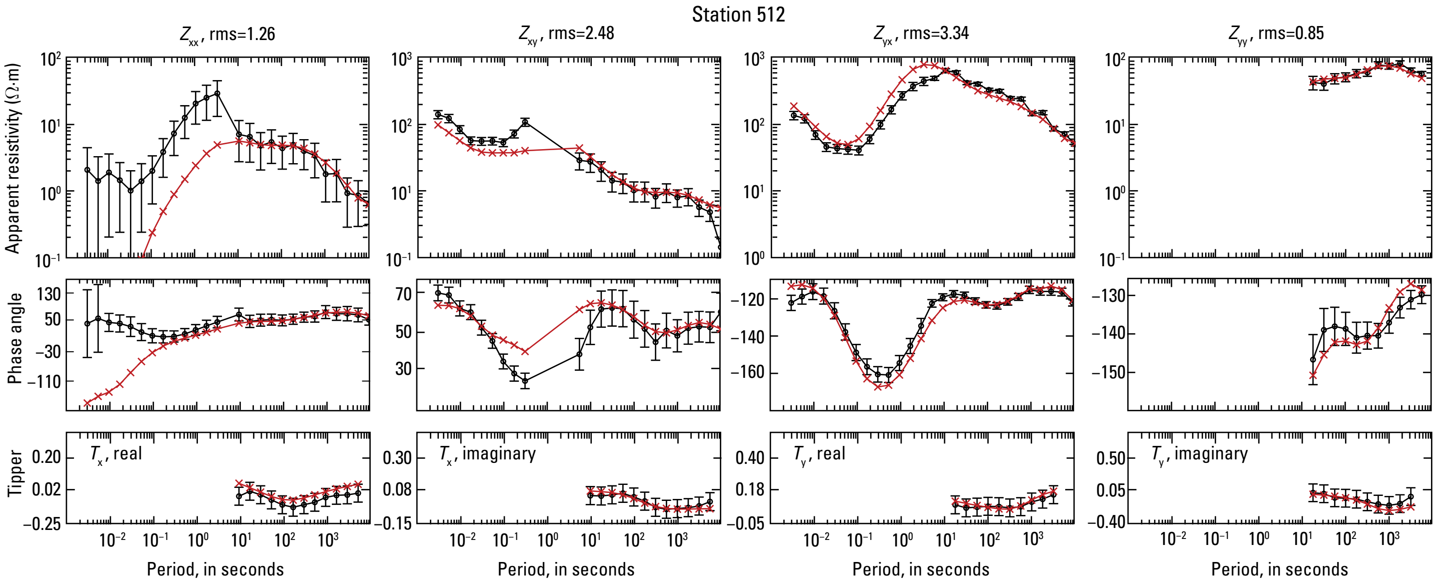

Figure 3.68. Station 512. Plots showing the data inverted (black) and the resistivity model response (red). Shown are all components of the impedance tensor (*Z*) as apparent resistivity (in Ohm meters, Ω·m) and phase angle (in degrees) and the induction vector (*T*), or tipper, as both real and imaginary parts of *T*. Data error bars are shown for the inverted data.

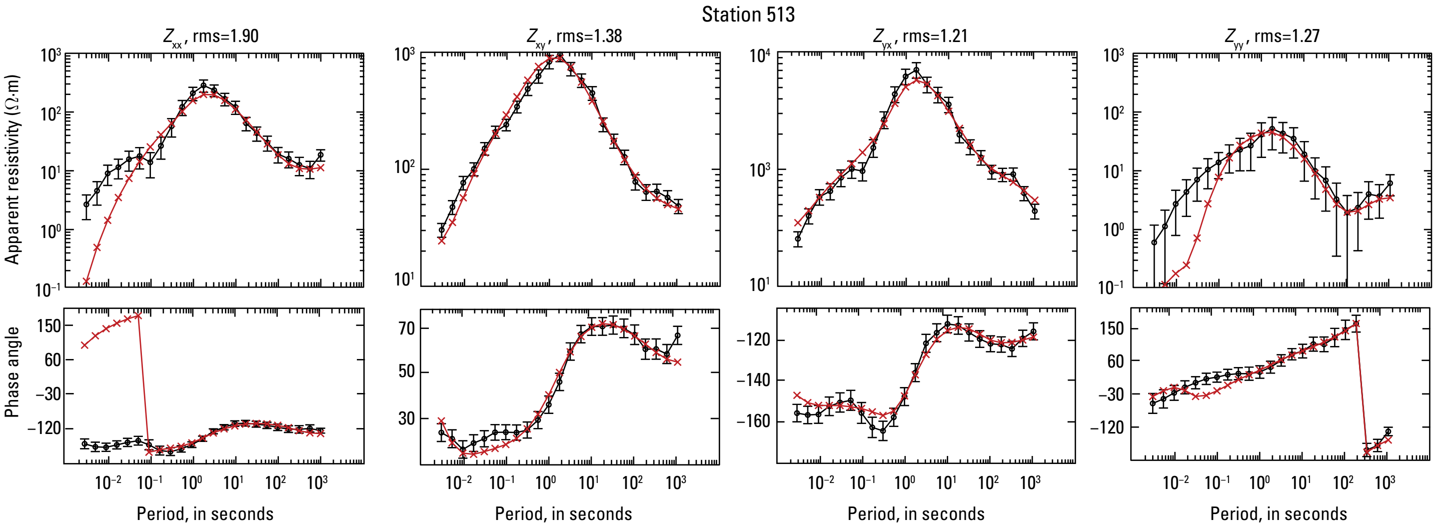

Figure 3.69. Station 513. Plots showing the data inverted (black) and the resistivity model response (red). Shown are all components of the impedance tensor (*Z*) as apparent resistivity (in Ohm meters, Ω·m) and phase angle (in degrees). Data error bars are shown for the inverted data.

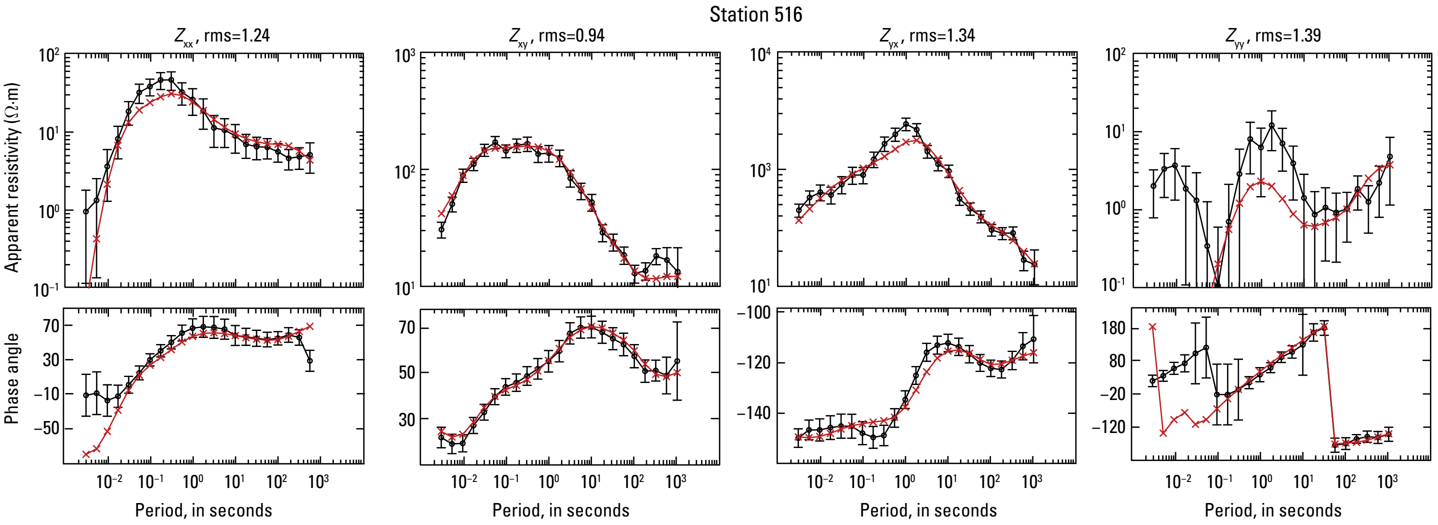

Figure 3.70. Station 516. Plots showing the data inverted (black) and the resistivity model response (red). Shown are all components of the impedance tensor (*Z*) as apparent resistivity (in Ohm meters, Ω·m) and phase angle (in degrees). Data error bars are shown for the inverted data.

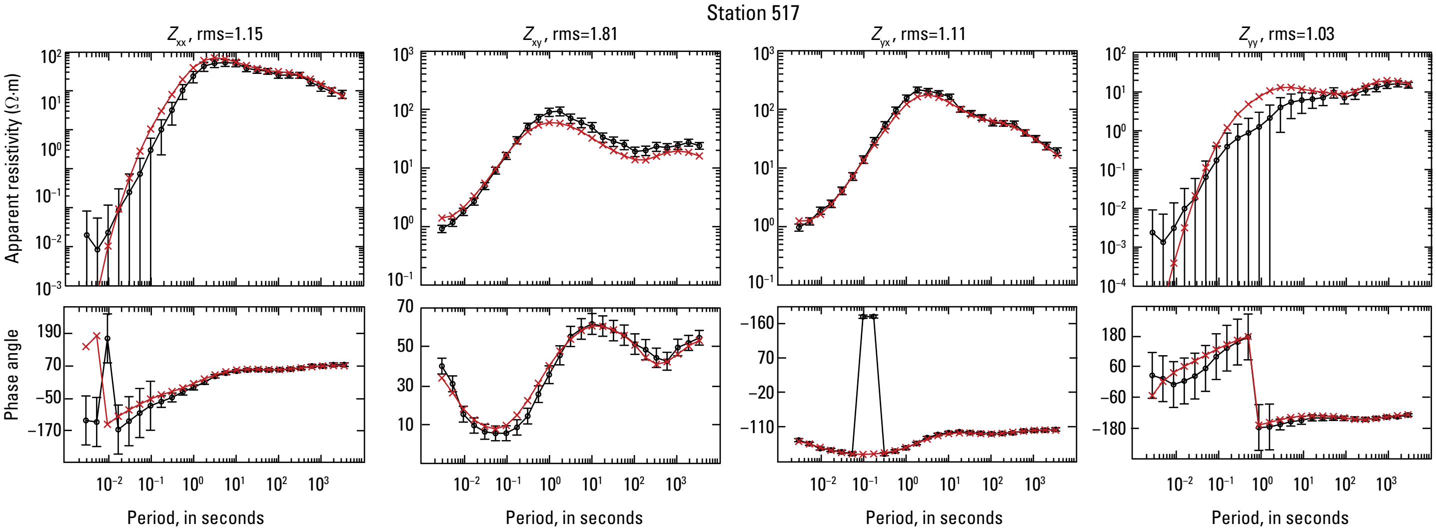

Figure 3.71. Station 517. Plots showing the data inverted (black) and the resistivity model response (red). Shown are all components of the impedance tensor (*Z*) as apparent resistivity (in Ohm meters, Ω·m) and phase angle (in degrees). Data error bars are shown for the inverted data.

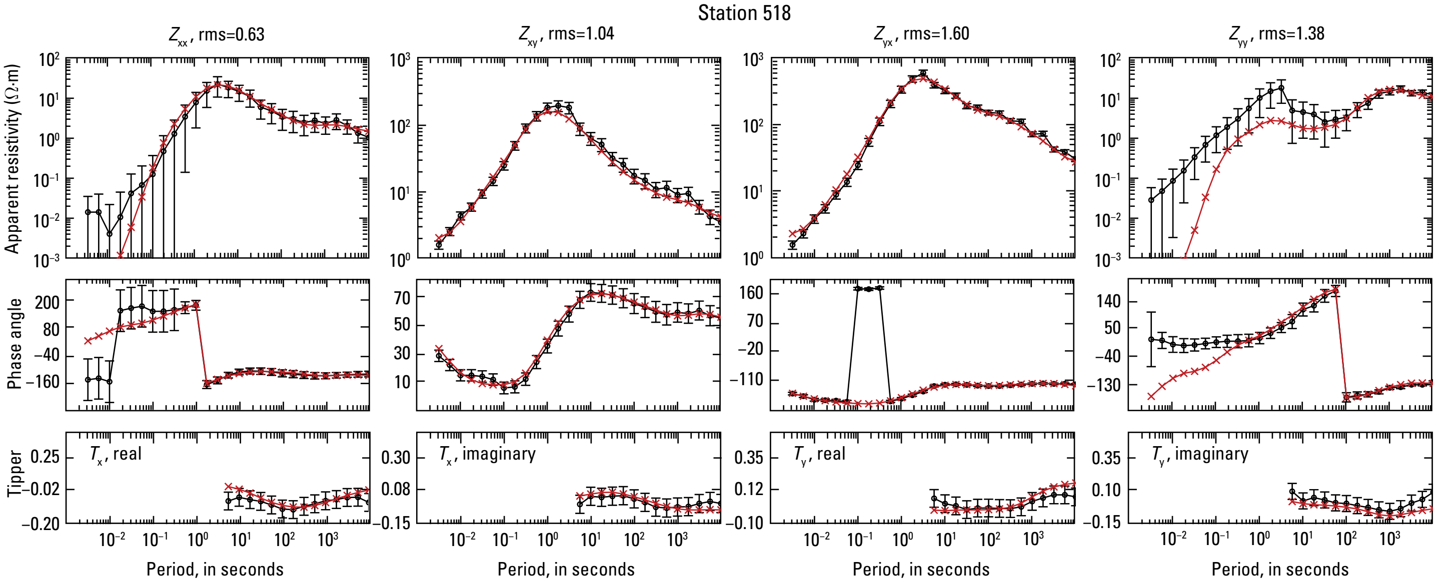

Figure 3.72. Station 518. Plots showing the data inverted (black) and the resistivity model response (red). Shown are all components of the impedance tensor (*Z*) as apparent resistivity (in Ohm meters, Ω·m) and phase angle (in degrees) and the induction vector (*T*), or tipper, as both real and imaginary parts of *T*. Data error bars are shown for the inverted data.

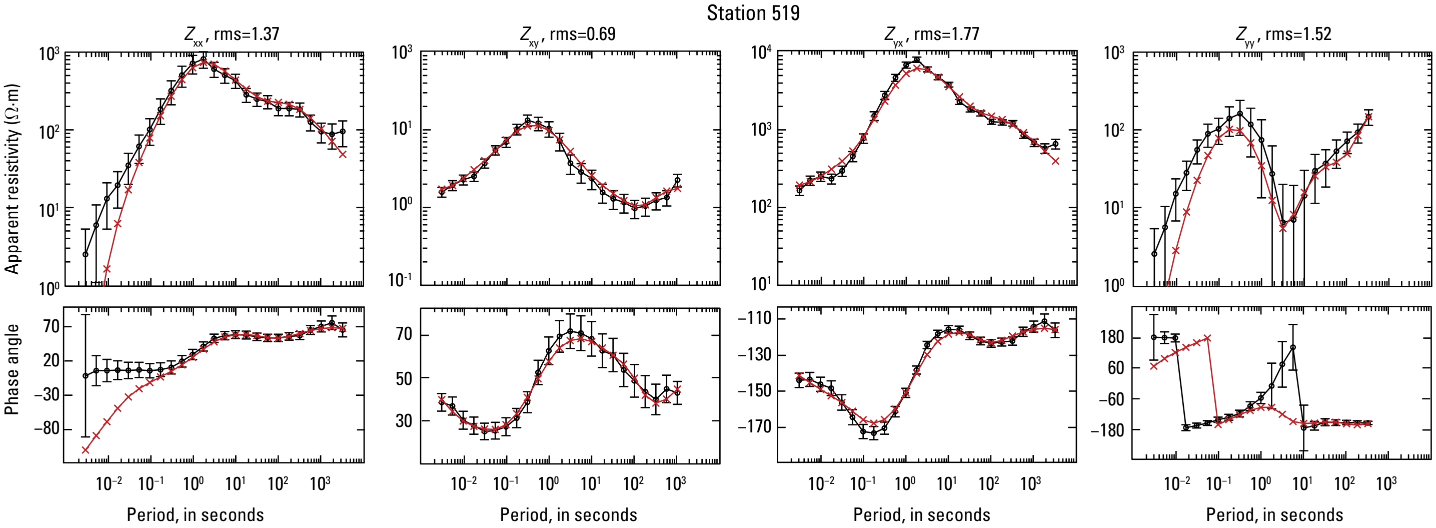

Figure 3.73. Station 519. Plots showing the data inverted (black) and the resistivity model response (red). Shown are all components of the impedance tensor (*Z*) as apparent resistivity (in Ohm meters, Ω·m) and phase angle (in degrees). Data error bars are shown for the inverted data.

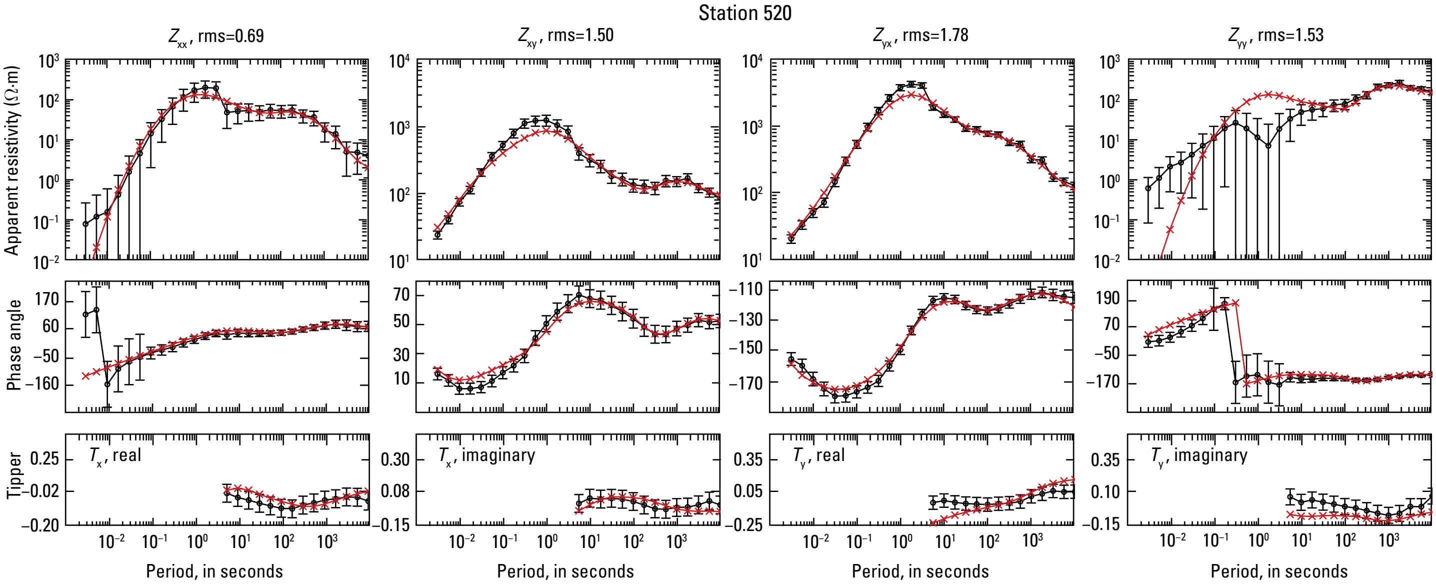

Figure 3.74. Station 520. Plots showing the data inverted (black) and the resistivity model response (red). Shown are all components of the impedance tensor (*Z*) as apparent resistivity (in Ohm meters, Ω·m) and phase angle (in degrees) and the induction vector (*T*), or tipper, as both real and imaginary parts of *T*. Data error bars are shown for the inverted data.

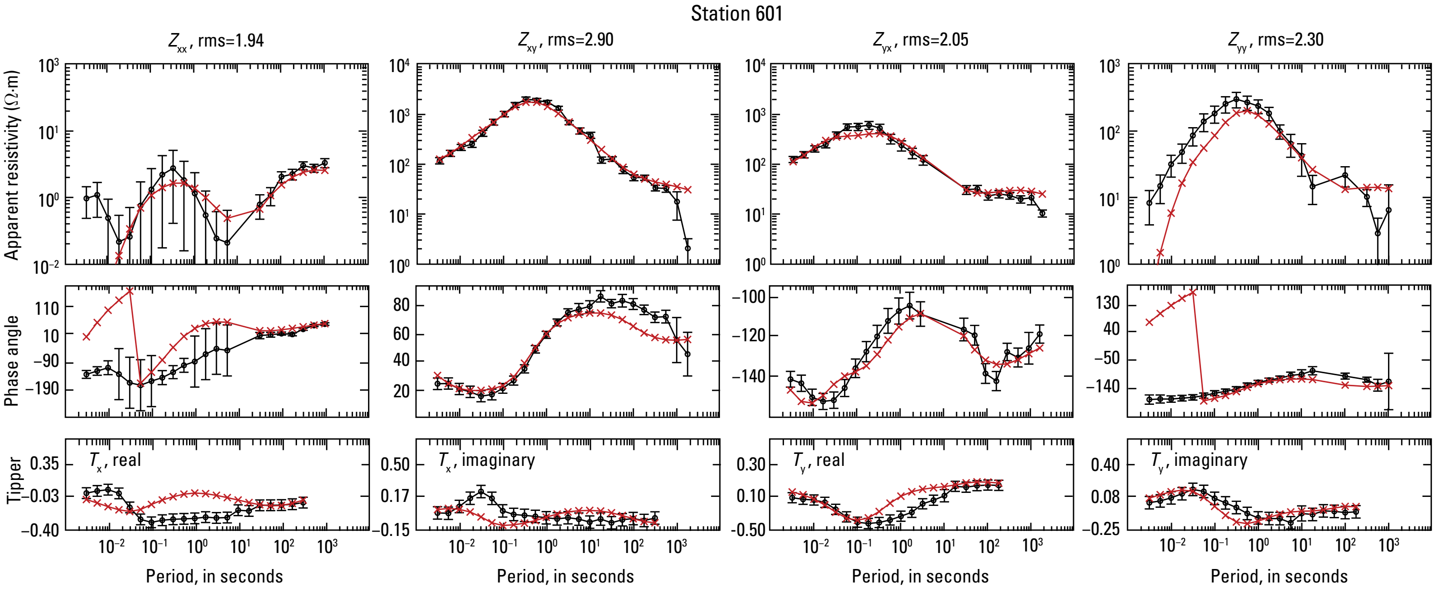

Figure 3.75. Station 601. Plots showing the data inverted (black) and the resistivity model response (red). Shown are all components of the impedance tensor (*Z*) as apparent resistivity (in Ohm meters, Ω·m) and phase angle (in degrees) and the induction vector (*T*), or tipper, as both real and imaginary parts of *T*. Data error bars are shown for the inverted data.

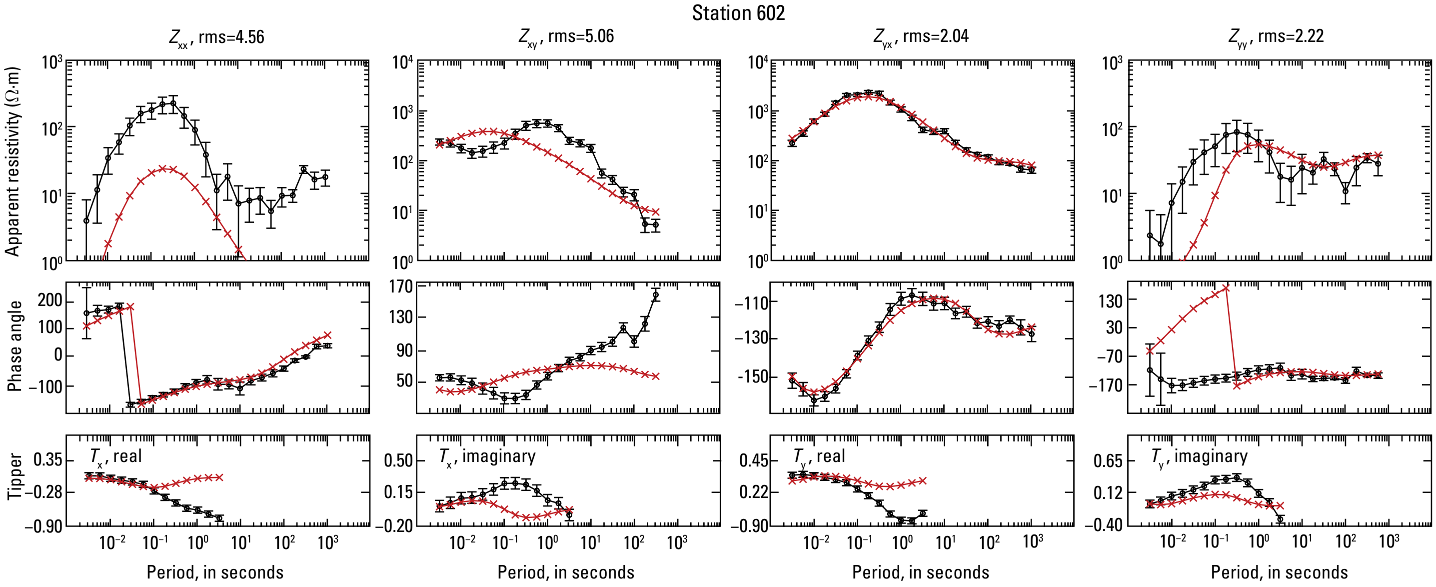

Figure 3.76. Station 602. Plots showing the data inverted (black) and the resistivity model response (red). Shown are all components of the impedance tensor (*Z*) as apparent resistivity (in Ohm meters, Ω·m) and phase angle (in degrees) and the induction vector (*T*), or tipper, as both real and imaginary parts of *T*. Data error bars are shown for the inverted data.

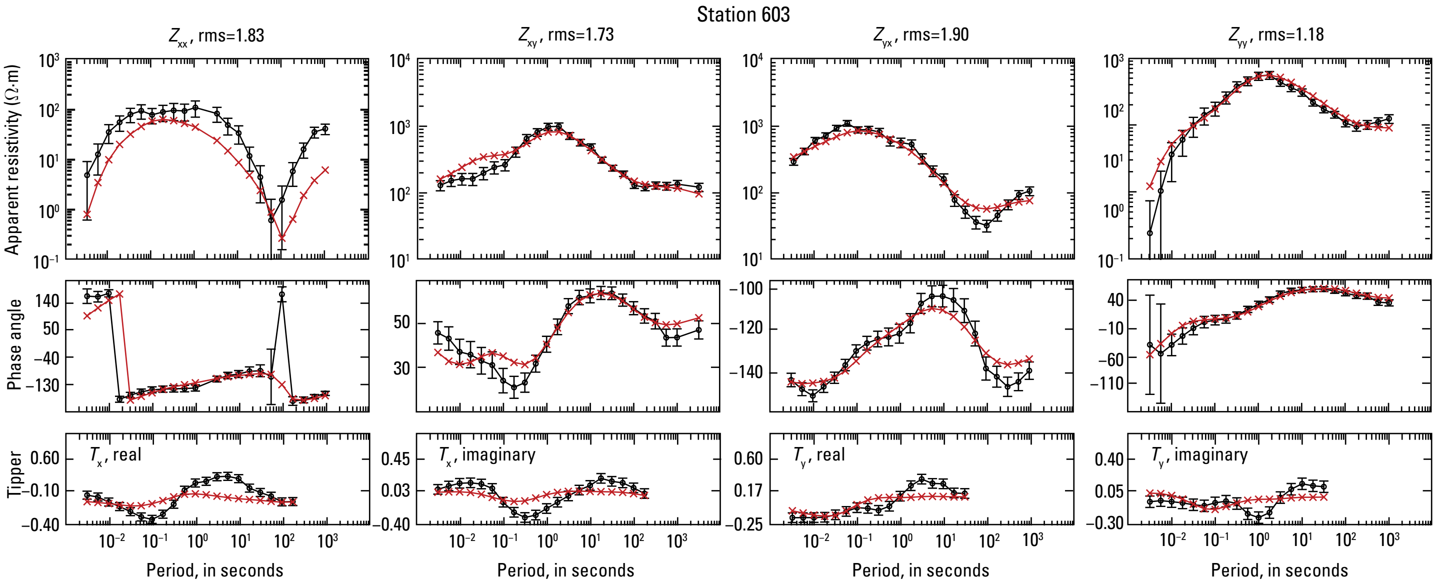

Figure 3.77. Station 603. Plots showing the data inverted (black) and the resistivity model response (red). Shown are all components of the impedance tensor (*Z*) as apparent resistivity (in Ohm meters, Ω·m) and phase angle (in degrees) and the induction vector (*T*), or tipper, as both real and imaginary parts of *T*. Data error bars are shown for the inverted data.

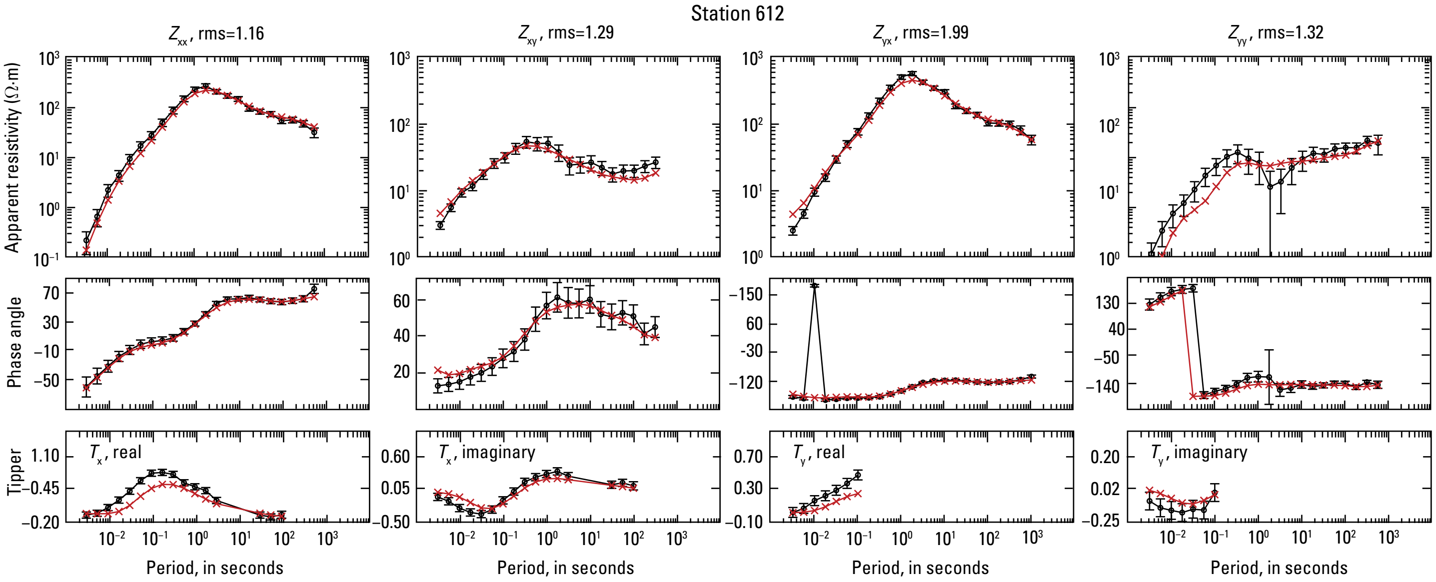

Figure 3.78. Station 612. Plots showing the data inverted (black) and the resistivity model response (red). Shown are all components of the impedance tensor (*Z*) as apparent resistivity (in Ohm meters, Ω·m) and phase angle (in degrees) and the induction vector (*T*), or tipper, as both real and imaginary parts of *T*. Data error bars are shown for the inverted data.

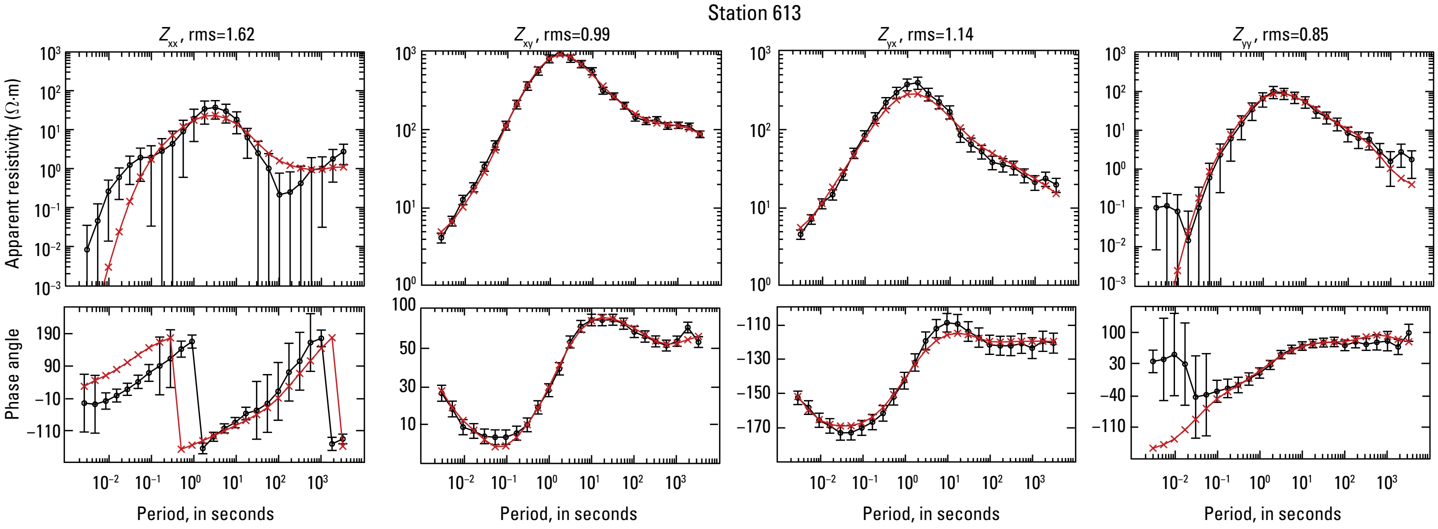

Figure 3.79. Station 613. Plots showing the data inverted (black) and the resistivity model response (red). Shown are all components of the impedance tensor (*Z*) as apparent resistivity (in Ohm meters, Ω·m) and phase angle (in degrees). Data error bars are shown for the inverted data.

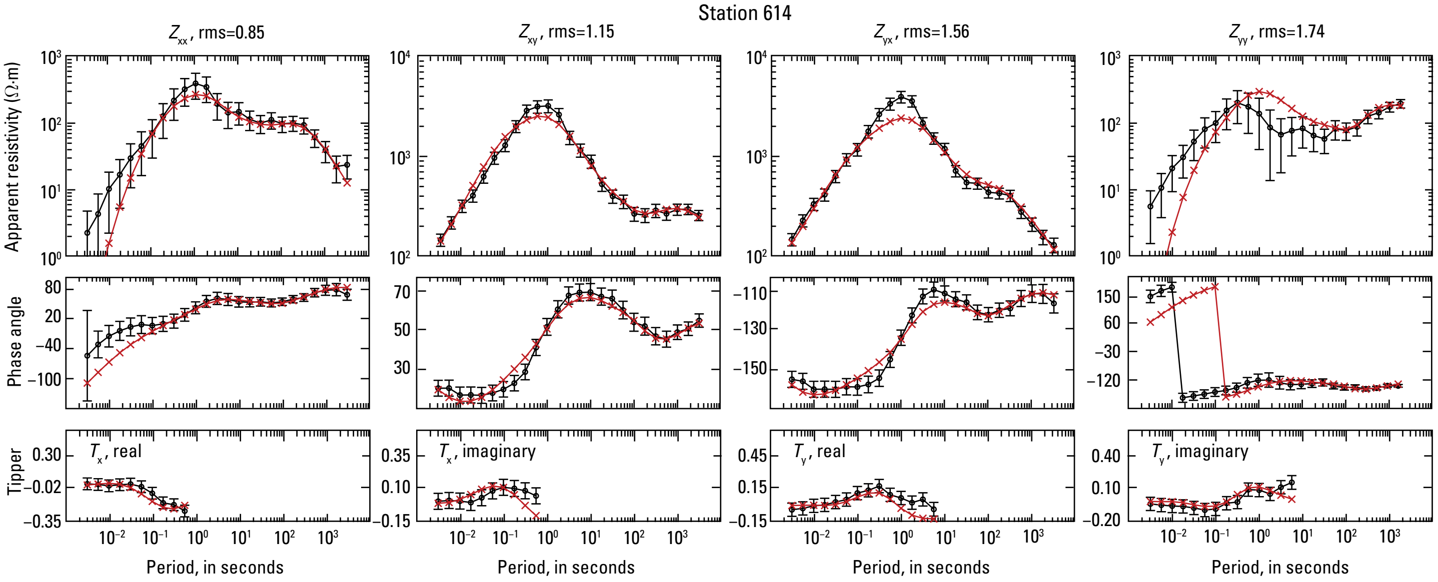

Figure 3.80. Station 614. Plots showing the data inverted (black) and the resistivity model response (red). Shown are all components of the impedance tensor (*Z*) as apparent resistivity (in Ohm meters, Ω·m) and phase angle (in degrees) and the induction vector (*T*), or tipper, as both real and imaginary parts of *T*. Data error bars are shown for the inverted data.

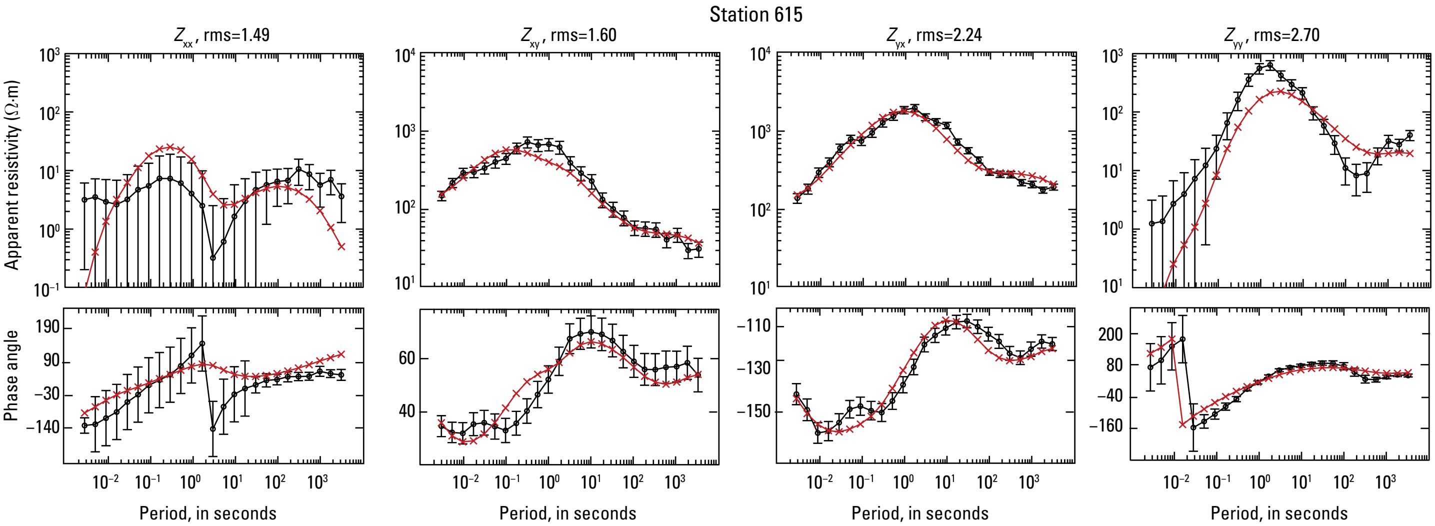

Figure 3.81. Station 615. Plots showing the data inverted (black) and the resistivity model response (red). Shown are all components of the impedance tensor (*Z*) as apparent resistivity (in Ohm meters, Ω·m) and phase angle (in degrees). Data error bars are shown for the inverted data.

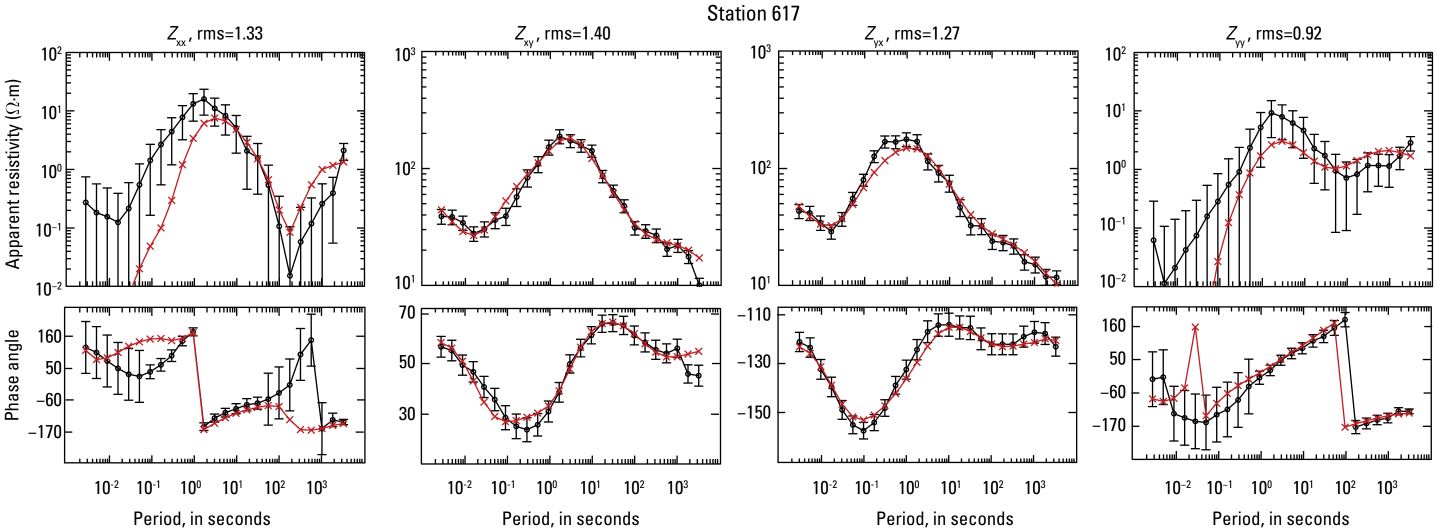

Figure 3.82. Station 617. Plots showing the data inverted (black) and the resistivity model response (red). Shown are all components of the impedance tensor (*Z*) as apparent resistivity (in Ohm meters, Ω·m) and phase angle (in degrees). Data error bars are shown for the inverted data.

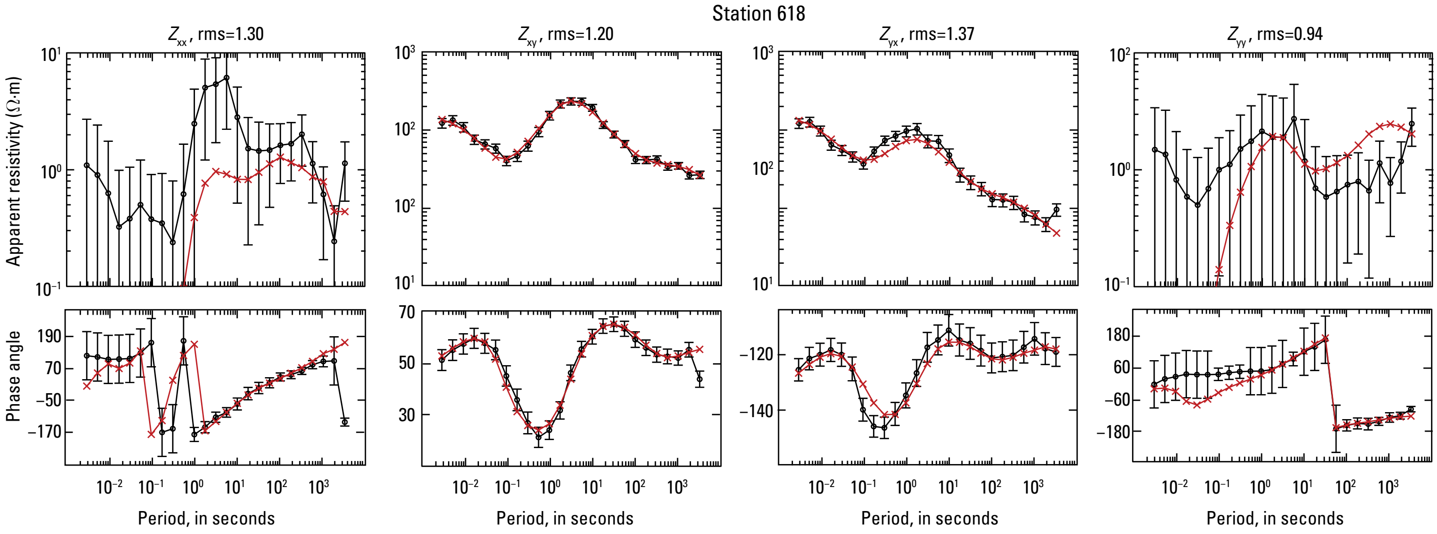

Figure 3.83. Station 618. Plots showing the data inverted (black) and the resistivity model response (red). Shown are all components of the impedance tensor (*Z*) as apparent resistivity (in Ohm meters, Ω·m) and phase angle (in degrees). Data error bars are shown for the inverted data.

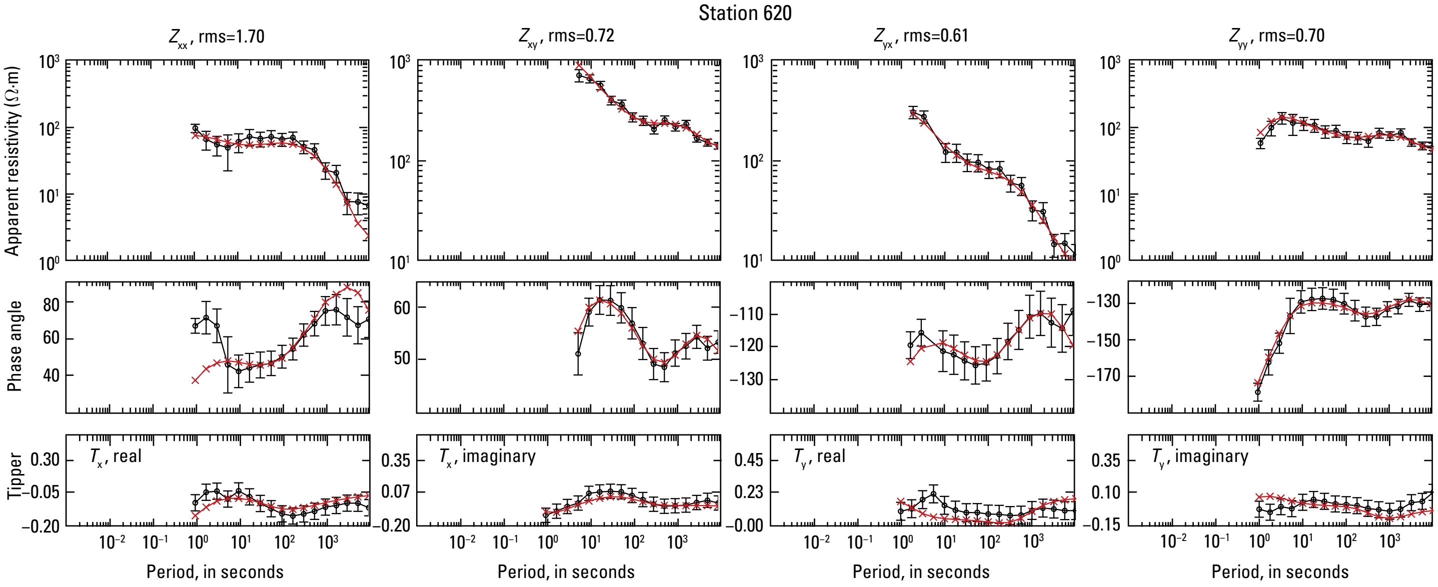

Figure 3.84. Station 620. Plots showing the data inverted (black) and the resistivity model response (red). Shown are all components of the impedance tensor (*Z*) as apparent resistivity (in Ohm meters, Ω·m) and phase angle (in degrees) and the induction vector (*T*), or tipper, as both real and imaginary parts of *T*. Data error bars are shown for the inverted data.

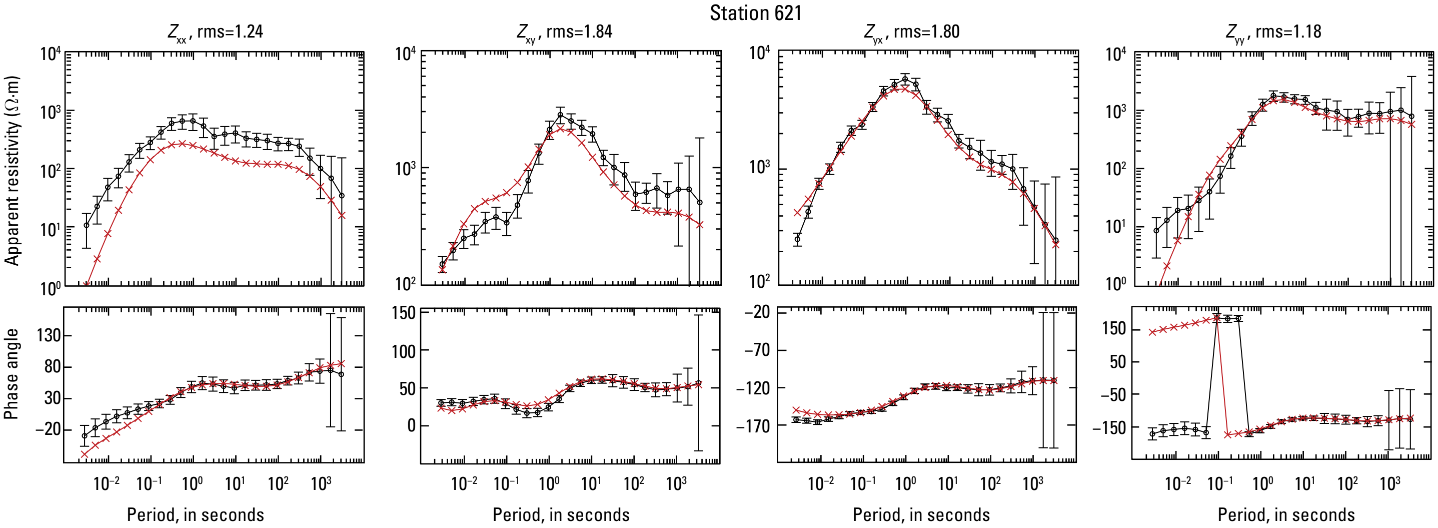

Figure 3.85. Station 621. Plots showing the data inverted (black) and the resistivity model response (red). Shown are all components of the impedance tensor (*Z*) as apparent resistivity (in Ohm meters, Ω·m) and phase angle (in degrees). Data error bars are shown for the inverted data.

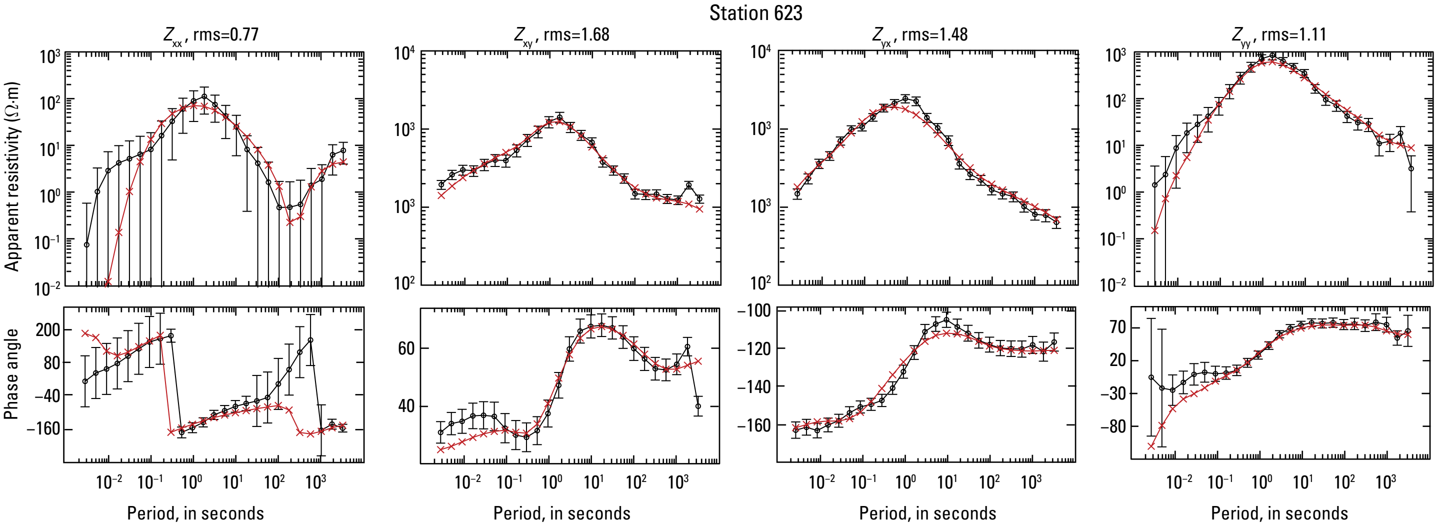

Figure 3.86. Station 623. Plots showing the data inverted (black) and the resistivity model response (red). Shown are all components of the impedance tensor (*Z*) as apparent resistivity (in Ohm meters, Ω·m) and phase angle (in degrees). Data error bars are shown for the inverted data.

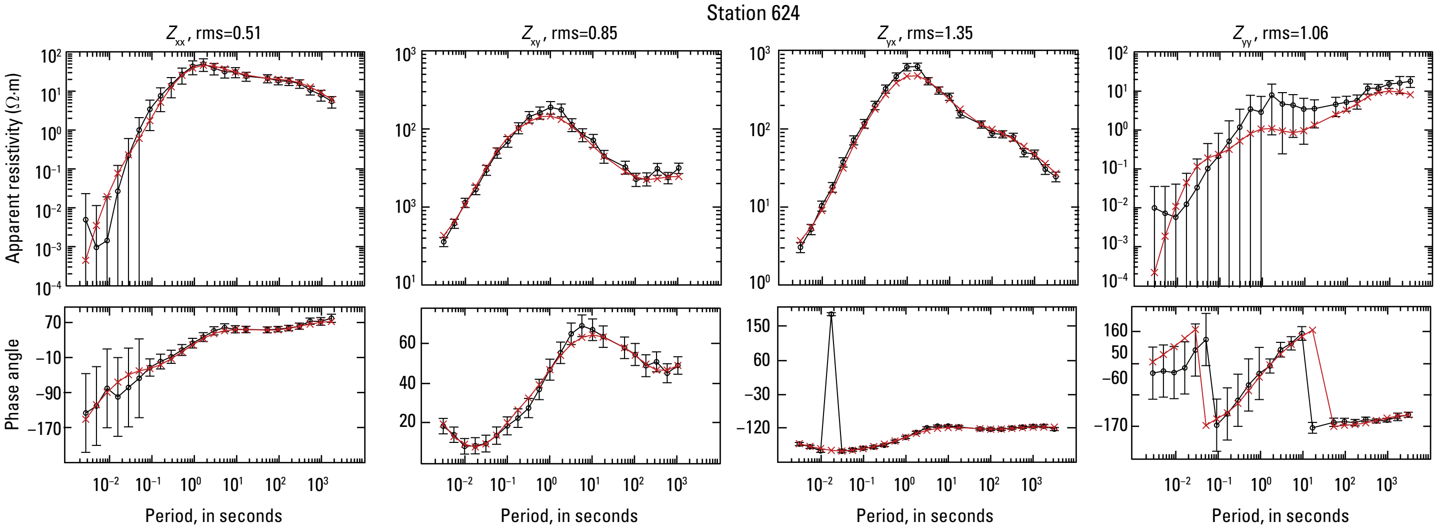

Figure 3.87. Station 624. Plots showing the data inverted (black) and the resistivity model response (red). Shown are all components of the impedance tensor (*Z*) as apparent resistivity (in Ohm meters, Ω·m) and phase angle (in degrees). Data error bars are shown for the inverted data.

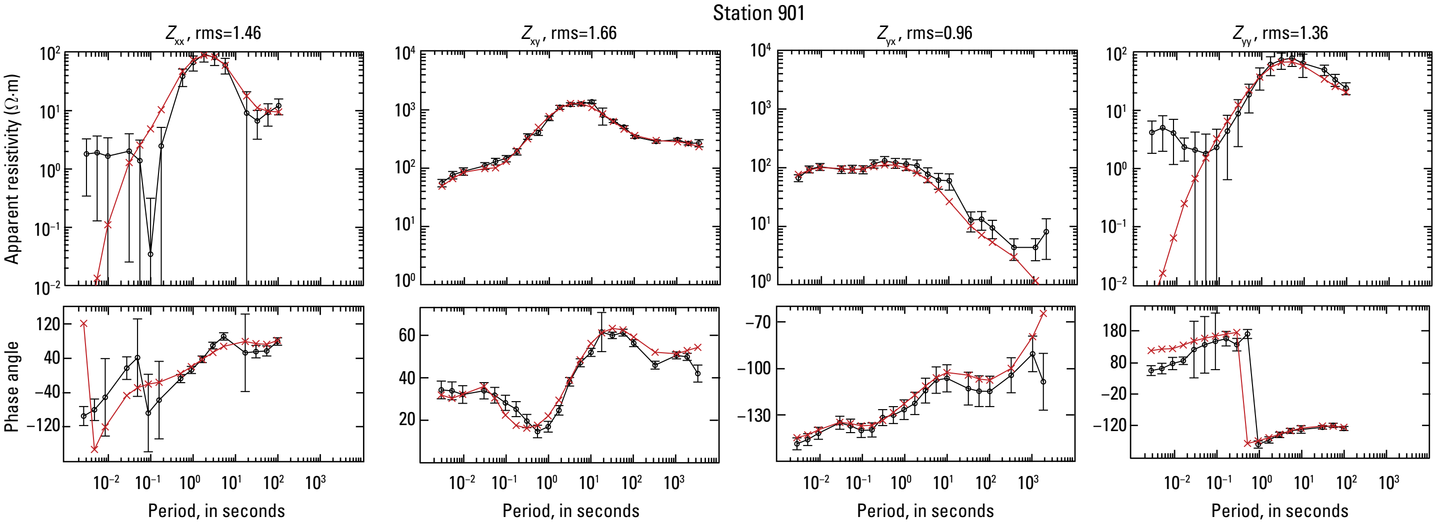

Figure 3.88. Station 901. Plots showing the data inverted (black) and the resistivity model response (red). Shown are all components of the impedance tensor (*Z*) as apparent resistivity (in Ohm meters, Ω·m) and phase angle (in degrees). Data error bars are shown for the inverted data.

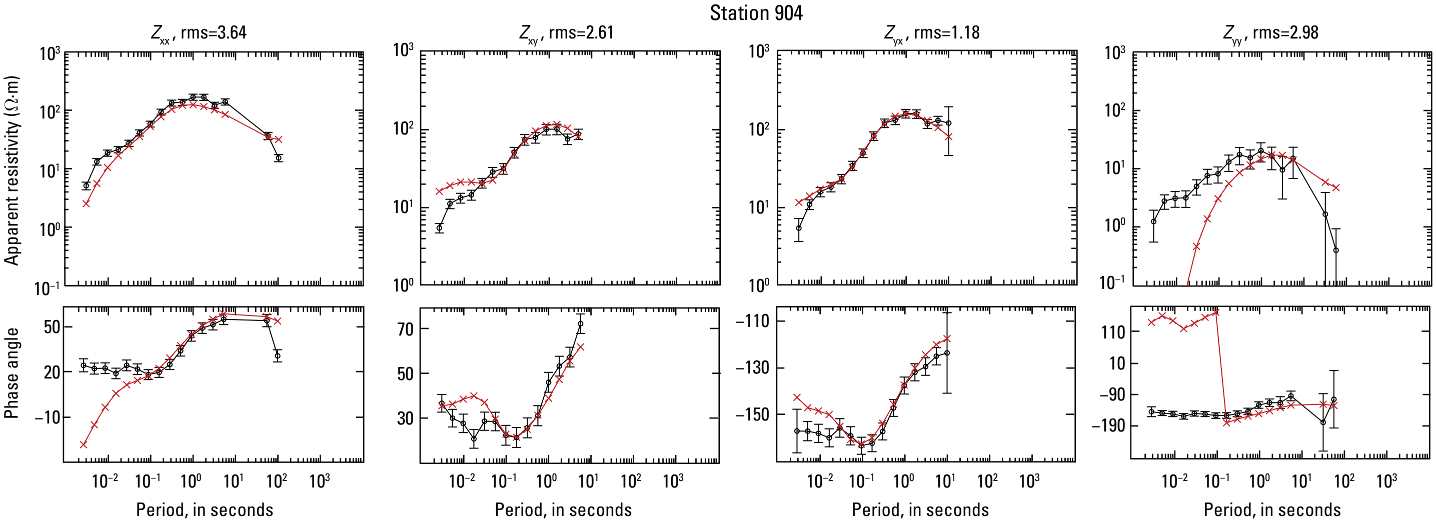

Figure 3.89. Station 904. Plots showing the data inverted (black) and the resistivity model response (red). Shown are all components of the impedance tensor (*Z*) as apparent resistivity (in Ohm meters, Ω·m) and phase angle (in degrees). Data error bars are shown for the inverted data.

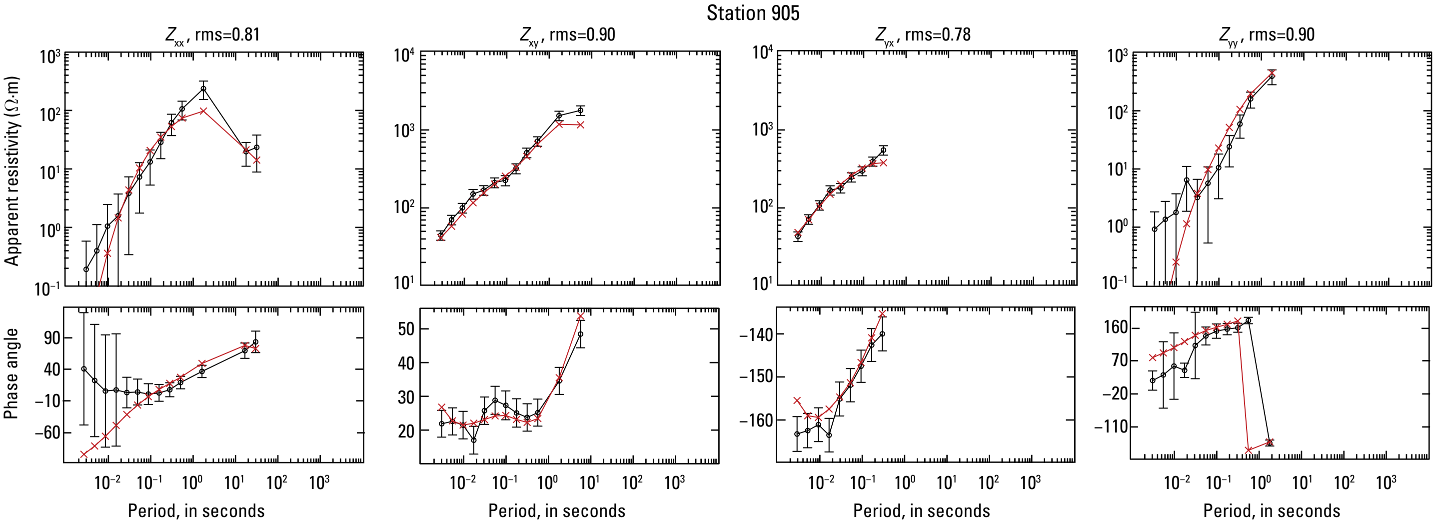

Figure 3.90. Station 905. Plots showing the data inverted (black) and the resistivity model response (red). Shown are all components of the impedance tensor (*Z*) as apparent resistivity (in Ohm meters, Ω·m) and phase angle (in degrees). Data error bars are shown for the inverted data.

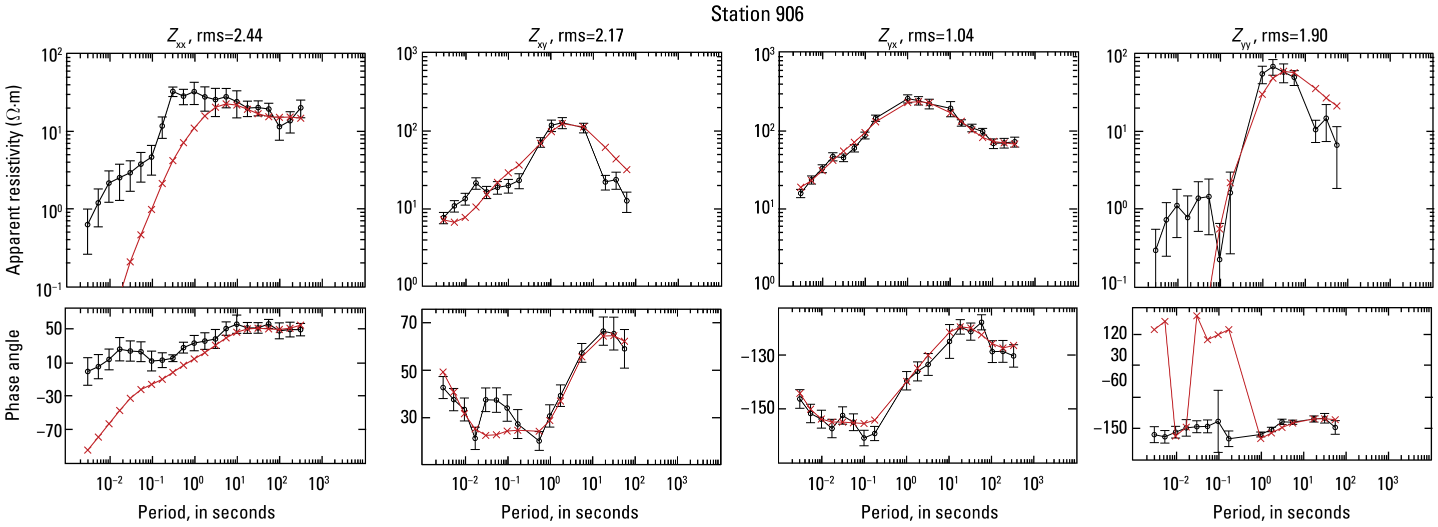

Figure 3.91. Station 906. Plots showing the data inverted (black) and the resistivity model response (red). Shown are all components of the impedance tensor (*Z*) as apparent resistivity (in Ohm meters, Ω·m) and phase angle (in degrees). Data error bars are shown for the inverted data.

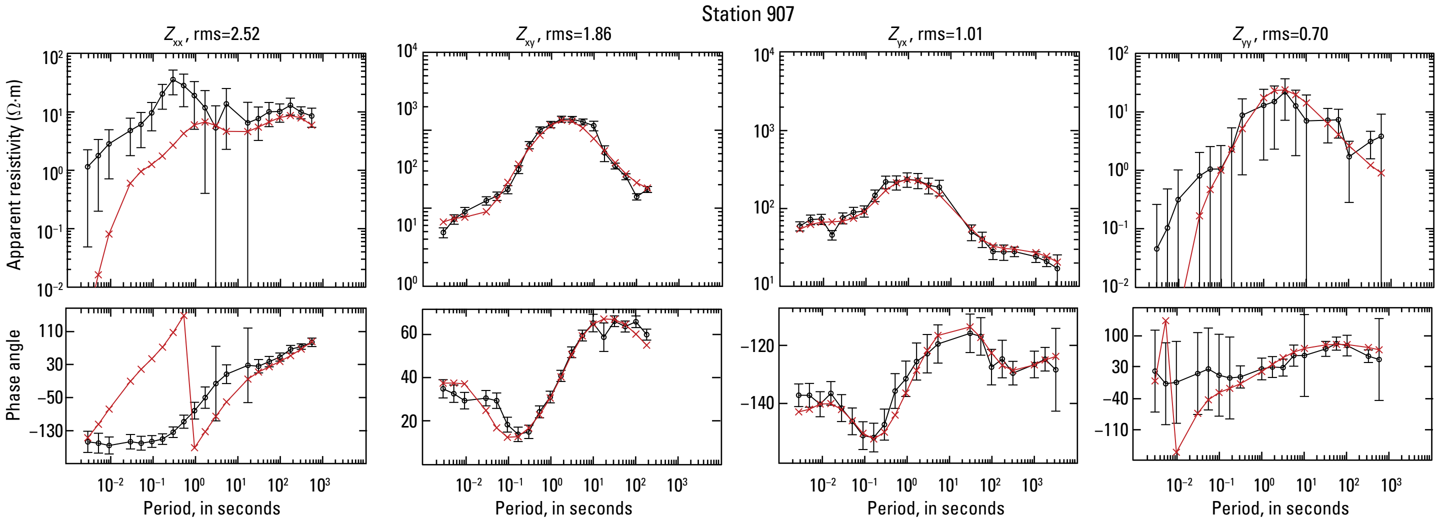

Figure 3.92. Station 907. Plots showing the data inverted (black) and the resistivity model response (red). Shown are all components of the impedance tensor (*Z*) as apparent resistivity (in Ohm meters, Ω·m) and phase angle (in degrees). Data error bars are shown for the inverted data.

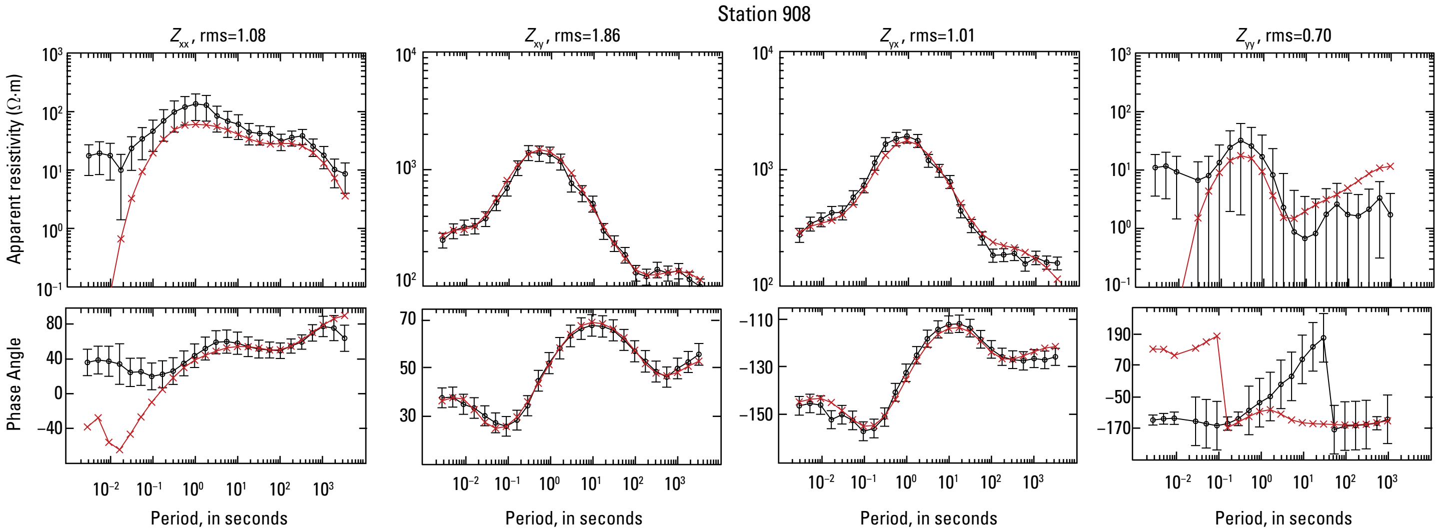

Figure 3.93. Station 908. Plots showing the data inverted (black) and the resistivity model response (red). Shown are all components of the impedance tensor (*Z*) as apparent resistivity (in Ohm meters, Ω·m) and phase angle (in degrees). Data error bars are shown for the inverted data.

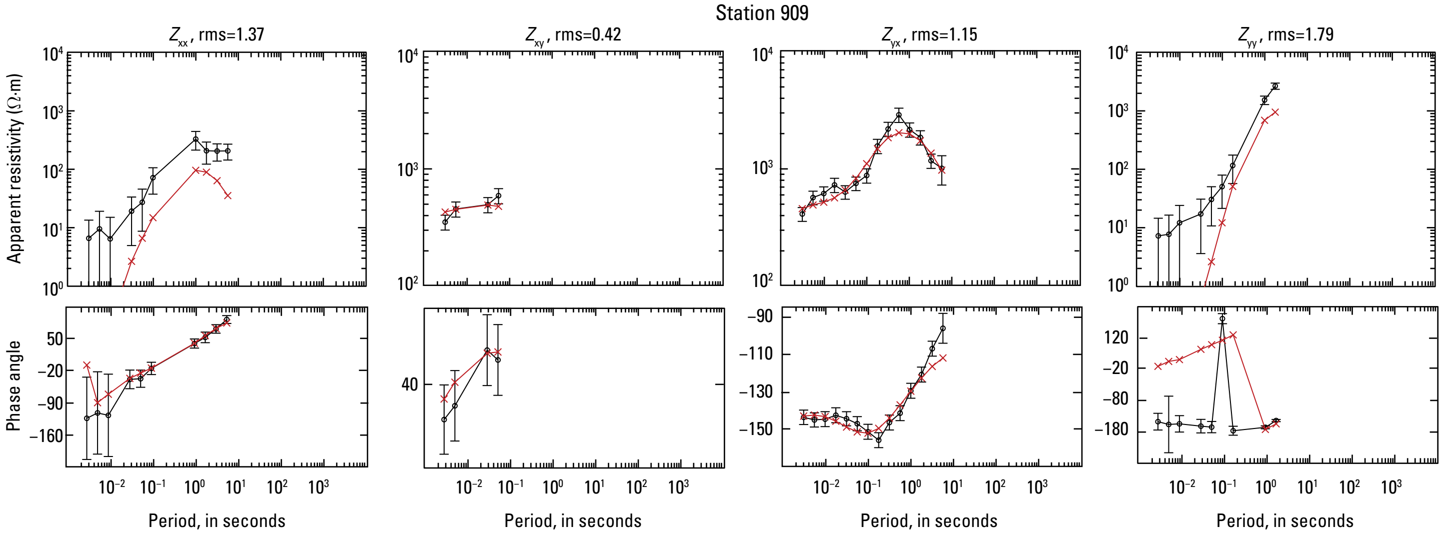

Figure 3.94. Station 909. Plots showing the data inverted (black) and the resistivity model response (red). Shown are all components of the impedance tensor (*Z*) as apparent resistivity (in Ohm meters, Ω·m) and phase angle (in degrees). Data error bars are shown for the inverted data.

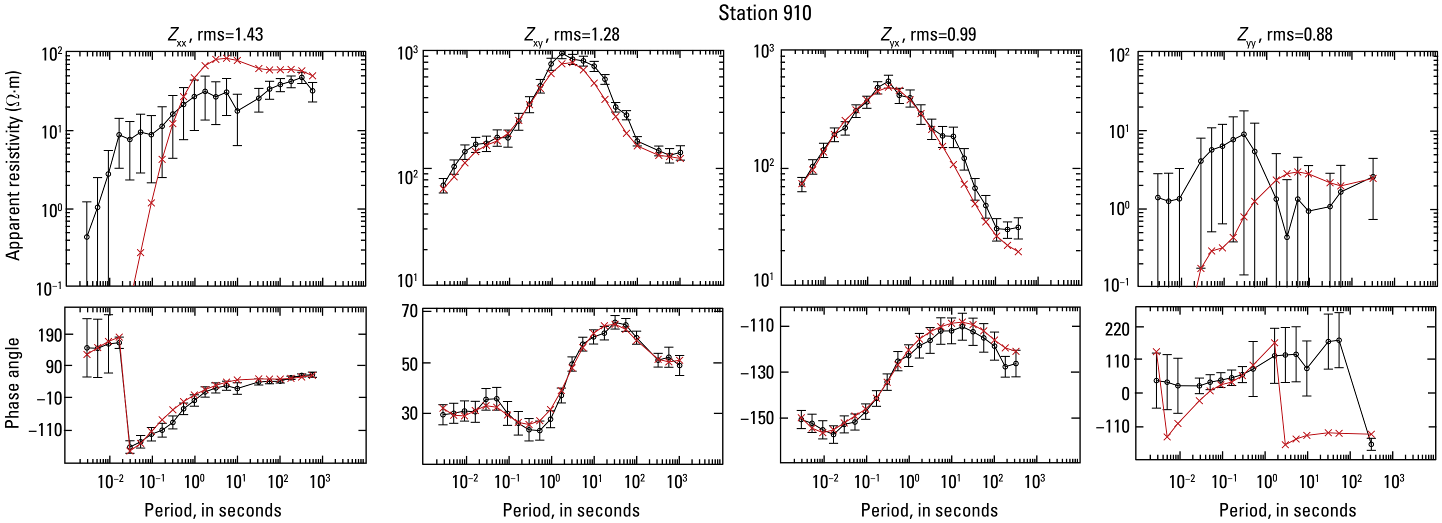

Figure 3.95. Station 910. Plots showing the data inverted (black) and the resistivity model response (red). Shown are all components of the impedance tensor (*Z*) as apparent resistivity (in Ohm meters, Ω·m) and phase angle (in degrees). Data error bars are shown for the inverted data.

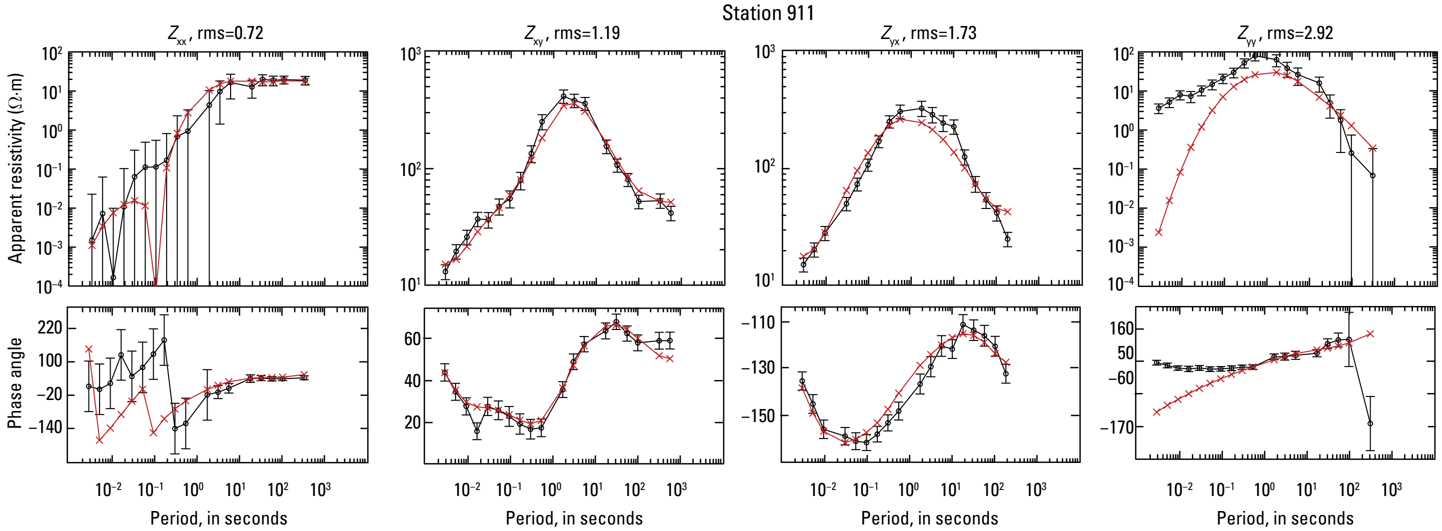

Figure 3.96. Station 911. Plots showing the data inverted (black) and the resistivity model response (red). Shown are all components of the impedance tensor (*Z*) as apparent resistivity (in Ohm meters, Ω·m) and phase angle (in degrees). Data error bars are shown for the inverted data.

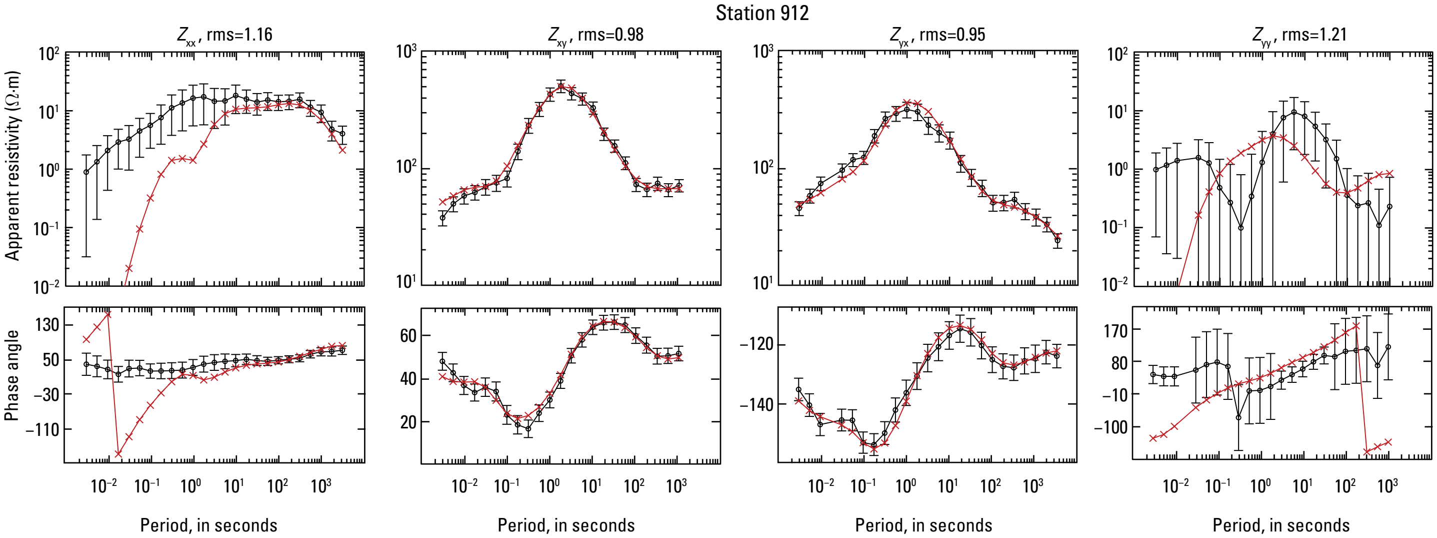

Figure 3.97. Station 912. Plots showing the data inverted (black) and the resistivity model response (red). Shown are all components of the impedance tensor (*Z*) as apparent resistivity (in Ohm meters, Ω·m) and phase angle (in degrees). Data error bars are shown for the inverted data.

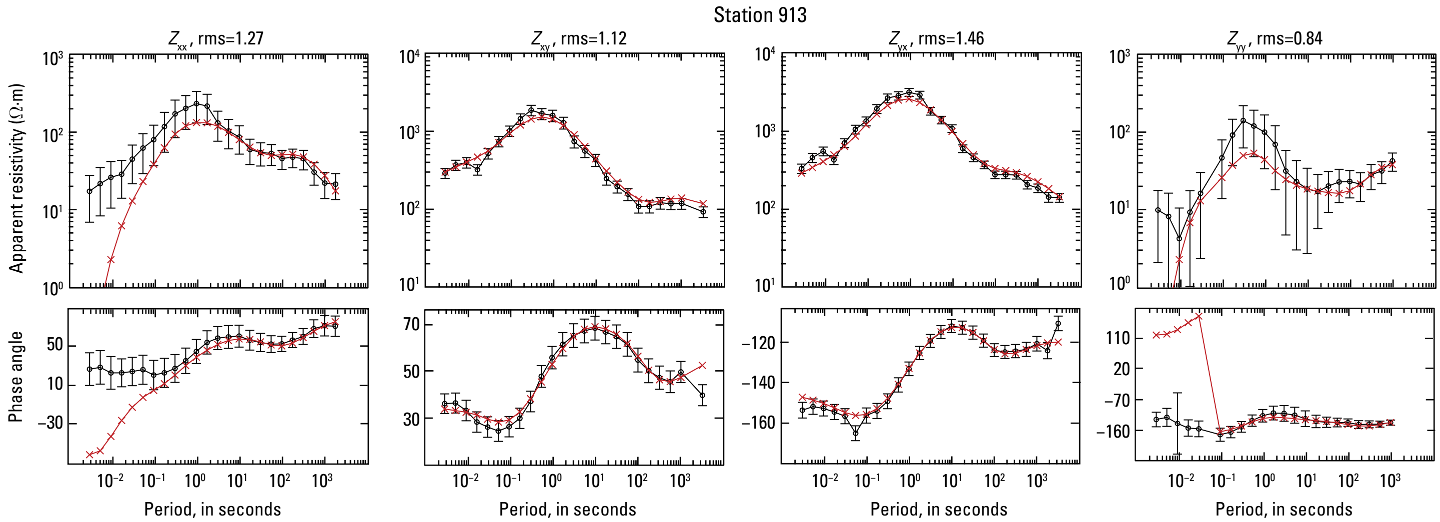

Figure 3.98. Station 913. Plots showing the data inverted (black) and the resistivity model response (red). Shown are all components of the impedance tensor (*Z*) as apparent resistivity (in Ohm meters, Ω·m) and phase angle (in degrees). Data error bars are shown for the inverted data.

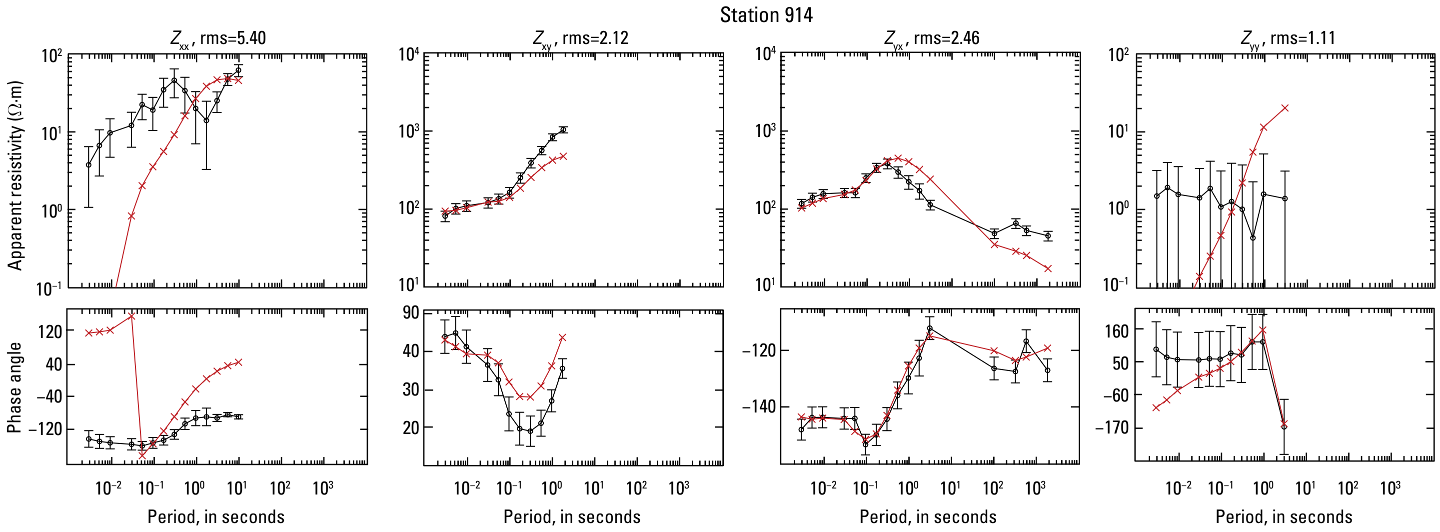

Figure 3.99. Station 914. Plots showing the data inverted (black) and the resistivity model response (red). Shown are all components of the impedance tensor (*Z*) as apparent resistivity (in Ohm meters, Ω·m) and phase angle (in degrees). Data error bars are shown for the inverted data.

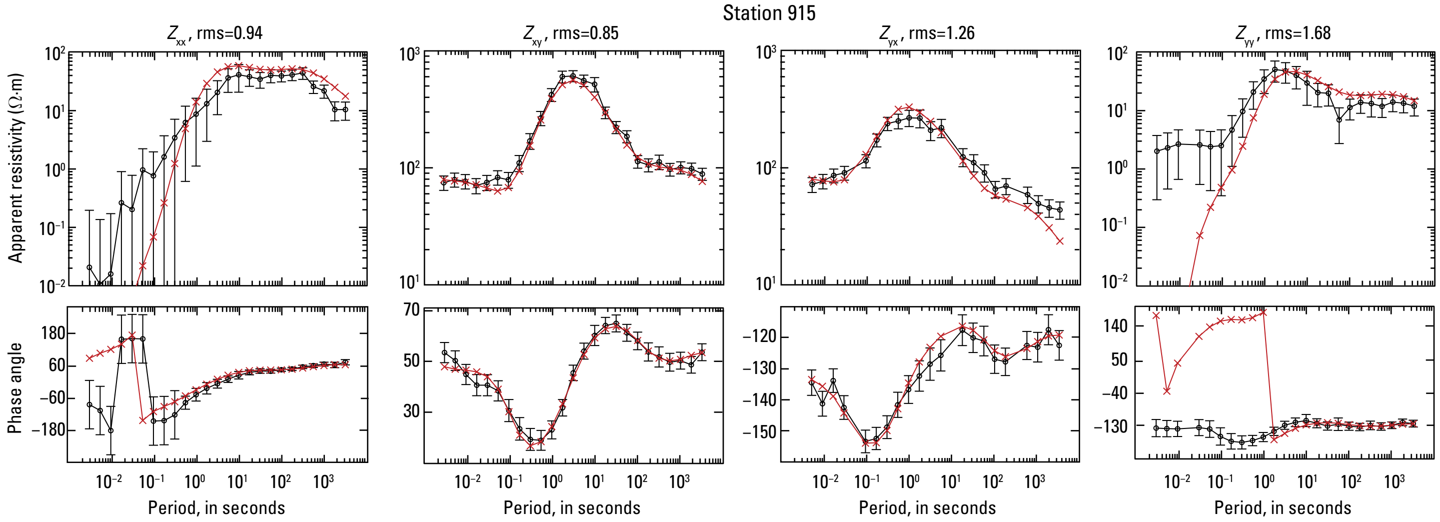

Figure 3.100. Station 915. Plots showing the data inverted (black) and the resistivity model response (red). Shown are all components of the impedance tensor (*Z*) as apparent resistivity (in Ohm meters, Ω·m) and phase angle (in degrees). Data error bars are shown for the inverted data.

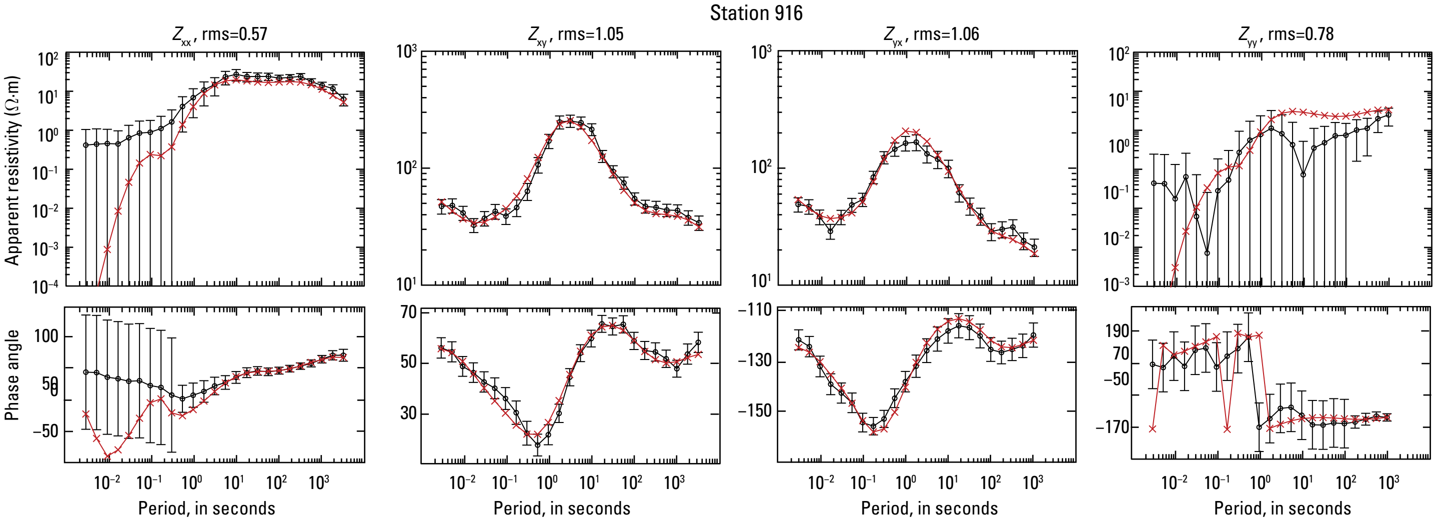

Figure 3.101. Station 916. Plots showing the data inverted (black) and the resistivity model response (red). Shown are all components of the impedance tensor (*Z*) as apparent resistivity (in Ohm meters, Ω·m) and phase angle (in degrees). Data error bars are shown for the inverted data.

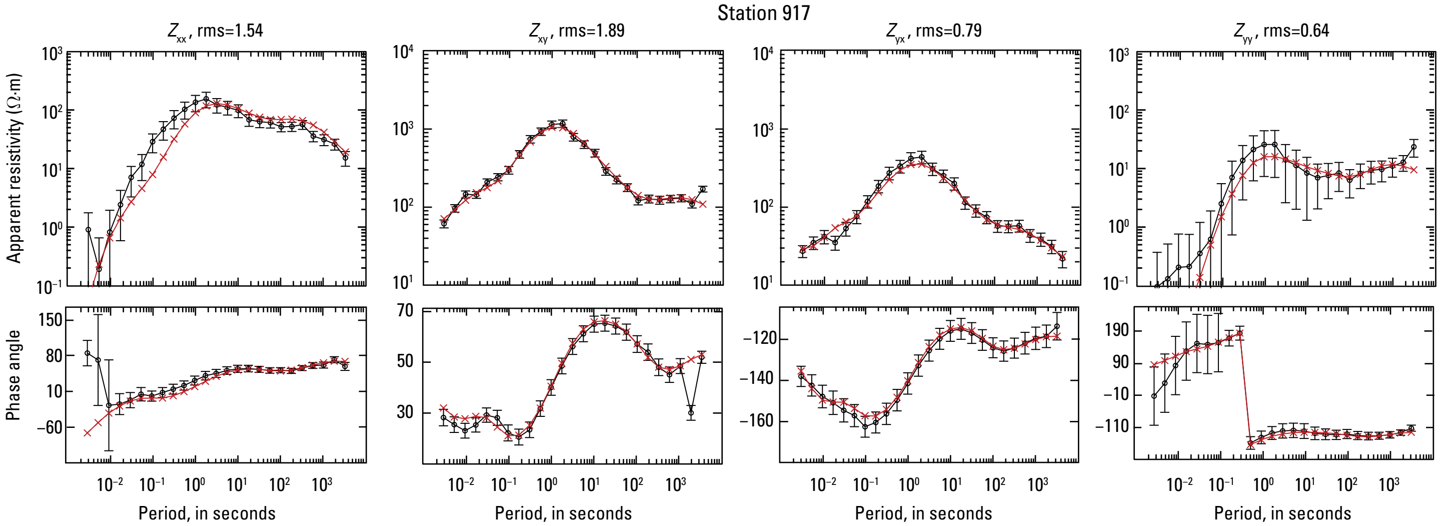

Figure 3.102. Station 917. Plots showing the data inverted (black) and the resistivity model response (red). Shown are all components of the impedance tensor (*Z*) as apparent resistivity (in Ohm meters, Ω·m) and phase angle (in degrees). Data error bars are shown for the inverted data.

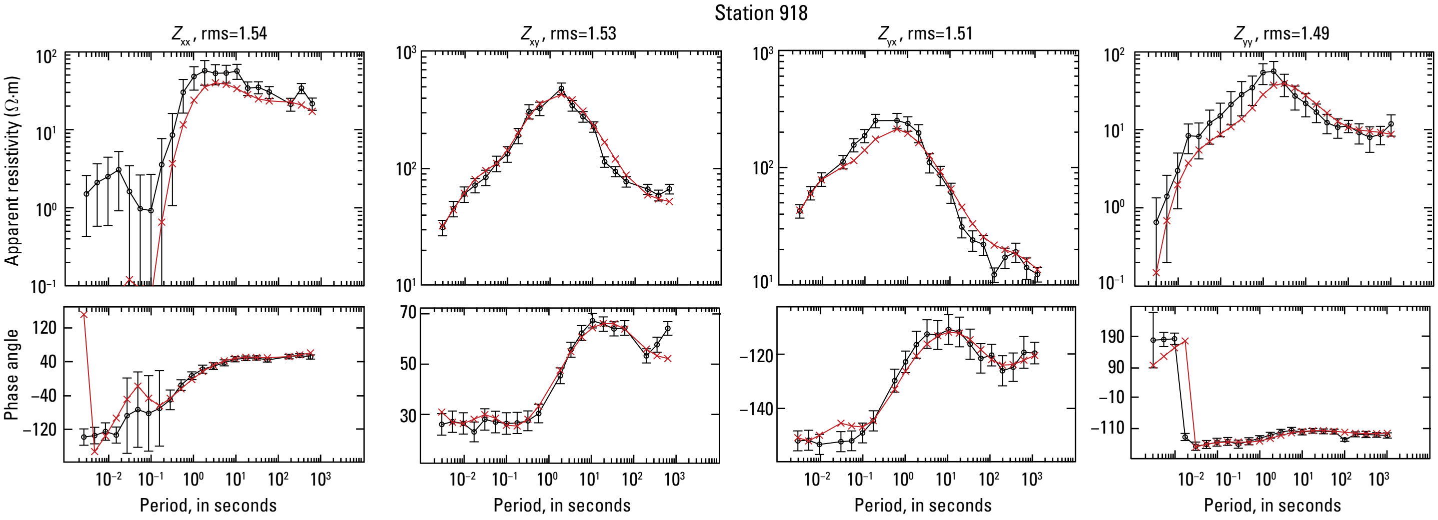

Figure 3.103. Station 918. Plots showing the data inverted (black) and the resistivity model response (red). Shown are all components of the impedance tensor (*Z*) as apparent resistivity (in Ohm meters, Ω·m) and phase angle (in degrees). Data error bars are shown for the inverted data.

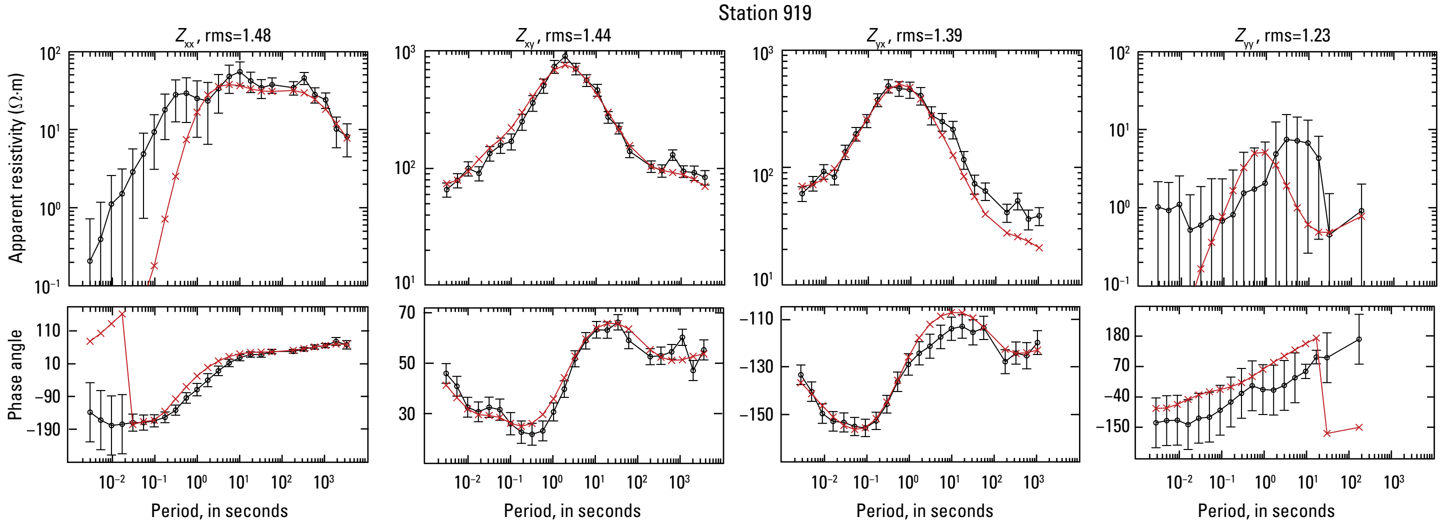

Figure 3.104. Station 919. Plots showing the data inverted (black) and the resistivity model response (red). Shown are all components of the impedance tensor (*Z*) as apparent resistivity (in Ohm meters, Ω·m) and phase angle (in degrees). Data error bars are shown for the inverted data.

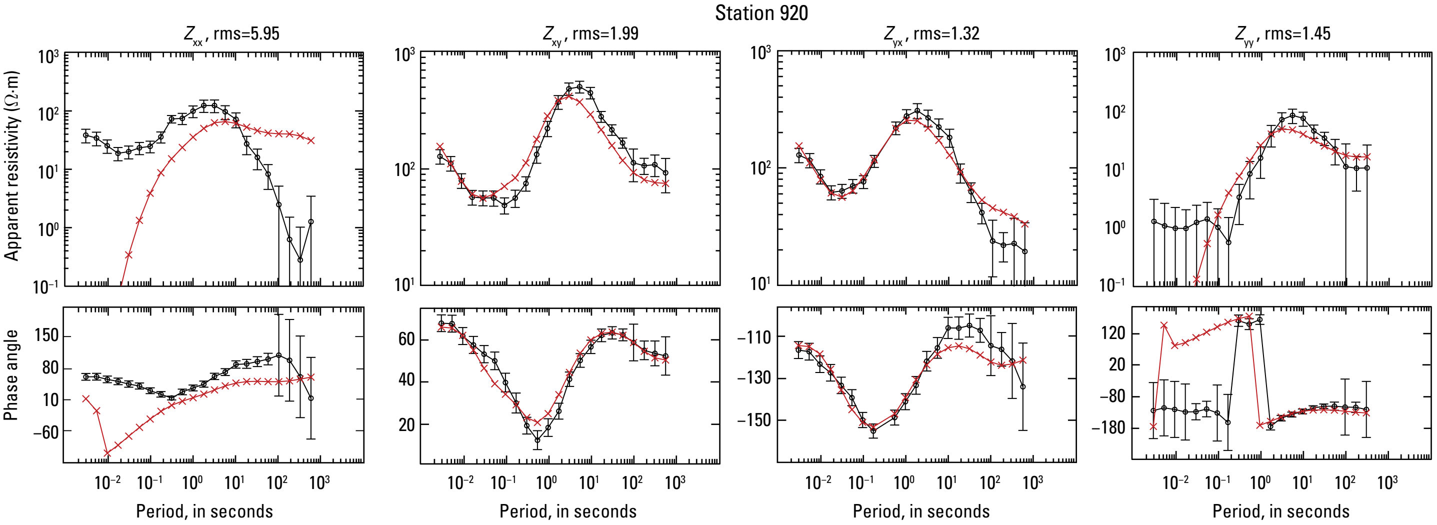

Figure 3.105. Station 920. Plots showing the data inverted (black) and the resistivity model response (red). Shown are all components of the impedance tensor (*Z*) as apparent resistivity (in Ohm meters, Ω·m) and phase angle (in degrees). Data error bars are shown for the inverted data.

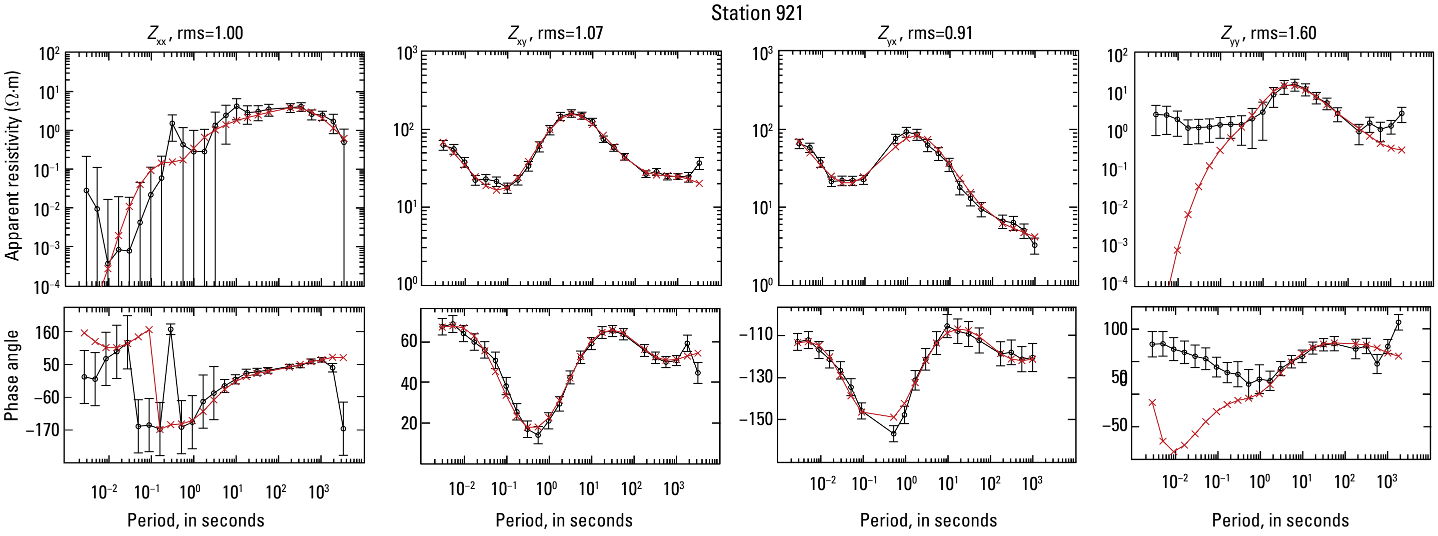

Figure 3.106. Station 921. Plots showing the data inverted (black) and the resistivity model response (red). Shown are all components of the impedance tensor (*Z*) as apparent resistivity (in Ohm meters, Ω·m) and phase angle (in degrees). Data error bars are shown for the inverted data.

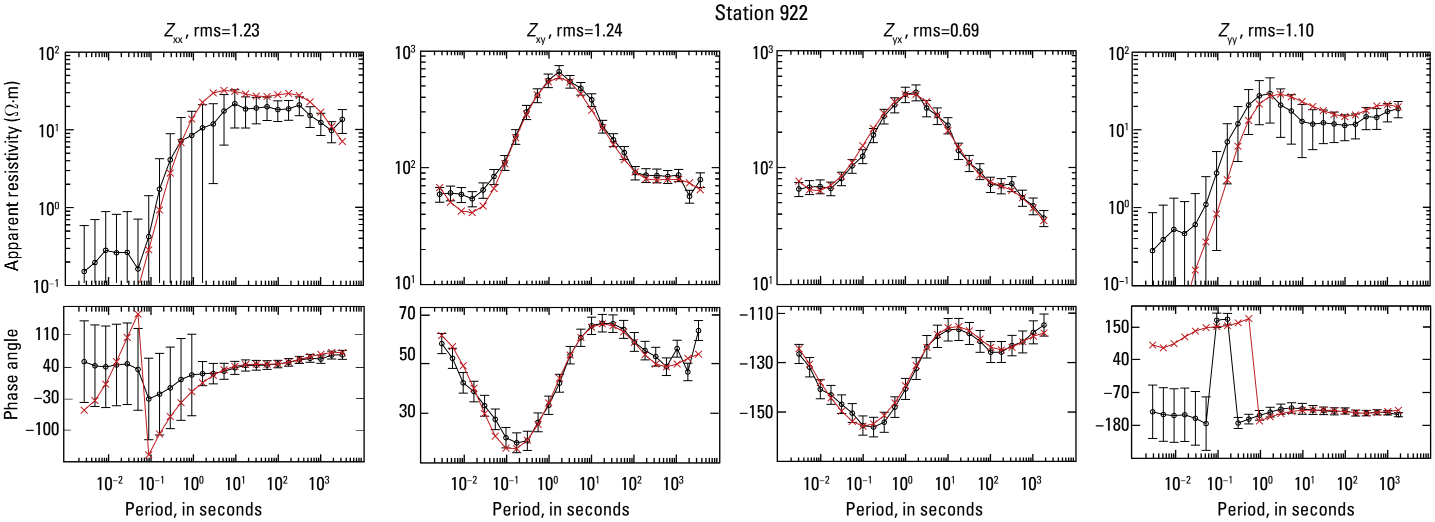

Figure 3.107. Station 922. Plots showing the data inverted (black) and the resistivity model response (red). Shown are all components of the impedance tensor (*Z*) as apparent resistivity (in Ohm meters, Ω·m) and phase angle (in degrees). Data error bars are shown for the inverted data.

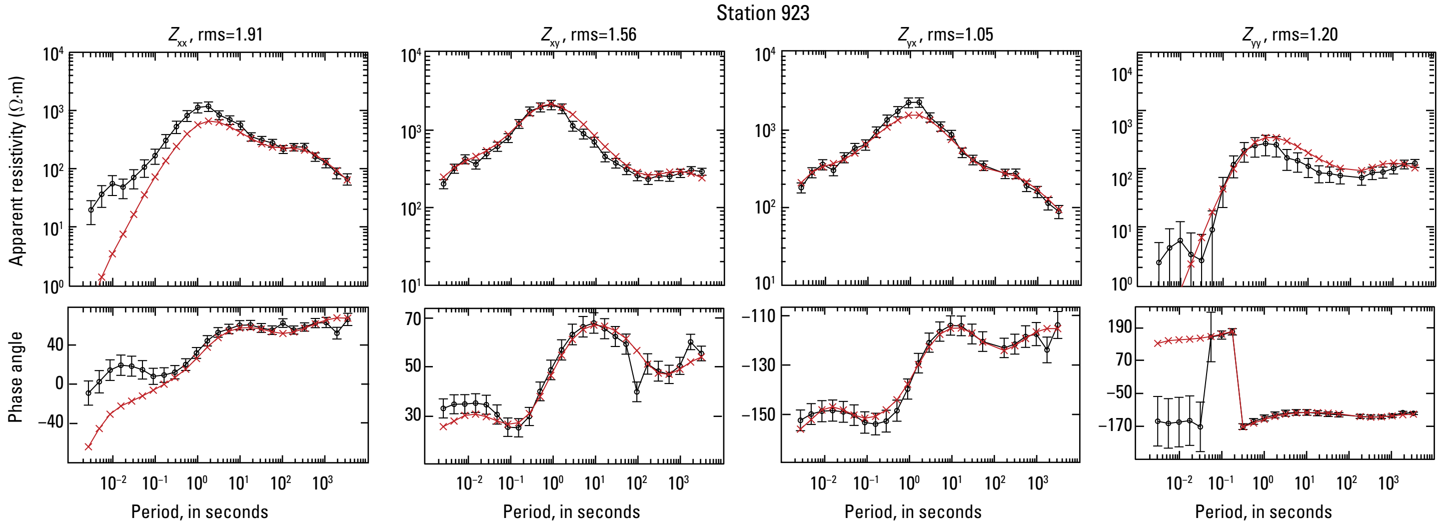

Figure 3.108. Station 923. Plots showing the data inverted (black) and the resistivity model response (red). Shown are all components of the impedance tensor (*Z*) as apparent resistivity (in Ohm meters, Ω·m) and phase angle (in degrees). Data error bars are shown for the inverted data.

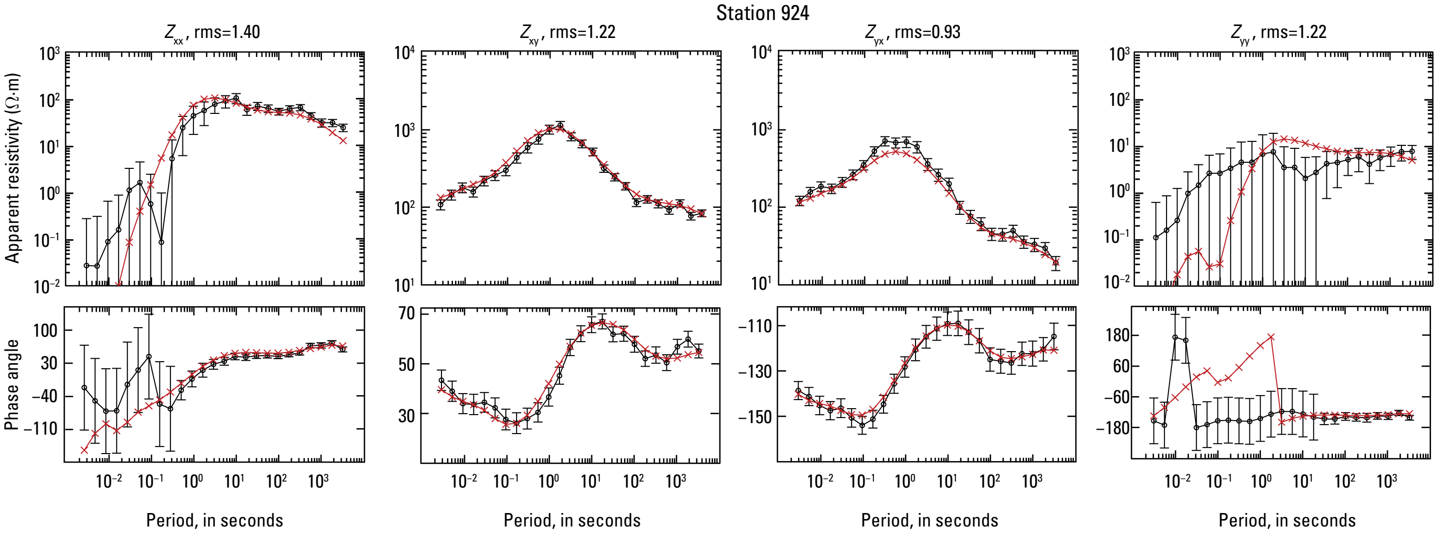

Figure 3.109. Station 924. Plots showing the data inverted (black) and the resistivity model response (red). Shown are all components of the impedance tensor (*Z*) as apparent resistivity (in Ohm meters, Ω·m) and phase angle (in degrees). Data error bars are shown for the inverted data.

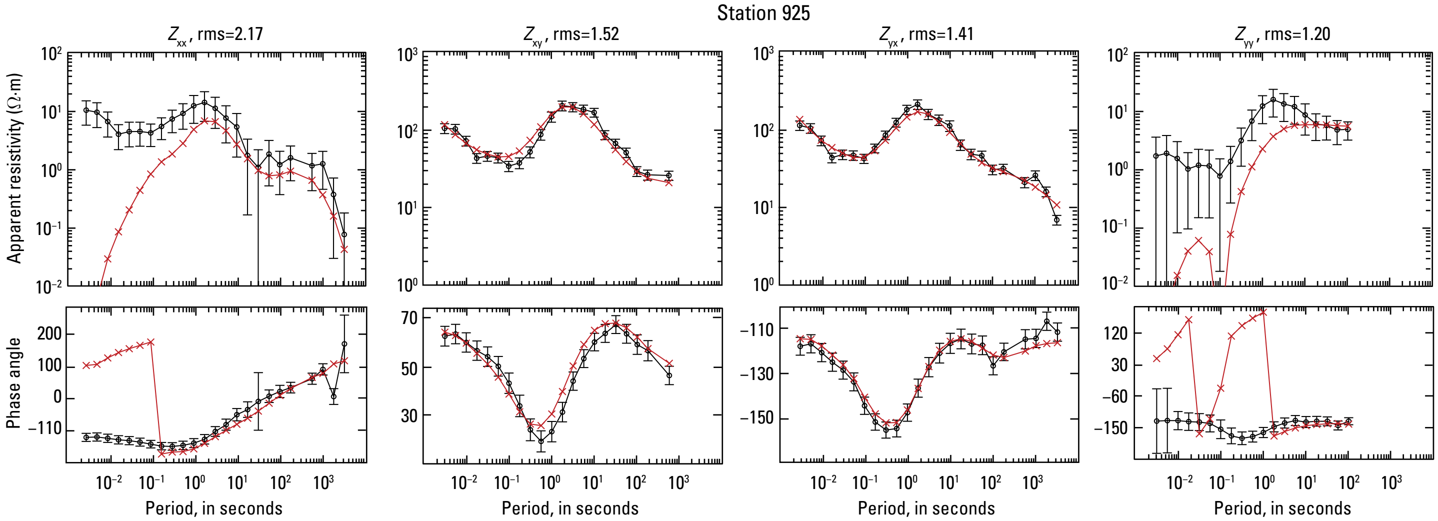

Figure 3.110. Station 925. Plots showing the data inverted (black) and the resistivity model response (red). Shown are all components of the impedance tensor (*Z*) as apparent resistivity (in Ohm meters, Ω·m) and phase angle (in degrees). Data error bars are shown for the inverted data.

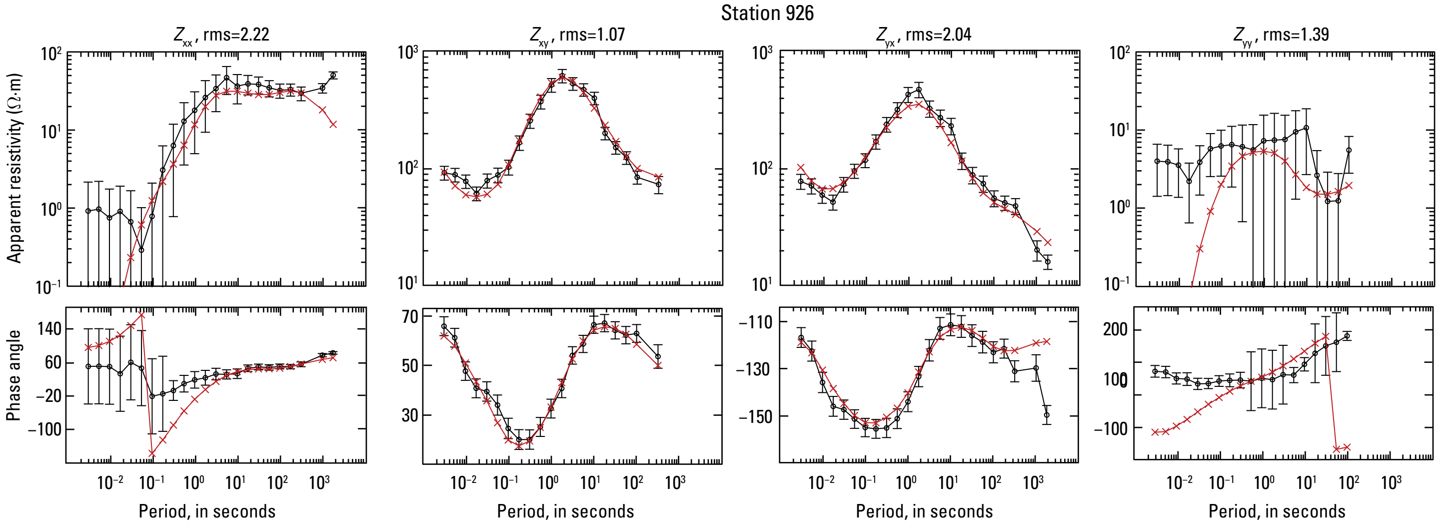

Figure 3.111. Station 926. Plots showing the data inverted (black) and the resistivity model response (red). Shown are all components of the impedance tensor (*Z*) as apparent resistivity (in Ohm meters, Ω·m) and phase angle (in degrees). Data error bars are shown for the inverted data.

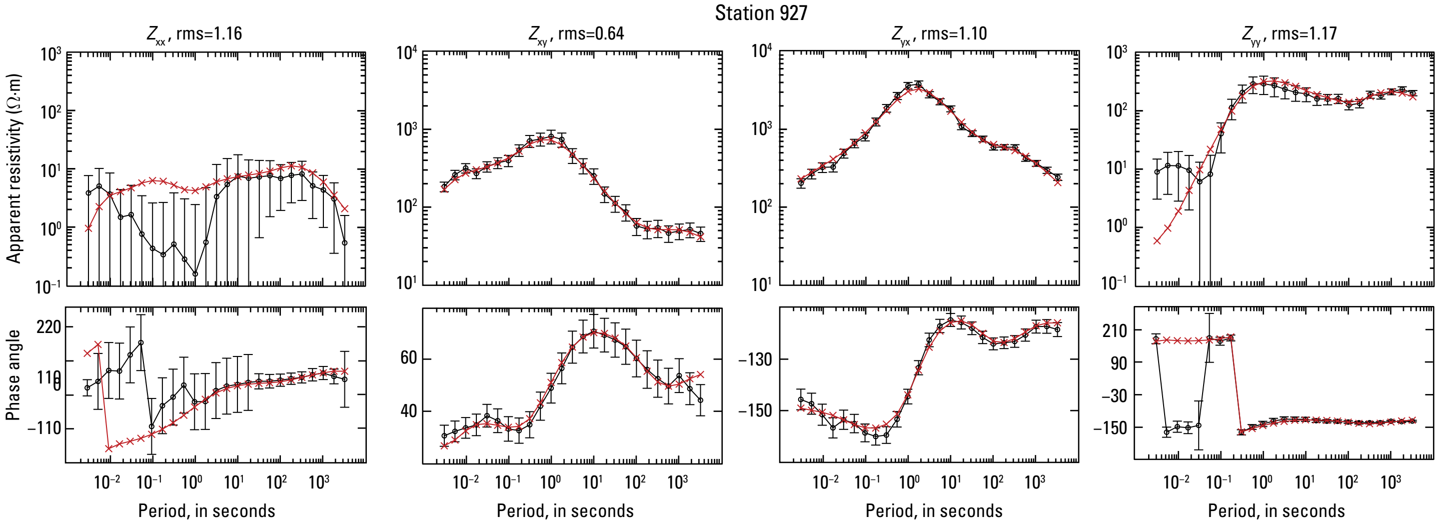

Figure 3.112. Station 927. Plots showing the data inverted (black) and the resistivity model response (red). Shown are all components of the impedance tensor (*Z*) as apparent resistivity (in Ohm meters, Ω·m) and phase angle (in degrees). Data error bars are shown for the inverted data.

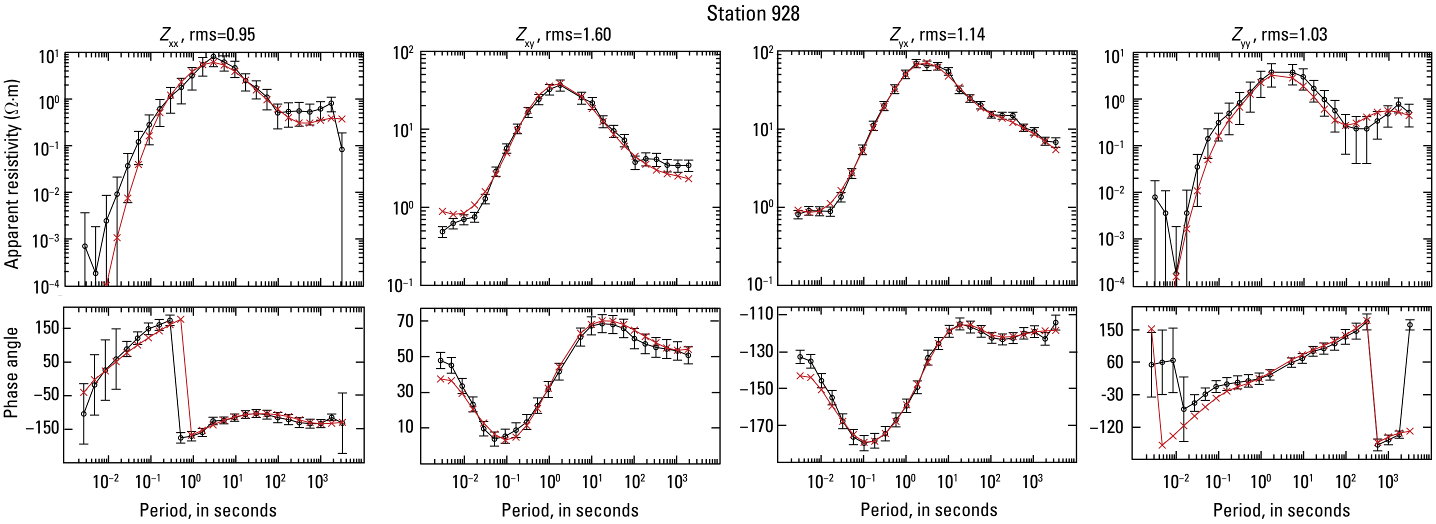

Figure 3.113. Station 928. Plots showing the data inverted (black) and the resistivity model response (red). Shown are all components of the impedance tensor (*Z*) as apparent resistivity (in Ohm meters, Ω·m) and phase angle (in degrees). Data error bars are shown for the inverted data.

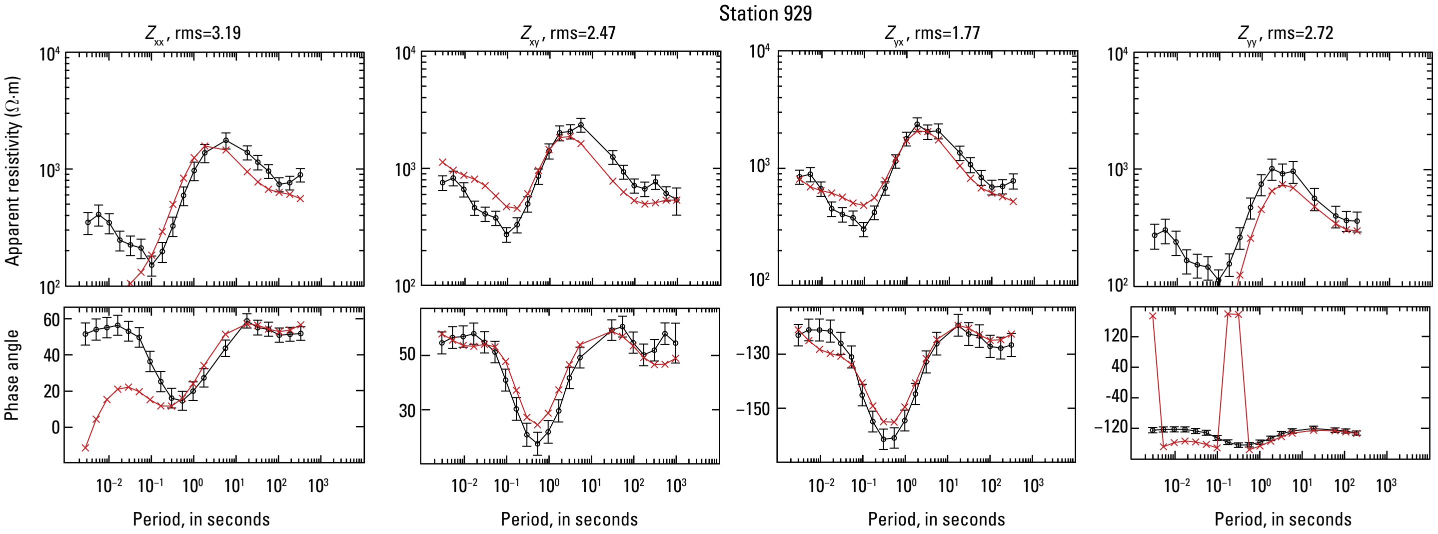

Figure 3.114. Station 929. Plots showing the data inverted (black) and the resistivity model response (red). Shown are all components of the impedance tensor (*Z*) as apparent resistivity (in Ohm meters, Ω·m) and phase angle (in degrees). Data error bars are shown for the inverted data.

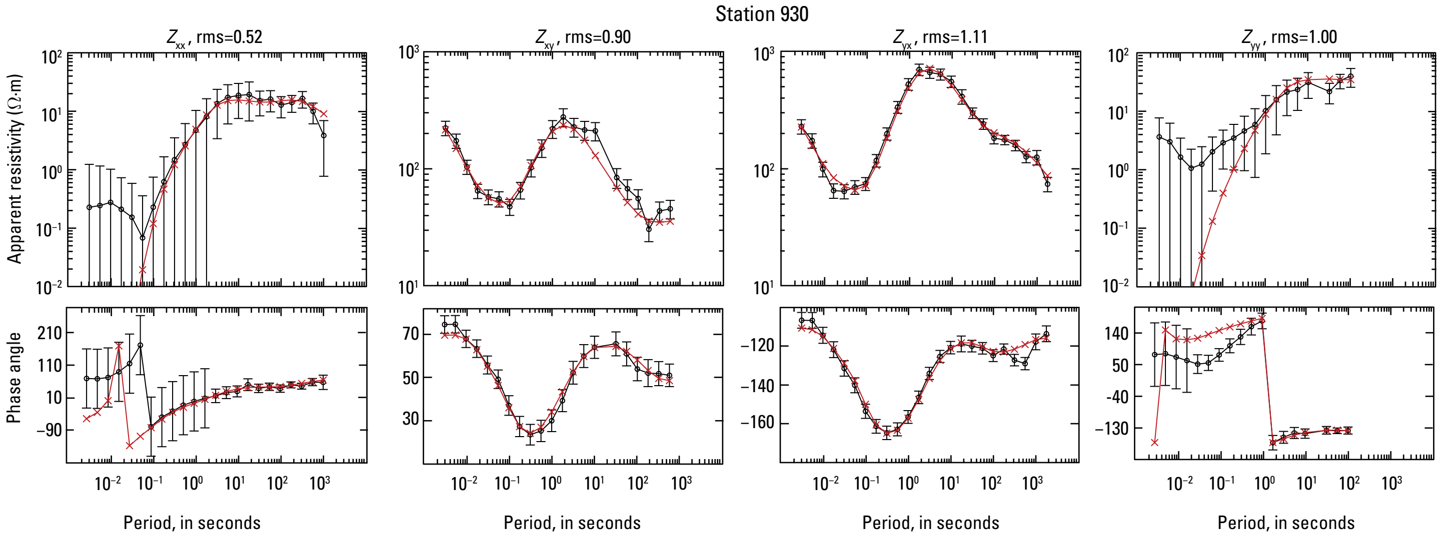

Figure 3.115. Station 930. Plots showing the data inverted (black) and the resistivity model response (red). Shown are all components of the impedance tensor (*Z*) as apparent resistivity (in Ohm meters, Ω·m) and phase angle (in degrees). Data error bars are shown for the inverted data.

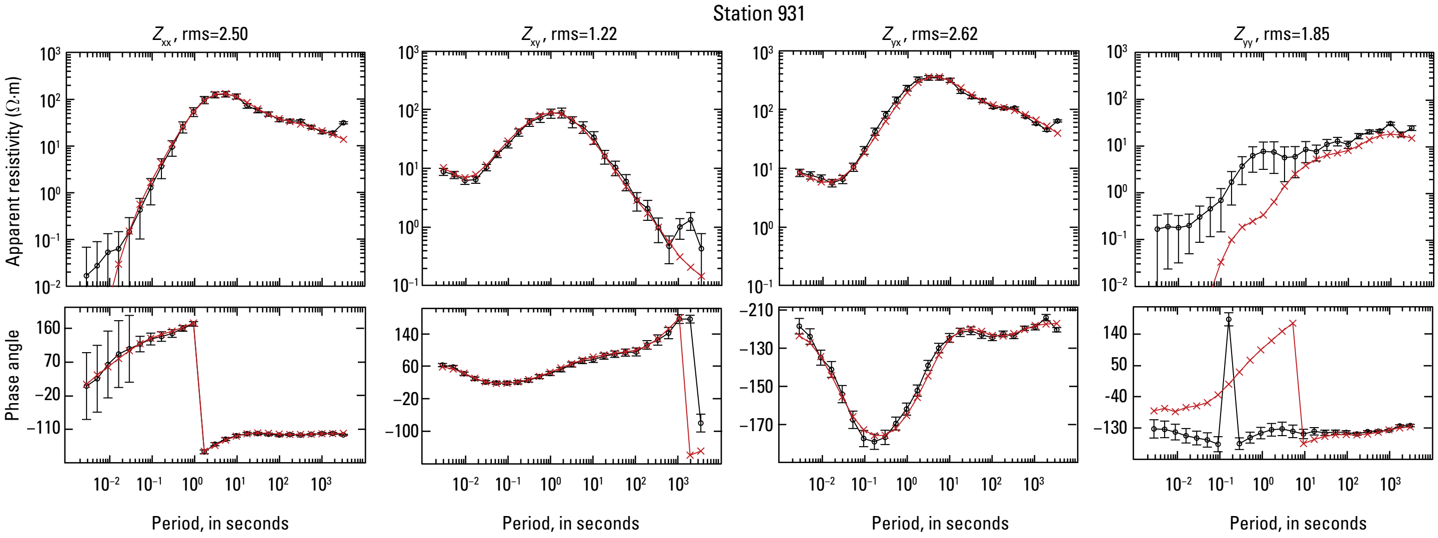

Figure 3.116. Station 931. Plots showing the data inverted (black) and the resistivity model response (red). Shown are all components of the impedance tensor (*Z*) as apparent resistivity (in Ohm meters, Ω·m) and phase angle (in degrees). Data error bars are shown for the inverted data.

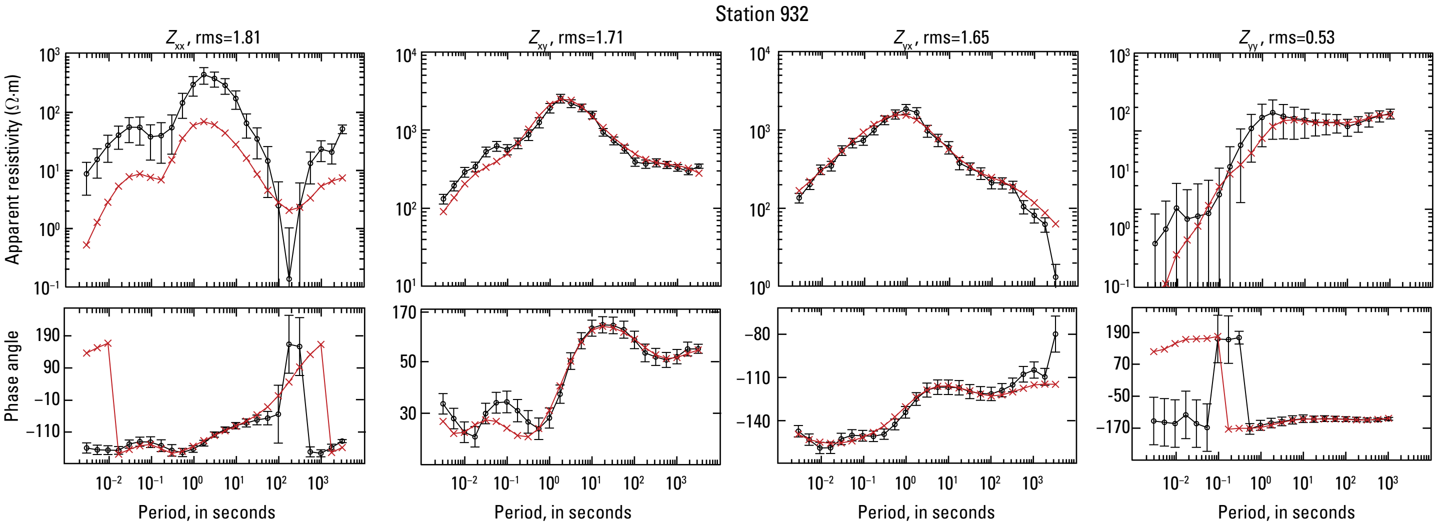

Figure 3.117. Station 932. Plots showing the data inverted (black) and the resistivity model response (red). Shown are all components of the impedance tensor (*Z*) as apparent resistivity (in Ohm meters, Ω·m) and phase angle (in degrees). Data error bars are shown for the inverted data.

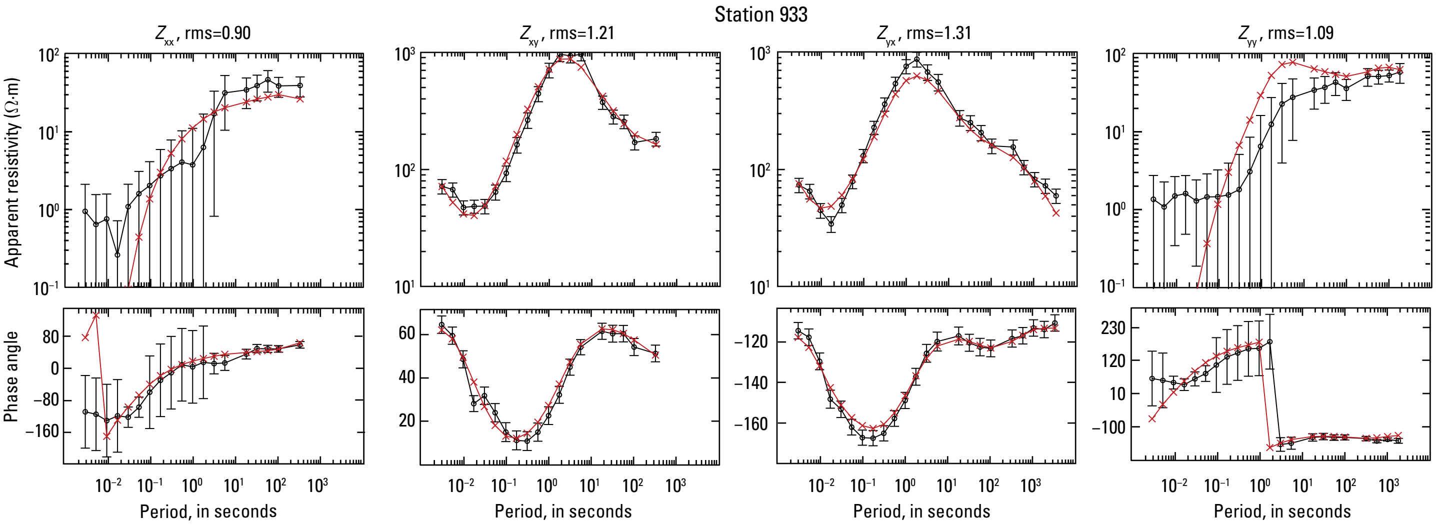

Figure 3.118. Station 933. Plots showing the data inverted (black) and the resistivity model response (red). Shown are all components of the impedance tensor (*Z*) as apparent resistivity (in Ohm meters, Ω·m) and phase angle (in degrees). Data error bars are shown for the inverted data.

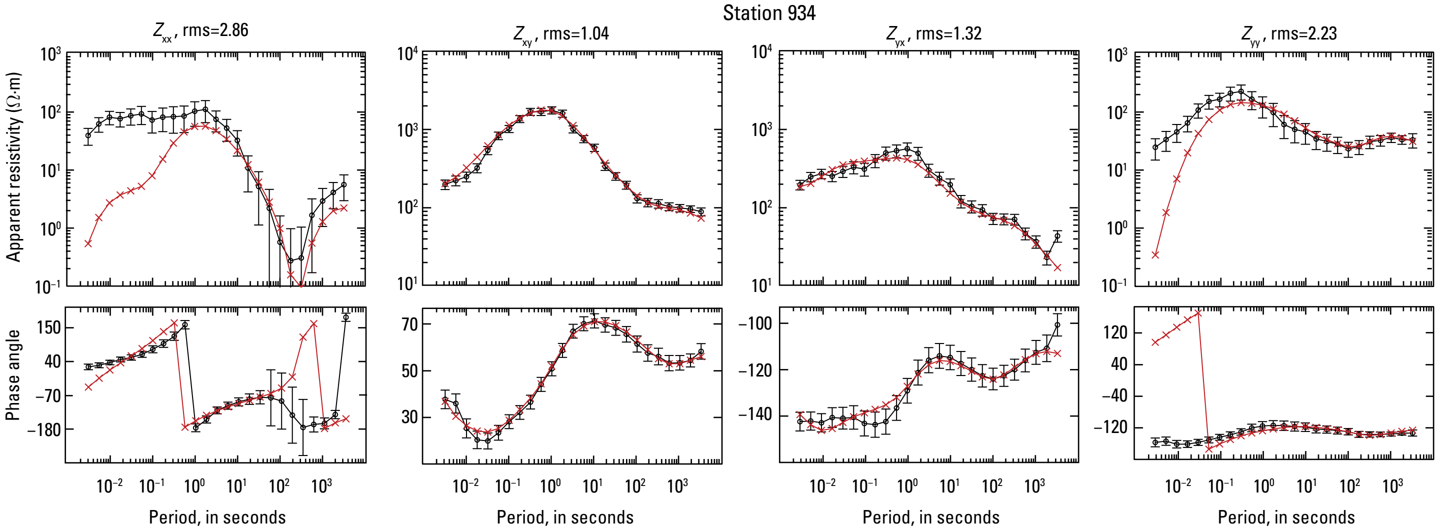

Figure 3.119. Station 934. Plots showing the data inverted (black) and the resistivity model response (red). Shown are all components of the impedance tensor (*Z*) as apparent resistivity (in Ohm meters, Ω·m) and phase angle (in degrees). Data error bars are shown for the inverted data.

Moffett Field Publishing Service Center, California
Manuscript approved October 15, 2019
Edited by Monica Erdman
Layout and design by Kimber Petersen
Illustration support by Katie Sullivan

Peacock and others—**Magnetotelluric Investigation of Northern Harrat Rahat, Kingdom of Saudi Arabia**—Professional Paper 1862–L

ISSN 1044-9612 (print)
ISSN 2330-7102 (online)
https://doi.org/10.3133/pp1862L